

CHARACTERISATION OF INFRARED RADIATIVE FLUX AND FLUX
DIVERGENCE EFFECTS USING A TWO-CHANNEL RADIOMETER –
APPLICATION TO COOLING ON CALM AND CLEAR NIGHTS

Thesis submitted by
Matthew Peter Wilson
BSc. (Hons)

in fulfillment of the
requirements for the Degree of


Doctor of Philosophy

University of Tasmania
November, 2005

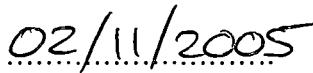
STATEMENT ON SOURCES

DECLARATION

I declare that this thesis contains no material that has been accepted for a degree or diploma by the University or any other institution, except by way of background information and duly acknowledged in the thesis, nor any material previously published or written by another person except where due acknowledgement is made in the text of the thesis.


.....

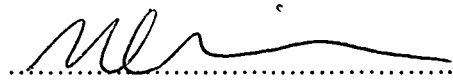
Matthew Peter Wilson


.....

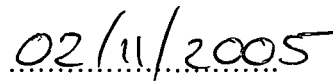
Date

STATEMENT OF AUTHORITY OF ACCESS

This thesis may be made available for loan and limited copying in accordance with the *Copyright Act 1968*.

A handwritten signature in black ink, appearing to read 'M. Wilson', written over a horizontal dotted line.

Matthew Peter Wilson

A handwritten date '02/11/2005' in black ink, written over a horizontal dotted line.

Date

ABSTRACT

This study examines the characteristics of longwave radiation in the nocturnal lower boundary layer atmosphere and its impact on nocturnal cooling. The approach uses field measurements from a purpose-built pyroelectric radiometer that obtains radiance measurements in two spectral channels simultaneously. One of those channels corresponded to a region of strong atmospheric activity and the other was a 'window' channel where atmospheric activity was negligible. Data from the instrument, in combination with predictive equation derived from results from the MODTRAN radiative transfer model, yield the full broadband radiation fluxes that are needed for the nocturnal cooling calculations.

Results of a field measurement program are presented, including comparison of predicted and measured cooling rates on calm clear nights in May, June and July of 2002. Field measurements were made at two sites: Hobart Airport (Lat:-42.8;Lon:147.5) and the University of Tasmania campus in Hobart (Lat:-42.9; Lon:147.3).

Comparison of expected and measured results from the radiometer's field trial showed a consistent underestimation by the MODTRAN model of the upwelling radiation flux in the active spectral channel over short path lengths. The measured values were found to consistently exceed the values predicted by the model. Causes for this underestimation were explored by modeling various atmospheric conditions, without a conclusive result. Comparison of predicted and measured cooling rates yielded a favorable comparison in their trends and a reasonable quantitative comparison. The cooling trend was highest in the early evening and decreased as the evening progressed. Beyond midnight there was a reversal in the cooling, characterised by a brief warming period. Reasons for this process are discussed.

ACKNOWLEDGEMENTS

I gratefully acknowledge the guidance, encouragement and support of my supervisor, Dr Manuel Nunez. His advice always turned my view of the trees back into a view of the forest, and kept the project on track.

I also would like to thank my fellow students Dr Kurt Fienberg, Dr Chris Kuchinke, Danijela Ivkovic, Lily Sekjulica and Dr Jol Desmarchelier for their encouragement and for providing enjoyable breaks from the grindstone. Also thanks to Dr Mick Russell for his technical advice and help in the lab, in addition to the above.

I am extremely grateful to Mr Ian Higginbottom and the management at SonarData Pty Ltd for their efforts to accommodate the completion of the thesis despite a busy work schedule. Their flexibility and encouragement has been key to its completion.

To Paul Waller, Peter Dove and John Davis of the CSL, thank you for your time and effort on the instrument and associated paraphernalia. Your patience for the continual revisions was wonderful and the work was always excellent.

Thanks also to Geoff Fulton and Ian Barnes-Keoghan at the Bureau of Meteorology – Geoff for your generosity in quickly providing additional data within a few days of my measurement nights and Ian for trawling back through the monumental BoM data archives to flesh out bits and pieces well after the fact.

Additional thanks to Denis Charlesworth for his assistance in the lab, Dr Kelvin Michael for recommendations concerning the cold calibration and Dr Ian Barton, Bob Cechet, Dr Peter Novotny and Dr Fred Prata for advice and ideas in the early stages of the project.

I have a deep gratitude to my family and friends who have been there throughout the project with encouragement and understanding. My apologies for the years of sporadic attention, refused invitations, endless conversations about ‘the’ thesis and thanks for putting up with me during the tense moments here and there. Thanks for sticking with me.

And finally, heartfelt thanks to my amazing and beautiful fiancé Anna, who has been with me through the last few years with encouraging words, uplifting smiles and a seemingly

endless supply of positive thoughts. As this chapter of our lives closes, we open the next with our wedding and a long-overdue holiday. Here's to having our weekends back!

TABLE OF CONTENTS

ABSTRACT	i
ACKNOWLEDGEMENTS	ii
Chapter 1: Introduction	1
1.1 Motivation	1
1.2 Study aims	7
1.3 Alternative means for the measurement of radiative flux divergence.....	7
1.4 Instrument design and construction.....	8
1.5 Field-proofing and field measurements	9
1.6 Analysis of radiative and total cooling rates	9
Chapter 2: A ‘virtual’ instrument for irradiance divergence measurement	10
2.1 Introduction	10
2.2 Radiance measurement.....	11
2.3 Avoiding instrument translation via dual-channel measurements.....	12
2.4 Downwelling broadband radiance divergence $divR_{\downarrow B}$	15
2.5 Effect of a dual-channel system on instrument sensitivity requirements	15
2.6 Selection of appropriate spectral bands for instrument filters	16
2.7 Use of brightness temperature T for radiance R	19
2.8 Calculation of upwelling irradiance divergence $divL_{\uparrow}$: testing the effectiveness of the filter selections	21
2.9 Relating upwelling narrow band radiance measurements to broadband radiance divergence $divR_{\uparrow B}$	22
2.10 Calculating upwelling irradiance divergence $divL_{\uparrow}$ by integrating angular measurements of upwelling radiance $divR$	23
2.11 Relating upwelling irradiance divergence $divL_{\uparrow}$ to a single pair of upwelling radiance measurements.....	28
2.12 Downwelling irradiance divergence $divL_{\downarrow}$	30
2.13 Characterising the downwelling irradiance L_{\downarrow} via radiance measurements at height h	31
2.14 Calculating the downwelling irradiance divergence $divL_{\downarrow}$	31
2.15 Calculation of total irradiance divergence $divL^*$	32

2.16	Validation of the virtual instrument's calculations	33
2.17	Summary	43
Chapter 3:	Instrument design and construction	46
3.1	Introduction	46
3.2	Instrument design requirements	46
3.3	Radiance detection using a pyroelectric detector	47
3.4	Reference cavity design and radiation modulation	49
3.5	Electronic design	57
3.6	Potential design improvements	61
3.7	Summary	62
Chapter 4:	Instrument control and sampling	63
4.1	Introduction	63
4.2	Internal instrument control and outputs	63
4.3	Instrument output sequence analysis	66
4.4	'Measurement sequence' definition and design	69
4.5	Summary	74
Chapter 5:	Instrument testing and calibration	75
5.1	Introduction	75
5.2	Rotating instrument mount	75
5.3	Instrument field of view test	79
5.4	A blackbody source for instrument calibration	83
5.5	Optimum instrument chopping speed	86
5.6	Calibration of the instrument – introduction	90
5.7	Calibration of the instrument – warm calibration	90
5.8	Calibration of the instrument – cold calibration	97
5.9	Calibration of the instrument – combined calibration results	102
5.10	Summary	112
Chapter 6:	Field measurement program	115
6.1	Introduction	115
6.2	Field sites	115
6.3	Equipment installation at field sites	120
6.4	Field measurement programs	124

6.5	Field data set description	125
6.6	Summary	126
Chapter 7:	Fieldwork results I – data set descriptions and metadata.....	127
7.1	Introduction.....	127
7.2	Net radiation	127
7.3	Downwelling longwave irradiance	128
7.4	Average air temperature (0.0 to 10.0 metres)	129
7.5	Air temperature stability index (0.1 to 10.0 metres).....	130
7.6	Relative humidity.....	131
7.7	DCR-measured ground brightness temperature.....	132
7.8	Average wind speed.....	133
7.9	Maximum wind speed.....	134
7.10	Wind direction	135
7.11	Cloud amount.....	136
7.12	Nightly data for the 1 st of May 2002.....	136
7.13	Nightly data for the 10 th of May 2002.....	140
7.14	Nightly data for the 13 th of May 2002.....	144
7.15	Nightly data for the 14 th of May 2002.....	147
7.16	Nightly data for the 18 th of June 2002	151
7.17	Nightly data for the 29 th of June 2002	154
7.18	Nightly data for the 30 th of July 2002	157
7.19	DCR measurement sequences.....	159
7.20	MODTRAN profiles for data analysis and results comparison.....	161
7.21	Summary	162
Chapter 8:	Fieldwork results II – instrument and model performance	164
8.1	Introduction.....	164
8.2	Calculation of downwelling irradiance L_{\downarrow} extrapolated from vertical downwelling radiance $R_{\downarrow}(0^{\circ})$ - results	164
8.3	Downwelling irradiance L_{\downarrow} from integration of directional radiance $R_{\downarrow}(\theta)$ - results	168
8.4	Downwelling irradiance L_{\downarrow} from DCR-measured brightness temperatures – data quality analysis.....	171

8.5	Downwelling irradiance L_{\downarrow} from DCR-measured brightness temperatures - reparameterisation of formulae	175
8.6	Downwelling irradiance L_{\downarrow} from DCR-measured brightness temperatures - recalibration of window-channel temperature	179
8.7	Downwelling irradiance L_{\downarrow} from DCR-measured brightness temperatures – combination of reparameterisation and recalibration	184
8.8	Brightness temperatures T_1 and T_2 calculated from upwelling radiance	188
8.9	Upwelling radiance divergence $divR_{\uparrow}$ predicted from brightness temperatures	191
8.10	Upwelling radiance divergence $divR_{\uparrow}$ at angles away from the vertical	195
8.11	Upwelling irradiance divergence $divL_{\uparrow}$	197
8.12	Downwelling irradiance divergence $divL_{\downarrow}$	200
8.13	Examination of the discrepancy between measured and predicted upwelling radiance R_{\uparrow}	206
8.14	Summary	211
Chapter 9:	Fieldwork results III – radiative divergence and cooling	213
9.1	Introduction	213
9.2	Radiative divergence and cooling of the air layer	214
9.3	Synthesis of cooling mechanisms	236
9.4	Summary	237
Chapter 10:	Discussion and conclusion	241
10.1	Virtual instrument	241
10.2	DCR design and construction	243
10.3	DCR measurement results and cooling analysis	244
10.4	Extensions and improvements	246
Bibliography	249
Appendix A:	Calibration reversal procedure	256
A.1	Introduction	256
A.2	Data logger program output	256
A.3	Internal instrument temperature extrapolation	257

Appendix B: ‘Standard” MODTRAN input data259

 B.1 Introduction.....259

 B.2 Example MODTRAN input file.....259

 B.3 MODTRAN parameters261

Appendix C: Analysis of the effects of errors in the measured temperatures on the
quantities calculated by the predictive equations266

Chapter 1

Introduction

1.1 Motivation

Radiative exchange in the atmosphere occupies a central role in the atmospheric heat balance. Much of the work focuses on the development of fast, highly accurate radiative transfer code in various forms. Driving the development of these algorithms has been their use as both predictive and invertible models for the effects of the atmosphere on remotely sensed land and sea surface temperatures (e.g Clerbaux *et al* 2003). Previously, models were developed for use in understanding the effects of radiative processes throughout the atmosphere. The earliest models (e.g Brooks 1950) were based on tabular computation. The computer-based models that followed (e.g Cerni and Parish 1984) conceded the potential accuracy of line-by-line models but improved the speed of calculation by using the concept of a broadband emissivity for each atmospheric layer.

Models more prevalent in recent times have used discrete spectral band models that use precomputed transmission functions for each band, or line-by-line models that individually model each spectral line (e.g Feigelson *et al* 1991). These models provide highly accurate calculations of radiance when sufficiently comprehensive and accurate input data is available. They can also provide indications of the response of that radiance to atmospheric conditions. The model-derived estimates can then be used to further improve models of the processes occurring in the atmosphere.

These models also play a role in the study of radiative processes in the atmosphere near the ground. These processes are defined as those occurring within the boundary layer, the layer of the atmosphere nearest the ground whose structure is determined by longwave infrared radiation, turbulent mixing, gravity waves and advection (Tjemkes and Duynkerke 1989). These broader processes have been studied extensively because their interaction and net effects determine the micrometeorology and microclimate of the atmospheric layer nearest the ground in which most human activity takes place.

This study is concerned with the radiative processes that occur within the boundary layer during the night. At night the radiative effects are dominated completely by longwave radiation due to the absence of shortwave solar radiation after sunset and before sunrise.

The key radiative effect in the nocturnal boundary layer is the longwave irradiance flux divergence (Gaevskaya *et al* 1963). This is a divergence in the longwave radiative flux with height, which indicates the combined effects of longwave absorption, scattering and emission by the atmosphere. The key atmospheric constituents in this process are water vapour and carbon dioxide, the concentration and distribution of which have some dependency on temperature and pressure (Funk 1961). The divergence in the longwave flux through a given volume of the atmosphere determines the radiative cooling of that volume. A convergence in the longwave flux will produce heating of the volume. Other cooling and warming effects include divergence in sensible and turbulent heat fluxes.

Early studies of the divergence of longwave radiation were focussed on the use of existing or modified numerical methods (Rider and Robinson 1951, Funk 1961) to predict the changes in flux with height. This early work suggested that the effect of radiation absorption by the air was comparable to the effect of divergence of sensible heat convection in the magnitude of its effect (Rider and Robinson 1951).

Direct measurements served to validate the importance of direct radiative heating and cooling of the air (Robinson 1950), and indicated radiative cooling rates orders of magnitude higher than would be required to produce the observed total cooling. Further measurements were delayed by the lack of suitably accurate radiometers but later measurements verified that the development of the surface inversion at night was predominantly due to radiative effects (Funk 1960). Another study (Funk 1962) measured radiative flux divergence in an effort to establish its driving nature in the development of radiation fog.

A further observation (Funk 1961) was that the sensible heat flux could be calculated by subtracting the predicted or measured radiative cooling rate from the observed total cooling rate and integrating the resultant temperature change. This technique was adopted in subsequent studies (Elliott 1964, Okamoto and Funk 1971, Nkemdirim 1978). However the use of this method for estimating the sensible heat flux was also argued against (Gaevskaya *et al* 1963, Kondratyev 1972) based on the hypothesis that radiative and sensible heat flux both contribute to and are affected by temperature change and that consideration of the two as additive effects was invalid.

An approach that considered these heat fluxes simultaneously required much greater complexity than previous models that had considered only radiative effects, and various numerical models were proposed that considered both sensible and radiative fluxes (Coantic

and Seguin 1971, Delage 1974). The understanding of the behaviour of the sensible heat flux was also advanced through measurement-based studies (Kondo *et al* 1978, Mahrt *et al* 1982). A comprehensive model emerged (Garratt and Brost 1984) that considered heat flux through and at the surface and the radiative heat fluxes throughout the nocturnal boundary layer (NBL). This model predicted that radiative effects would not greatly affect the bulk properties of the NBL, but also predicted that radiative cooling would dominate the total cooling in two relatively thin layers at the top and bottom of the NBL, corresponding to the lowest 0.1 and highest 0.2 of the boundary layer height.

Further model-based studies (Cerni and Parish 1984, Estournel and Guedalia 1985, Koracin *et al* 1989, Grisogono 1990, Tjemkes and Nieuwstadt 1990, Grisogono and Keislar 1992) evolved and supplemented the existing studies by considering various additional aspects of the NBL structure and processes. A trend throughout these was the progressive introduction of more and more detailed models with the advent of more powerful computing technology.

Beyond the early direct measurements of radiative flux divergence, very few direct measuring attempts were made (Andre and Mahrt 1982). Measurements of the radiative flux divergence within urban canyon structures (Nunez and Oke 1976) yielded predicted radiative cooling rates that compared favourably with the observed total cooling. More recently during the CASES 99 experiment, radiative flux divergence measurements were also made directly and also compared with observed cooling rates (Burns *et al* 2000). The measurements were also considered as part of a study of the heat balance in the NBL (Sun *et al* 2003).

An understanding of the cooling effects of longwave radiation divergence is crucial to the further development of theories regarding the development of radiation fog (Funk 1962, Bergot and Guedalia 1994) and radiation frost (Leuning and Cremer 1988, Leuning 1988, Gardner *et al* 1991), the role of canopies – both urban and vegetative – in slowing the radiative cooling (Oke 1982, Nunez and Sander 1982) and the effects of topography on cooling at night (Kyle 1987, Kobayashi *et al* 1994). The effects of radiative cooling on land surface temperatures are also an important consideration for satellite brightness temperature measurements (Platt and Prata 1993). The requirement for accurate measurements of radiative divergence is important for both the continuation of the development of the theory regarding the NBL, and the consequences of that theory for aviation safety and telecommunications (radiation fog), agriculture (radiation frost), urban and forest planning (heat island studies and cold stress protection) and remote sensing applications (accurate land and sea surface temperature measurements).

Measurements of radiative flux divergence are crucial for the validation of models and for studies of the influence of radiative flux divergence. In situations where radiation frost or fog poses a potential hazard to people, communications or crops, a simple and fast method for the accurate prediction of those phenomena is desirable and was the primary aim of this study.

Past measurement studies of the radiative flux divergence over a horizontal layer have either used twin net radiometers at the top and bottom of the studied layer (Funk 1960) or two sets of similarly arranged opposing pyrgeometers (Burns *et al* 2000). A pair of radiometers facing in opposite directions and vertically translated between two heights has also been employed (Funk 1962). A study involving the radiative flux within a partially enclosed volume (Nunez 1976) used mobile arrays of net radiometers. The use of multiple instruments in this way presents the problem of inter-instrument calibration and the physical mechanics of the required instrument translation.

Further and subtler effects include the difference in the view seen by instruments at different heights. Unless the viewed surface is perfectly homogeneous, an instrument at the land surface will view a different portion of the land surface than an elevated instrument. There is also the problem of the interference of the mounting (for example an instrumentation tower) in the hemispherical field of view of a net radiometer or pyrgeometer.

Instruments with a hemispherical field of view are also not well suited for use in environments with a diversity of structure or surface characteristics such as urban canyons or forests. In such environments an instrument with a narrow field of view can provide information about the effect of the surface or canopy structure on the directionality of the radiant flux (Wilson and Nunez, 2001). Integration of directional measurements can then be used to provide hemispherical fluxes if the required measurements could be obtained in a short period of time relative to the expected changes in the flux.

So for simplified measurements of radiative flux divergence, the ideal instrument is a scanning type (e.g Philipona 2001, Wilson and Nunez 2001) that can provide fast and accurate radiance measurements in the longwave part of the spectrum. Further, the development of a method that facilitates the translation of the instrument or that renders physical translation unnecessary would yield great improvement and simplification in the measurement of radiative flux divergence.

In addition to studies and development of the theory of the role played by longwave radiative divergence in the development of the NBL, the incoming and outgoing longwave radiation have also been studied in depth. Both quantities play an important role in the microclimatology of the atmosphere in the NBL and are crucial to understanding the radiative flux divergence. The flux divergence over a given layer of the atmosphere is defined by the ingoing and outgoing fluxes at its boundaries. The ingoing fluxes for a horizontal layer at the ground are the longwave radiation emitted by the ground surface and the downwelling sky longwave radiation.

The downwelling longwave irradiance from the sky has been the topic of much study. Early micrometeorological research was focussed on the development of empirical formulae in an attempt to accurately predict the downwelling longwave radiation from screen-level measurements of temperature, and in some cases relative humidity or water vapour pressure (Brunt 1932, Swinbank 1963). These studies were based on relating empirical measurements of both the radiation and the quantities used in the prediction. Theoretical formulae were also introduced (Brutsaert 1975).

These formulae introduced the notion of sky emissivity, with the sky's radiation considered as equivalent to that of a greybody at a temperature T . Planck's equation then provided the means of calculating the downwelling irradiance. A review of the available empirical expressions at the time (Arnfield 1979) found systematic departures of the predicted values from the measured values although these errors were generally within the errors for the direct flux measurement.

Further studies either developed these models further, tested their validity under different conditions (Jimenez *et al* 1987) or introduced new formulae (Prata 1996). Other studies were concerned with the application of more advanced radiative transfer models (Fasullo and Sun 2001) or more advanced instruments (Philipona 2001) and instrument-related corrections (Pascal and Josey 2000). Models and comparisons have also been extended to account for the impact of such variables as ground elevation or topography (Saunders and Bailey 1997) and cloudy skies (Iziomon 2003). Downwelling long-wave radiation from clear skies has been used as a test of the radiative components in climate models (Garratt 2001) because it is easily measured, is well characterised and is affected to some extent by a wide variety of atmospheric variables such as temperature and water vapour structure, haze and aerosol content.

A smaller field of study has been the angular variation in the downwelling longwave radiation. Measurements have typically been made using pyrgeometers or net radiometers, which measure the flux from a complete hemisphere. Studies have used hemispherical instruments such as these, angled to give directional readings (Unsworth and Monteith 1975), and scanning narrow field-of-view instruments (Philipona 2001) to measure the angular distribution. Angular effects have also been incorporated into some irradiance models (Olyphant 1986).

The ability to accurately measure or predict the nocturnal downwelling longwave irradiance has important implications for studies of its effect on nocturnal cooling. Many studies consider the net longwave radiation at a given point as an indicator of the relative strength of cooling at that point (Karlsson 2000), and others require it as a component of the energy budget at the surface (Arnfield 1982) for analysis of heat transfer properties. Any instrument that is used to measure radiative flux divergence should also be capable of measuring the longwave downwelling radiation from the sky.

A similar argument applies to the importance of the measurement of upwelling longwave irradiance from a surface as a component of the net radiation and further as a component of the overall heat balance (Choudhury *et al* 1986). The radiative properties of solid surfaces are well known and more easily predicted than the radiative properties of the sky. Analyses of surface emissions have focussed on radiative temperature measurements, either close to the surface via tower-mounted (Lhomme *et al* 1987) or aircraft-mounted (Lagouarde *et al* 2000) radiometers, or via satellite remote sensing. Many studies have been concerned with the effect of urban surfaces (Kobayashi and Takamura 1994) or vegetative canopies on the upwelling longwave radiation. As ground-truthing for remote sensing applications, direct measurements near the ground have also been conducted in order to assess the effect that the structure of the surface has on the directivity of the emitted longwave radiation (Otterman *et al* 1999, Chebhouni *et al* 2001, McAtee *et al* 2003).

Hence it is important in any study considering the radiative flux divergence in the NBL that the upwelling and downwelling radiative flux are also considered separately. In most of the cases mentioned previously these quantities have been measured via the use of the multiple pyrgeometers that are required to yield a radiative divergence measurement - typically two sets of one upward and one downward-facing instrument at different heights. Any instrument that is used to measure radiative flux divergence should also be capable of measuring the longwave upwelling radiation from the ground or any other surface.

1.2 Study aims

The aims of this study are as follows:

1. To establish and test an alternative method for the measurement of radiative flux divergence in the lowest part of the NBL and of broadband longwave radiation flux anywhere in the atmosphere.
2. To design and construct an instrument that is capable of making those measurements.
3. To field-proof the measurement process and the instrument by incorporating the instrument into a field program designed to measure radiative divergence and total cooling rates.
4. To analyse the radiative and total cooling rates in the context of the established theory.

These aims are discussed further in the following sections.

1.3 Alternative means for the measurement of radiative flux divergence

The initial focus of the project was to develop a small, easily transportable, single-channel instrument of the scanning type, for measuring narrowband longwave radiation. The purpose of the instrument would be to provide directional brightness temperature measurements within a forest or urban canopy or above open ground. The extension of the instrument's use to measure radiative flux divergence would require translation through the volume under consideration.

It was determined initially that a dual-channel system would be able to provide the required radiative flux measurements from both the sky and solid surfaces. A channel in the 'window' part of the spectrum (free from major water-vapour and CO₂ bands) could be used to provide brightness temperature measurements of surfaces, as is common practise in infrared thermography. A second channel in a region of strong water vapour and CO₂ activity (an 'active' channel) could then also provide a measure of the atmospheric effects in the intervening atmosphere. The process that was used to choose specific channels is detailed in Chapter 2.

The 'window' channel radiance would then characterise the emission of the solid surface and the water-vapour continuum (Cerni and Parish 1984) in the broadband (3.0 to 50.0 microns) while the 'active' channel would characterise the effect of the atmosphere on the broadband

flux. Together these measurements, along with an appropriate algorithm for the narrow to broadband conversion, could be used to predict broadband radiative flux. Methods and algorithms similar to this are widespread in remote sensing applications (e.g Coll and Caselles 1997, Liang 2000) for improved measurement of land and sea surface brightness temperatures. These studies used multi-channel radiometric measurements together with the inversion of suitable models to provide an estimate of the effect of the intervening atmosphere on the measured surface temperatures. The measured temperatures were then corrected to account for this effect. To the author's knowledge such methods had not been considered previously for measurement of the downwelling longwave flux from clear skies at night.

It became evident during the conceptual development of this study that an instrument measuring in two narrowband channels as specified above could also be used to measure the radiative flux divergence in a layer between the instrument and the land surface. This would alleviate the need for physical translation of the instrument and therefore greatly facilitate the measurement of divergence. The original aim of the project was therefore modified to encompass the development of this concept, which will be presented in full detail in Chapter 2. The aim was to develop an invertible model of the instrument's response to surface longwave emission, longwave emission from a clear sky and longwave activity in the atmosphere. The inversion of the model could then be used to calculate the radiation divergence and associated broadband radiative quantities from the instrument's narrowband radiance measurements.

1.4 Instrument design and construction

A further aim was to design and construct an instrument with which to test this theory. The development of the instrument and the associated model would be interlinked by the choice of spectral band filters for the instrument. The key desirable characteristics of the instrument were as follows:

- Small and lightweight for easy transport and mounting.
- Relatively narrow field of view for directional measurements.
- Scanning ability, either via an internal mechanism or an external scanning mount.
- Fast measuring capability to allow the integration of scanned directional measurements into hemispherical fluxes.
- High-accuracy simultaneous radiance measurements in two narrowband channels.

The design, construction, testing and calibration of the instrument will be presented in Chapters 3, 4 and 5.

1.5 Field-proofing and field measurements

Once the instrument and the associated model-based algorithms for interpretation of its measurements were developed, it was to be incorporated into a field measurement program designed to measure both longwave radiative flux divergence and downwelling longwave flux. In the case of the radiative flux divergence measurements it was desirable to also measure a range of additional parameters such as the temperature and relative humidity throughout the studied layer.

These additional data would provide ‘real’ profiles of temperature and relative humidity, therefore allowing the theoretical calculation of the longwave radiation fluxes and their related divergence. Ideally this would serve to validate the instrument output and the theoretical narrowband to broadband conversion.

The installations used for the field measurement programs will be described in Chapter 6 and the additional data gathered with each measurement sequence will be described in Chapter 7. Chapter 8 will present the results of the comparisons between the model-predicted and instrument-measured results.

1.6 Analysis of radiative and total cooling rates

Depending on the success of the comparisons in Chapter 8 and therefore the success of the instrument in determining radiative cooling rates, the radiative cooling rates could then be compared with the total cooling rates. Insights gained from this comparison could then be compared with those gained from previous studies. The additional data gathered with each measurement sequence would also provide further insight into the dominance or otherwise of the radiative cooling during the night. The results of these analyses and a hypothesis relating to the effect of radiative cooling on the total cooling will be presented in Chapter 9.

Chapter 2

A ‘virtual’ instrument for irradiance divergence measurement

2.1 Introduction

This chapter describes the feasibility of using two thermal infrared channels – a ‘window’ channel and an ‘active’ channel – to obtain longwave irradiance divergence from a stationary sensing platform. Before developing an instrument with which to accomplish this task, it must be demonstrated on theoretical grounds that there is a sufficient degree of coherence in the response to atmospheric constituents in all of the absorption bands of the thermal infrared. This would allow, for example, representation of all of the longwave radiance in the absorption bands by the radiance in one narrow band. This is best accomplished using a radiative transfer model such as MODTRAN 3.7.

MODTRAN (MODerate resolution TRANsmittance) code calculates atmospheric transmittance for electromagnetic radiation frequencies from 0 to 50,000 wavenumber at 2 wavenumber resolution in the infrared portion of the spectrum. MODTRAN is based on the LOWTRAN series of band model algorithms but uses a higher spectral resolution in its molecular band model parameterisation (Berk *et al* 1989). MODTRAN has been used in the development of split-window algorithms (Wan and Dozier 1996) and calculation of atmospheric corrections (Schadlich *et al* 2001) for Land Surface Temperature (LST) derivations from remote sensing data. The original LOWTRAN 7 radiative transfer code upon which MODTRAN is based has been used extensively for estimation of downwelling long-wave radiation (Prata 1996, Michael and Nunez 1991). LOWTRAN has also been used for angular brightness temperature measurements of forest canopy (Lagouarde *et al* 2000) and for determination of cloud infrared optical depths (Prata and Barton 1993).

Reasons for the choice of MODTRAN 3.7 for use in this study were manifold. As illustrated above, its use as a means for deriving longwave radiation fluxes is almost standard across the published literature. If the only requirement had been for near-ground radiative transfer modeling then a specialised model (e.g Tjemkes and Nieuwstadt 1990) could have been considered, however the need to model downwelling longwave radiation as well as near-surface radiative transfer meant that the algorithm used was required to have been well proven for full-atmosphere modeling. The public availability of the code was also a major factor in the choice.

The inputs required by MODTRAN and their format is described in Appendix B, and the model atmospheres used as inputs are well described in the sections to follow.

Using MODTRAN, a ‘virtual’ two-channel instrument is developed that operates in one ‘window’ channel and one ‘active’ channel of the thermal infrared spectrum. The model is then run for a wide range of conditions, allowing the calculation of radiation divergence. The divergences are then compared with the modeled equivalent outputs from the virtual instrument and useful relationships are derived. This task essentially precedes the establishment of a calibration relationship by which the instrument alone may be used to obtain a measure of the required divergences.

2.2 Radiance measurement

The desired result of measuring divergence is to calculate cooling rates for a volume of air via

$$\frac{\Delta T}{\Delta t} = \frac{divL_{\uparrow} - divL_{\downarrow}}{\rho C_p H} \quad (2.1),$$

where ΔT is the change in the average air temperature in °C,

Δt is the period of time over which the change occurs in seconds,

ρ is the density of the air mass in kg/m³,

C_p is the specific heat of the air mass in J/kg/m³,

$divL_{\uparrow}$ is the magnitude of the upwelling longwave hemispherical irradiance divergence in W/m²,

$divL_{\downarrow}$ is the magnitude of the downwelling longwave hemispherical irradiance divergence in W/m² and

H is the height interval over which the divergences are measured, in metres.

H will depend on the configuration of the measuring apparatus.

This leaves $divL_{\uparrow}$ and $divL_{\downarrow}$ as the quantities that must be measured in order to calculate predicted cooling rates based on the divergence of broadband infrared radiation. We have that

$$divL_{\uparrow} = L_{\uparrow}(h_2) - L_{\uparrow}(h_1) \quad (2.2),$$

$$\text{and similarly } divL_{\downarrow} = L_{\downarrow}(h_2) - L_{\downarrow}(h_1) \quad (2.3)$$

for some height interval H between h_1 and h_2 .

Since L is the longwave hemispherical irradiance incident from a given hemisphere, it is also true that

$$L_{\uparrow}(h) = \int_{\cup} R_{\uparrow}(h, \theta, \varphi) \cdot \cos(\theta) \cdot d\Omega \quad (2.4),$$

where $R_{\uparrow}(h)$ is the radiance in watts/m²/steradian incident at height h from a given direction described by zenith and azimuth angles θ and φ respectively. $d\Omega$ denotes the portion of solid angle associated with that radiance and \cup denotes the lower hemisphere. Similarly $L_{\downarrow}(h)$ can be defined as the integral over the upper hemisphere of the radiance $R_{\downarrow}(h)$. If sufficient measurements of the incident radiance can be made over a hemisphere, the irradiance incident from that hemisphere can be calculated by numerically integrating the radiances.

This approach, where the irradiance is partitioned into its component radiances, allows for an instrument that measures with a field-of-view that comprises some smaller portion of a hemisphere. There are many advantages in measuring irradiance via a series of spatially distributed radiances. Most importantly, instruments that measure radiance are simpler to design and construct. Also, measuring radiance allows for greater flexibility in analysing the resulting information, as spatial variability and environmental obstructions or anomalies can be identified and accounted for in the analysis. It is also possible that under certain atmospheric conditions the radiance incident from a single angle may be sufficient to calculate the irradiance for the relevant hemisphere.

2.3 Avoiding instrument translation via dual-channel measurements

As discussed earlier, there are also significant advantages in utilising a measurement system that does not require translation of the instrument in space. Rotation of the instrument is necessary to obtain the required irradiance, but the errors that result from rotating the instrument are substantially smaller than those involved in moving the instrument to a different location. Avoiding translational movement of the instrument would result in a better-performing and more flexible system.

The key to avoiding translational movement lies in using spectral measurements to account for changes in incident radiance with height. It will be shown that a dual spectral channel instrument can bypass the need for instrument translation, provided suitable spectral

channels are selected and the instrument limitations are known and taken into consideration. The following section describes the approach.

Considering the infrared spectrum as a set of discrete bands and using B to denote the broadband infrared spectrum (3-50 μ), it can be said that

$$B = W + A \quad (2.5),$$

where W is the set of all non-contiguous bands that are effectively infrared ‘windows’ in the atmosphere and A is the set of all non-contiguous bands in which the atmosphere is active in the infrared. Assuming that at some spectral resolution all bands can be classified as either a window or active band (without overlap) it follows that W and A can be expressed as

$$W = \sum_B w_i \quad (2.6),$$

$$\text{and } A = \sum_B a_i \quad (2.7)$$

respectively, where w_i and a_i are individual window and active bands across the 3-50 μ range of the spectrum and B denotes the entire 3-50 μ range of the spectrum.

Considering first the upwelling radiance, if the radiance from a solid emitting surface at temperature T in a spectral band w defined by $(\lambda_{w1}, \lambda_{w2})$ can be given by

$$R_w(T) = \int_{\lambda_{w1}}^{\lambda_{w2}} P(\lambda, T) d\lambda \quad (2.8),$$

where P is Planck’s function, and assuming that emissivity is 1 across the full spectrum then equation (2.8) can be inverted to give T if R_w is known. Equation (2.8) can then be used, with the same values of T and the emissivity, to determine R_a for some other spectral band a .

Consider a height interval H over which radiance differences are to be measured, in particular the special case where $h_1=0$, that is the lower boundary of the height interval H is the ground. Equation (2.8) applies to the ground as a solid emitting surface and by definition of a window band w_i we have that

$$R_{\uparrow w}(h_2) \cong R_{\uparrow w}(0) \quad (2.9)$$

other than continuum effects and if and only if w is some spectral interval comprised only of contiguous window bands and is therefore defined by

$$w = \sum_{\lambda_{w1}}^{\lambda_{w2}} w_i \quad (2.10).$$

Inversion of equation (2.8) allows that the ground surface temperature T_g can be calculated from $R_{\uparrow w}(0)$, which according to equation (2.9) can be very closely approximated by measuring $R_{\uparrow w}(h_2)$ if the condition on the spectral band w stated in equation (2.10) is true. Further, since $h_1=0$ and there is no intervening air mass that might radiate or absorb in the active spectral bands, it can be asserted that

$$R_{\uparrow a}(0) = \int_{\lambda_{a1}}^{\lambda_{a2}} P(\lambda, T_g) d\lambda \quad (2.11),$$

where a is any active spectral band, and also that

$$R_{\uparrow B}(0) = \int_B P(\lambda, T_g) d\lambda \quad (2.12),$$

where B is the broadband infrared spectrum.

If we choose the spectral band a such that it is comprised of active bands a_i in the spectrum and it can be shown that $R_{\uparrow A}(h)$ – the combined radiance in all active spectral bands – is some function of $R_{\uparrow a}(h)$, then $R_{\uparrow B}(h)$ can be calculated via

$$R_{\uparrow B}(h) = R_{\uparrow B}(0) + R_{\uparrow A}(h) - R_{\uparrow A}(0) \quad (2.13),$$

which when rearranged gives the broadband radiance divergence $divR_{\uparrow B}$ via

$$divR_{\uparrow B} = R_{\uparrow B}(h) - R_{\uparrow B}(0) \cong R_{\uparrow A}(h) - R_{\uparrow A}(0) \quad (2.14)$$

where $R_{\uparrow B}(0)$ is calculated from a measurement in the window band via equations (2.12) and (2.8), $R_{\uparrow A}(0)$ via equation (2.11) and $R_{\uparrow A}(h)$ via $R_{\uparrow a}(h)$ and the relationship between $R_{\uparrow A}(h)$ and $R_{\uparrow a}(h)$.

In summary, if it can be said that for two functions f_1 and f_2

$$R_{\uparrow B}(0) = f_1(R_{\uparrow w}(h)) \quad (2.15)$$

$$\text{and } R_{\uparrow B}(h) = f_2(R_{\uparrow a}(h)) \quad (2.16),$$

then it holds that for some function f_3 that

$$divR_{\uparrow B} = f_3(R_{\uparrow w}(h), R_{\uparrow a}(h)). \quad (2.17).$$

Equation (2.17) then shows that the broadband upwelling radiance divergence over a height interval H defined by two heights h_1 and h_2 (where $h_1=0$ and $h_2=h$) can be calculated from two narrow band radiance measurements $R_{\uparrow w}(h)$ and $R_{\uparrow a}(h)$, both at height h . If unique relationships exist between narrow and broadband radiances which have the general form expressed in equations (2.15) and (2.16), then there will also exist some unique relationship

between broadband divergence and the radiance measured in two narrow bands, one a window band and the other an active band.

2.4 Downwelling broadband radiance divergence $divR_{\downarrow B}$

The divergence $divR_{\downarrow B}$ of downwelling broadband radiance must also be considered. Although there is the same absorptive and emissive capacity by the atmosphere in the layer H , downwelling infrared radiation is typically significantly less in magnitude than the upwelling. The divergence

$$divR_{\downarrow B} = R_{\downarrow B}(h) - R_{\downarrow B}(0) \quad (2.18)$$

is likely to be smaller than the divergence of the upwelling. However, it must still be quantified so that the broadband divergence $divR_B$ where

$$divR_B = divR_{\uparrow B} - divR_{\downarrow B} \quad (2.19)$$

can be calculated. It will be shown that $divR_{\downarrow B}$ is a function of $R_{\uparrow A}$, $R_{\uparrow W}$, $R_{\downarrow A}$ and $R_{\downarrow W}$, and can be calculated by defining a function based on the results of a large set of atmospheric modelling results.

2.5 Effect of a dual-channel system on instrument sensitivity requirements

The use of a dual-channel measuring instrument has an additional benefit for the measurement of divergence in that the sensitivity required of the measurement instrument is reduced. This reduction is a result of the separation of the spectrum into active and non-active bands.

Upwelling broadband radiance at any height can be given by

$$R_{\uparrow B} = \sum_W R_{\uparrow w_i} + \sum_A R_{\uparrow a_i} \quad (2.20).$$

We have seen from equation (2.14) above that

$$R_{\uparrow B}(h) - R_{\uparrow B}(0) \equiv R_{\uparrow A}(h) - R_{\uparrow A}(0),$$

and therefore that

$$\Delta R_{\uparrow B} = \Delta R_{\uparrow A} = \Delta \sum_A R_{\uparrow a_i} \quad (2.21).$$

Any instrument such as a standard pyrgeometer that measures divergence via the broadband radiance at two heights h_1 and h_2 must measure both the active and window components of the full broadband spectrum. The sensitivity of the instrument signal – defined as the ratio of

the smallest detectable difference in the measured radiance against the maximum measurable radiance – must be at least sufficient to detect any difference in the active bands. The minimum sensitivity over the broad band (S_B) required to measure such a change is given by

$$S_B = \frac{\Delta R_{\uparrow B}}{R_{\uparrow B}} = \frac{\Delta R_{\uparrow A}}{R_{\uparrow A} + R_{\uparrow W}} \quad (2.22).$$

If another instrument were capable of measuring only in the active bands of the spectrum, then the minimum sensitivity S_A required to measure the change would be given by

$$S_A = \frac{\Delta R_{\uparrow A}}{R_{\uparrow A}} \quad (2.23).$$

Although the ratio between the relative sensitivities S_A and S_B will depend on the fractional distribution of the bands, it is obvious that $S_A > S_B$ always, which eases the requirement of minimum sensitivity of a candidate instrument and facilitates instrument design. This condition holds for S_a , the sensitivity in a narrow active band a , if we can show that $R_a(h)$ is some function of $R_d(h)$ as discussed previously.

2.6 Selection of appropriate spectral bands for instrument filters

In order to implement the theory described above, two appropriate filter bands a and w were chosen. The band choice was made based on spectral modelling performed using the MODTRAN (v3.7) radiative transfer model. The choice of bands was somewhat restricted by manufacturing constraints, but was made based on two main factors – firstly the amount of atmospheric activity in the given band (or lack of it) and secondly the relative amount of blackbody radiance in the band. As seen above, these two quantities are key factors in determining the sensitivity of which the instrument is capable.

Filter choices were made based on the results of a specific model test case designed to highlight the atmospheric spectral activity. The model was based on an atmospheric profile that produces significant upwelling radiance divergence over fifteen metres. The spectral radiance curve produced by the model at zero height was then subtracted from the radiance curve produced at fifteen metres. The resulting curve was examined for significant areas of maximal and minimal atmospheric activity. Sections of the curve showing minimal and maximal atmospheric activity are shown in Figures 2.1a and 2.1b below. Note the relative scales on the vertical axes of each graph.

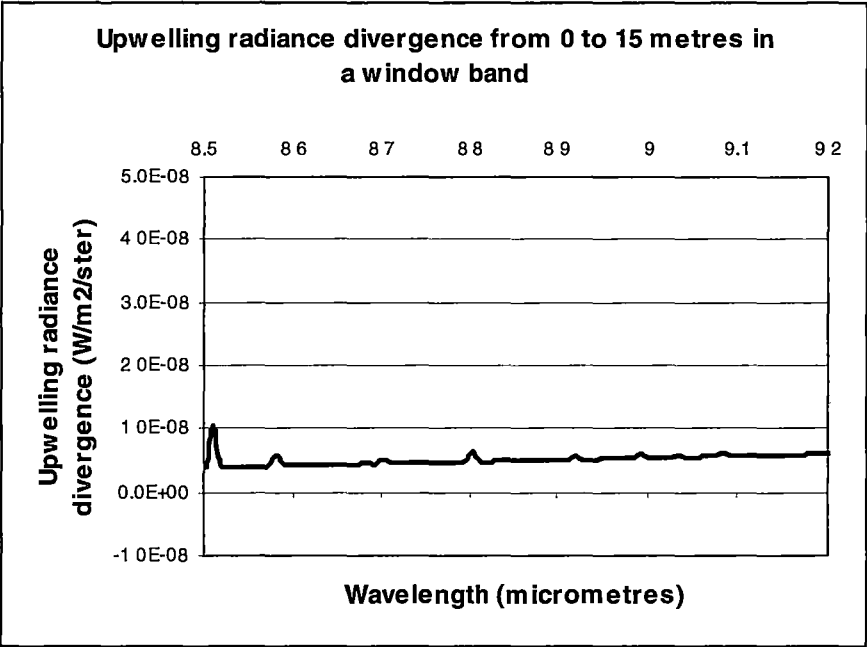


Figure 2.1a. Illustration of atmospheric activity in a window spectral channel (8.5-9.2 μm).

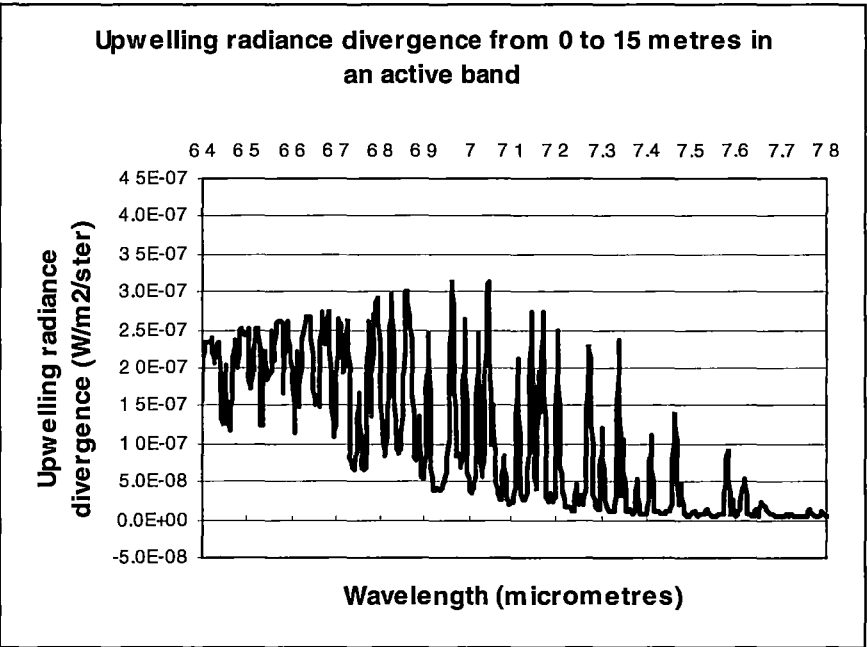


Figure 2.1b. Illustration of atmospheric activity in an active spectral channel (6.4-7.8 μm).

The spectral response curves corresponding to the chosen filters are shown below. The two filter regions were chosen which best represented the window and the active channel. The response curves for these filters are shown in Figure 2.2a and 2.2b below. The exact pass

bands of the filters and the shape of the response curve were determined by manufacturing constraints – the choice was based on finding a best-case match between the available filters and the spectral response curves such as those shown in Figures 2.1a and 2.1b above.

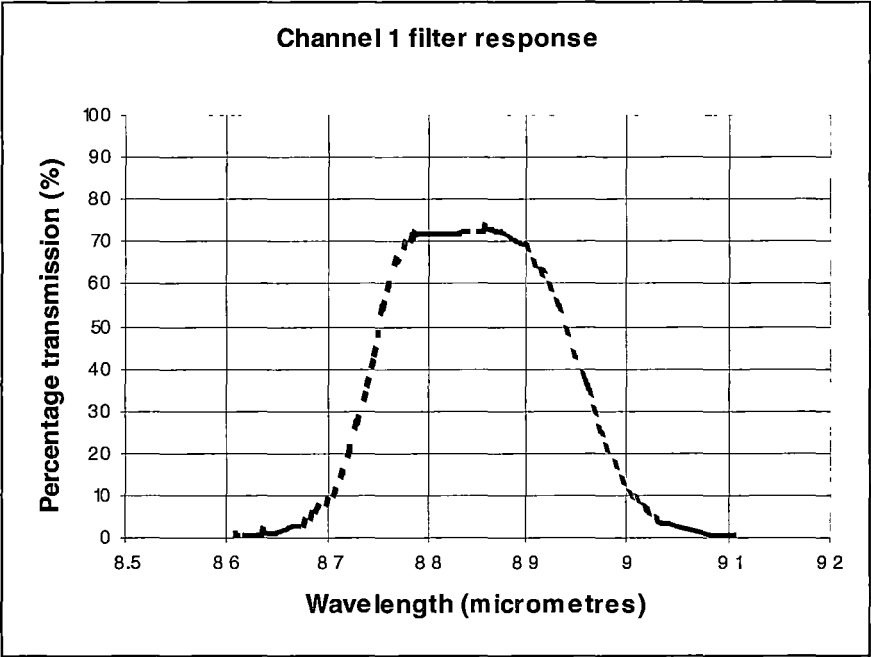


Figure 2.2a. Channel 1 filter response (8.5-9.2 μm).

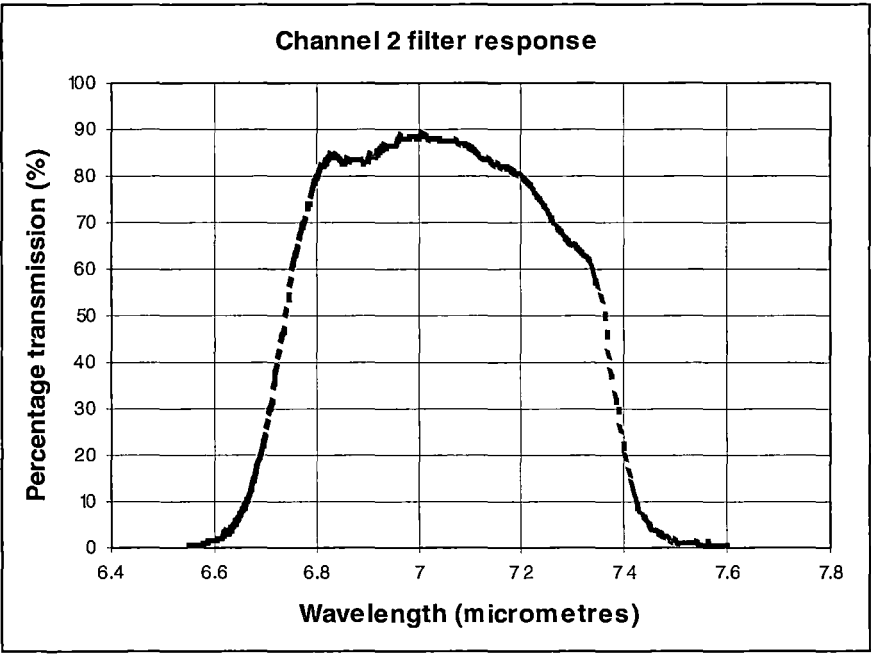


Figure 2.2b. Channel 2 filter response (6.4-7.8 μm).

The upwelling divergence in the modeled broadband radiance over the fifteen-metre height difference was calculated to be 1.40 W/m²/steradian compared to a total broadband radiance of 118.74 W/m²/steradian, a ratio of 1.18%. In comparison, the radiance in the channel 1 window filter band was calculated to be 1.16 W/m²/steradian compared to a divergence of 9.5x10⁻⁴ W/m²/steradian, a ratio of 8.2x10⁻²%, while the radiance and divergence in the channel 2 active filter band were 2.79 W/m²/steradian and 0.11 W/m²/steradian respectively, yielding a ratio of 3.94%. The advantage of choosing to measure in two distinct channels is plain, and if the ratios can be considered as a guide to the required relative sensitivity of a candidate instrument, these example calculations serve to reinforce the benefits described earlier.

2.7 Use of brightness temperature T for radiance R

Conversion of radiances *R* to effective (brightness) temperatures effectively inverts the relationships described in equations (2.8), (2.11) and (2.12) above, and allows the instrument's eventual blackbody calibration (which is referenced to blackbody source temperatures in °C) to be applied directly rather than via a theoretical conversion to radiances. This conversion was achieved using a large set of modeled radiance measurements, detailed in Table 2.1 below:

Air temperature T_A (°C)	Ground surface temperature T_G (°C)	Instrument Height above ground (m)	Relative Humidity RH (%)	Direction (° zenith)
0, 5, 10	T _A -5, T _A -4,..., T _A , T _A +1,... T _A +5	0, 5, 10, 15	40, 60, 80	0, 180
-2.5, 2.5, 7.5, 12.5	T _A -5, T _A -2.5, T _A , T _A +2.5, T _A +5	0, 5, 10, 15	40, 60, 80	0, 180

Table 2.1. Combinations of air temperature, ground temperature, instrument height, relative humidity and viewing direction for each model profile.

The input parameters listed here define 1272 separate scenarios. These were used with the MODTRAN v3.7 radiative transfer model to output spectral radiance over the entire broadband infrared spectrum from 3.0 to 50.0 microns. Appendix B describes the common elements of the MODTRAN input file that was used. Each of the 1272 spectral radiance distributions were then multiplied by each of the filter responses in Figures 2.2a and 2.2b

(giving two results per radiance distribution, one for each channel) as well as the response curve of a Barium Fluoride (BaF_2) window, thus mimicking the radiance as seen in each of the two channels of the ‘virtual’ radiometric instrument. The BaF_2 window was found to be necessary during construction of the ‘real’ instrument (see Chapter 3). These multiplications were performed at single wavenumber resolution, the results then integrated to give per-channel radiance values. MODTRAN also produces an integrated broadband radiance value as a part of the model output - this was recorded and used as the broadband radiance in future calculations.

Each ‘scenario’ corresponds to one unique combination of values from the table above. The air temperature (T_A) and relative humidity (RH) values are set constant from zero height to one kilometre. Figure 2.3 below shows the additional temperature and humidity profiles (the same for each scenario) beyond 1km height:

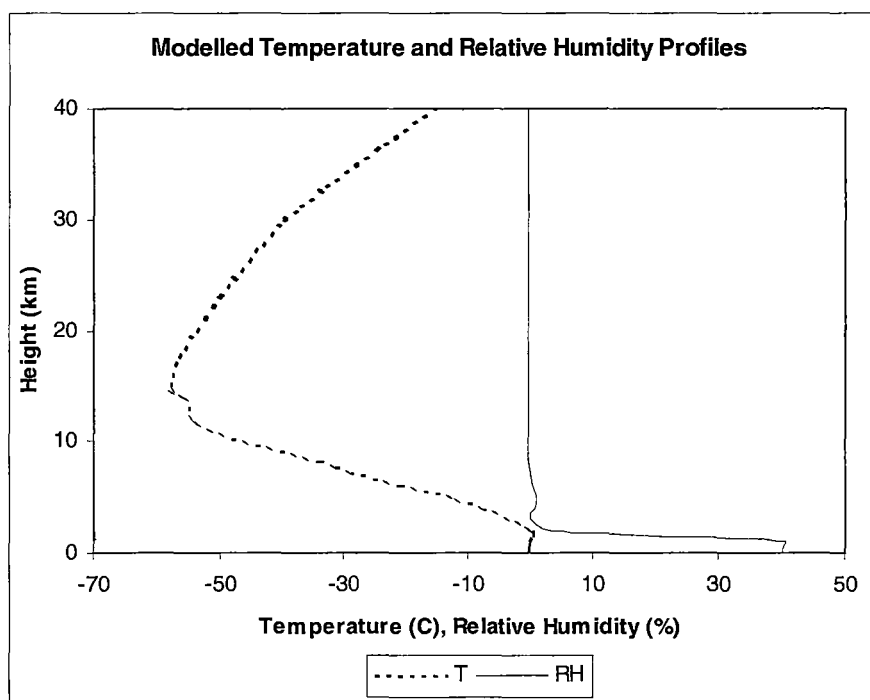


Figure 2.3. Modeled temperature and relative humidity profiles above 1km height.

This treatment of the values over the first kilometre of atmosphere was not intended to reflect realistic atmospheric profiles. The intent was that a relationship linking the narrow window and active band radiances to the broadband radiance could be found that was independent of profile shape and other atmospheric parameters. It is shown later that this process worked well for the upwelling radiances but was not appropriate for downwelling

radiance, as these are more strongly dependent on ‘realistic’ atmospheric profiles above the measurement height. It was also established through these tests that the profile data above the measurement height have very little impact on the modeled upwelling radiance values.

The first step in analysis of the MODTRAN results was to examine the form of the relationships between the upwelling radiance in the two narrow band channels and the ground surface temperature T_G when the radiance measurement is made at a distance of zero metres from the surface. The formulae describing these relationships were established by fitting third-order polynomial curves to the modeled data and resulted in the following:

$$T_1 = 0.78249 \cdot R_a^3 - 8.1286 \cdot R_a^2 + 41.707 \cdot R_a - 55.076 \quad (2.24),$$

$$\text{and } T_2 = 10.531 \cdot R_w^3 - 47.808 \cdot R_w^2 + 112.34 \cdot R_w - 67.474 \quad (2.25),$$

where 2 and 1 denote spectral bands w and a , in window and active parts of the broadband spectrum respectively. The relationships described in both equations give an R^2 value of 1.0000, and the RMS errors in these parameterizations are 0.0051°C (0.08%) for T_1 and 0.0025°C (0.04%) for T_2 . Each relationship was established based on 159 data. All of the above formulae for T are derived from the upwelling radiance R_\uparrow in the given spectral band at zero distance from a surface with modeled temperature T_G .

Equations (2.24) and (2.25) effectively invert equations (2.11) and (2.8) respectively. In the operational mode R_a and R_w represent radiance at any height above the surface. Therefore T_1 and T_2 give the brightness temperature at any arbitrary level. Because the fundamental purpose of these equations is to represent radiance as a brightness temperature, they maintain their validity when applied to radiance data measured at angles away from the vertical and irrespective of upwelling or downwelling direction.

2.8 Calculation of upwelling irradiance divergence $\text{div}L_\uparrow$: testing the effectiveness of the filter selections

T_2 was calculated from $R_{\uparrow w}$ for all heights h – for the 636 data corresponding to the upwelling radiance – making it possible to examine the maximum change in effective temperature over distance, or maximum δ where

$$T_2(RH, T_A, T_G, h) = T_2(RH, T_A, T_G, 0) + \delta(RH, T_A, T_G, h) \quad (2.26),$$

where δ is the incremental change in brightness temperature corresponding to change in height from 0 to h . Over the parameter ranges shown in Table 1 above, it was found that

$$0 \leq |\delta| \leq 0.06^\circ\text{C} \quad (2.27),$$

and that the RMS error in the relationship between $T_2(h=0)$ and $T_2(h \neq 0)$ is 0.0095°C (0.15%). This illustrates the effectiveness of the choice of window band channel – over any distance up to fifteen metres and over a broad range of atmospheric conditions, the change in brightness temperature with distance is effectively negligible. This allows the accurate estimation of ground temperature $T_2(h=0)$ from a brightness temperature T_2 measured at a distance. This result confirms the validity of equation (2.8) for this choice of window band filter.

Further, the effective temperatures T_1 and T_2 are in close agreement (RMS error of 0.0033°C or 0.05% for 159 data) for all modeled parameter sets with the direction set to upwelling and height zero. This close agreement provides a straightforward calculation of divergence in the active band via $R_{\lambda_a}(h) - R_{\lambda_a}(0)$, since $R_{\lambda_a}(h)$ is measured via T_1 and $R_{\lambda_a}(0)$ is provided by $R_{\lambda_w}(0)$ (with negligible error as seen above) which is in turn provided by $R_{\lambda_w}(h)$, also with negligible error as seen above. As $R_{\lambda_w}(h)$ is measured via T_2 , the two brightness temperature measurements at height h provide the necessary information for calculating the radiance divergence of the upwelling longwave radiance in the active narrow band.

2.9 Relating upwelling narrow band radiance measurements to upwelling broadband radiance divergence $\text{div}R_{\lambda_B}$

The modeling detailed above provides an extensive range of radiance data in the broadband spectrum. Divergences were calculated by subtracting the broadband radiance at zero height from the broadband radiance at each non-zero height (5, 10, 15m) for every set of input conditions. The relationship between the upwelling broadband radiance divergence and the effective temperatures in the narrow and active bands was then plotted and quantified. The resulting relationship is independent of height and atmospheric conditions, an essential requirement in establishing the independence of the measurement process. It was found that the relationship between the broadband radiance divergence and the effective temperatures takes the form

$$\text{div}R_B = 7.128 \times 10^{-3} T_{\lambda_1}^2 - 7.008 \times 10^{-3} T_{\lambda_2}^2 + 0.697 T_{\lambda_1} - 0.698 T_{\lambda_2} + 2.162 \times 10^{-3} \quad (2.28),$$

with $R^2=0.9986$, standard error of $0.0189 \text{ W/m}^2/\text{ster}$ (or 4.7%) and the parameterisation based on 477 data.

Equation (2.28) essentially provides an explicit relationship between the broadband divergence in the upwelling longwave radiance and $T_1(h)$, $T_2(h)$ which in turn are related to

$R_{\uparrow a}$ and $R_{\uparrow w}$. The equation thus defines the functional form of the general equation presented in equation (2.17).

Figure 2.4 below shows the predicted values (a function of T_1 and T_2) versus the MODTRAN modeled values (modeled based on T_G , T_A , RH , h):

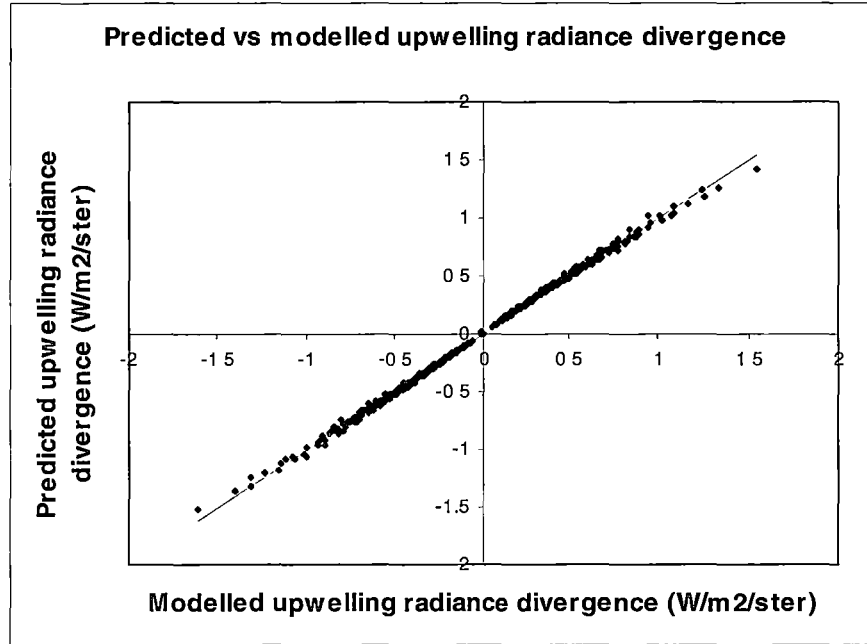


Figure 2.4. Predicted versus modeled upwelling radiance divergence. Predicted values calculated using equation (2.28).

2.10 Calculating upwelling irradiance divergence $divL_{\uparrow}$ by integrating angular measurements of upwelling radiance divergence $divR$

While equation (2.28) allows radiance divergence to be calculated from the effective temperatures in two channels, in the case where the cooling rate of a horizontally homogenous atmospheric layer is to be calculated via equation (2.1) the irradiance divergence must either be measured or calculated. In the earlier case, equation (2.28) must be applied to the effective temperatures measured at any angle of incidence to calculate the radiance divergence at that angle of incidence. The radiance divergences can then be integrated over a hemisphere to give the divergence in the irradiance via

$$divL_{\uparrow}(h) = \int_{\Omega} divR(\theta, h) \cdot \cos \theta \cdot d\Omega \quad (2.29).$$

To verify the validity of equation (2.29) as a means of calculating the upwelling broadband irradiance divergence, a further set of atmospheric models were run using MODTRAN.

These models were based upon real profiles and intended to mimic realistic atmospheric conditions. The profiles extended from the ground up to 40km height, further than was necessary for the upwelling case but necessary for also modeling the downwelling angular radiance. Details of the model input profiles used for computing L_{\uparrow} , L_{\downarrow} and the radiative flux divergence are given in Tables 2.2 and 2.3 below. Each yielded 192 different profiles. An indication of the scope of the irradiance values present in the results is given in Figure 2.5. The radiant incidence angle values used were (from the vertical): 0, 15, 30, 45, 60 and 75°.

Layer index	Height (km)	Relative Humidity RH (%)
0	0.0	RH(2)
1	0.01	RH(2), RH(2)-5
2	0.02	75.0, 85.0, 95.0
3	0.2	55.0, 65.0
4	1.7	75.0, 85.0
5	2.0	RH(6)-10.0
6	3.5	RH(7)+5.0
7	4.0	RH(8)-10.0
8	8.0	25.0, 35.0
9	10.0	25.0, 40.0
10	12.0	25.0, 40.0
11	13.0	~0
12	22.0	~0
13	30.0	~0
14	40.0	~0

Table 2.2. Relative humidity at each layer height used to generate model profiles.

Layer index	Height (km)	Temperature T (°C)
0	0.0	T(1)-3.0, T(1)-1.0, T(1)+1.0, T(1)+3.0
1	0.02	T(2)-4.0, T(2)-2.0, T(2)
2	0.2	3.0, 6.0, 9.0, 12.0
3	1.7	-3.0, 3.0
4	2.0	0.0, 6.0
5	12.0	-60.0
6	22.0	-60.0
7	30.0	-37.3
8	40.0	-13.5

Table 2.3. Temperatures at each layer height used to generate model profiles.

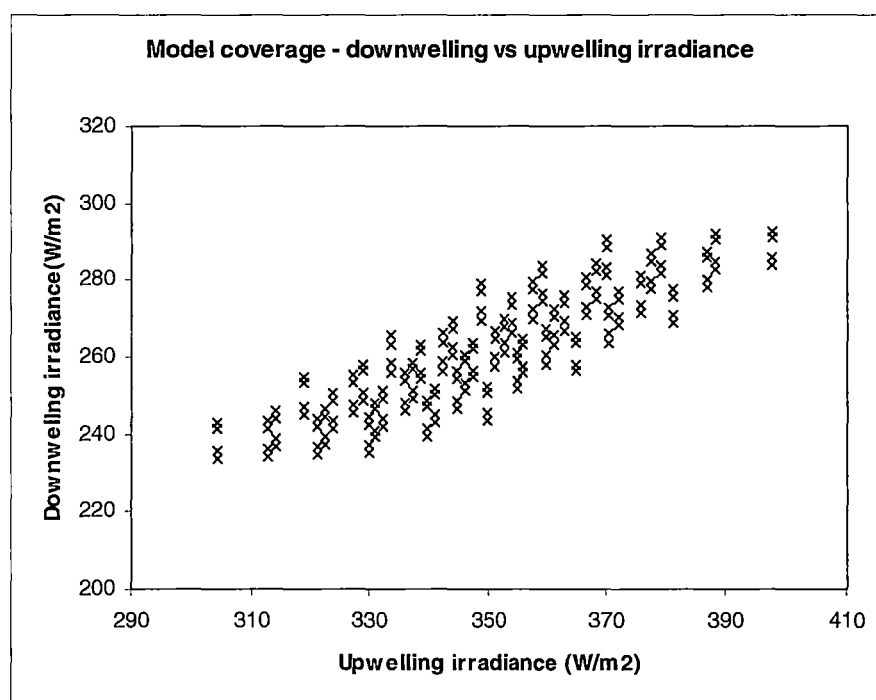


Figure 2.5. Combinations of upwelling and downwelling total longwave irradiance produced by the modeled profiles.

To validate the application of equation (2.28) to upwelling radiance divergence calculations away from the vertical, modeled values for the upwelling radiance divergence were compared with values predicted by equation (2.28). This test was essential to determine that the calculation of radiance divergences expressed by equation (2.28) could legitimately be applied to measurements at angles away from the vertical. For the 1152 values modeled and

predicted (192 different atmospheric profiles with six angles of incidence each) it was found that the RMS error between the predicted and modeled values for all angles was 0.0472 W/m²/steradian. When each angle of incidence was considered individually it was found that the RMS error between modeled and predicted radiance divergence exhibits some angular dependence, with values from 0.0353 W/m²/steradian at 0° incident angle to 0.0691 W/m²/steradian at 75° incidence. However the relative RMS error remains reasonably constant across the range of angle values, as shown in Table 2.4 below. This demonstrates that the parameterisation in equation (2.28) produces an acceptably uniform degree of accuracy for upwelling radiance divergence at all angles of incidence.

Incident angle (°)	RMS error (W/m ² /ster)	Average magnitude of $divR_{\uparrow B}$ (W/m ² /ster)	RMS error (%)
0 ($i=0$)	0.0353	0.350	10.1
15 ($i=1$)	0.0360	0.357	10.1
30 ($i=2$)	0.0384	0.372	10.3
45 ($i=3$)	0.0432	0.404	10.7
60 ($i=4$)	0.0521	0.463	11.2
75 ($i=5$)	0.0691	0.585	11.8

Table 2.4. RMS error in the predicted values of the angular upwelling radiance divergence.

The relative differences between predicted and modeled values are obviously present to a similar degree in the irradiance divergence values. The irradiances were calculated by summing the radiance values. This was achieved using a weighted sum as follows:

$$divL_{\uparrow}(h) = \sum_{i=0}^5 divR_{\uparrow_i}(h, \theta_i) \cos \theta_i \cdot \delta\Omega_i \quad (2.30),$$

where

$$\delta\Omega_i = 2\pi((1 - \cos \phi_{1,i}) - (1 - \cos \phi_{2,i}))$$

and in general

$$\phi_{1,i} = \theta_i + \frac{\theta_{i+1} - \theta_i}{2} \text{ and } \phi_{2,i} = \phi_{1,(i-1)},$$

where θ_i is the angle of incidence. For $i=0$ ($\theta_i=0^\circ$) and $i=5$ ($\theta_i=75^\circ$), the boundary conditions are $\phi_{2,0}=0^\circ$ and $\phi_{1,5}=90^\circ$. The formula for $\delta\Omega_i$ is based on the fact that the solid angle Ω , symmetrical about zenith angle zero and subtended by an angle 2ϕ is given by

$$\Omega = 2\pi(1 - \cos \phi).$$

To calculate the solid angle of a band (shown in red in the figure below) spanning two zenith angles that remain constant with azimuth angle, the smaller solid angle (shown in blue) is subtracted from the larger (which consists of both red and blue portions).

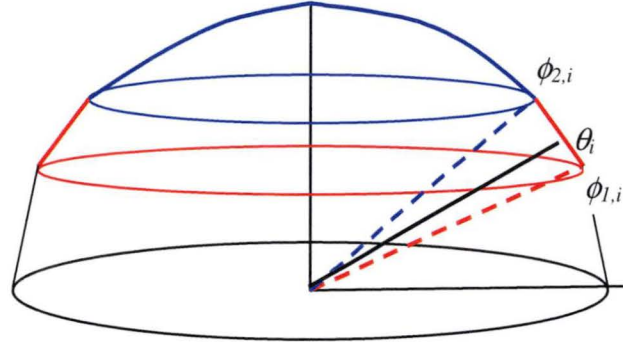


Figure 2.6. Illustration of the solid angle produced by the two angles $\phi_{1,i}$ and $\phi_{2,i}$ enclosing the measurement angle θ_i .

Comparing integrated modeled values with integrated predicted values of $divL_{\uparrow}$ for the 192 modeled atmospheric profiles gives a RMS error of 0.159 W/m^2 , or 10.9% relative to the average magnitude of the integrated divergence. A chart of the predicted versus modeled values is given below:

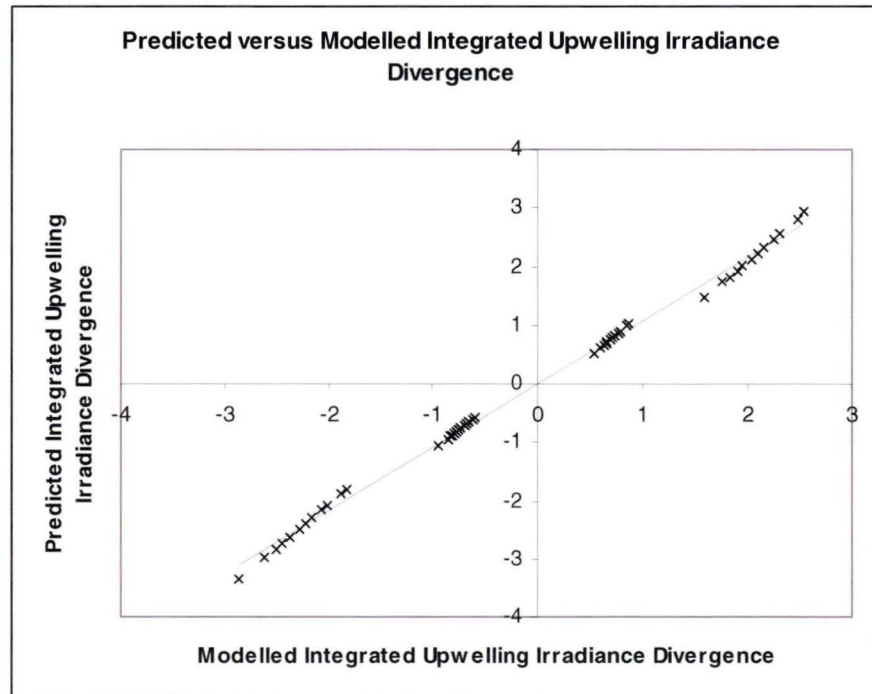


Figure 2.7. Predicted versus modeled angular upwelling longwave radiative divergence. Predicted values calculated using equation (2.29). The four clusters of points correspond to the four temperature values at $h=0$, indicating the dominant effect of that temperature value.

2.11 Relating upwelling irradiance divergence $divL_{\uparrow}$ to a single pair of upwelling radiance measurements

A further comparison was made in order to assess the possibility of parameterising the upwelling irradiance divergence with respect to the vertical radiance divergence under certain conditions. Under clear sky conditions at night in flat, open and uniform ground it is reasonable to assume that the directly vertical upwelling radiance divergence may be in some way representative of the upwelling irradiance divergence. The existence of a simple relationship between the two would simplify the measurement process considerably for the upwelling case as it would require only a single measurement in each channel. These conditions are implicitly included in the model – in practice the constraints on the environmental conditions will apply to the conditions under which measurements must be made if such a parameterisation is to be applied.

The equation resulting from the parameterisation has the following form:

$$divL_{\uparrow} = -1.1263divR_{\uparrow B}^3 - 0.01052divR_{\uparrow B}^2 + 4.2583divR_{\uparrow B} \quad (2.31)$$

with standard error 0.0810 W/m^2 and $R^2=0.9979$. The parameterisation was based on 192 data, and a chart of the 192 predicted versus modeled values is shown in the figure below:

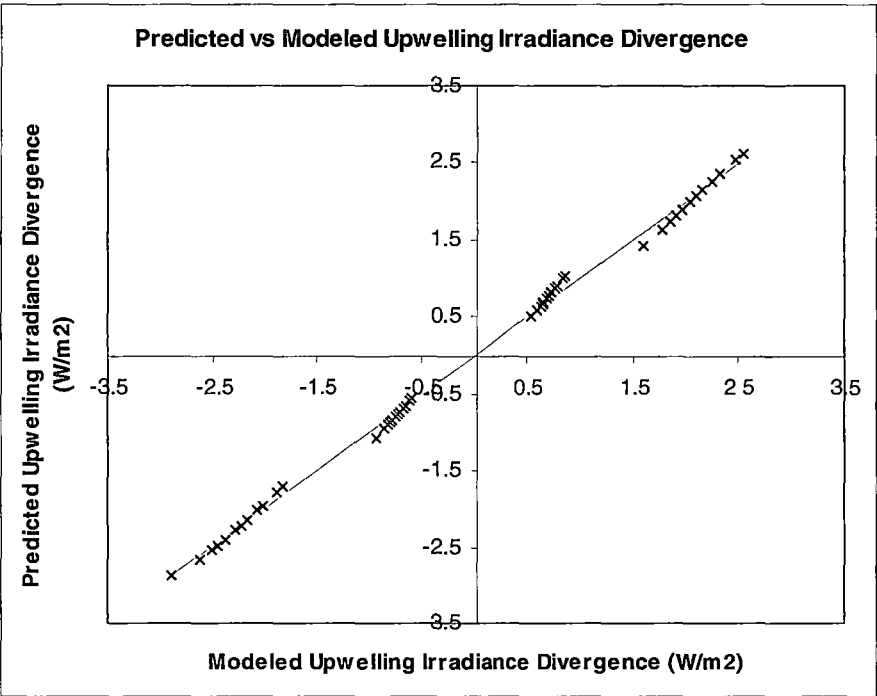


Figure 2.8. Predicted versus modeled upwelling longwave radiative divergence. Predicted values calculated using equation (2.31).

Although the standard error for this parameterisation is of smaller magnitude than the standard error for the modeled and predicted integrated values, it is evident from the patterns in this chart that this parameterisation relating upwelling irradiance divergence with upwelling radiance divergence at the zenith will be most effective under a restricted set of atmospheric conditions.

This parameterisation can be considered reliable for conditions similar to those defined by the model input parameter set described earlier in this section. For conditions deviating significantly from those, reliable results could only be obtained by gathering radiance divergence data for a representative range of angles and integrating those values to obtain the irradiance. Measuring radiance at multiple angles would also account for any changes in surface emissivity with angle, which would introduce further uncertainty into the parameterisation above.

One further relationship was investigated, in this case the conversion of brightness temperatures to radiance divergence $divR_{\uparrow}$ was bypassed and the upwelling irradiance divergence $divL_{\uparrow}$ was related directly to the upwelling radiance in both channels through the brightness temperatures $T_{\uparrow 1}$ and $T_{\uparrow 2}$.

The equation resulting from this parameterisation takes the following form:

$$divL_{\uparrow} = 3.211 \times 10^{-3} T_{\uparrow 1}^2 - 2.410 \times 10^{-3} T_{\uparrow 2}^2 + 3.127 T_{\uparrow 1} - 3.138 T_{\uparrow 2} - 1.143 \times 10^{-2} \quad (2.32)$$

with RMS error 0.0339 W/m² or 2.25% for 192 data. A plot of the predicted versus original values is given in the figure below.

It can be seen immediately that avoiding the conversion to radiance divergence markedly improves the accuracy of the prediction. The accuracy in this case also far exceeds the prediction of $divL_{\uparrow}$ using integrated radiance divergence values, but it must be remembered that integrating angular values will outperform this prediction in less than perfect conditions where there may be inhomogeneities in the ground surface emissivity.

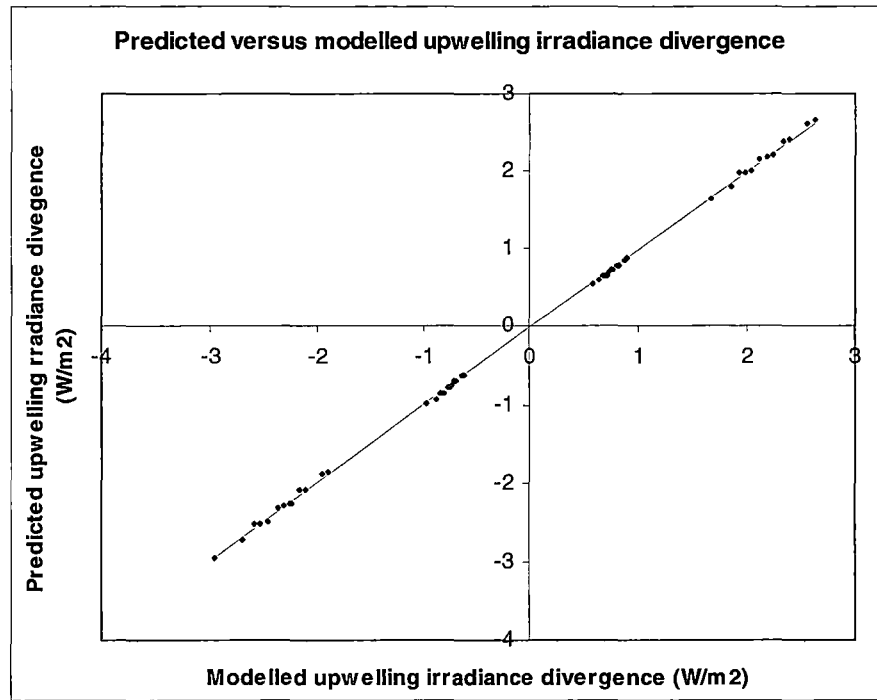


Figure 2.9. Predicted versus modeled upwelling longwave radiative divergence. Predicted values calculated using equation (2.32).

2.12 Downwelling irradiance divergence $divL_{\downarrow}$

For net irradiance divergence $divL$ to be calculated, the downwelling irradiance divergence $divL_{\downarrow}$ must also be known. The arguments and calculations presented above for the calculation of upwelling irradiance divergence from radiance measurements in two channels have no analogue for the downwelling case, as there is no concept of a solid boundary such as the ground when looking upwards at the night sky.

Therefore to calculate $divL_{\downarrow}$ it is necessary to consider the response of the air mass between the ground at zero metres and the upper boundary height h_2 , to the active and window components of the downwelling irradiance at height h_2 . If the magnitude of the downwelling irradiance divergence between height h_2 and the ground can be calculated using the components of the incident irradiance at height h_2 and some measure of the upwelling irradiance divergence $divL_{\uparrow}$ at height h_2 , then the net irradiance divergence between the ground and height h_2 can obviously also be calculated.

2.13 Characterising the downwelling irradiance L_{\downarrow} via radiance measurements at height h

The first necessary step towards calculating the downwelling irradiance divergence is to calculate the downwelling irradiance at height h_2 . Assuming that a dual-channel radiance measuring instrument is to be used facing upwards at height h_2 , the calculation of downwelling irradiance $L_{\downarrow}(h_2)$ must be able to be performed using two radiance measurements $R_{\downarrow a}$ and $R_{\downarrow w}$ in active and window bands of the spectrum respectively. The conversions of radiances $R_{\downarrow a}$ and $R_{\downarrow w}$ to effective temperatures $T_{\downarrow 1}$ and $T_{\downarrow 2}$ (given in equations (2.24) and (2.25) above) are dependent only on the spectral response of the instrument used to measure the radiance. Therefore the effective temperatures $T_{\downarrow 1}$ and $T_{\downarrow 2}$ can be computed and used in place of the downwelling radiances $R_{\downarrow a}$ and $R_{\downarrow w}$ to calculate the broadband incident radiance, which can then be integrated to give the irradiance.

It was found using results from the same model profiles described in Tables 2.2 and 2.3 that the relationship between downwelling radiance and effective temperatures $T_{\downarrow 1}$ and $T_{\downarrow 2}$ for all angles of incidence is given by

$$R_{\downarrow B} = 0.8194T_{\downarrow 1} + 0.6493T_{\downarrow 2} + 103.44 \quad (2.33),$$

with $R^2=0.996$ and standard error $0.3729 \text{ W/m}^2/\text{steradian}$, or 0.48% of the average radiance.

Since the downwelling irradiance is simply the radiance integrated over the hemisphere, it is reasonable to expect that some relationship may exist between the downwelling irradiance L_{\downarrow} and the effective temperatures $T_{\downarrow 1}$ and $T_{\downarrow 2}$ measured only at vertical incidence. In fact this relationship takes the form

$$L_{\downarrow} = 2.514T_{\downarrow 1} + 3.238T_{\downarrow 2} + 416.67 \quad (2.34),$$

with $R^2=0.999$ and standard error 0.3511 W/m^2 , or 0.13% of the average irradiance value. It then follows that if L_{\downarrow} is an influential parameter in the calculation of the downwelling irradiance divergence then $T_{\downarrow 1}$ and $T_{\downarrow 2}$ can be used in its place in any subsequent parameterisation.

2.14 Calculating the downwelling irradiance divergence $divL_{\downarrow}$

The downwelling irradiance divergence was parameterized based on the four vertical effective temperature measurements $T_{\downarrow 1}$, $T_{\downarrow 2}$, $T_{\uparrow 1}$ and $T_{\uparrow 2}$. Equation (2.34) above justifies the use of $T_{\downarrow 1}$ and $T_{\downarrow 2}$ in place of the downwelling irradiance, and equation (2.31) together with

equation (2.28) justifies the use of $T_{\uparrow 1}$ and $T_{\uparrow 2}$ in place of the upwelling irradiance divergence $divL_{\uparrow}$. As this step is a further parameterization, using the four temperature values directly avoids building the standard error that would result from combining the three contributing parameterizations that would be required to calculate the final value. The relationship between $divL_{\downarrow}$ and the four effective temperatures was found to take the form:

$$divL_{\downarrow} = -1.4165 \times 10^{-3} T_{\uparrow 1}^2 - 1.3690 \times 10^{-2} T_{\uparrow 2}^2 + 9.0305 \times 10^{-3} T_{\downarrow 1}^2 + 1.1248 \times 10^{-2} T_{\downarrow 2}^2 - 7.2250 \times 10^{-2} T_{\uparrow 1} - 0.52877 T_{\uparrow 2} + 0.68433 T_{\downarrow 1} + 1.1257 T_{\downarrow 2} + 27.654 \quad (2.35),$$

with $R^2=0.996$ and standard error 0.1026 W/m^2 . A chart of the predicted versus modeled values is shown in Figure 2.10 below.

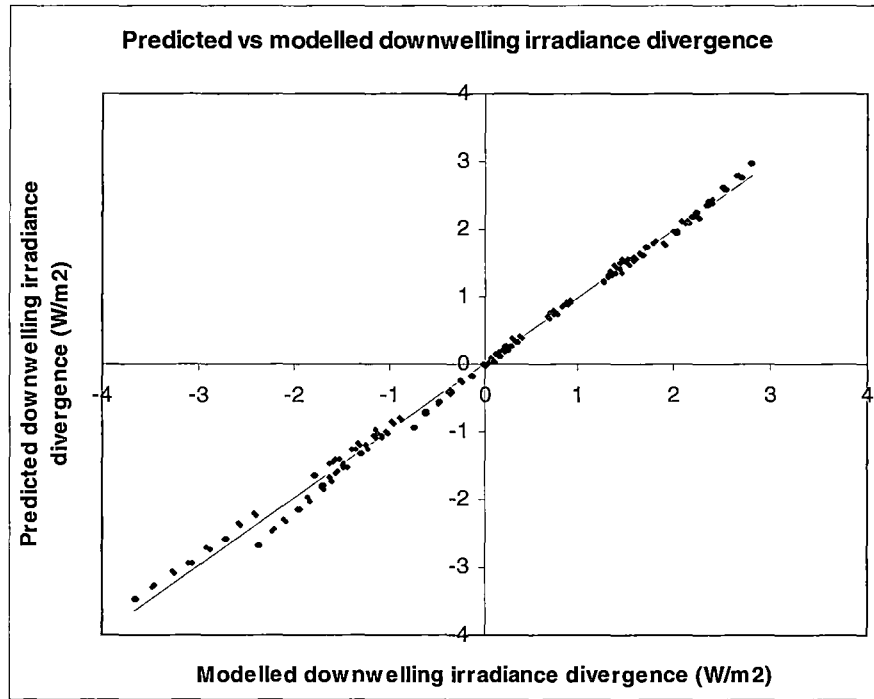


Figure 2.10. Predicted versus modeled downwelling longwave radiative divergence. Predicted values calculated using equation (2.35).

2.15 Calculation of total irradiance divergence $divL^*$

The parameterizations of $divL_{\uparrow}$ and $divL_{\downarrow}$ via equations (2.28), (2.32) and (2.35) provide the necessary quantities for the calculation of the net irradiance divergence $divL^*$, where

$$divL^* = divL_{\uparrow} - divL_{\downarrow} \quad (2.36).$$

If the effective temperatures in both channels and both directions are used in conjunction with the aforementioned equations to give $divL^*$, the calculated value can be compared with

the modeled value calculated directly from the MODTRAN modeled irradiances at two heights and in both directions. The calculated values were found to relate well to the modeled values, with an R^2 value of 0.9433 and a RMS error between the two of 0.131 W/m² or 26.7% relative to the average magnitude of the modeled values. A plot of the 192 calculated versus modeled values is given in Figure 2.11 below.

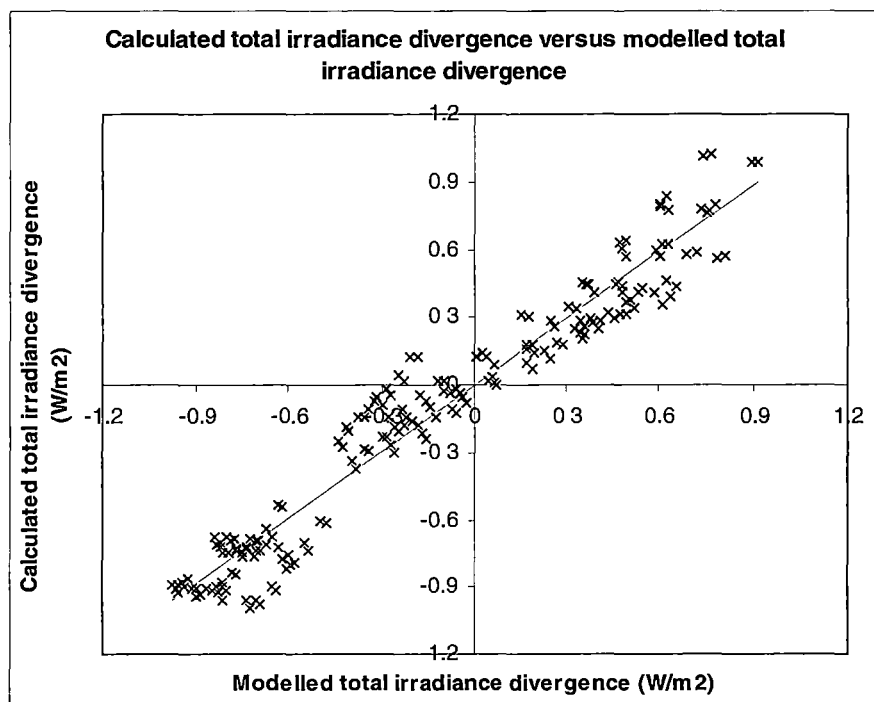


Figure 2.11. Predicted versus modeled net longwave radiative divergence.

2.16 Validation of the virtual instrument's calculations

The performance of the virtual instrument described in this Chapter was tested against 'real' profile models. The aim was to examine the accuracy of the parameterisations described over the course of this Chapter when applied to the results of MODTRAN model runs with independent profile input data.

While the result of ultimate interest was the accuracy of the calculated total irradiance divergence, other validation tests were also performed. The results of these will also be given in this section for completeness.

The modeling was performed using the MODTRAN v3.7 radiative transfer model, with five different input profiles of temperature, pressure and relative humidity. The test cases will be referred to as Test Cases 1 to 5, these indices also referring to the profiles used in the input models. Three of these profiles (1,4 and 5) were 'real' profiles, measured in the field using

data from a vertical array of five temperature and humidity sensors from zero to ten metres appended to radiosonde data beginning at 21 metres. Further details of the data gathering arrangement will be presented in Chapter 6. The equations were derived from an ensemble of profiles intended to represent as broad as possible range of conditions at the expense of a realistic representation of expected measurement conditions. The profiles used here were representative of expected measurement conditions.

Profiles 2 and 3 were based on profile 1, with additional constant temperature offsets of +2 and -1 degrees centigrade respectively. The pressure and relative humidity profiles for cases 2 and 3 were not altered from profile 1.

The temperature and relative humidity profiles are shown, each at two resolutions, in Figures 2.12 a,b,c and d. The model was then run for each of these profiles in twenty-four configurations, corresponding to all possible combinations of two instrument heights (0 and 15 metres) and twelve pointing directions: 0 (vertically upwards), 15, 30, 45, 60, 75, 105, 120, 135, 150, 165 and 180 degrees (vertically downwards). These configurations matched those used in the modeling parameter set described in Section 2.10.

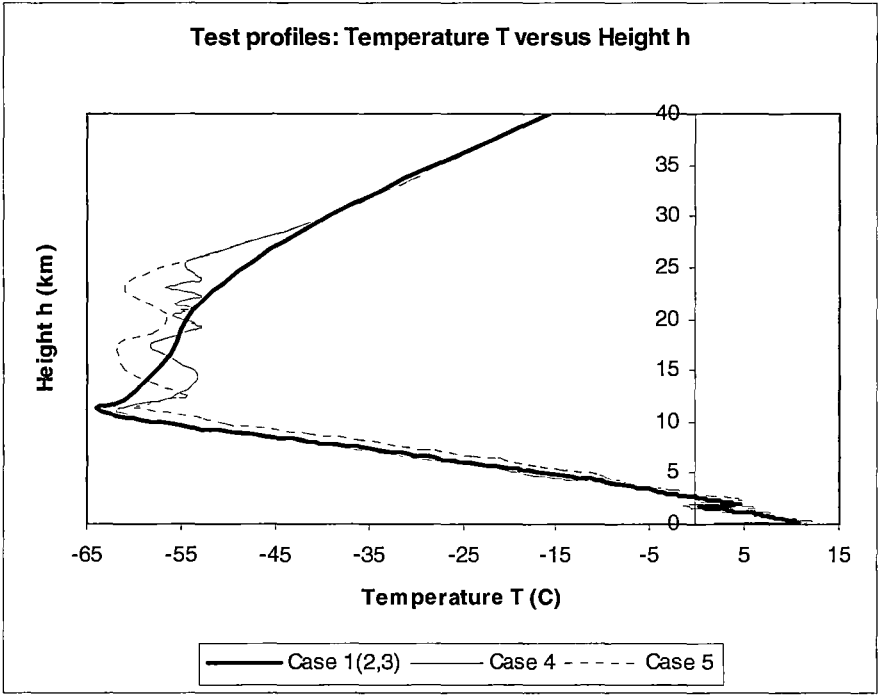


Figure 2.12a. Profiles of temperature for test cases 1-5, presented on a 0 to 40km height scale.

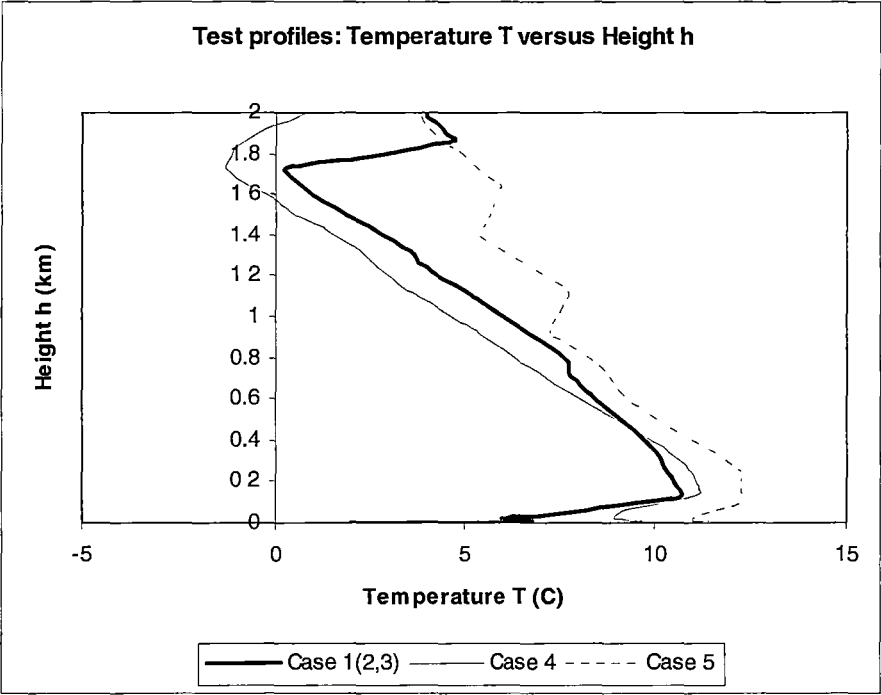


Figure 2.12b. Profiles of temperature for test cases 1-5, presented on a 0 to 2km height scale.

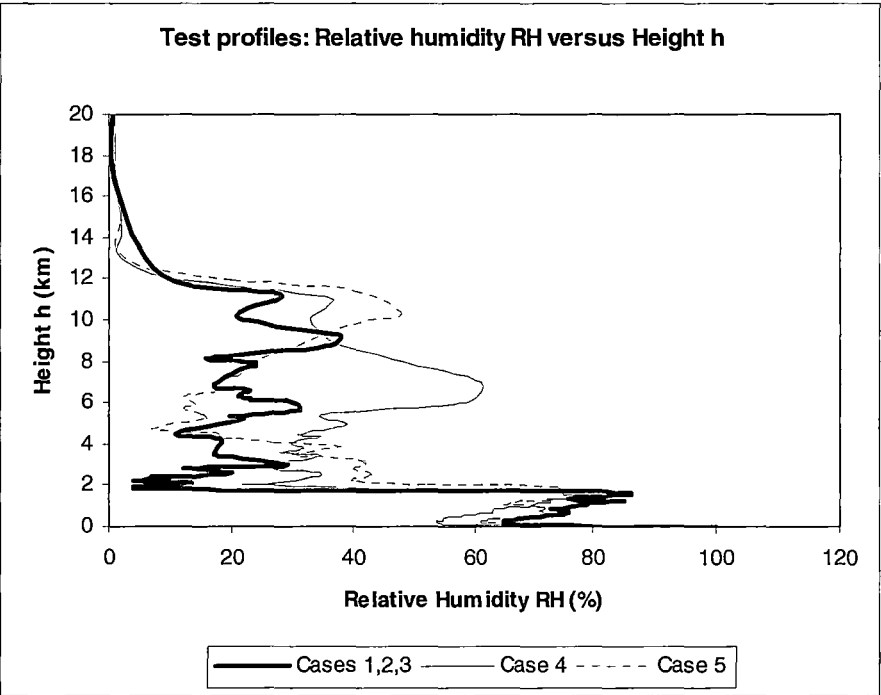


Figure 2.12c. Profiles of relative humidity for test cases 1-5, presented on a 0 to 20km height scale.

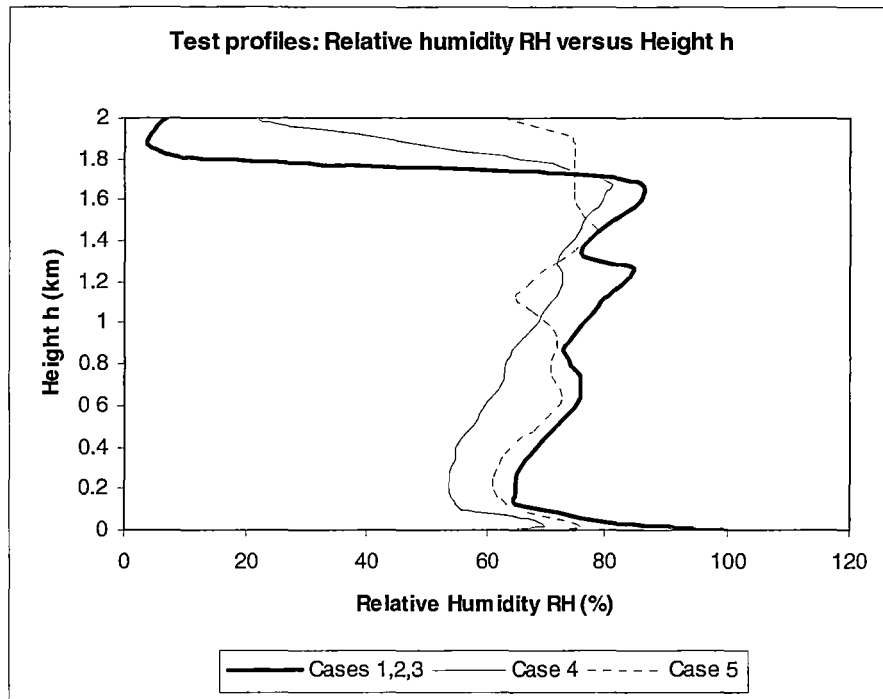


Figure 2.12d. Profiles of relative humidity for test cases 1-5, presented on a 0 to 2km height scale.

The range of modeled values allowed a comprehensive suite of comparisons to be performed. The angular radiance values were considered alone and integrated to give irradiance values. They were also converted to effective brightness temperatures using equations (2.24) and (2.25). The spectral curves described in the model output were again converted to radiance values (one per channel and one broadband) using the process described in Section 2.7. These radiances were then converted to brightness temperatures for use in the equations where appropriate.

The first test was intended to assess the performance of equation (2.28) in calculating the upwelling radiance divergence $divR_{\uparrow B}$ from the pair of ‘measured’ brightness temperatures. The radiance divergence was calculated simply by subtracting the model-output broadband radiance at zero metres from the broadband radiance at fifteen metres, for all values of the incident angle. Standard errors were then calculated for all values combined, then also by test and by angle. The RMS error for all predicted values combined was $0.1476 \text{ W/m}^2/\text{steradian}$, against an average magnitude of $1.447 \text{ W/m}^2/\text{steradian}$ or 10.1%. RMS errors, average magnitudes and standard error for the test-by-test and angle-by-angle calculations are given in the tables below.

Test Case	RMS error (W/m ² /ster)	Average magnitude of $divR_{\uparrow B}$ (W/m ² /ster)	RMS error (%)
1	0.1315	1.539	8.54
2	0.1845	1.637	11.3
3	0.1051	1.492	7.04
4	0.1569	1.546	10.1
5	0.1428	1.020	14.0

Table 2.5. The accuracy of equation (2.28) for the prediction of upwelling broadband longwave radiance divergence, expressed as absolute and relative (%) RMS errors on a test-by-test basis.

Incident angle (°)	RMS error (W/m ² /ster)	Average magnitude of $divR_{\uparrow B}$ (W/m ² /ster)	RMS error (%)
0	0.1086	1.225	8.86
15	0.1111	1.242	8.94
30	0.1192	1.295	9.21
45	0.1353	1.397	9.68
60	0.1648	1.579	10.4
75	0.2123	1.942	10.9

Table 2.6. The accuracy of equation (2.28) for the prediction of upwelling broadband longwave radiance divergence, expressed as absolute and relative (%) RMS errors on an angle-by-angle basis.

Comparing Tables 2.4 and 2.6 revealed strong similarities – both sets of results exhibited an increase in both RMS error and $divR_{\uparrow B}$ with angle, together resulting in a slight increase in the % RMS error with angle. RMS error values were very similar, in fact smaller for this comparison test than for the original parameterisation.

The second analysis of the modelling results was intended to assess the accuracy of the prediction of $divL_{\uparrow}$ from the ‘measured’ brightness temperatures. The prediction methods described in Sections 2.10 and 2.11 provided three avenues for a calculated prediction of $divL_{\uparrow}$, via equations (2.29), (2.31) and (2.32) respectively.

Equation (2.29) predicts $divL_{\uparrow}$ by integrating angular radiance divergence values over the lower hemisphere. These integrations were performed on the radiance divergence values predicted by equation (2.28) for all test cases. These were then compared against integrated broadband radiance measurements produced by the model. The results are shown in Table 2.7 below. It can be seen in these results that the relative errors in the predictions were consistent with the standard error calculated for the original modelling set (10.9%).

Test Case	MODTRAN modeled $divL_{\uparrow}$ (W/m ²)	Predicted $divL_{\uparrow}$ (W/m ²)	Absolute difference (W/m ²)	Relative difference (%)
1	5.287	5.732	0.443	8.40
2	5.621	6.248	0.627	11.2
3	5.129	5.481	0.352	6.87
4	5.315	5.843	0.529	9.95
5	3.504	3.988	0.485	13.8

Table 2.7. The accuracy of equation (2.29) for the prediction of upwelling longwave irradiance divergence, expressed as absolute and relative (%) differences.

Equation (2.31) predicts $divL_{\uparrow}$ from the vertically upwelling radiance divergence alone. These calculations were also performed to test the ‘real world’ performance of the parameterisation. It was found that the accuracy of the prediction made by this equation was poor for the test cases used. The results are presented in Table 2.8 below.

Test Case	Modeled $divL_{\uparrow}$ (W/m ²)	Predicted $divL_{\uparrow}$ (W/m ²)	Absolute Difference (W/m ²)	Relative difference (%)
1	5.287	2.860	2.427	45.9
2	5.621	2.443	3.178	56.5
3	5.129	2.996	2.133	41.6
4	5.315	2.802	2.513	47.3
5	3.504	3.100	0.404	11.5

Table 2.8. The accuracy of equation (2.31) for the prediction of upwelling longwave irradiance divergence, expressed as absolute and relative (%) differences.

As mentioned in Section 2.11, the reliability of this parameterisation was considered likely to decrease as the values of $divL_{\uparrow}$ diverged from those used in the original parameterisation. This behaviour was evident in these results, with the accuracy of the prediction in Test Case 5 – which had a lower value of $divL_{\uparrow}$ and one more consistent with the original modeled set – markedly better than the accuracy of the prediction in the other test cases. The results of this test confirmed the obvious hypothesis that better results are achieved by integrating multiple radiance divergence measurements over the hemisphere than by attempting to extrapolate the irradiance divergence from a single radiance divergence measurement.

Equation (2.32) calculates the upwelling irradiance divergence from the upwelling brightness temperature measurements. It does this directly, as opposed to equation (2.31), which requires that the brightness temperatures be converted to an upwelling radiance divergence via equation (2.28) as an intermediate step. While the prediction by equation (2.32) requires that the measurements be made under ideal conditions, the original parameterisation performed much better than either of the previously described methods for calculating $divL_{\uparrow}$.

Test Case	Modeled $divL_{\uparrow}$ (W/m ²)	Predicted $divL_{\uparrow}$ (W/m ²)	Absolute Difference (W/m ²)	Relative difference (%)
1	5.287	5.905	0.618	11.7
2	5.621	6.259	0.638	11.3
3	5.129	5.731	0.602	11.7
4	5.315	5.670	0.385	7.23
5	3.504	3.706	0.202	5.77

Table 2.9. The accuracy of equation (2.32) for prediction of the upwelling longwave irradiance divergence, expressed as absolute and relative (%) differences.

As with the results predicted by equation (2.29), where the angular radiance divergence were integrated, these test results showed a similar degree of inaccuracy to that seen in the original parameterisation of the integrated radiance divergence values. This indicated that under ideal conditions of a clear sky and uniform ground surface, equation (2.32) could be used to calculate $divL_{\uparrow}$ from two temperature measurements with the same approximate accuracy as integrating multiple angular measurements. This in turn opened an avenue to a greatly simplified measurement procedure under appropriate conditions.

The third test analysis was conducted in order to test the accuracy of the calculation of the downwelling broadband radiance $R_{\downarrow B}$ from the brightness temperatures $T_{\downarrow 1}$ and $T_{\downarrow 2}$ as described by equation (2.33). The calculation was performed for all downwelling radiance values generated by the model – for the six modeled incidence angles and at heights 0 and 15 metres. Overall, the accuracy of the calculated values was significantly less than the accuracy of the initial parameterisation. While the parameterisation data set yielded a 0.48% standard error, the results of this test yielded a standard error of 12.3%. There was little if any pattern across the test cases, but the table below indicates that there was some dependency of the accuracy upon the angle of incidence.

There is no obvious explanation for the improvement in accuracy with angle away from the vertical, as the increase is due to both a decrease in the RMS error and an increase in the magnitude of $R_{\downarrow B}$. While the accuracy of the parameterisation in equation (2.33) was disappointing when applied to ‘real’ atmospheric profiles, the result is not damaging because equation (2.33) is not used in the final calculation of the irradiance divergence.

Incident angle (°)	RMS error (W/m ² /ster)	Average magnitude of $R_{\downarrow B}$ (W/m ² /ster)	RMS error (%)
0	10.28	78.81	13.0
15	10.27	79.13	13.0
30	10.23	80.12	12.8
45	9.993	81.97	12.2
60	9.164	85.18	10.8
75	6.464	91.71	7.05

Table 2.10. The accuracy of the prediction equation for the angular longwave radiance divergence, expressed as absolute and relative (%) RMS ($x_i - y_i$) errors.

The fourth test consisted of a comparison between MODTRAN modeled values of the downwelling irradiance L_{\downarrow} and values predicted using equation (2.34), which calculates L_{\downarrow} from the brightness temperatures measured at vertical incidence. In contrast to the downwelling radiance predictions in the third test, the predictions of downwelling irradiance showed excellent accuracy for the five test cases. Over all five tests the RMS error was 0.467 W/m² and the average magnitude was 279.6 W/m², giving a relative RMS error of 0.17%. A table of the result for each test is given below.

Test Case	Modeled L_{\downarrow} (W/m ²)	Predicted L_{\downarrow} (W/m ²)	Relative difference (%)
1	274.4	273.8	0.22
2	286.8	286.4	0.14
3	268.4	267.8	0.24
4	274.6	274.3	0.12
5	293.6	293.9	0.08

Table 2.11. The accuracy of the prediction equation for the downwelling longwave irradiance, expressed as relative (%) differences.

These results indicate that a single pair of measurements of radiance - one in each of the two channels - serves to characterize the downwelling broadband irradiance to a very high degree of accuracy.

The fifth test analysis was conducted in order to assess the accuracy of the prediction of the downwelling irradiance divergence $divL_{\downarrow}$, which equation (2.35) calculates using brightness temperatures in both channels measured in both upwelling and downwelling directions. Again the divergence values were calculated directly from integrated modeled radiance values and separately using equation (2.35). The results are shown in the table below.

Test Case	Modeled $divL_{\downarrow}$ (W/m ²)	Predicted $divL_{\downarrow}$ (W/m ²)	Absolute difference (W/m ²)	Relative difference (%)
1	2.795	3.860	1.065	38.1
2	2.983	4.133	1.149	38.5
3	2.703	3.745	1.042	38.5
4	1.734	3.242	1.509	87.0
5	1.503	2.337	0.833	55.5

Table 2.12. The accuracy of the prediction equation for the downwelling longwave irradiance divergence, expressed as absolute and relative (%) differences.

While these results do not indicate a high degree of accuracy in the prediction of $divL_{\downarrow}$, the result must be considered in the context of the calculation of the net irradiance divergence $divL^*$. $divL^*$ is calculated by subtracting $divL_{\downarrow}$ from $divL_{\uparrow}$ and therefore the relative

magnitudes of each component will play a part in determining the impact of any inaccuracy in their respective prediction.

The final test was performed in order to assess the accuracy of the overall prediction of $divL^*$. The calculation was performed using a simple subtraction as mentioned above, involving the modeled values of $divL_{\downarrow}$ and $divL_{\uparrow}$ in one case and the predicted values in the other. The calculation of $divL^*$ used $divL_{\uparrow}$ from the integration of predicted $divR_{\uparrow B}$ as shown in Table 2.7 above. The values of $divL_{\downarrow}$ were sourced from the calculations using equation (2.35) and are shown in Table 2.12 above. The results of the $divL^*$ calculation are given in Table 2.13 below.

Test Case	Modeled $divL^*$ (W/m ²)	Predicted $divL^*$ (W/m ²)	Absolute difference (W/m ²)	Relative difference (%)
1	2.492	1.872	0.621	24.9
2	2.638	2.115	0.522	19.8
3	2.426	1.736	0.690	28.4
4	3.581	2.601	0.980	27.4
5	2.001	1.652	0.349	17.5

Table 2.13. The accuracy of the prediction equation for the net longwave radiative divergence, expressed as absolute and relative (%) differences.

The RMS error and standard error were also calculated for the five tests together, yielding an RMS error of 0.666 W/m² in an average magnitude $divL^*$ of 2.628 W/m² – a relative RMS error of 25.3%. It was also evident that the prediction always underestimated the modeled value, although there was insufficient data to form a meaningful hypothesis about systematic patterns in the relationship. As might be expected, performing the $divL^*$ calculation again using values of $divL_{\uparrow}$ from equation (2.32) as listed in Table 2.9 yielded very similar results, with a relative RMS error of 25.9%.

2.17 Summary

This chapter has described the development and theoretical performance testing of a ‘virtual’ radiometric instrument that measures upwelling and downwelling narrowband infrared radiance in two channels. Various applications have been explored with the ultimate goal of obtaining broadband irradiance divergence over some height interval h between two heights h_2 and h_1 , with $h_1=0$ metres above the ground.

The primary condition on these measurements is that they are to be made from the single height h_2 . This condition means that vertical translation of the instrument and any associated difficulties inherent in such a translation are avoided. Using a narrow (less than hemispherical) instrument field of view means that angular radiance effects and any obstructions can be accounted for in analysis of the measured data.

Based on a pair of selected narrowband filters, the MODTRAN v3.7 radiative transfer model was used both to simulate the ‘virtual’ instrument (via extraction of modeled brightness temperatures) and to obtain ‘real’ results (via extraction of broadband radiances) for comparison. Relationships were then developed between the ‘real’ modeled values and those that would be observed by the instrument under the imposed measurement conditions. The performance of these predictive relationships was then tested using model runs driven by independently measured atmospheric profiles. A summary of key results of these tests is given in the table below.

Quantity	Equation	Relative RMS error (%)
Upwelling broadband radiance divergence $divR_{\uparrow B}$	(2.28)	10.1%
Upwelling irradiance divergence $divL_{\uparrow}$	(2.29)	10.0%
Downwelling broadband radiance $R_{\downarrow B}$	(2.33)	12.3%
Downwelling irradiance L_{\downarrow}	(2.34)	0.17%
Downwelling irradiance divergence $divL_{\downarrow}$	(2.35)	48.7%
Net irradiance divergence $divL^*$	(2.36)	25.3%

Table 2.14. The accuracy of the prediction equations for various quantities, expressed as RMS ($x_i - y_i$) error in %.

It can be seen immediately that the predictions perform with varying degrees of success and that the quality of these predictions must be carefully accounted for in analysis of measurement results.

There are two main factors that contribute to the quality of these predictions, both of which could be tuned to give better performance. Firstly, the choice and range of coverage of the original modeling data sets affected the accuracy of the predictions and range of the application of the predictive equations. In this case the choice was intended to give an unbiased result set - a range of divergences from negative through zero to positive. While this choice represents a broad range of possible conditions, it is conceivable that better results might be achieved through biasing the models towards ‘conditions of interest’ – those that are more likely to produce strong positive divergence. While this might be seen as adding a bias to the results, these conditions are the ones under which measurements are most likely to be made and would give valid results for applications within their scope. If the results of the above tests are examined closely and compared to the original parameterisation curves, it can be seen that the atmospheric conditions described by the modeled profiles yield results that are close to or just beyond the scope of the results of the original modeled data sets. This has most likely had a negative effect on the test results.

Secondly, the choice of filter bands was constrained by two factors. As mentioned earlier, manufacturing constraints mean that the choice of filter bands is not totally flexible. Also, in this case the impending manufacture of the physical instrument on a restrictive timeline meant that the choice of filter bands had to be made prior to this full analysis – the choice was based on a simple test as detailed in Section 2.6. Given sufficient computing power, it is conceivable that the filter choices could be more finely tuned using an iterative approach that performs the entire analysis described in this chapter for each available filter option. Manufacturing constraints aside, such an approach could also yield a theoretical ‘best possible’ performance assessment for this approach in general.

While there is room for improvement of the performance of the ‘virtual instrument’, the analysis in this chapter serves as proof of the initial concept – that multiple narrowband radiance measurements can be used to effectively reconstruct the broadband radiance curve, and integrated to give irradiances. The equations derived here that effectively calculate the broadband irradiance divergence and other quantities will be used in Chapter 8 to calculate those quantities from field measurements of radiance made by a real instrument, the development of which is described in Chapters 3,4 and 5.

Chapter 3

Instrument design and construction

3.1 Introduction

This chapter describes the design and construction of a two-channel infrared radiometer. The radiometer was built with the intention of verifying the concepts and results introduced in the context of a ‘virtual’ instrument in Chapter 2.

The implementation of the instrument design was an iterative process through which the design evolved through various stages. The detail of these stages will be presented only where it is considered useful to the reader, otherwise it will be assumed for brevity that in general the design and subsequent implementation was a two-step process.

The first instrument prototype was built by Mr Chris Ashworth. Mr Peter Dove of the University’s Central Science Laboratory (CSL) implemented changes to the physical instrument design. Mr Paul Waller, also of CSL, was responsible for the majority of the electronic design and construction of the final instrument.

3.2 Instrument design requirements

There were two main categories of requirements that contributed towards the instrument design. The first of these was the category of radiometric performance requirements. The second was the category of requirements relating to the intended application. These requirements were identified through consideration of the eventual field application of a working instrument and the constraints imposed by the application environment.

In terms of radiometric performance, the key index is sensitivity as defined in Chapter 2 – an instrument’s ability to resolve changes or differences in the measured radiance. The requirements were difficult to quantify at the early design stage. The project timeline meant that the analysis presented in Chapter 2 was performed concurrently with the design and construction of the instrument, and so a precise measure of the required sensitivity could not be calculated. The overall requirement was that the instrument could be used to detect irradiance divergence over five metres sufficient to cause a 1°C per hour radiative cooling in a five-metre layer of air. In practical terms this requirement translated to building as sensitive

an instrument as possible and using the requirement as a benchmark – a point at which the instrument could be usefully deployed.

The requirements relating to the instrument's intended application were size, weight and power consumption. If the instrument were to be mounted on an arm - in turn attached to a pole or tower - then the size and weight had to be kept within reasonable limits. The intention to rotate the instrument to point in different directions would also involve mounting it on a moving platform of some kind, which further constrained the size and weight. For field applications and potentially long-term installations, low to moderate power consumption was required. A general rule of thumb was that the instrument should be able to operate unattended and running from a single car or boat battery for at least 48 hours.

A further constraint on the instrument design was that of cost. While the decision to design and construct the instrument in-house was made in order to retain full control of the process, the cost demands of the full development process meant that in some cases decisions had to be made based on cost rather than on measures of performance or suitability.

3.3 Radiance detection using a pyroelectric detector

After some study of the options available for narrowband infrared radiance detection, a choice was made to use a pyroelectric detector as the primary component in the instrument. The only true alternative was a thermopile-based detector, which in most of their low-cost forms cannot match the speed of pyroelectric sensors. Also, the requirement that the radiation incident on a pyroelectric sensor be modulated facilitates the use of a dual filter system as will be seen later in this chapter. This and other features of pyroelectric detectors will be discussed further in the following text.

Pyroelectricity is the property of a class of materials known as pyroelectrics. These are typically insulating materials and exist in the form of crystals. Just as piezoelectric materials generate current when placed under physical strain, pyroelectric materials respond to homogeneous changes in their temperature by generating an electric dipole moment (Hossain and Rashid 1991).

The important difference between pyroelectrics and other materials used for sensing temperature is that pyroelectrics respond to changes in temperature rather than their absolute temperature. Thus detection of infrared radiation by pyroelectric detectors is a two-step process – the crystal absorbs radiation and undergoes a change in temperature, which then

generates a current. The materials used in pyroelectric detectors are chosen for both their pyroelectric response characteristics and their thermal response to incident radiation.

Pyroelectric detectors are constructed by building a capacitor that uses the pyroelectric material as its insulator. Electrodes are added to the crystal by deposition on the two faces of the crystal that are normal to the polar axis. Either the electrode facing the incident radiation or the surface of the pyroelectric crystal facing the incident radiation is blackened to enhance absorption, the latter in the case where the electrode is transparent (Hossain and Rashid 1991).

The response of pyroelectric detectors to changes in the incident radiation has had important consequences for instrument design. It means that radiation incident on the detector must be artificially modulated using a chopping mechanism in order to produce changes in crystal temperature. This modulation can be considered as turning the radiance incident on the detector 'on' and 'off'. The incorporation of the physical chopping mechanism is a major factor in the instrument design. Also, some measure of the radiance in the 'off' position is required to calibrate the output generated from the sensor by the off/on and on/off transitions.

The pyroelectric detector's ability to generate current means that it can be considered in electrical terms as a charge generating capacitor (Hossain and Rashid 1991). There are then two options for the mode of incorporation into an electrical circuit, as the accompanying circuitry can be designed to either measure the short-circuit current of the detector or its open-circuit voltage. Other than differences in the circuitry that is used to achieve this measurement, the primary difference between the two modes is their response to modulating frequency. In "current mode" the responsivity increases with frequency before flattening at high frequencies beyond approximately 10Hz. In "voltage mode" the responsivity decreases with modulating frequency. However at frequencies lower than approximately 10Hz, the "voltage mode" responsivity is substantially higher – approximately ten times larger at 1Hz and one hundred times larger at 0.1Hz (Heinze 1999).

This behaviour was an important consideration in the selection of an appropriate detector for the instrument, as the electronics that determine the measurement mode are typically built into commercial detector components. Whilst use of a "current mode" detector allows very fast modulating frequencies to be used, the amplification electronics required for such fast modulation frequencies are significantly more complicated than those required for more slowly modulated signals. For this reason, as well as the increased responsivity at lower

modulation frequencies, a voltage mode detector was chosen for use in the instrument. Modulation frequencies of 1 to 10Hz were determined to be sufficient to meet the measurement speed requirements.

The instrument detectors were sourced from InfraTec Infrarotsensorik und Meßtechnik in Germany. The instrument in its first and other early incarnations employed a model LIS 114 detector. The LIS 114 was based on a 6mm diameter pyroelectric sensor with a voltage preamplifier. Incorporated in the design were mirror optics that focus the incident radiation onto the sensor chip, increasing the signal response and also effectively lensing the incident radiation to a 20° acceptance angle (Heinze 1999).

The performance of the LIS 114 was found to be contributing to generally poor instrument performance later in the development phase. It was exchanged in the design for an LIE 307 model detector. The LIE 307 did not contain mirror optics, which were deemed unnecessary since the instrument's reference cavity (see Section 3.4) effectively acts as the instrument's waveguide. It incorporated a voltage preamplifier in the same way as the LIS 114, but the major improvement was the inclusion of a compensation element – a second pyroelectric sensor that is used to compensate for changes in the detector's overall temperature that can cause drift in the detector's offset voltage. These drifts can introduce inconsistencies in the output measurements, and large changes in output were observed during calibration that corresponded to only minor changes in detector temperature. The change to the LIE 307 detector immediately resulted in improved instrument performance.

Both detectors incorporated a Lithium Tantalate (LiTaO_3) pyroelectric crystal as a substrate material. The LIS 114 had a Calcium Fluoride (CaF_2) window covering the detection electronics while the LIE 307 had by choice a Barium Fluoride (BaF_2) window. The BaF_2 window had an essentially flat transmission curve through to 12 μm , while the CaF_2 window's transmission begins to drop just before 9 μm . The choice of BaF_2 in the second detector was intended to minimise the negative effect of transmission loss at the upper wavelengths.

3.4 Reference cavity design and radiation modulation

The use of a detector that requires modulated radiation input means that a reference radiation level is required during the 'off' portion of the modulation cycle, as mentioned in the previous section. This is most commonly achieved in one of two ways. Modulation or

“chopping” of the incident radiation is performed using a rotating wheel or disc that consists of alternating solid and empty portions. If the temperature of the chopping wheel can easily be measured, often the solid portions of the lower surface of the wheel (facing the detector) are painted black and considered as a radiating blackbody at the wheel’s temperature. Measurement of the wheel’s temperature can be achieved through contact thermometry using a contact sensor built into or onto the disc. Alternatively the wheel temperature can be controlled by enclosing it in a carefully temperature-controlled housing and rendering its top surface reflective so that incident radiation has little or no effect on the temperature of its lower surface.

If measurement or control of the temperature of the chopping wheel is impractical in a given application, a simpler solution is to create a reference cavity that encloses the detector and is closed above by the lower surface of the chopping wheel. The reference cavity can either be artificially heated or cooled, or its temperature measured as it fluctuates with fluctuations in the ambient temperature. If the lower surface of the chopping wheel can then be rendered close to 100% reflective, the wheel will reflect the radiation from the reference cavity yielding a reference radiance level that can be calculated or inferred from the cavity temperature.

This general method of a radiating, non temperature-controlled cavity in conjunction with a reflective chopping wheel was used in the instrument design, although the cavity underwent several evolutionary changes as the design advanced. Several of these evolutionary design iterations – only those that resulted in significantly enhanced performance – will be discussed in this section.

To obtain dual-channel measurements two filters were used. These filters were selected by their transmission characteristics from a list made available by their manufacturer. The transmission curves of the chosen filters are shown in Chapter 2, Figures 2.2a and 2.2b. The method of incorporation of the filters into the radiance path of the instrument was found to be a key contributor to the instrument’s performance, and is discussed in the following text.

The cavity design in the first instrument prototype was very straightforward. The cavity consisted of a cylindrical section of aluminium tube approximately 60mm long, 100mm external diameter and 2mm thickness. The portion of tube was capped at both ends by circular aluminium discs approximately 2mm thick, each attached using three equispaced screws.

A hole of diameter 14mm was drilled into the top plate, placed halfway between the center and edge of the plate. This hole allows entry of the incident radiation into the cavity. The detector, which was delivered in a standard ‘can’ container, was placed facing upwards through a similarly sized hole in the base plate, aligned with the viewing hole in the top plate. All internal surfaces of the cavity were blackened using highly absorptive paint to improve radiation absorption.

In the first instrument design the filters were incorporated into the chopping wheel, which consisted of an aluminium disc 90mm in diameter and 2mm thick. The disc was mounted on a driving rod that was connected to a motor at the rear of the instrument. The end of the driving rod was inserted into a plastic bezel mounted on the lower surface of the cavity’s top plate, and a plastic ring was attached to the cavity’s bottom plate as a guide. A hole drilled in the bottom plate allowed the rod to enter the cavity. The filters were mounted in large holes in the chopping wheel and secured above by brass fittings. A simplified schematic of the original cavity design is shown in Figure 3.1 below.

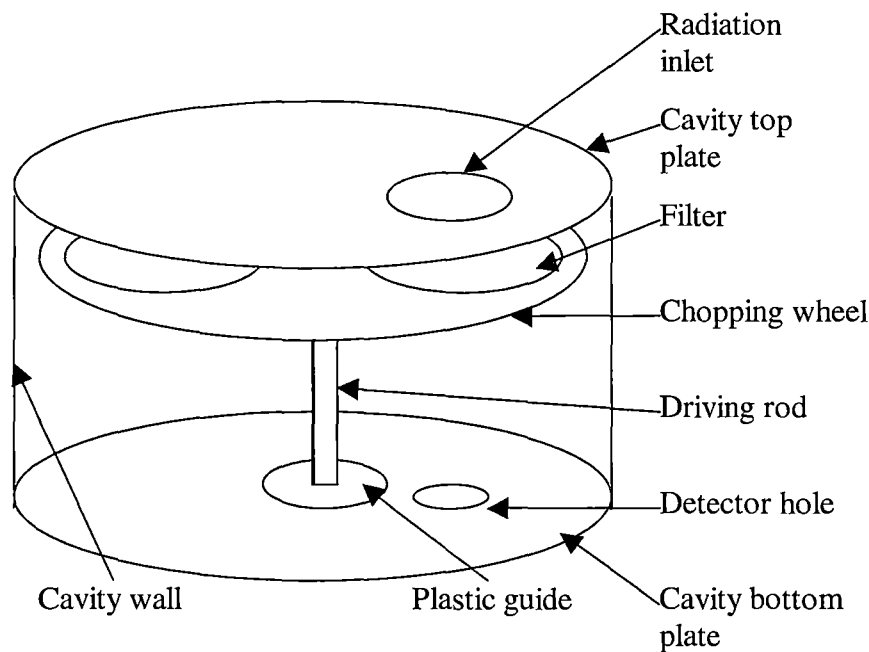


Figure 3.1. Schematic diagram of the initial instrument cavity design.

This instrument cavity was built by Chris Ashworth as part of an initial prototype version of the instrument. In this initial design, the cavity temperature was measured by a thermistor attached to the lower surface of the bottom plate of the cavity. The temperature reading was shown on a small LCD panel on the rear of the instrument and required manual recording. This cavity temperature measurement system was replaced early in the development cycle by

a pair of copper-constantan thermocouples, positioned in small holes drilled into the walls of the cavity.

The incorporation of the filters into the chopping wheel was an attempt to simplify the design – allowing the filtering and chopping to be performed by a single rotating wheel. This design feature was based on the assumption that the filters were reflective where they were not transmissive – that the filters themselves would not absorb radiation and hence would only undergo changes in temperature through conduction. It was assumed that any conductive temperature changes would be accompanied by matching changes in the temperature of the wheel, yielding no net difference between measured and cavity reference radiation levels.

At one point in the design development, artificial heating of the cavity was attempted as a method for raising the reference temperature and therefore increasing the output signal of the detector (since the intended target would in most cases be at some temperature less than the reference temperature). This was attempted using a coil of resistive wire wrapped around the cavity, with 12 volts DC current passed through it from an external source. This was found to have a detrimental effect both on the uniformity of the cavity temperature through uneven heating and on the quality of the output signal through electrical interference. The attempt was subsequently abandoned. Cost limitations also ruled out the use of a Sterling-cycle cooler to lower the cavity temperature to a point far below the expected target temperature.

The cavity, chopping wheel and filters were then all assumed to be at the same temperature. The lower side of the chopping wheel was polished to give high reflection and it was assumed that there would be negligible difference in reflectivity between the chopping wheel and the filters in the portions of the spectrum where the filters are non-transmissive. The change ‘seen’ by the detector as the filter wheel rotates would then be the transition from the chopping wheel surface that reflects the cavity radiance, to the filter that reflects the cavity radiance in all parts of the spectrum where it does not transmit. This change is then only ‘seen’ in the regions of the spectrum where the filters transmit and it was assumed that the detector’s response would be wholly due to that change.

This original design did not perform well and changes were subsequently made to the cavity design. The first hypothesis was that the gap between the chopping wheel and the cavity walls was allowing radiation to leak into the cavity. The brass fittings that attached the filters to the wheel were approximately 1mm thick, so the upper surface of the wheel was not flat,

and any radiation leakage would be effectively modulated at some frequency close to the chopping frequency.

The effects of this modulated broadband signal leakage could be approximately measured by temporarily covering the entire lower surface of the chopping wheel with highly reflective aluminium Mylar. If there was negligible leakage then the detector should have given no response, but it was found that there was in fact a strong response to the 'false' modulation. This prompted cavity design changes in order to eliminate leakage. The changes to the cavity design are shown in schematic form from a side view in Figure 3.2 below.

The addition to the cavity was a cylindrical aluminium tube with internal diameter slightly larger than the diameter of the detector. The inner surface of the tube was blackened to enhance radiation absorption. The lower end of the tube was fixed to the base of the cavity and the upper end extended as close to the chopping wheel as possible without touching it. A blackened lip was added to the top of the tube to further prevent light leakage.

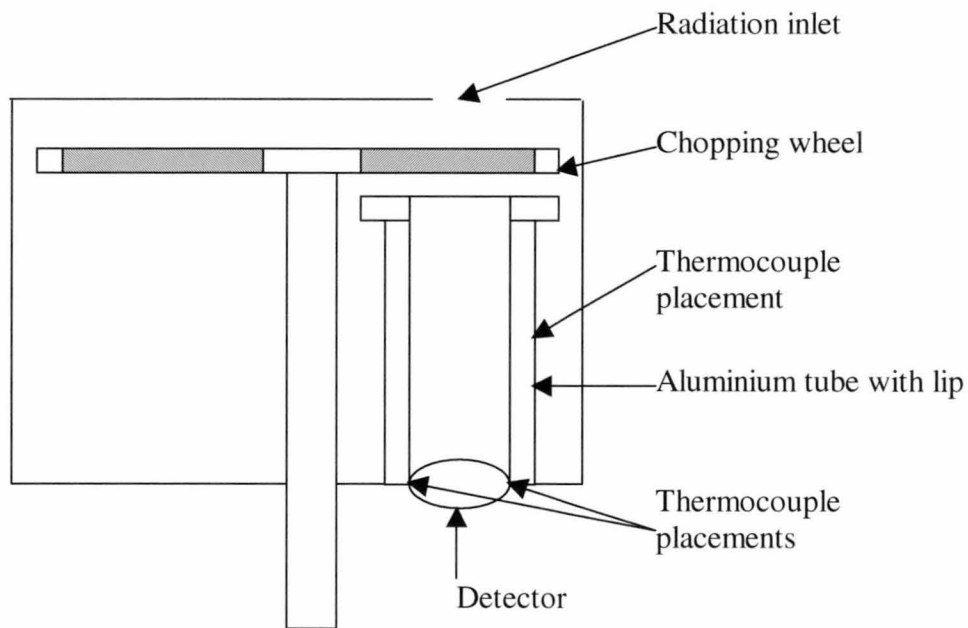


Figure 3.2. Schematic diagram of revised instrument cavity design.

When these changes were made, the original thermocouples were also replaced and their positions moved. The true reference cavity had become the smaller aluminium tube and so its temperature had to be measured rather than that of the outer cavity. The new thermocouples were placed in the positions indicated and were each connected to a Linear Technology LTK001 Thermocouple Cold Junction Compensator and Matched Amplifier.

The LTK001 chips were built into the instrument, alleviating the need for long runs of thermocouple wire back to a data logger. This amplification and reduction of wire lengths from approximately 10 metres down to 10 centimetres improved the accuracy of the cavity temperature measurements. The original long thermocouple leads were introducing significant electrical interference and the very small (μV) signals were prone to disturbance by electrical noise. The LTK001 system provides a compensated output signal of the order of $10\text{mV}/^\circ\text{C}$ and is buffered against antenna lead pickup of electromagnetic interference.

The change to the cavity described above yielded better performance from the instrument – the detector’s response to a target was found to be more consistent than in the previous instrument design. However a test was again performed to check for light leakage. In this case the radiation inlet of the cavity was covered from the inside with a small sheet of highly reflective aluminium Mylar. This in theory rendered the cavity “closed” and the detector should have given no response.

It was found however that the detector still responded to some change in the incident radiation. At this point it was hypothesized that one or both of two phenomena were occurring. On one hand the transitions from filter to chopping wheel surface observed by the detector may have been causing it to generate a signal. The unfiltered detector responds to all incident radiation up to the cutoff wavelength of its BaF_2 window ($12\mu\text{m}$). Thus any small change in surface emissivity or temperature that is viewed by the unfiltered detector will compete in response magnitude with comparatively large changes viewed by the filtered detector.

The other possibility was that despite the changes made to the cavity, some misalignment between the top of the new aluminium tube and the chopping wheel was causing leakage into the tube, modulated at the chopping frequency and therefore difficult to distinguish from ‘genuine’ filtered radiation.

It was decided that in order to prevent the detector from responding to any ‘fast’ temperature changes (changes at or near the modulating frequency), all fast-moving components in the detector’s view should be moved beyond the filters. The filters themselves would be switched slowly and a delay allowed for the detector’s response to settle after the filter transition. Essentially the chopping frequency was decoupled from the filter-swap frequency by incorporating a new chopping wheel and using the original chopping wheel to switch

between the filters at a much lower frequency. The revised and final cavity design is shown in Figure 3.3 below.

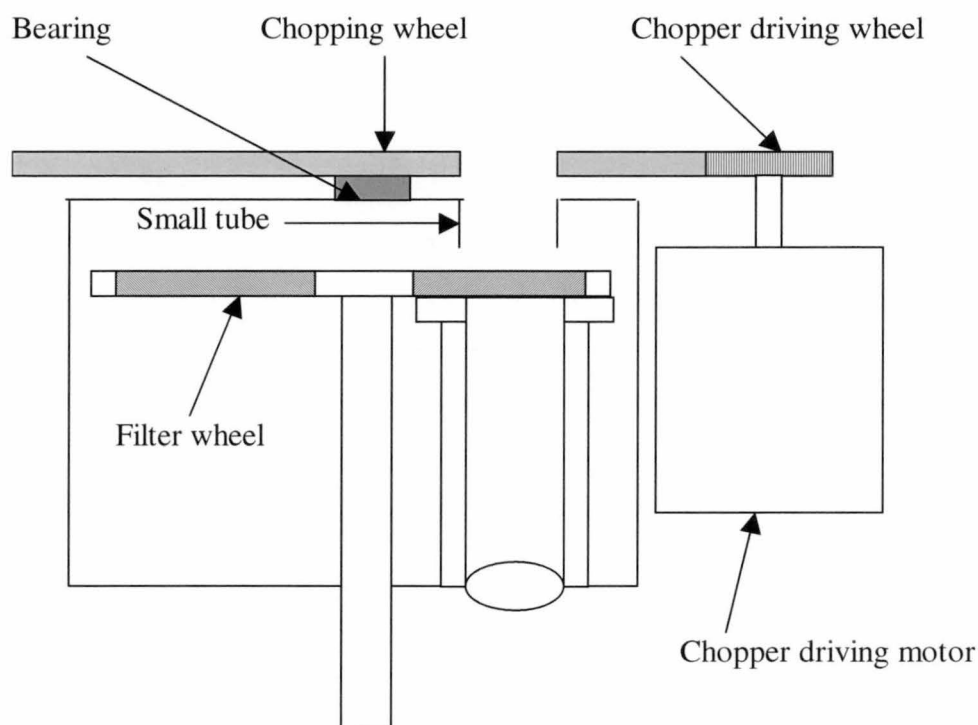


Figure 3.3. Schematic diagram of final instrument cavity design.

The chopping wheel was moved outside the cavity and attached via a bearing to the top surface plate of the original cavity. It was driven via contact with a driving wheel that was attached to a DC motor. The filter wheel was lowered even closer to the top of the internal cavity – in the previous design some gap was always maintained in order to minimise the possibility damage to the filters through high speed contact between the wheel and the cavity lip.

In this design the radiation inlet was bored slightly larger than the previous design to maximise the allowed radiation. A small section of tube was then added to the inlet, as shown in the diagram, in order to minimise leakage. It was also in this design that the LIE 307 model replaced the original LIS 114 detector. It is this cavity design that was retained in the final instrument prototype. A later and more advanced version of the instrument built for and in collaboration with other researchers (Soux *et al* 2003) retained the combination of filters and chopping in a single wheel – superior manufacturing allowed the new configuration to work well and without the problems associated with the implementation used in this study. This indicated that radiation leakage through wheel misalignment was the

most likely cause of the problems with the second design of this DCR. The second instrument mentioned above was not available for use in this study.

Figure 3.4 is a photograph of the exterior of the instrument reference cavity viewed from the front. The exterior of the cavity can also be seen from a side view in Figure 3.6 later in this Chapter.

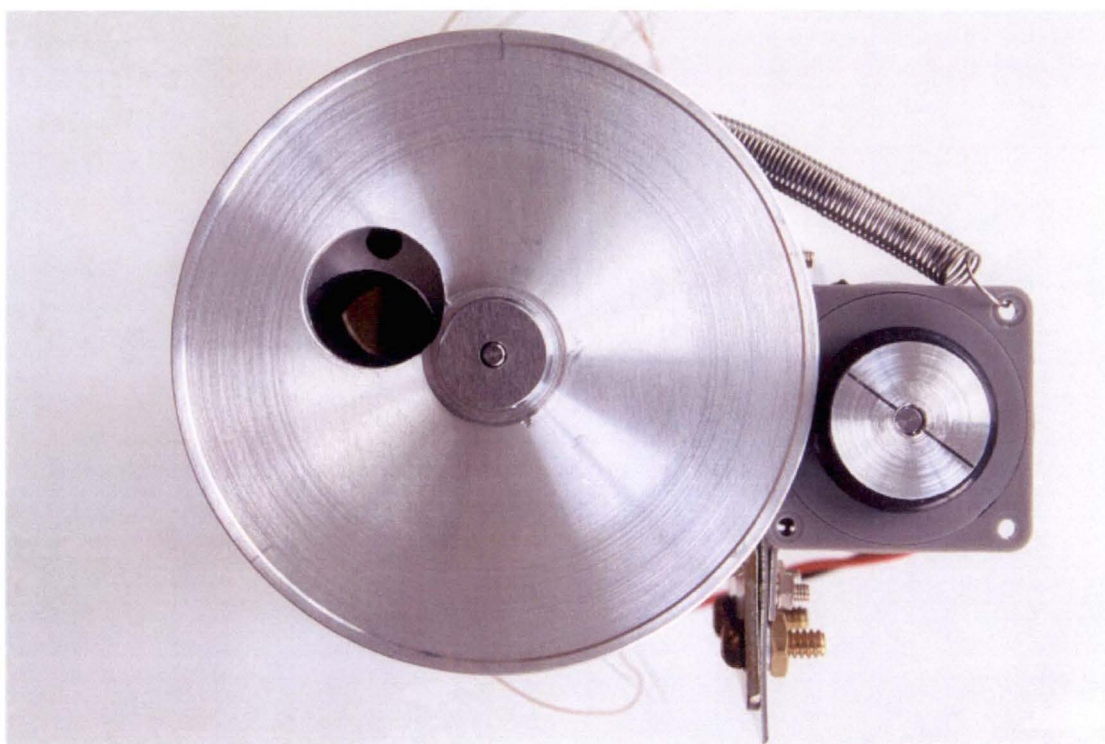


Figure 3.4. Front view of the instrument. The chopping wheel and the head of the chopper driver motor can both be seen. The admission hole in the main cavity can be seen through the hole in the chopper wheel.

The additional motor used to drive the new chopping wheel was a non-stepping DC type. However variable speed control was implemented through a dual potentiometer system that allowed two motor speeds to first be tuned by adjusting the relevant potentiometer and then selected via external control of a relay switch. The intention at the time was that the instrument might operate in a ‘fast’ or ‘slow’ mode, depending on the accuracy requirements. While this operational mode was never used, the tunable motor speeds proved useful in determining the optimum speed for the chopper wheel. The process for determining the optimum speed is discussed further in Chapter 5.

3.5 Electronic design

While contractors were employed to build both the instrument reference cavity and the instrument electronics, the reference cavity was designed as a part of the project. In contrast, the final instrument prototype's electronics were designed and built by Paul Waller at CSL, with regular consultative input from the author. For that reason, the topic of the instrument's electronic design will be treated here in a purely demonstrative fashion.

In its very first form the instrument used an operational amplifier (op-amp) to amplify the detector's output signal. The amplified signal was converted to digital form using an 8-bit analogue to digital converter or ADC. An optical switch was used to reference the position of the chopper wheel. The sampled digital output and information from the optical switch was then output via a serial cable. The serial cable was then connected to a PC and control software on the PC selected successive maxima in the output signal as the detected peak voltages. The information from the optical switch was used to identify the sequence of filters in order to correctly assign the peak values to their respective channels. The output was a magnitude relative to voltage, in the range -12.7 to 12.8 units in increments of 0.1 units. The control software simply displayed the measurement value for each channel on the PC screen as they were obtained, and did not provide any facility for logging the data.

The most effective change to the instrument's electronic design was a product of the need for better resolution in the output signal and the requirement that the instrument operate as a stand-alone field unit attached to a data logger. This meant that the peak detection functionality that was originally present in the PC program was moved into the instrument unit itself. This was achieved using 'sample and hold' circuitry that detects conditions on its input voltage and can 'hold' a particular value as its output voltage. A diagram of the sample and hold sequence for a single voltage peak is shown in Figure 3.5 below. The sampling rate is shown in the diagram as lower than in the real circuit for ease of interpretation.

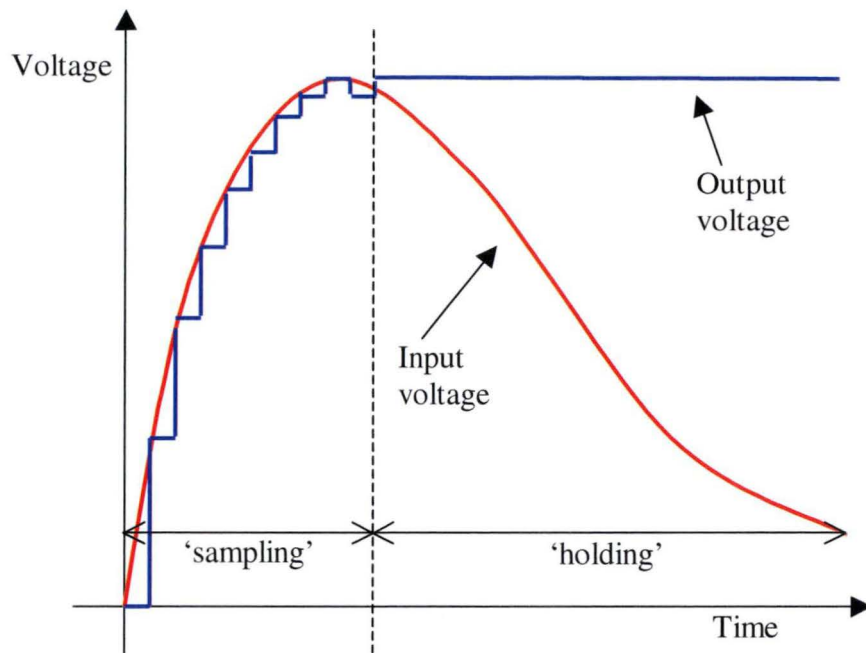


Figure 3.5. Diagram of the operational concept of the instrument's sample and hold circuitry.

An optical switch directed at the chopping wheel was used to determine the starting point for the sample and hold sequence and also to determine a reset point later in the sequence. A logical on/off output line was also added for each channel to indicate the point where the maximum value was 'held' and therefore the point where sampling of the output voltage would give a valid result. This process and the process for switching between channels will be discussed further in the next chapter.

The original instrument design used a DC motor to drive the combined chopping and filter wheel. As part of early modifications, a stepper motor and its associated control circuitry replaced this. Initially the change was made purely to provide more precise modulation, but the control circuitry later became more important. When the chopping wheel became the filter wheel, its movement changed from a continuous rotation (for chopping) to a periodic stop/start movement (for positioning the filters). The control circuitry was used in conjunction with the original optical switch to determine the correct positioning for the two filters.

Another important addition to the instrument's electronics was the cavity thermocouple measurement and output circuitry. The LTK001 measurement devices have already been discussed in some detail in Section 3.4. These were mounted on a circuit board and their outputs provided via a single output wire for each thermocouple and a shared ground wire.

The final major addition to the instrument's electronics was the circuitry for the DC motor that drove the chopping wheel. In essence this took the form of two tunable potentiometers and a relay. The relay was switched via an external control signal, implemented for compatibility with a data logger. Each potentiometer could be tuned to modify the resulting motor speed and the relay was used to switch between these two speeds where required.

Photographs of the final instrument design from both sides are shown in Figures 3.6 a, b and c below.

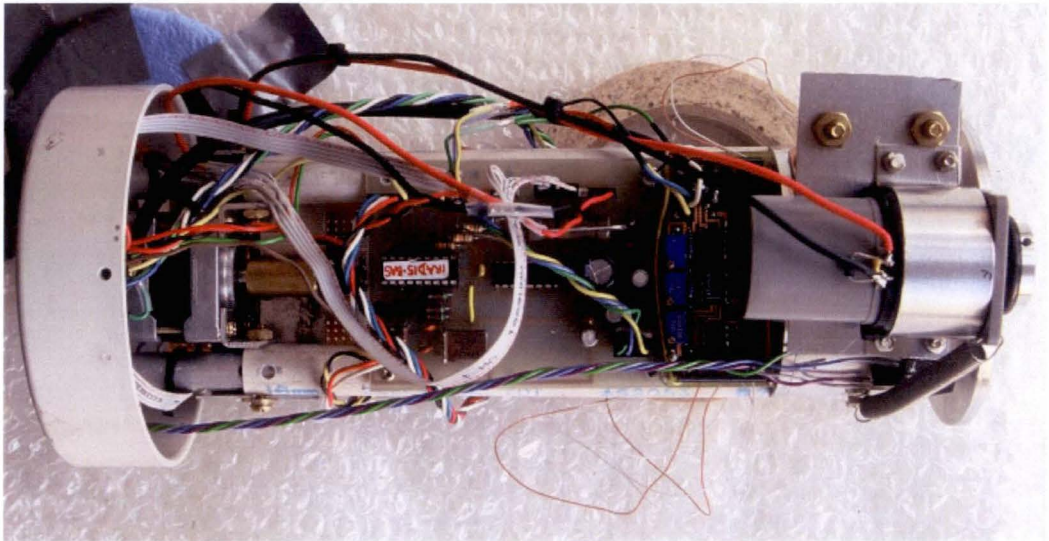


Figure 3.6a. View of the instrument's circuitry. The filter wheel's stepper motor can just be seen at the left. The central pale printed circuit board holds the instrument's stepper motor control circuitry. The darker printed circuit board to the right holds the internal thermocouple circuitry. Furthest to the right, the chopping wheel's driver motor obscures the instrument cavity.

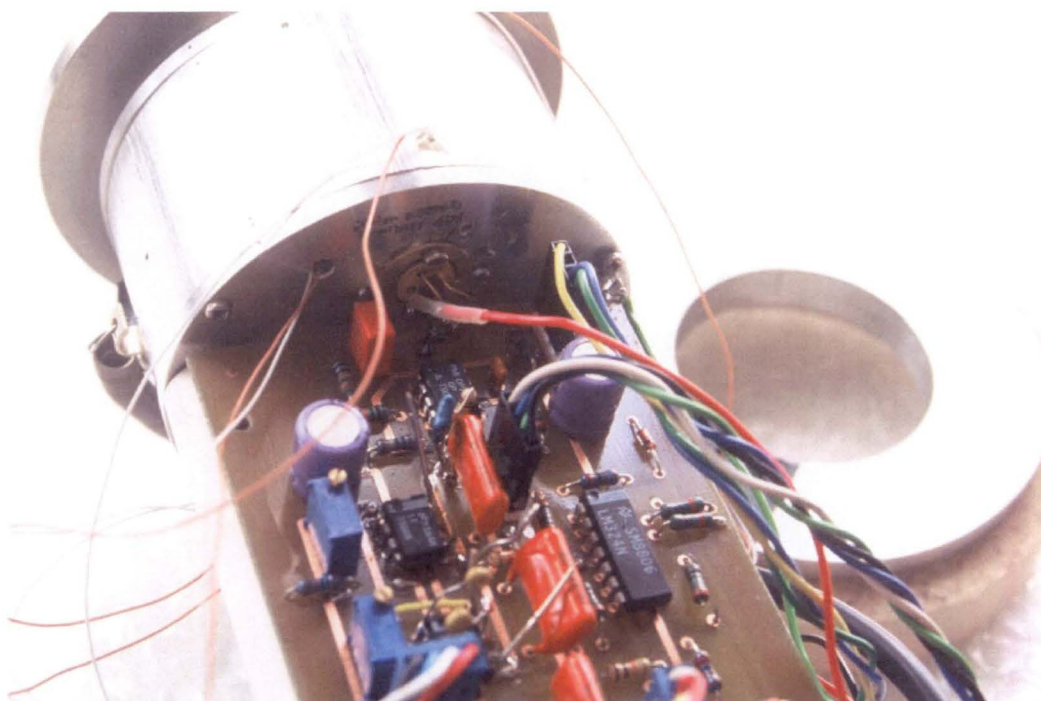


Figure 3.6b. View of the instrument's circuitry. The instrument cavity can be seen at top left, with the pyroelectric detector mounted in its lower surface. The visible printed circuit board holds the detector circuit and the sample and hold circuitry.

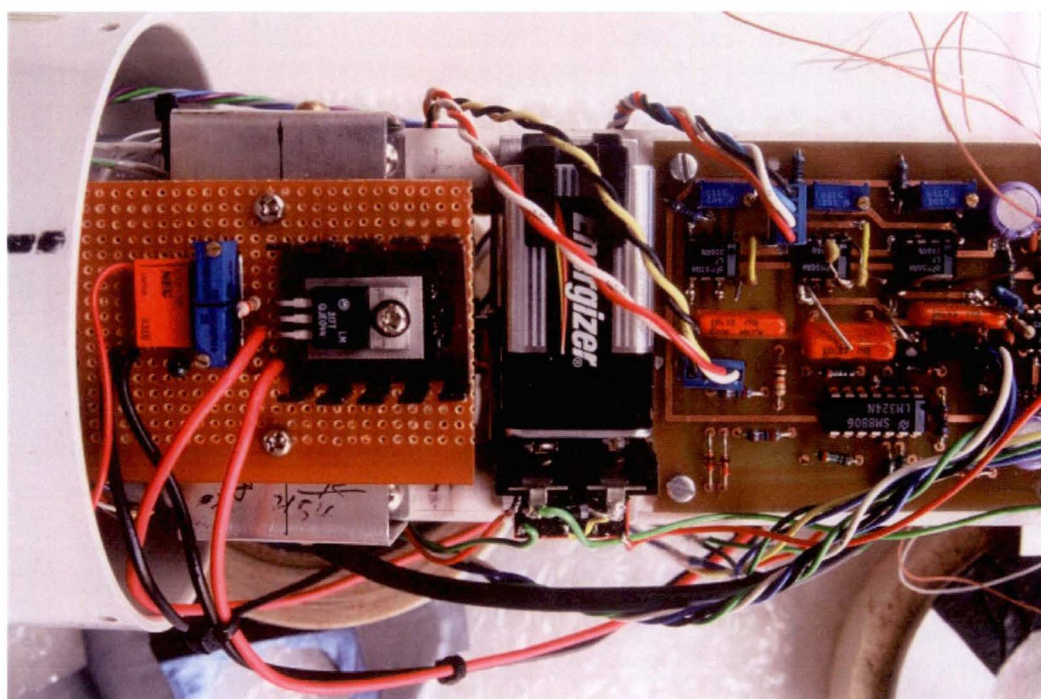


Figure 3.6c. View of the instrument's circuitry. The sample and hold circuitry can be seen at the right, the internal battery in the centre and the chopping wheel driver motor's circuitry at the left.

3.6 Potential design improvements

There are potentially many improvements in the instrument construction and design that would yield better performance. Some of these are applicable within the general constraints of the current design.

The choice of detector is an obvious item for potential improvement. While the LIE 307 detector used in the final instrument was an improvement over the original LIS 114 model, there are many more detector types that are designed specifically for radiometric applications such as this. InfraTec, for example, can supply a “special line” of detectors designed specifically for high-performance applications.

Construction quality of the instrument is also a determining factor in its performance. Changes to the instrument were added to its original chassis and as the design evolved, space for additional components was limited. Improvements in the physical robustness of the instrument could also have improved the quality of its performance by avoiding vibration effects. Pyroelectric devices are slightly microphonic, meaning that vibrations cause noise in the detector signal and should be avoided.

The instrument cavity could also benefit from changes in its physical construction. Space limitations meant that the aluminium tube added to the cavity had to be fairly thin, which limits its thermal inertia. A later version of the instrument used a thick disc of solid brass with the cavity bored out of the disc (Soux *et al* 2003). This creates a uniform, stable and more easily measured cavity temperature.

A second class of potential improvements involves major changes to the instrument design, which would in turn require a redesign of the entire instrument. Still, these are worthy of brief mention.

The speed of the instrument was limited by the choice of processing electronics. As mentioned earlier, the use of a lock-in amplifier allows small signals at the modulating frequency to be selectively amplified. The selective amplification eliminates much of the electrical noise at frequencies away from the modulation frequency. The individual samples from a large number of very fast measurements are then integrated to give a ‘measurement’ value. Modulation frequencies are typically hundreds, up to thousands of Hertz. Such high frequencies obviously increase the measuring speed of the instrument, but also further ensure

that any slow changes in temperature of either the detector or the reference radiator have little effect on the measurement.

As opposed to using a polished chopping wheel to reflect the radiance from the reference cavity, another option is to use the chopping wheel itself as a reference. This requires accurate measurement of the chopping wheel temperature as mentioned earlier, which is not a simple exercise for a rotating wheel.

One final potential improvement is the use of an internal blackbody source as the reference. This could be achieved by heating the cavity in the design described earlier, but doing so would also heat the detector and possibly cause detrimental effects. A better option is to use a reflective chopping wheel, angled so that in the 'off' position the wheel reflects the radiance from a heated blackbody source at known temperature. A more complicated design might use dual detectors and an emissive chopping wheel, with one detector directed towards the incoming radiation and the other directed at an internal blackbody source. This would eliminate the need to measure the temperature of the chopping wheel, because taking the difference between the dual signals would effectively cancel the modulation reference. However, this method would also require that the responses of the two detectors would not drift relative to each other between calibrations of the instrument.

3.7 Summary

This chapter has described the design and construction of a prototype dual-channel narrowband radiometer intended to measure irradiance divergence. The design and construction was iterative and evolutionary in nature and took place over more than two years from January 2000 to June 2002. Whilst the intention has been to avoid unnecessary detail, description of important developments and changes in the design has been included.

While there are many potential improvements that could be made, the intention was to physically realize the 'virtual' instrument described in Chapter 2 as a working prototype. This was achieved in the instrument design, and the process by which the design evolved also provided useful direction in the construction of a more advanced instrument (Soux *et al* 2003). Improvements made in the second instrument were primarily related to improved machining and increased thermal stability of the reference cavity. The second instrument was designed by the author, Manuel Nunez, Paul Waller of the CSL's electronics lab and Peter Dove of the CSL's workshop and built by the CSL. The second instrument was not available for use in the fieldwork component of this study.

Chapter 4

Instrument control and sampling

4.1 Introduction

This chapter details the methods used to log data from the instrument. The instrument itself contained no data logging facilities but was designed to output data in a form easily logged by a Campbell CR10X data logger. The data logger and its programmed measuring sequence then became an integral part of the instrument.

Rather than only employing a data logger for the purpose of recording measured values, this system required the data logger for short-term data recording, storage, calculation and averaging. This process defined a ‘measurement’, the final values of which were recorded in long-term storage during field operation of the instrument. Discussion of the practical field logging will be left to the relevant chapter. This chapter will detail the concept of the ‘measurement’ mentioned above and provide details of why such a concept was necessary and how it was developed and refined during development and testing of the instrument.

4.2 Internal instrument control and outputs

This section details the instrument’s internal control process and the resulting outputs. The final instrument design used a PIC Basic-programmed microchip to control the sequence of the filter wheel stepping motor and sample and hold circuitry. The program used output from two optical switches (mentioned in Section 3.5) to detect reference points on the filter wheel and chopping wheel.

An important factor in the sampling sequence was the detector’s settling time relative to the time taken to change between the two filters. As noted in Chapter 3, it was desirable that the frequency of switching between the filters be significantly less than the chopping frequency in order to avoid corruption of the chopped signal by the detector’s response to a filter change. For this reason the sampling sequence was designed to consist of multiple measurements for each filter. Later in the development of the instrument, this proved to be a useful choice as it also provides an opportunity for reduction of the effects of noise through averaging multiple measurements.

Nine full chopping cycles was decided upon as the period for changing between filters. Once the appropriate filter was moved into place (referenced in position by an optical switch), nine cycles of the chopping wheel were counted (also with an optical switch) before the filters were changed again.

Logical values were output on two lines – one for each filter (or channel). These were used to denote times at which measurement of the instrument output was ‘valid’. Considering the diagram of the sample and hold output for a single chopping cycle in Figure 3.5, it can be seen that the output voltage only reflects the detected peak value after the peak is detected. Any measurements made before that time will give a ‘false’ or invalid reading of the output voltage.

Not shown in that figure is the necessary re-set of the output voltage that must occur before sampling can again begin. This occurs at a time determined by the chopping wheel’s optical switch. When the pulse from the switch was detected, the sample and hold circuits changed from holding mode to sampling mode and the relevant logical value was set to ‘low’.

The logical output channel indicated the channel from which the voltage output was produced and therefore the instrument output line that should be sampled. Figure 4.1 below is a simplified representation showing a portion of the normal output sequence of the instrument. The logical values are labeled DA1 and DA2, for ‘Data Available (channel 1)’ and ‘Data Available (channel 2)’ respectively.

The ‘down time’, or portions of the sequence during each set of nine chopping cycles in which both DA values are zero, have been shown longer than their true relative length for ease of interpretation. Pulses from the chopping wheel’s optical switch are also shown although these were used only internally and did not form part of the instrument’s output. The output voltage V_{out} has been shown as a single line in the illustration although in reality there were two output lines, one line for each channel. This simplified illustration of the output sequence does not show certain anomalies that were found to exist in the output voltage. These will be discussed further in the next section.

It is obvious from this figure that any process intended to measure the output voltage from the instrument would also need to monitor the logical values on the DA lines and only sample the output voltage when appropriate. The CR10X data logger was well suited to this purpose, as it provides a set of eight control ports that are designed to read logical values from such outputs.

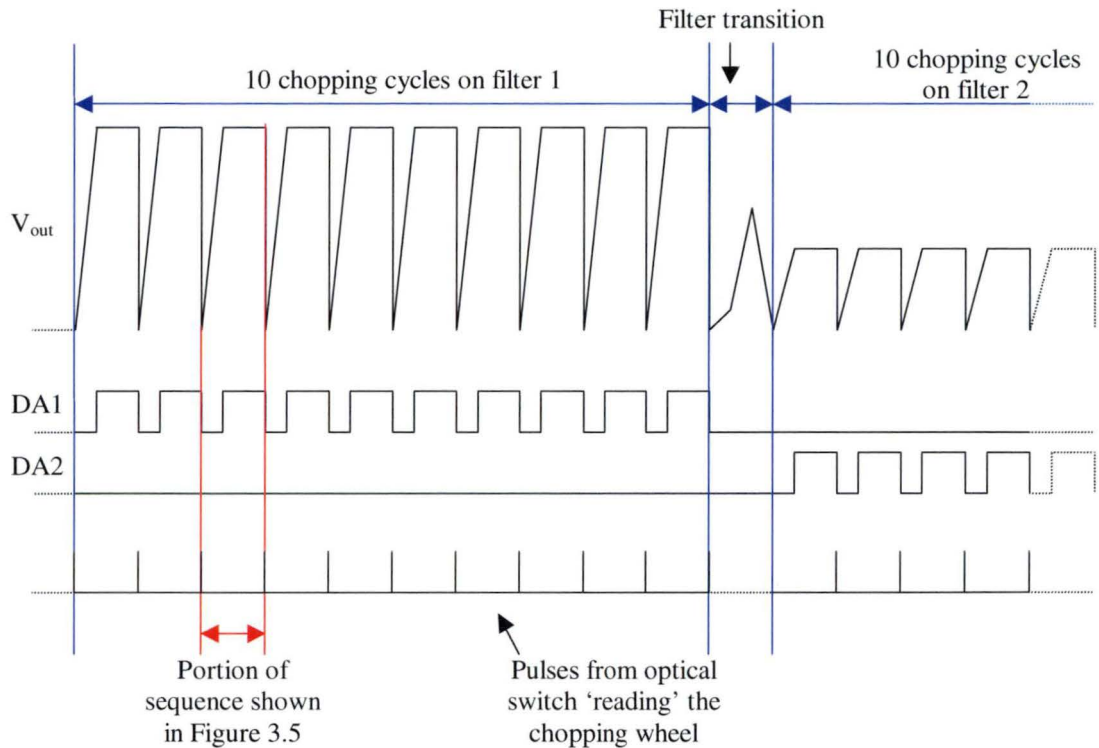


Figure 4.1. Instrument output summary. DA1 and DA2 are logical lines indicating availability of valid data on the instrument voltage line. V_{out} corresponds to the instrument's output voltage, shown as a single line here but carried by two output lines in the instrument.

The pair of V_{out} (instrument signal output) lines and the pair of DA lines account for four of the instrument's outputs. In addition to these, three lines carried the internal instrument temperature values from the LTK001 thermocouple and cold junction compensator circuits. These circuits were discussed in Chapter 3 – they provided the temperature measured by the relevant internal thermocouple as a millivolt-scale signal output. These values are easily read by the data logger and are not as susceptible to noise as microvolt-scale thermocouple voltages.

Two separate ground lines – one for the set of LTK001 circuits and one for the instrument voltage output and DA lines – and a 12V speed selection relay completed the set of instrument connections. The relay was intended for use as a switch between 'fast' and 'slow' chopping speeds mentioned in Section 3.4, but was never used in practice.

The third of the three internal temperature measurement circuits was found to be faulty early in the instrument testing process and was not used from that point onwards. This left four lines of voltage output from the instrument; one each for the voltage output for the two

channels and two temperature outputs. The data logger program measured all of these using single-ended voltage measurements. A single ended voltage measurement measures the voltage on an input terminal against a common ground terminal. These are distinct from differential measurements that measure the voltage difference between two terminals, effectively allowing for a floating ground.

The two DA lines were wired into two of the eight available control ports on the CR10X data logger. These ports detect logical 'high' and 'low' values and can also be set to a given value. 'High' and 'low' logical values correspond to voltages greater than 3.5V and less than 1.5V respectively. The data logger program was able to effectively monitor the 'state' of the instrument using the detected DA1 and DA2 values together with a series of flags and counting variables. This process will be discussed in more detail in the following section.

4.3 Instrument output sequence analysis

This section examines the process used to obtain useful information about the instrument's output sequence using the CR10X data logger. Knowledge of the temporal and electrical characteristics of the output sequence was necessary to allow a data processing and logging process to be defined.

The first of these goals – correct and accurate sampling of the instrument output – was achieved using a repetitive process within the program. This process was designed based upon initial testing that involved relatively fast (32Hz) sampling of the two instrument signal voltage lines and the two DA lines.

Figure 4.2 below shows the results of 32Hz sampling of the two signal output lines and the DA lines. The DA lines are plotted on a zero (logical 'low') to twenty-millivolt (logical 'high') scale for ease of interpretation. Channel one is shown in red and channel two in blue. This chart corresponds to approximately fifteen seconds of sampling.

In this plot the effects of the filter transitions are obviously present where both DA lines are in the low state. Noise (probably microphonic) with approximately ten millivolts amplitude is introduced on both signal output lines. It is also clear that the 'down-time' of the relevant DA line between chopping cycles is significantly shorter than the time of the cycle itself, as mentioned earlier. Only two incidences of inter-cycle down-time were sampled in a total of 477 samples. These can be seen as interruptions in the high state of DA2. The signal output appears unaffected, most likely a fortunate effect of the time interval between the DA2

sample and the signal output sample. In practice the risk of contamination of the logged signal output data can be avoided by monitoring the DA outputs and only sampling the signal output when appropriate.

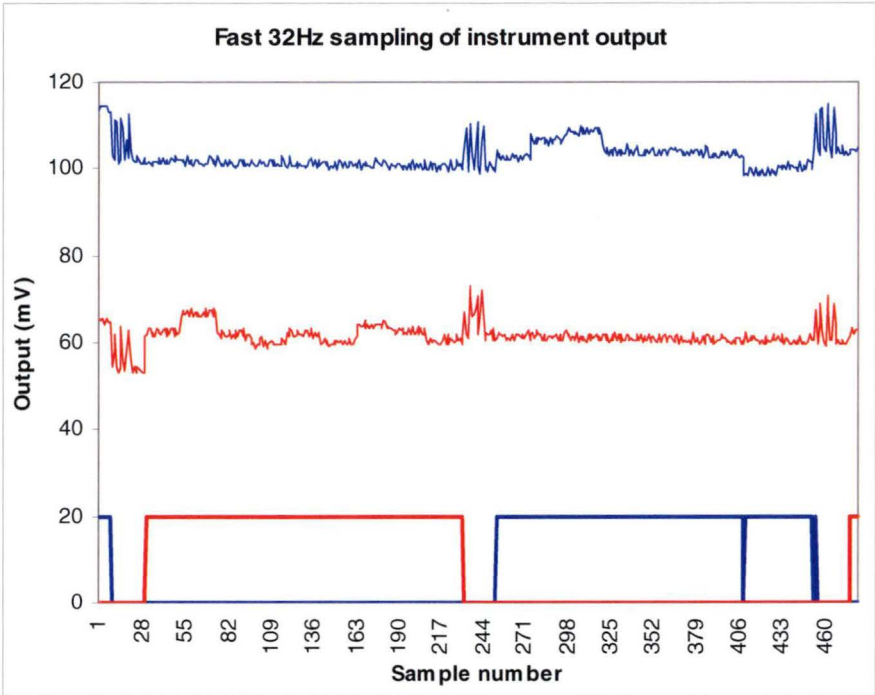


Figure 4.2. Instrument outputs (DA1, DA2 and V_{out} for both channels) sampled at 32Hz. Channel 1 is shown in red and channel 2 in blue. The plotted sequence represents approximately 15 seconds of sampling.

Another important feature is the visibility of the individual cycles within each output phase. These reveal themselves in the step-like nature of the signal output, occurring on a scale significantly larger and at a frequency significantly lower than the obvious electrical noise that is present in the signal. These individual cycles correspond to one cycle of the chopping wheel and therefore one value detected by the sample and hold circuits.

Figure 4.3 below shows the results of sampling more of these sets of nine cycles, with sampling performed at 16Hz. The sampling was also filtered using the DA channels – only valid signal output values were measured. This removed the effects of the filter transitions. Output signal values for both channels are shown as a single line. This chart corresponds to approximately 45 seconds of sampling.

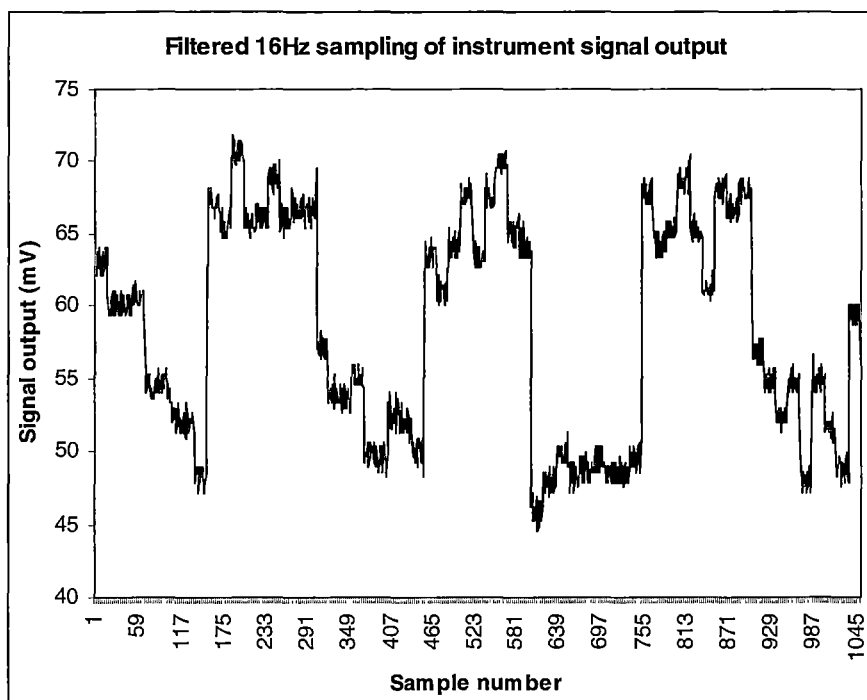


Figure 4.3. Combined filtered voltage output from both channels, sampled at 16Hz.

In this plot there are obvious features at three frequencies. At the highest frequency – at or greater than the sampling frequency - there is small-amplitude noise in the output signal. This was most likely introduced during the signal output or data logger sampling stage, as the sample and hold circuit outputs did not exhibit any such noise when measured directly with an oscilloscope.

At a lower frequency, approximately one Hz, the individual cycles are evident as steps. At a lower frequency than that – approximately 0.12 Hz – the changes between channels are evident as larger steps. The variation between individual cycles within each set of nine is due to variation in the detector’s response to the measured target. In this test case, the instrument was aimed at a constant-temperature target at ambient temperature. While the instrument’s self-heating produces a small difference between the cavity temperature and the ambient room temperature, the detector response was close to the minimum that would be expected for any practical measurements.

As this testing was conducted in order to assess the instrument’s output sequence, the obvious variation in the output signal was not considered a significant concern, particularly when the very small amplitude of the output signal was taken into account.

Figure 4.2 above showed slightly more than a single iteration of the complete instrument output sequence. If left sufficiently powered for any length of time, the instrument would simply repeat this output sequence. The next stage in the instrument design was to create a measurement sequence ‘around’ this continuous stream of output, to sample and manage the flow of data and then log the results.

4.4 ‘Measurement sequence’ definition and design

The logger program was designed to perform three interdependent functions. Firstly, the instrument output had to be correctly and accurately sampled. Secondly, the resulting samples had to be processed to give an averaged ‘measurement’ of the instrument’s output. Thirdly, the ‘measurements’ had to be sequenced in a fashion that allowed regular time-based logging of results in the field.

A summary of definitions of the various components of the intended program is given in Table 4.1 below.

Name	Approximate frequency (Hz)	Description
Cycle	1.1	One cycle of the chopping wheel – a single detected output signal value is sampled and held
Measurement	0.12	Nine sequential cycles on the same channel, followed by a filter transition
Measurement sequence	Flexible - to be determined by the logger program	A set of measurements on both channels, yielding a single averaged value of the output signal voltage for each channel

Table 4.1. Definition and description of terms relating to the measurement process of the DCR.

The data logger program did not explicitly sample individual cycles. Rather, the program performed multiple samples of each measurement. With appropriate filtering of the DA lines in place, each measurement could be considered as a continuously valid signal output.

It was observed during initial testing that the first cycles in a measurement – those immediately following a filter transition – were more likely to contain highly variable output

signal values than later cycles. It was assumed that the detector required a number of cycles to settle after the filter transition. For this reason the data logger was programmed to sample a select group of values around the middle of a measurement. Ignoring the values at the end of the measurement avoided the risk of biasing the averaged result in the case that there was some temporal trend across the nine cycles in the measurement.

A complicating factor was the time-dependence of the sampling. The instrument output sequence is based on the optical switch reference points and so it is essentially independent of chopping speed and therefore of time. As will be discussed shortly, much of the program was designed to use the DA lines as a reference in order to count measurements. However the portion of the program that sampled the signal values within measurements was time-based, using data logger execution intervals as a unit of time.

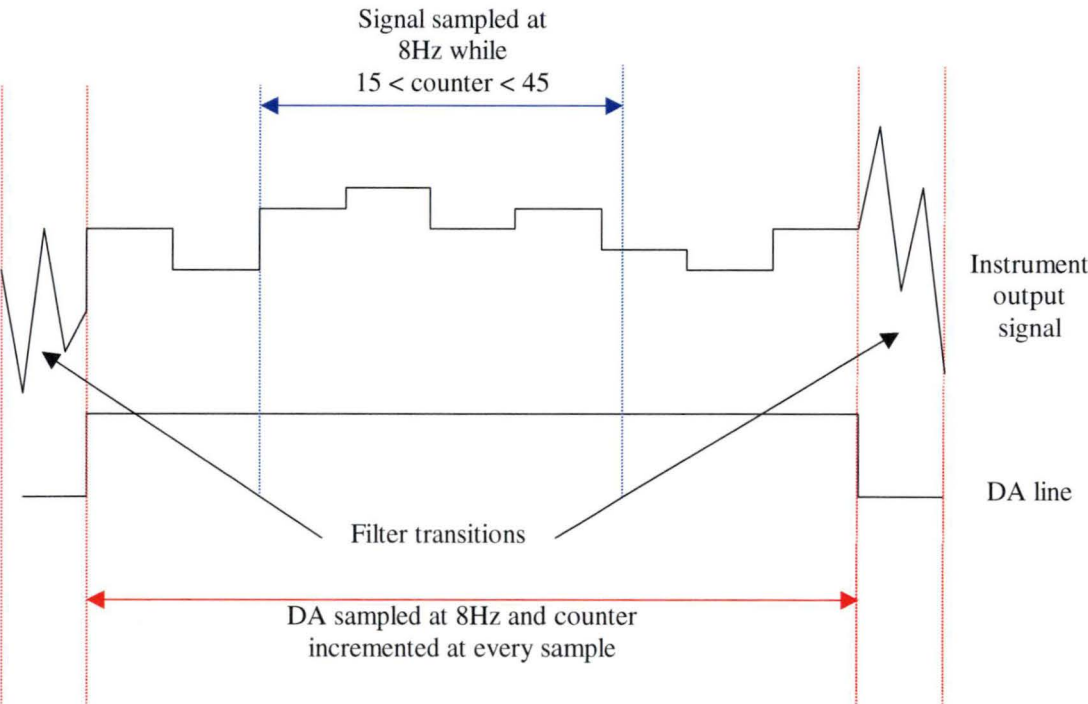


Figure 4.4. Data logger sampling regime during a single ‘measurement’ as defined by Table 4.1.

Figure 4.4 above illustrates the process used to sample each measurement. The same process was used for each channel in succession, but the sampled values were stored and later averaged according their channel number. Although the instrument’s internal temperature values were independent of the output sequence, these were sampled when the output signal values were sampled. This decision was made in order to avoid unnecessary complication of the logger program. Sufficient samples are gathered to reduce the effect of electrical noise by

averaging, and the internal temperatures undergo only slow changes, so no useful temperature information was lost through this measurement regime.

The sampling rate was set at 8Hz based upon a calculation of the time required for a full iteration of the program. The programs used for initial testing were simple and therefore fast and allowed time for sampling to occur at 16 or 32Hz. The final program was more complex and required approximately 90 milliseconds to complete. This was rounded up to an execution interval of 0.125 seconds, effectively an 8Hz sampling rate. It is evident from Figure 4.4 that any change to the chopping speed would necessitate a change to the counter values at which sampling begins and ends.

Each measurement yields 29 samples of the output signal and internal temperature per channel. It can be seen in Figure 4.4 that the samples are gathered during the third, fourth, fifth, sixth and a portion of the seventh cycle in each measurement.

The next stage in the program design was to define the measurement sequence. This was achieved through further fast-sample testing and analysis of data gathered during the instrument calibration process. Another important factor was the time taken for a measurement sequence to complete. While a long sequence provides more samples that can be averaged, it is desirable that the sequence completes in a time period that does not allow significant changes in the target temperature. Also, measurement sequences performed in the field must occur frequently to provide a dense time series of logged data.

The first feature of the measurement sequence was to allow two full measurements to occur unsampled on each channel before sampling begins. This was in response to observations made during calibration, in which the instrument was pointed at a blackbody source. It was observed that the instrument's response in the first two measurements from each channel was not consistent with the response from later measurements.

It is likely that this inconsistency was due to the almost instantaneous change in the incident radiation due to the sudden introduction of the blackbody source into the instrument's field of view. The relevance of this adjustment time would depend in practice on the intended application of the instrument. Measurement targets that do not change or do not change their temperature rapidly may not require such a period of adjustment. However, it was decided that it was important to maintain the same measurement sequence for both calibration and measurement and so the adjustment time was retained in the program.

The program allowed for settling of the instrument's response by leaving the first two measurements in each channel unsampled. This was achieved using 'flags' – constructs of the CR10X instruction set – to track changes in the condition of the two DA lines. Once two full measurements had passed on each channel, the program counted five measurements on each channel, sampling each one as described earlier. This process is illustrated in Figure 4.5 below.

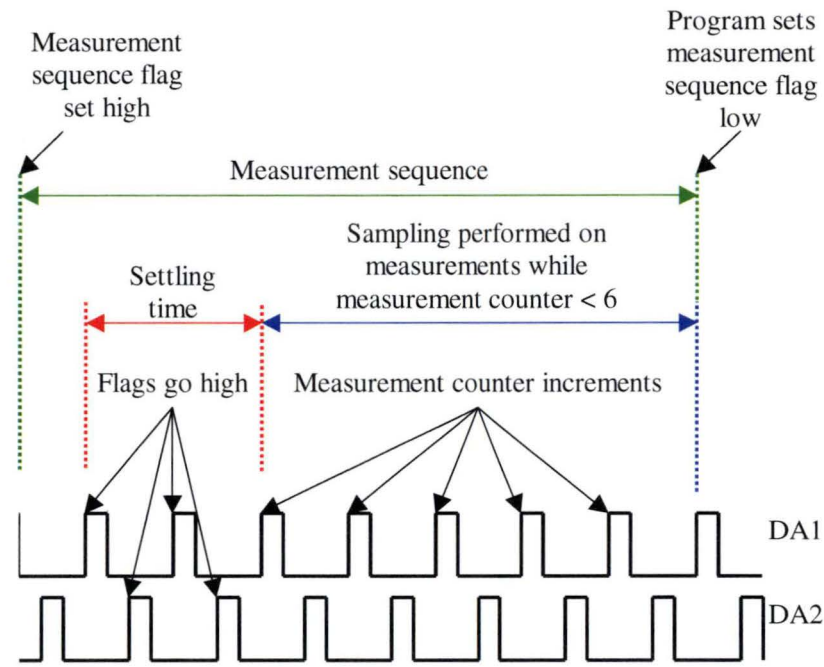


Figure 4.5. Data logger sampling regime for a single 'measurement sequence' as defined in table 4.1.

Only the values of the DA lines are shown here for simplicity, as these are the variables that control the sequence. The length of the DA pulses has been compressed to better illustrate the gaps between measurements. Voltage measurement sampling was performed on the signal output and internal temperature for each measurement, as shown in Figure 4.4. With a cycle frequency of 1.1 Hz, this measurement sequence takes approximately two minutes and six seconds to complete.

This definition of the measurement sequence required an additional flag in the logger program. A high condition on this flag served to initiate the sequence and the flag was set low at the end of the sequence. This flag was then set high by the program in different ways, depending on the application. For calibration purposes a switch was used to manually set the measurement sequence flag. This allowed individual measurement sequences to be performed on demand. For field measurements the program set the flag high at

predetermined time intervals so that a measurement sequence was initiated based on the current time.

When the measurement sequence flag was set low by the program to indicate the end of the measurement sequence, data was output to storage. A running average of the signal voltage and internal temperature voltages was kept throughout each measurement sequence. At the end of the sequence, each running average was the average of 145 values; 29 values per measurement over five measurements on each channel. A summary of the data output to storage is given in Table 4.2 below.

Output	Units / data format	Description
S_1	uncalibrated mV	Average signal level sampled on channel 1
Ti_{11}	mV, 10mV = 1°C	Average internal temperature from thermocouple 1, sampled during channel 1 measurements
Ti_{12}	mV, 10mV = 1°C	Average internal temperature from thermocouple 2, sampled during channel 1 measurements
S_2	uncalibrated mV	Average signal level sampled on channel 2
Ti_{21}	mV, 10mV = 1°C	Average internal temperature from thermocouple 1, sampled during channel 2 measurements
Ti_{22}	mV, 10mV = 1°C	Average internal temperature from thermocouple 2, sampled during channel 2 measurements

Table 4.2. Data output to long-term storage in the data logger program.

Two data logger parameters were added to the outputs. One was the program line in which the output was performed – a mandatory component of the CR10X output. The second was the voltage measured across the data logger's power supply, monitored for maintenance purposes.

Several versions of the logger program were created for specific purposes. At the core of all of the programs was the fundamental measurement sequence, which remained unchanged deliberately throughout.

4.5 Summary

This chapter has described the instrument's internal control processes and their subsequent outputs. A program for recording, processing and logging the instrument's output has also been discussed. One aim of this program was to sample and process the instrument's output, yielding useful averaged results of all of its important outputs, ready for further processing. Another aim was to 'manage' the instrument, so that the instrument in combination with the CR10X data logger could be used as a laboratory instrument for calibration or as a short to medium term field-based instrument for practical experiments.

These goals were both achieved through the definition of a 'measurement sequence' within the data logger program that can be used as a fundamental process within more complex programs. This sequence yields averaged values for six instrument outputs, with each average calculated from 145 individual sample values in order to reduce the effects of noise.

The individual sample values were filtered from a total of 455 potentially available samples in the same period. The selection of samples was based on the instrument cavity's settling time, the detector's settling time after filter transitions and the avoidance of sampling during instrument 'down-time'. If data was simply recorded and averaged, these factors would have caused contamination of the averaged result. If all data were sampled at the program's sampling frequency and recorded for post-processing, the data storage requirements would have been unmanageable. This program and the measurement sequence that it defines provided a significant additional stage in the instrument's functionality.

Chapter 5

Instrument testing and calibration

5.1 Introduction

This chapter describes the final testing and calibration of the instrument – the final stages of the instrument's development. Tests were performed to establish the instrument's field of view and optimum chopping speed. The calibration of the instrument involved quantifying its response to blackbody targets at a range of temperatures. The end goal of the calibration process was to prepare an equation for converting the instrument's averaged millivolt outputs to the brightness temperature of the blackbody target in each channel.

One section in this chapter describes the design and construction of a mount for the instrument that provided a rotating platform. The platform's rotation was controlled by the CR10X data logger and was an essential addition to the instrument for field of view (FOV) testing and for further practical use. A further section is dedicated to the description of a blackbody source that was designed and built specifically for the instrument's calibration.

5.2 Rotating instrument mount

In Chapter 2, various reasons were given for the choice of a narrow field of view for the instrument, relative to a hemispherical FOV instrument such as a pyrgeometer. Such a design provided the capability for directional measurements, but also limited the coverage of the measurement when the instrument was pointed in only one direction. Therefore it was necessary to enable the instrument to 'scan' in at least one rotational plane in order to extend the instrument's measurement coverage.

This scanning capability was provided through the use of a rotating platform to which the instrument could be attached. Early in the design phase of the instrument, other options were considered including mirror-based internal scanning. This option proved infeasible due to cost and design considerations and so an external platform was used, in the form of an instrument mount. The mount was built by Peter Dove, John Davis and Paul Waller of the University of Tasmania's Central Science Laboratory.

The desirable characteristics of the instrument mount were accuracy, speed, ease of control and flexibility of installation. For FOV testing and field measurements the instrument had to be rotated quickly between pre-determined positions. The position of the instrument had to be accurately specified in both cases. To maintain a single control and logging package, the instrument mount had to be controlled by the same data logger that was used to log the instrument data. This provided ease of installation and transportation, and also allowed rotation of the instrument to be included in the same program that controlled the measurement sequence and data logging. For practical use the instrument mount needed to be attached to various platforms such as tripods and scaffolding. This requirement for flexible installation options was considered in the design of the mount.

The physical design of the mount is shown in Figure 5.1 below, including additional parts designed for the various installation requirements. The majority of the effort in the mount design was required for the mount control box.

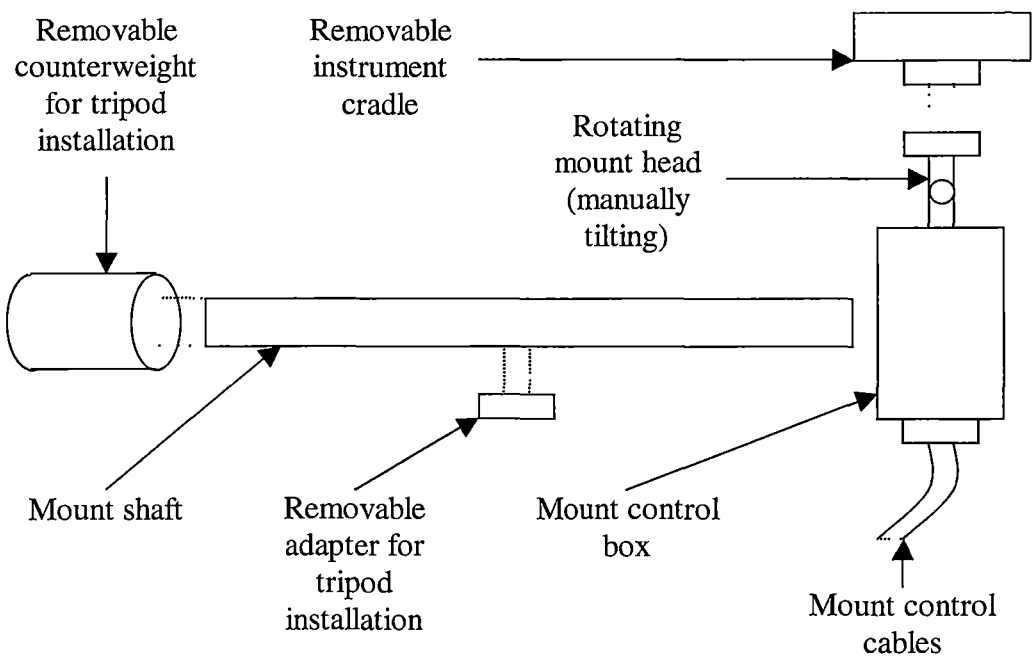


Figure 5.1. Physical design of the rotating-head instrument mount.

The physical design consisted of a control box, instrument cradle, shaft, tripod adapter and counterweight. The tripod adapter allowed the mount shaft to be screwed onto a large tripod. When the mount was installed on a tripod, the counterweight was required to balance the weight of the control box, instrument and instrument cradle.

The section of the control box that bolted onto the mount shaft allowed the control box to be attached perpendicular to the shaft (as shown in the figure) or aligned along the length of the shaft. These two configurations corresponded to rotation of the instrument cradle in planes respectively parallel and perpendicular to the shaft. The mount head could also be manually tilted and then fixed at any angle, effectively tilting the plane of rotation. Although the tilt could not be adjusted automatically, the ability to tilt the instrument provided a useful additional option for the scanning configuration.

The mount control box contained a stepper motor, gearing mechanism and control circuitry. The gearing mechanism was required for two reasons. It reduced the stepper motor's rotational step size by a factor of 50, from 1.8° to 0.036° per step, greatly increasing the accuracy with which the rotating head could be positioned. It also reduced the power required by the mount. The stepper motor alone could not hold the weight of the instrument unless it was powered, meaning that the mount would have to be powered continuously when used. This was not possible for any reasonable length of time if the mount were powered by battery, a likely requirement in the field. The gearing mechanism provided sufficient resistance to hold the instrument's weight, meaning that power needed only to be supplied to the mount during periods of rotation.

The control circuitry was designed to act as an interface between the stepper motor and the data logger used to control the mount. It also provided some additional functionality for ease of control and safety. The input and output from the control circuit took the form of four logic lines that were connected and controlled by four of the control ports on the CR10X. The mount control box and mount head are shown in detail in Figure 5.2 below.

The mount head was fitted with the shoe of a quick-release tripod head, removed from a tripod designed for heavy-duty video use. The foot of the quick-release tripod head was attached to the base of the instrument cradle. This allowed fast (less than one second) attachment and removal of the instrument cradle from the mount head. It also allowed the instrument to be semi-permanently secured to the instrument cradle, which when detached from the mount head added very little to the instrument's size and weight.

The instrument mount was controlled by sequences of instructions in the data logger program. The data logger was able to provide a sequence of pulses at a rate that translated to 50 seconds for a 180° rotation.

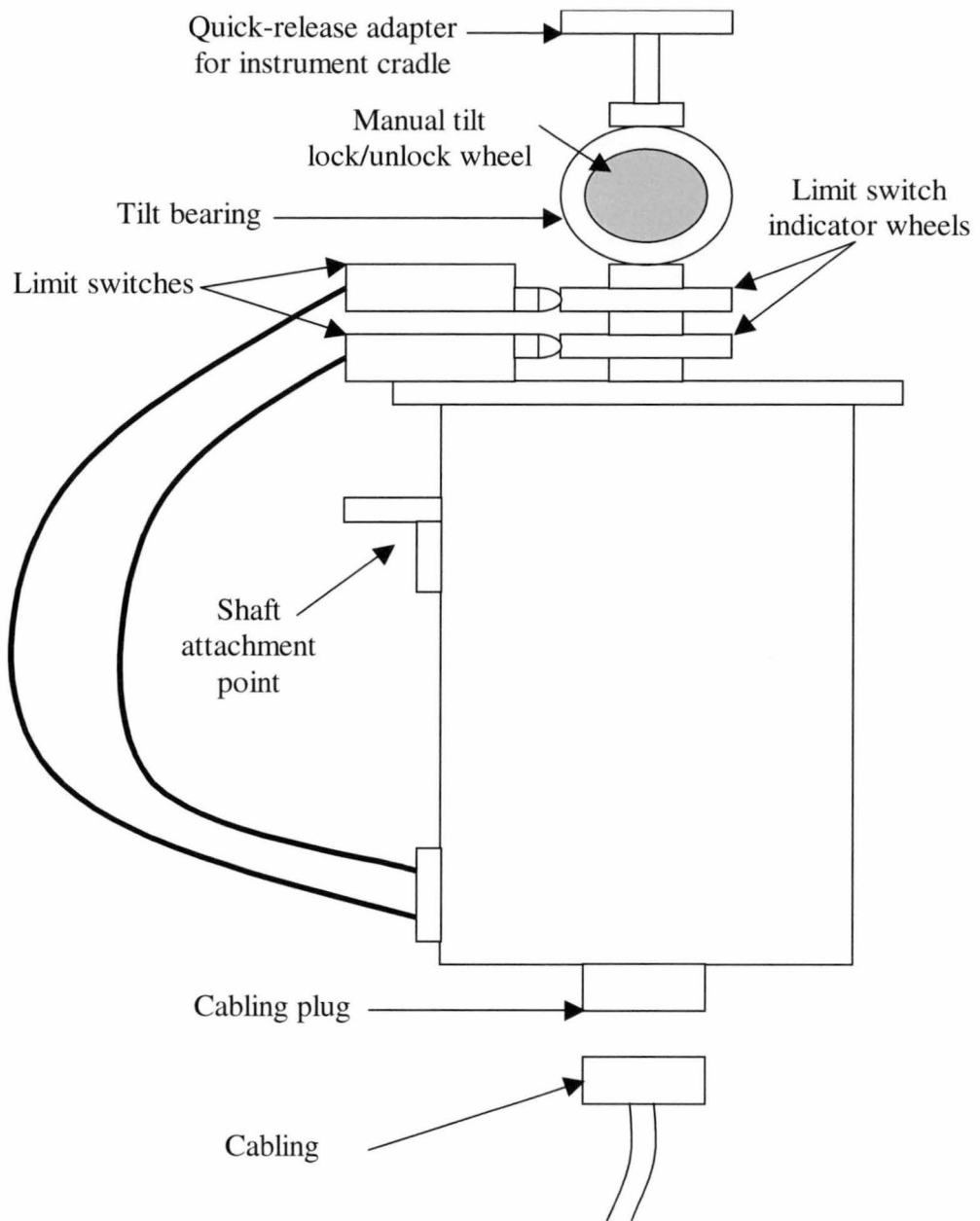


Figure 5.2. Physical design of the rotating instrument mount head.

The instrument mount formed an integral part of the complete instrument package. It provided fast rotational scanning capability, an essential component of the instrument's functionality in field use. It was transported and installed easily and was controlled by the same data logger program as the instrument. It was also weatherproof and used power efficiently, two important factors in any field installation. Field and laboratory applications of the instrument mount will be seen in the next section and in chapters to follow.

5.3 Instrument field of view (FOV) test

A laboratory test was conducted on the instrument in order to determine its field of view (FOV). The instrument cavity was designed to yield a FOV of approximately $\pm 15^\circ$ but it was necessary to empirically test this after the instrument's construction to verify that the desired outcome had been achieved. The essence of the FOV testing method was adapted from a method used to test the FOV for a thermal infrared camera (Legrand *et al.* 1999).

The test was performed using apparatus as shown in Figure 5.3. The apparatus consisted of the instrument, instrument mount with tripod-mounting attachments, soldering iron and a large sheet of aluminized Mylar. A hole was punched in the Mylar sheet to provide an aperture for the infrared radiation emitted by the soldering iron. The hole acted to restrict the field of emission of the soldering iron to a narrow cone.

The figure presents a side view of the apparatus, with the plane of instrument rotation vertical and perpendicular to the page. The hole in the Mylar sheet and the instrument aperture are shown larger than their true relative size for clarity.

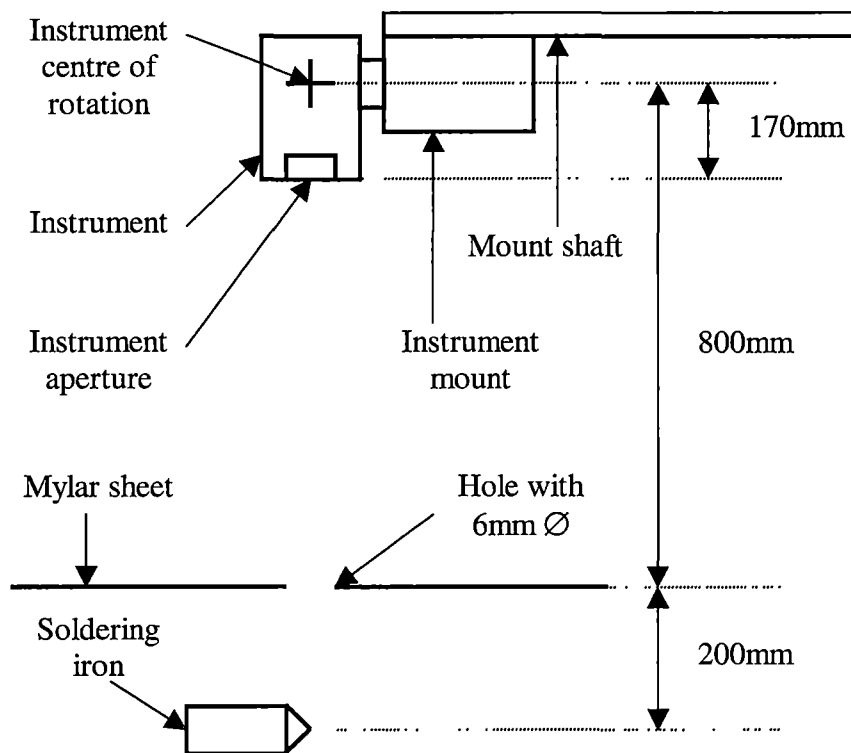


Figure 5.3. Instrument, instrument mount and target arrangement for the FOV measurement.

The instrument was positioned so that its aperture pointed directly at the hole when it was in the vertically down-looking position. The instrument mount's reference point was positioned at ninety degrees from the vertically down-looking position.

For the purpose of this test the full measurement sequence was not used to produce a value for the instrument's response. Instead, a single 'measurement' as defined in Chapter 4 was used at each rotational position. This allowed a faster scan through the required set of angular positions. The program was set to sample once during each of the nine cycles in each measurement. The sampled values were then averaged to give a signal response value for each angular position. Only channel one was used in the FOV testing, as only a magnitude response values was required and comparison between channels was unnecessary. Using measurements as opposed to measurement sequences meant that a single step in the scan was completed in approximately twenty seconds, where full measurements sequences would have required approximately 130 seconds per step.

An initial scan was performed using 3° angular steps with the soldering iron turned on. This was done to roughly determine the range of angle values that need to be included in the final test. Analysis of these results yielded a measurement range of $\pm 30^\circ$ around the vertically down-looking point.

The initial scan also showed signs of lingering detector response for a significant period following the measurements made when looking vertically downwards. This was more severe than had been expected – some settling effects were anticipated due to the use of short measurements. Unlike measurement sequences, 'measurements' do not allow for detector or instrument cavity settling time and are therefore much more susceptible to such detrimental settling effects.

For this reason the FOV scan was performed once for each direction of rotation. Each scan consisted of two passes, the first pass with the soldering iron turned off and the second pass with the soldering iron turned on. The first pass provided a background response level at each angular position, which was then subtracted from the instrument's response to the soldering iron. This removed any potentially corrupting background radiation effects.

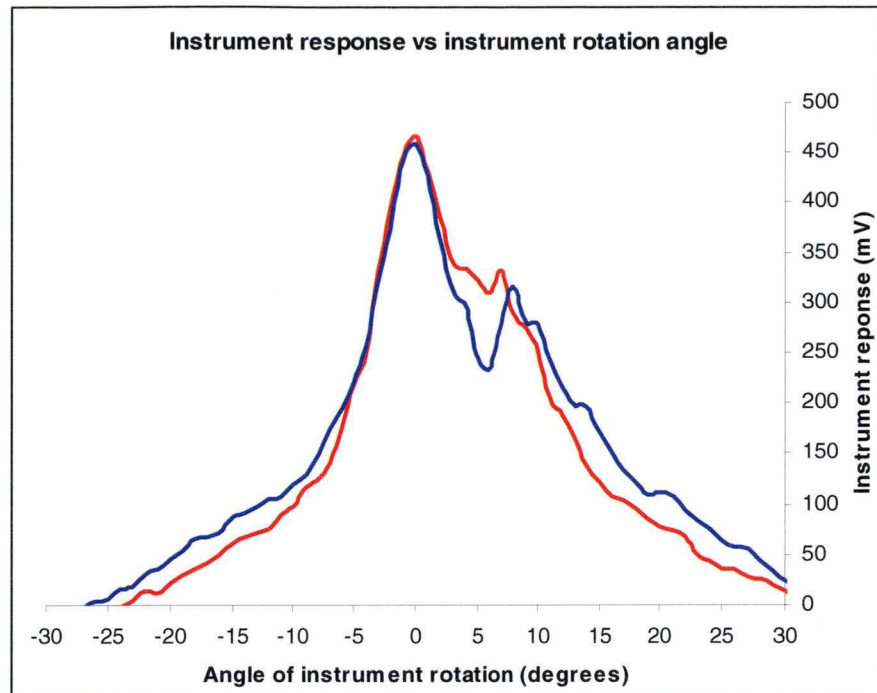


Figure 5.4. Instrument response with angle of rotation. The first pass (right to left looking along the mount shaft) is shown in red and the second (left to right looking along the mount shaft) is shown in blue. The angle of instrument rotation was centered at the vertically down-looking point.

The instrument signal response is shown against the instrument rotational angle away from the vertical in Figure 5.4. It is immediately obvious that the instrument's response is not perfectly symmetrical about its maximum. This asymmetry could be due to a slight misalignment of the cylinder inside the instrument cavity or the short reflective cylinder in the instrument tube's front cap. Its negative impact could only be assessed once the FOV calculation was performed.

Calculation of the FOV was based on integrating the response and seeking the point at which a threshold amount of the integrated response was reached. Integrals were performed by summing all response values within a series of windows around the central point. The integral over a $\pm 25^\circ$ window was chosen as the reference value and all other integrals were normalized to this reference.

The normalised integrals, taken at five-degree intervals of window size, were then plotted against the window size and a second order polynomial fitted to the data. This resulted in two polynomials, one for each FOV scan. The polynomials could then be inverted to determine the size of the angular window within which some chosen fraction of the 'total'

response was measured. A plot of the normalized integrated response against window size is shown in Figure 5.5 below. The plot includes curves representing the fitted polynomials and their equations. The results of the first scan are shown in red and the results of the second in blue.

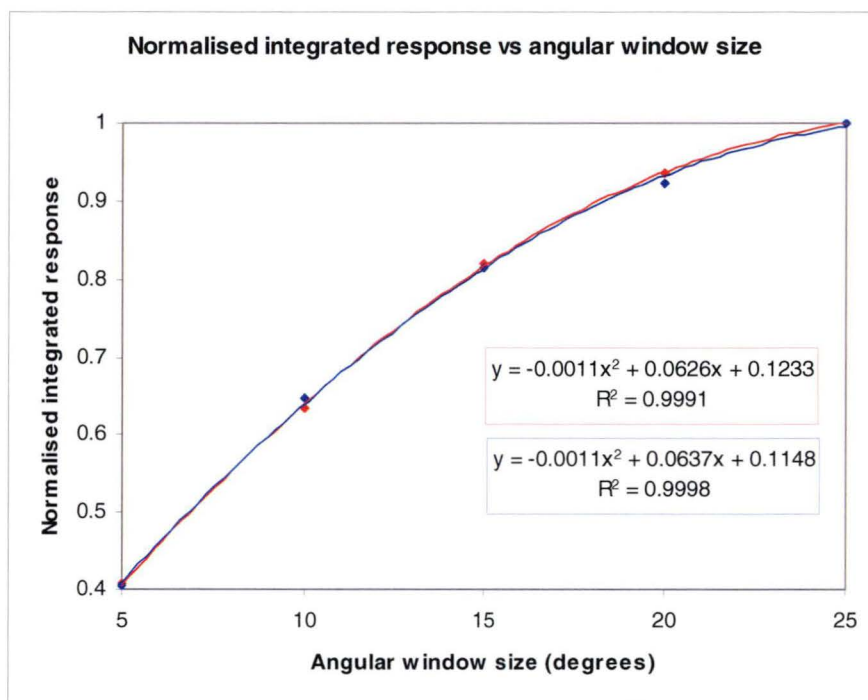


Figure 5.5. Fraction of the normalized integrated instrument response with the size of the field-of-view window in degrees.

Eighty percent of the normalized integrated voltage response (approximately 90% of the integrated power response) was chosen as the fraction of the total that represented the instrument's FOV. Inverting the polynomials and setting the normalized integrated response to 0.8 yielded 14.51° and 14.28° as the corresponding window sizes for the first and second scan respectively. The asymmetry of the instrument's response exists primarily within this window and is therefore not of great concern.

A further correction was made to the obtained values. This was required to convert the instrument's angle of rotation to a value for the FOV. The FOV does not correspond directly to the instrument's angle of rotation because the instrument's center of rotation does not correspond exactly with the front aperture of the instrument, as can be seen in Figure 5.3. A schematic diagram of the required correction is shown in Figure 5.6 below.

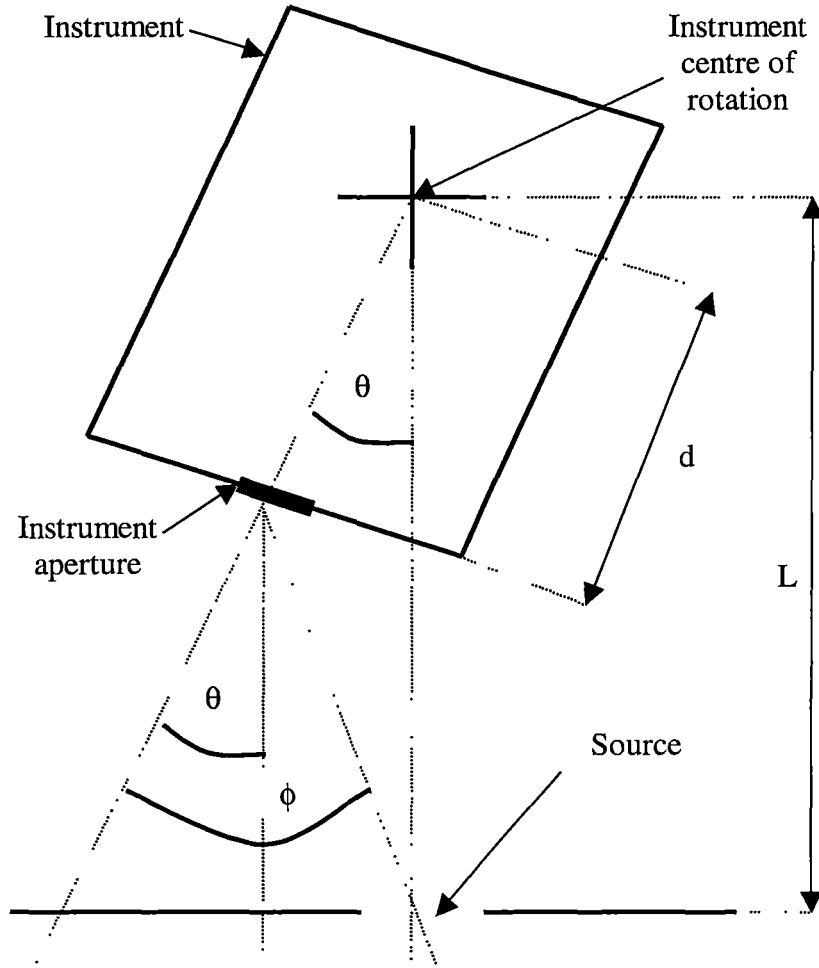


Figure 5.6. Schematic diagram of the required corrective calculations for determining field of view from instrument rotation.

It is obvious from this diagram that the true FOV, shown as ϕ , differs from the instrument's angle of rotation, shown as θ . Although the scale of the figure greatly accentuates the difference, it was necessary to explicitly correct the angles of instrument rotation to give a more accurate value for the FOV. The correction was achieved using the following equation:

$$\phi = \theta + \left(\frac{\pi}{2} - \arctan \left(\frac{L - d \cos \theta}{d \sin \theta} \right) \right) \quad (5.1)$$

The corrected values of the instrument's FOV were 18.34° and 18.31° , derived from the first and second scan respectively. These show excellent agreement and a value of $\pm 18.3^\circ$ was adopted as the instrument's FOV, although in most applications $\pm 18^\circ$ is an adequately accurate expression. Accurate knowledge of the instrument's FOV was important in design of laboratory experiments such as calibration (Section 5.6) and measurement programs for field applications (Chapter 6).

5.4 A blackbody source for instrument calibration

To calibrate the instrument, a measurable and reliable source of infrared radiation was required. Other desirable properties of the source were an easily modified source temperature and uniformity of the emitted radiation. Typically a blackbody source is used to calibrate and test longwave radiometers.

The choice of design for the blackbody source – hereafter referred to as the blackbody – was a cylinder of thin copper sheet, capped with a cone at one end and tapered to an aperture at the other. The inside of the cylinder was coated with highly emissive black paint. The dimensions of the cylinder are shown in Figure 5.7 below.

The aperture of the cylinder was attached to the lid of a large watertight cylindrical container, from which both ends could be unscrewed. The container was made from heavy-duty plastic and fitted with two handles and an inlet/outlet plug in the base. A second opening in the base allowed cables to be inserted into the interior of the container. This opening was designed to be sealed once cables were installed.

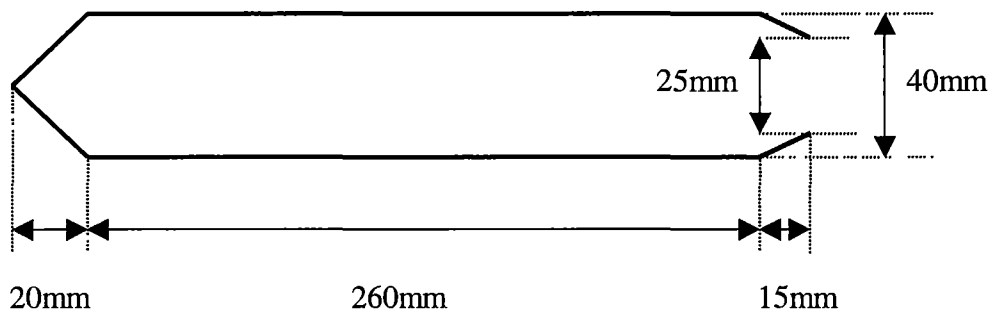


Figure 5.7. Shape and dimensions of the copper cylinder that formed the core of the blackbody source. The blackbody aperture is at the right, and its base on the left.

This design meant that the copper cylinder was completely immersed in the contents of the larger container, which could be changed quickly and easily through the inlet/outlet plug. Instruments for measurement of the temperature of either the container's contents or the copper cylinder itself could be installed inside the container and the necessary cabling run through the base of the container. The design of the container is shown in Figure 5.8 below.

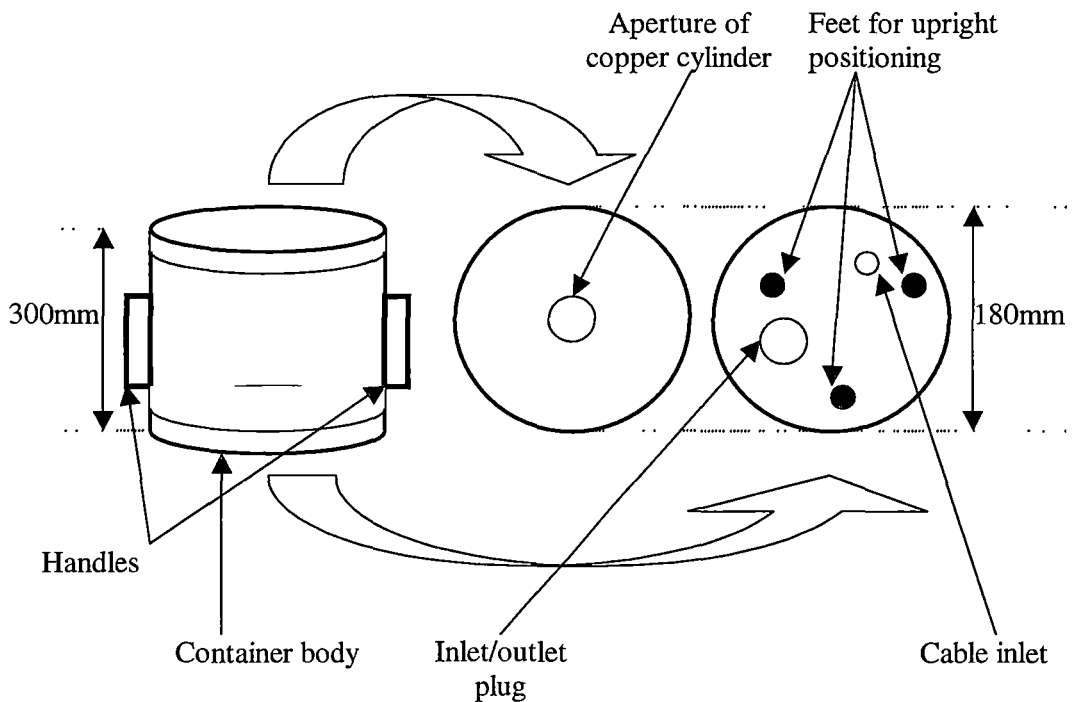


Figure 5.8. Dimensions and configuration of the blackbody source container.

Two thermistors measured the temperature of the copper cylinder and the surrounding liquid. These were aligned along the length of the cylinder and attached using clips that held them pressed against the copper surface. One was positioned approximately 10mm from the closed end of the cylinder and the other at the cylinder's middle point along its length and on the opposite side. The thermistors' cables were passed through the cable inlet, which was then sealed.

The thermistors' response was converted to temperature values using the appropriate commands in a CR10X data logger program. The thermistors were calibrated against a platinum resistance thermometer (PRT) in ice water and water at ambient temperature and the appropriate linear corrections were made in the program.

A test was performed to compare the responses of the thermistors under the expected operating conditions. The blackbody was filled with ice water and then agitated firmly for twenty seconds and then rested on its side for at least ten minutes, in the position that it would take during calibration. While the average measured temperature changed over the ten-minute period, the thermistors' temperature differential did not exceed 0.1°C. This showed that the thermistors were well matched and also that the temperature inside the blackbody was spatially uniform.

The decision to orient the blackbody on its side was an important one because it reduced the potential effects of temperature stratification. While only a small degree of stratification will naturally occur over a period of several minutes, if the copper cylinder is aligned along the strata then the effects of the layering are minimised. Further, the measurements of the water temperature occur within a narrow subset of the strata. If the cylinder were positioned vertically through the strata, the temperature gradient across the length of the cylinder would be stronger and additional temperature measurements would need to be made to ensure that the gradient was properly quantified.

A Raytek commercial infrared thermometer with specified 0.1°C accuracy was used to test the uniformity of the blackbody's radiation emission. One test involved pointing the Raytek thermometer along the axis of the copper cylinder and moving it past the blackbody aperture without changing the pointing direction. The passes were performed at 45° intervals. The aperture of the Raytek thermometer's sensor was approximately one half of the aperture of the blackbody, allowing a reasonable pass across the aperture itself, with no portion of the blackbody's upper lid in the Raytek's field of view. All such passes yielded the same temperature measurement.

The second test involved placing the Raytek infrared thermometer at the center of the blackbody's front aperture and performing angular scans out to the edges of the aperture. Again no temperature difference was observed for all portions of the scan that observed only the inside of the copper cylinder. These tests proved the relative uniformity of emission from the blackbody. An absolute test of the emitted blackbody temperature (as measured by the Raytek) against the internal blackbody temperature (as measured by the thermistors) was not performed as the Raytek thermometer had not been calibrated sufficiently recently.

The design of the blackbody source and its subsequent realization met the intended criteria that were stated at the beginning of this section. The use of the blackbody source for the calibration of the instrument will be discussed later in this chapter.

5.5 Optimum instrument chopping speed

A test was performed to determine the instrument's optimum chopping speed. This was necessary after the addition of the variable chopping speed capability in the final stages of the instrument's construction. As discussed in Chapter 3, the response of the pyroelectric detector varies with chopping speed – it decreases with increasing chopping speed for a

voltage-mode detector such as the one used in the instrument. Pyroelectric detectors are also susceptible to microphonic noise – conversion of mechanical vibration into electrical signals. Another reason for performing this test was to examine any effects of vibration from the DC chopping motor on the detector's response.

The voltage input to the DC chopping motor was used to represent the chopping speed. Chapter 4 refers to the frequency of 'cycles' in the context of the time taken for individual cycles within a measurement, however the frequency of cycles does not directly represent the chopping speed. The reason for this is the design of the chopping wheel – a circular aperture within a larger disk. Because the aperture is some fraction of the diameter of the disk, the effective chopping speed as seen by the detector is not the rotational frequency of the chopping wheel itself. Hence the voltage input to the chopping motor was as useful an indicator of the chopping speed as the chopping wheel's rotational frequency and was easier to measure.

The instrument's response was fast-sampled at 8Hz and all valid samples in each measurement were output to storage. The program recorded these data for two measurements, one on each channel. The DA lines were used to select samples and to indicate the beginning and end of the sampling. Tuning the relevant potentiometer (see Section 3.4) at one-volt increments from 3.5 to 9.5 volts set the chopper motor's voltage. This range of voltages represented a range of chopping cycle frequencies from approximately 25 seconds (3.5 volts) to 7 (9.5 volts) respectively.

Once the test was complete the data were output to a file and analysed. The samples in the second half of each measurement were averaged to give the detector response. This avoided any contamination of the data due to settling of the detector's response in the initial part of the measurement. Any effects of chopping frequency on the average response would be present across the entire measurement and therefore ignoring the first half of each measurement would not adversely affect the result of the test.

To show the relationship between detector response and chopping frequency, the averaged detector responses were then plotted against the motor voltage. The values for each channel are shown in Figure 5.8 below. The detector response shows very little variation with chopper motor voltage – linear trendlines were added to the plot to display any general trend. In channel one, the trend of response against motor voltage is an increase of less than one millivolt (0.78mV) per volt of motor voltage. In channel two the trend is negative as expected, but only two millivolts (2.02mV) in response per volt of motor voltage. The

response on both channels is very weakly dependent on the motor voltage, as evidenced by the R^2 values of 0.18 and 0.34 for channels one and two respectively.

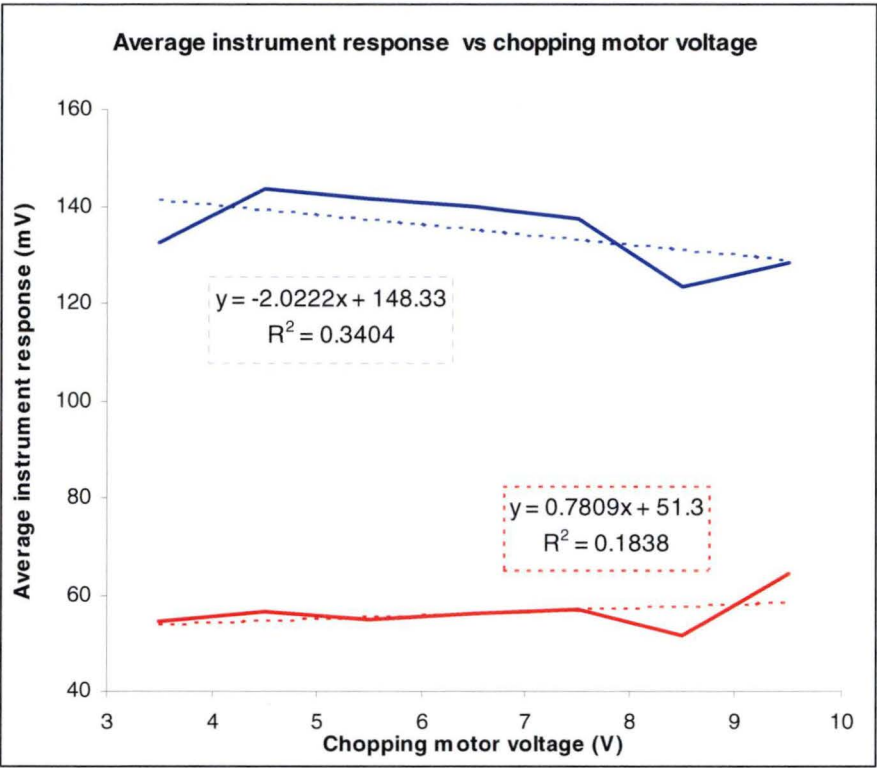


Figure 5.8. The instrument’s response to a constant-temperature target as the chopping motor voltage was varied. Channel one is shown in red and channel two in blue.

The standard deviation of the averaged samples was also taken for each measurement. These standard deviation values provide a measure of the instability of the detector’s response within the averaged samples for each measurement. Microphonic pickup was likely to be evident at frequencies higher than the motor’s rotational frequency, as vibrations would most likely occur at the rotational frequency and above.

A direct measurement of the detector’s spectral response to vibration would have provided an exact relationship between detector noise and chopping frequency. In this case such a measurement was impractical, however the sample-and-hold circuitry within the instrument samples the peak detector response providing an essentially random sampling of any noise on the detector response. If the averaged response is considered to be the ‘true’ detector response then a measurement of the deviation around that average can give an indication of the noise that has been introduced to the signal. A plot of the standard deviation within the averaged samples for each channel is given in Figure 5.9 below. The figure shows the

normalised standard deviations. The standard deviation for channel one is shown in red, channel two in blue.

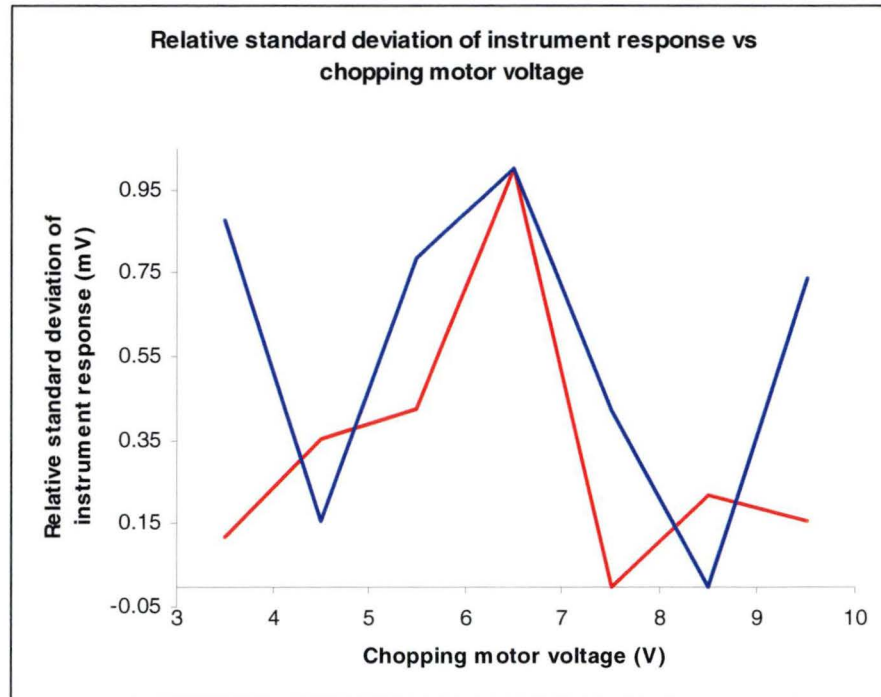


Figure 5.9. The standard deviation in the average instrument response against chopping motor voltage. A peak is evident in both channels at 6.5 volts, with local minima either side.

The peak at the center of the plot is obviously the main feature. The peak coincides with the 6.5 volts setting for the chopper motor input, and may in reality be centred at a slightly lower value given the shape of the peak. The standard deviation on both channels drops away to its minimum value beyond the peak, at 7.5 volts for channel one and 8.5 volts for channel two. The standard deviation for channel one increases with voltage up the peak while channel two has a local minimum at 4.5 volts.

In qualitative terms the rotation of the chopping wheel was noticeably ‘smoother’ at the settings where the local minima occur. At the 6.5 volt setting there was noticeable vibration and noise. This provides the obvious explanation for the observed peak – a vibrational resonance in the instrument or the chopping motor, at or near the 6.5 volt setting.

The chopping motor’s input voltage was set at eight volts. The results of this test show that such a setting minimises the microphonic noise in the detected signal with no significant loss in the overall signal magnitude.

5.6 Calibration of the instrument - introduction

Calibration of the instrument was the final step in its preparation for field use. The various outputs from the instrument were discussed in Chapter 4. The aim of the calibration process was to establish two equations – one for each channel – that yielded values for the effective blackbody brightness temperature of the instrument’s target. The brightness temperature values could then be used to calculate the radiative quantities described in Chapter 2. The equations had to be functions of the instrument’s outputs, taking the form shown in equation (5.2) below. The subscript i denotes the channel number and the three variables are those defined in Table 4.2.

$$T_i = T_i(S_i, Ti_{i,1}, Ti_{i,2}) \quad (5.2)$$

Calibration of the instrument was a process that occurred many times throughout the two-year development of the instrument. A calibration was the ultimate test of all of the major design changes, because the calibration results also yielded an estimate of the accuracy of the instrument’s measurements. Many design changes were motivated by unsuccessful calibrations. As the instrument evolved, the calibration process also evolved although in most cases this was due to changes in the required logger program. Such small changes were often necessary when modifications were made to the instrument’s internal control sequence.

The following sections describe the final calibrations of the instrument, one ‘warm’ and one ‘cold’ calibration. These respectively refer to calibrations performed with the instrument at ambient (room) temperature and in an artificially chilled room. For the ‘warm’ calibration, iced and heated water was used to set the initial blackbody temperature. The warm calibration also served to provide further testing of the instrument, which will be detailed where relevant in the following section. For the ‘cold’ calibration the blackbody was filled with oil and chilled below zero degrees centigrade. The data from these calibrations were later combined to give a single pair of calibration equations.

5.7 Calibration of the instrument – warm calibration

Warm calibration of the instrument was performed over a five-day period in March 2002. Measurements were made over ten ‘runs’ with differing lengths, each corresponding to a

different combination of initial blackbody and internal instrument temperatures. These combinations are shown in Table 5.1 below.

Calibration run	Initial Blackbody temperature (°C)	Initial Internal Instrument temperature (°C)	Number of measurement sequences
1	20.0	22.6	23
2	20.9	28.7	4
3	21.0	29.2	10
4	11.7	29.7	8
5	13.0	29.4	491
6	21.7	21.8	18
7	9.3	23.8	224
8	26.6	28.0	229
9	12.7	25.3	27
10	6.4	26.4	19

Table 5.1. Description of data-gathering sequences or ‘runs’ for the instrument’s warm calibration. The total number of measurement sequences was 1053.

For calibrations runs 1, 2, 3 and 6, the blackbody was left at ambient temperature. For calibration runs 4, 5, 7, 9 and 10, iced water was added to the blackbody to reduce its temperature. For calibration run 8, hot water was added to the blackbody to increase its temperature.

The laboratory in which the calibration was performed was not temperature-controlled and therefore both instrument and blackbody temperatures fluctuated with the ambient room temperature. In general this proved advantageous as it provided a gentle temperature gradient that affected both the blackbody and instrument temperatures. A plot of internal instrument temperature against the blackbody temperature during all calibration runs is shown in Figure 5.10, in which the effect of changes in the ambient temperature can be seen. Especially notable is the local minimum at approximately (13, 18) at which both instrument and blackbody temperatures cease to decrease and begin to increase with the ambient temperature.

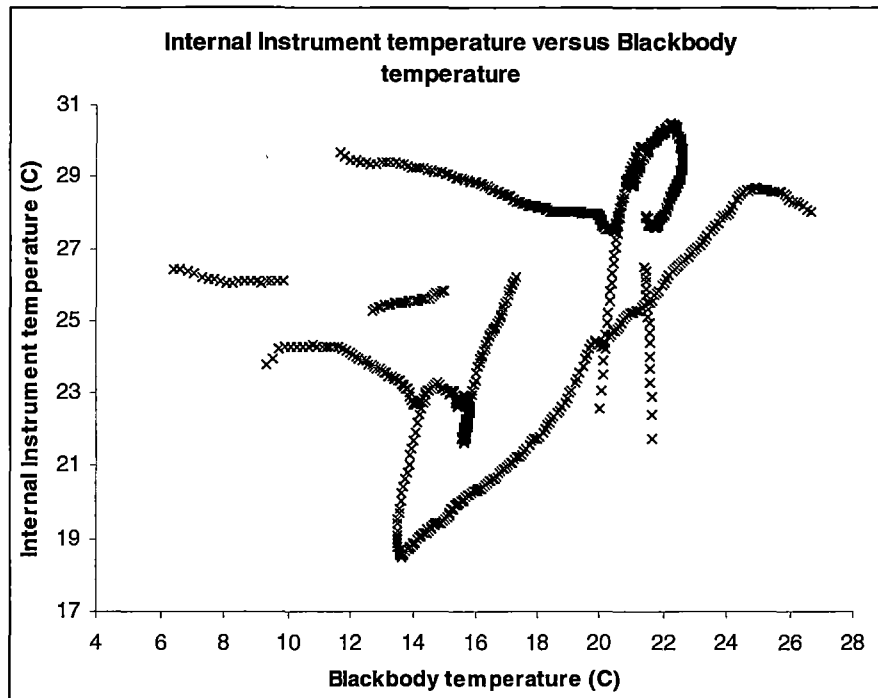


Figure 5.10. Illustration of the coverage of the various warm calibration runs. Ideal coverage would encompass the entire plane, but this was difficult to achieve without the ability to artificially warm and cool the instrument.

This figure also illustrates the coverage achieved by the calibration. The instrument's response should be able to be essentially described by a function of two variables, the internal instrument temperature and the blackbody or target temperature. A desirable outcome of the calibration was to include as much coverage as possible of the two-dimensional plane of temperature values shown in Figure 5.10 above. The ability to achieve full coverage was limited by the internal self-heating of the instrument and the variability in temperature of the laboratory. However, with deliberate manipulation of the initial temperatures and careful choice of timing of the calibration runs, a reasonable degree of coverage was achieved.

Before each calibration run, the blackbody's temperature was adjusted as required. The blackbody was then shaken thoroughly and positioned horizontally on the test bench. Three minutes was allowed for settling of the blackbody's contents and for equilibrium to be established between the copper cylinder and the surrounding fluid. The instrument was positioned at the beginning of each calibration run with its aperture exactly level and aligned centrally with the blackbody's aperture. Each calibration run yielded a series of sets of output from the instrument and blackbody, one set per measurement sequence. These data were then combined for further analysis.

An initial test was the examination of the nature of the instrument's response to the difference between the internal instrument temperature and the blackbody temperature. For a perfect pyroelectric detection system the response should correlate exactly with the temperature difference, as the detector responds to the change between incident radiation and the reference radiation level. Early testing during the design phase had already indicated that this was not the case for this instrument, most likely due to a dependence of the detector on its absolute temperature. The results of this test are shown in Figures 5.11a and 5.11b below.

The two channels were also tested for consistency. If the detector's response is essentially linear with temperature difference and is also consistent, then the response from one channel should correlate strongly with the other. The instrument's response in channel one was plotted against its response in channel two, with the resulting plot shown in Figure 5.12 below.

It can be seen that essentially the instrument responds linearly to the temperature difference. For both channels, the trendline equations shown on the plots were used to calculate a predicted value for the temperature difference from the instrument response. The standard errors in the predicted values were 0.24°C for channel one and 0.22°C for channel two.

The response from the two channels is obviously very highly correlated, with a response ratio of approximately 3:10. This difference in response is due to three factors; the relative amount of blackbody emission within the spectral band represented by each channel, each filter's maximum transmission and each filter's bandwidth.

The approximate ratio of maximum filter transmission is 0.81:1 (72%:89%) and the approximate ratio of (half-maximum) filter bandwidths is 0.37:1 (0.23 μ :0.62 μ). Assuming perfectly square filter response curves, these combined give a ratio of 3:10 that accounts for the difference in response between the two channels. These approximate ratios are derived from the filter response curves shown in Figures 2.2a and 2.2b.

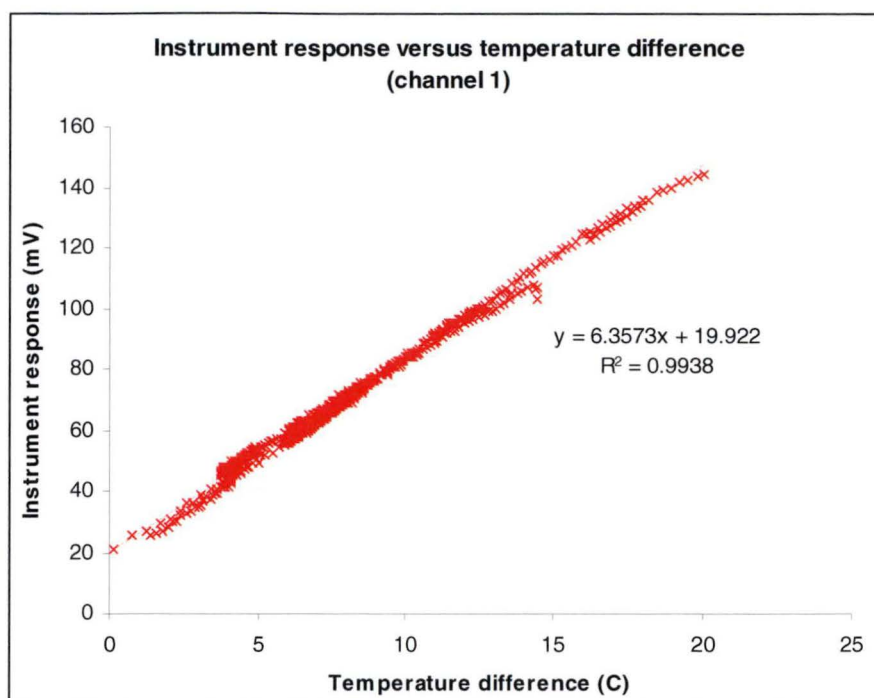


Figure 5.11a. Instrument response plotted against the difference between the blackbody source temperature and the internal instrument temperature, for channel one.

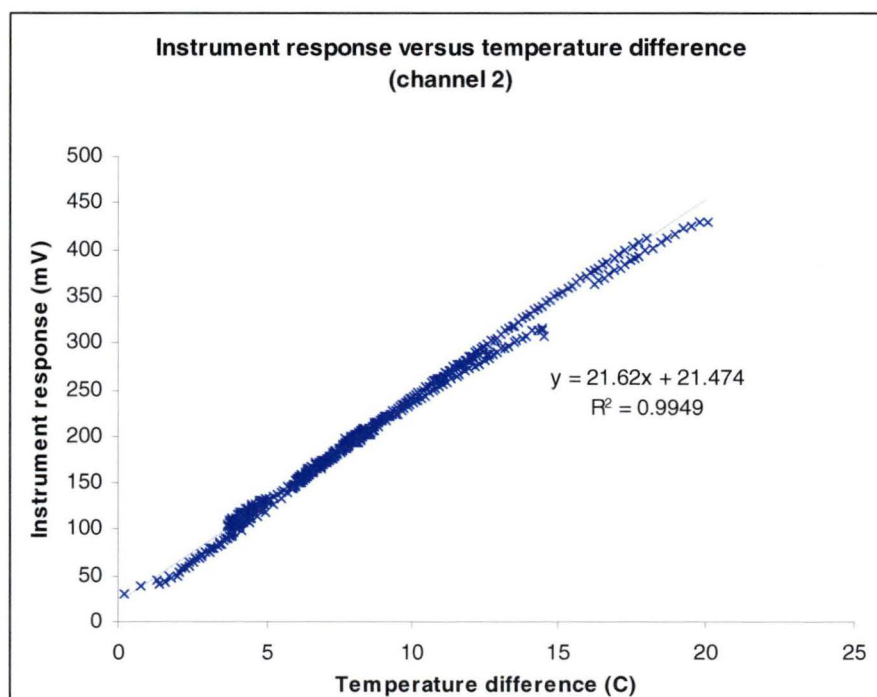


Figure 5.11b. Instrument response plotted against the difference between the blackbody source temperature and the internal instrument temperature, for channel two.

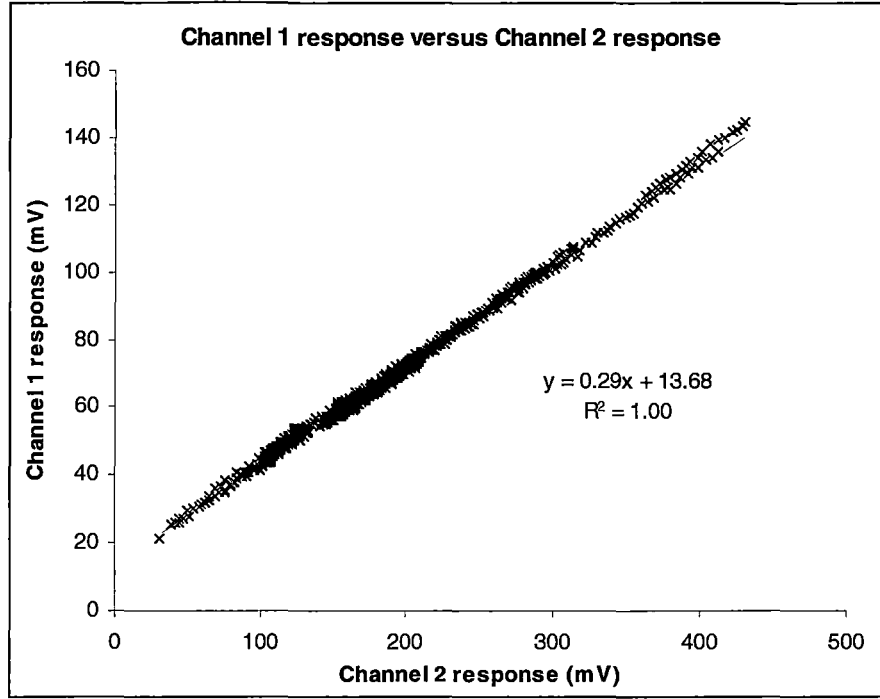


Figure 5.12. Instrument response in channel one plotted against instrument response in channel two. The straightness of the plot indicates relative consistency of the response in the two channels. The slope of the plot is due to the differing filter window sizes and hence differing levels of incident radiation.

The final step in the warm calibration process was to establish the exact form of the general relationship expressed in equation (5.2). A more specific form of the relationship was expressed as

$$T_i = c_{i7}S_i + c_{i6}\sqrt{S_i} + c_{i5}Ti_{i2} + c_{i4}Ti_{i1} + c_{i3}Ti_{i2}^2 + c_{i2}Ti_{i1}^2 + c_{i1} \quad (5.3)$$

with coefficients c_1 to c_7 indexed to their respective channel through the i subscript. The coefficients were determined using a multiple linear regression fit to the 1053 data available for each channel. The coefficients of the calibration equations for both channels are given in Table 5.2 below.

The standard error in the multiple linear regression fit was 0.128°C for channel one and 0.106°C for channel two. Each of these is approximately half of the standard error present in the linear fit of instrument signal to temperature difference (discussed earlier in this section). This reduction in standard error – and resulting increase in effective instrument accuracy – justifies the added complexity in the calibration equation.

Coefficient	Channel 1 ($i=1$)	Channel 2 ($i=2$)
$c_{i,1}$	20.73	19.90
$c_{i,2}$	-0.2100	-0.2698
$c_{i,3}$	0.1942	0.2475
$c_{i,4}$	8.315	10.99
$c_{i,5}$	-7.855	-10.48
$c_{i,6}$	0.3529	0.3964
$c_{i,7}$	-0.1838	-0.06302

Table 5.2. List of empirically-derived coefficients in both channels for equation (5.3).

Plots of the blackbody temperature as predicted by equation (5.3) against the measured blackbody temperature are given below in Figures 5.13a and 5.13b. The improvement over the simple linear relationship between instrument response and temperature difference (see Figures 5.11a and 5.11b) is obvious.

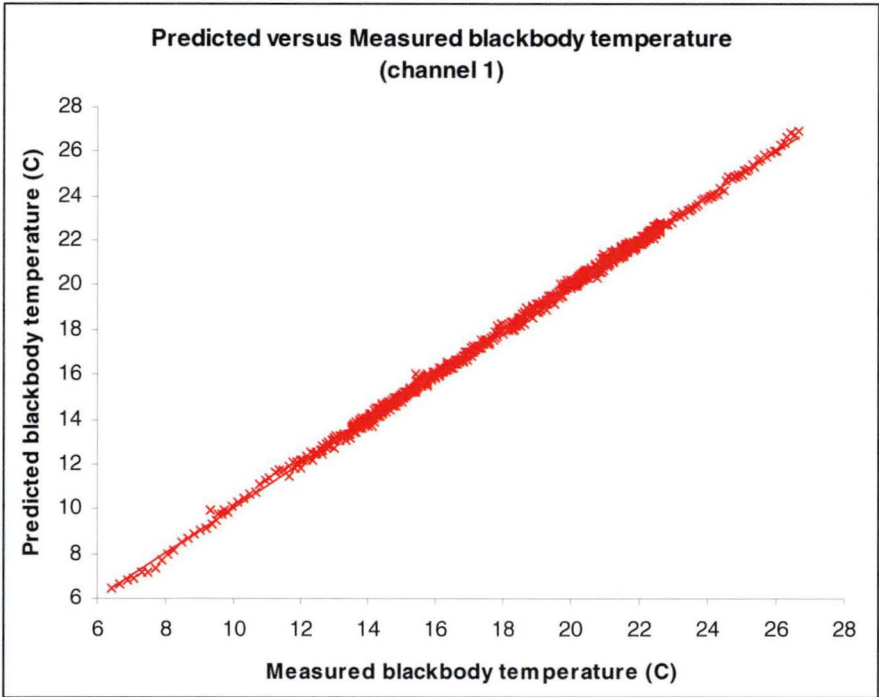


Figure 5.13a. Target brightness temperature predicted by the calibration equation for channel one, plotted against the measured blackbody temperature.

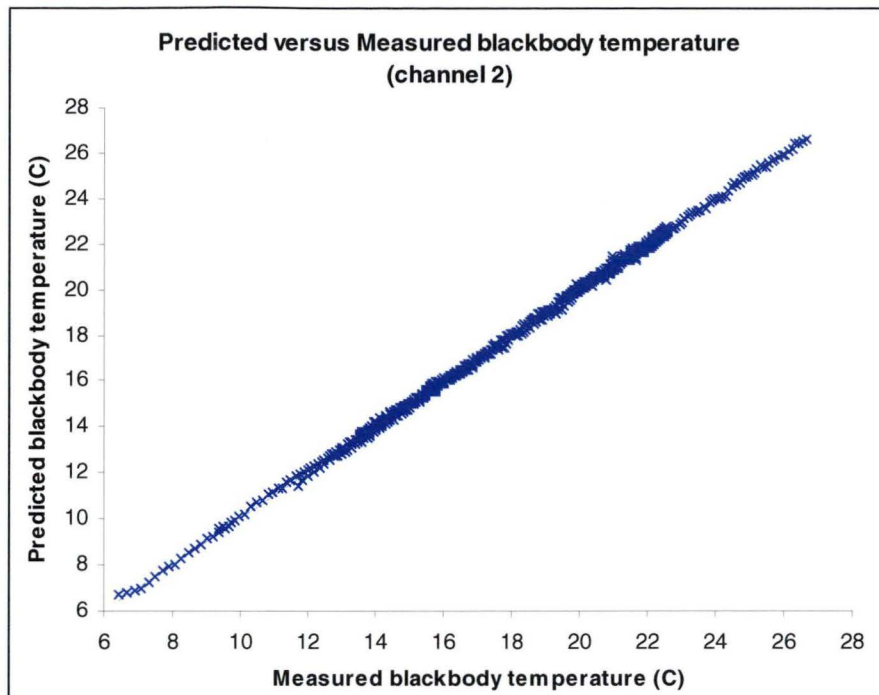


Figure 5.13b. Target brightness temperature predicted by the calibration equation for channel two, plotted against the measured blackbody temperature.

The warm calibration of the instrument provided an equation relating the instrument's outputs to the brightness temperature of a blackbody source. The equation was valid for use over a target temperature range of 6 to 27 °C and internal instrument temperature range of 18 to 31 °C. The standard error in the resulting brightness temperature measurements was 0.128°C for channel one and 0.106°C for channel two. After completion of this calibration the instrument was fit for measuring the temperature values required for calculation of upwelling irradiance divergence (as described in Chapter 2), with the condition that the measured temperatures fell within the calibrated range.

5.8 Calibration of the instrument – cold calibration

The cold calibration served two purposes. Firstly, it extended the range of target temperatures below the range covered by the warm calibration. This extension included temperatures closer to those likely to be measured when the target is a clear night sky, a very important feature of the intended measurement program.

It also extended the range of internal instrument temperatures well below the range covered by the warm calibration. This extension included internal instrument temperatures of the

order of those likely to occur when the instrument was used in an outdoor environment at night in a temperate-climate location.

These purposes were met through the use of a series of cold rooms at the Institute for Antarctic and Southern Ocean Studies (IASOS) at the University of Tasmania's Hobart campus. There were four sections within the cold-room complex, kept at 8, 0, -10 and -18 °C. The calibrations were performed in the first of these rooms, while the three other rooms were used to chill the blackbody to the required target temperature. Although sky brightness temperatures can fall to below -50° on clear nights, unfortunately there were no available means of reducing the blackbody temperature below -18°C.

To allow the blackbody to be chilled to temperatures as low as -18°C, its contents were changed. Obviously the use of water as the temperature-controlling medium was impossible at such temperatures as it would freeze and possibly damage the blackbody container. Diesel engine oil with a quoted freezing point of -34°C was used instead. This required a slight change in the operational procedure, as it was impractical to regularly remove oil from or add oil to the container. Instead, the entire blackbody was placed in the appropriate cold room for several hours or in some cases overnight to chill its contents.

An initial test was performed to assess the efficiency of the oil as a temperature-controlling medium and to measure the rate of change of the blackbody temperature when the chilled blackbody was moved into a relatively warm room. The test involved thoroughly shaking the blackbody once every four minutes while taking internal thermistor measurements and relative skin temperature measurements every two minutes. The internal thermistor measurements were made using the CR10X data logger and the relative skin temperature was measured using the handheld Raytek infrared thermometer described in Section 5.4.

The skin temperature measurements were only relative because the Raytek instrument had not recently been calibrated. While this did not provide an absolute measurement against which to compare the internal measurement, the purpose of the test was to determine whether or not the internal temperature and skin temperature diverged with time. Any divergence would limit the length of time during which measurements could be made, as the internal temperature measurements would be less reliable with time if the oil and blackbody skin warmed differentially. While such a test may have proved useful during the warm calibration, it was essential for the cold calibration because the blackbody was exposed to larger internal/external temperature differentials.

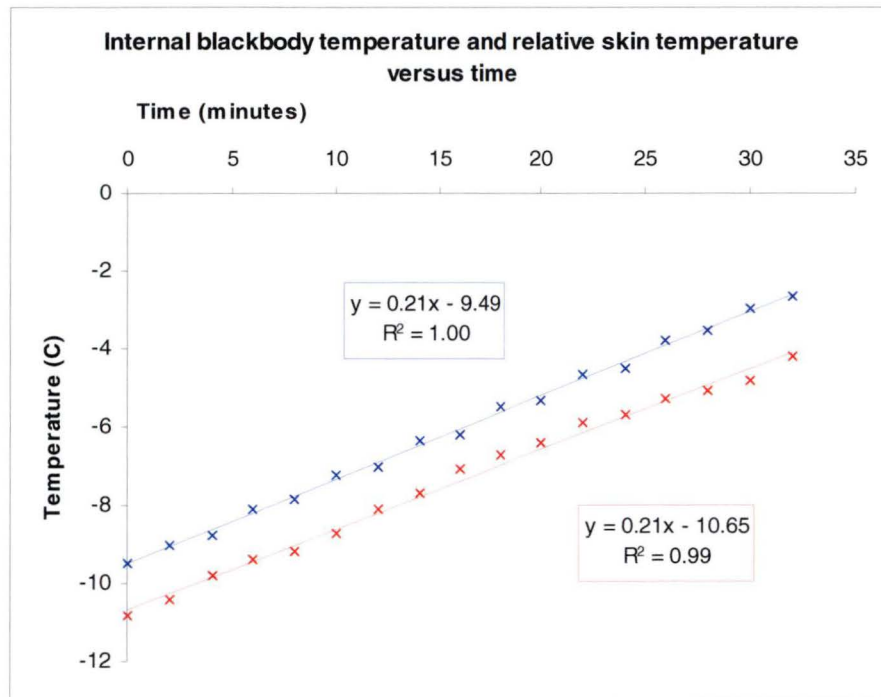


Figure 5.14. Internally-measured blackbody temperature (blue) and relative measured brightness skin temperature (red) against time. This test was performed to identify any divergence between the internal and brightness temperatures.

The internal and relative skin temperatures are plotted against time in Figure 5.14. The internal (thermistor-measured) temperature is shown in blue and the relative skin temperature in red. Linear trendlines were fitted and are displayed with their equations in the plot.

The linear fit reveals an absolute temperature difference of approximately 1.16°C but no divergence of the two temperatures with time. A regular step pattern is present in the internal temperature data, due to the blackbody being shaken just prior to every second temperature measurement, starting at the second. It is evident that every odd-numbered measurement (those prior to which the blackbody was not shaken) falls below the general temperature trend, and every even-numbered measurement falls above it. There is no such pattern in the skin temperature data. Hence while the result of the test is that there is no divergence between the two temperatures, the result is conditional on regular agitation of the blackbody.

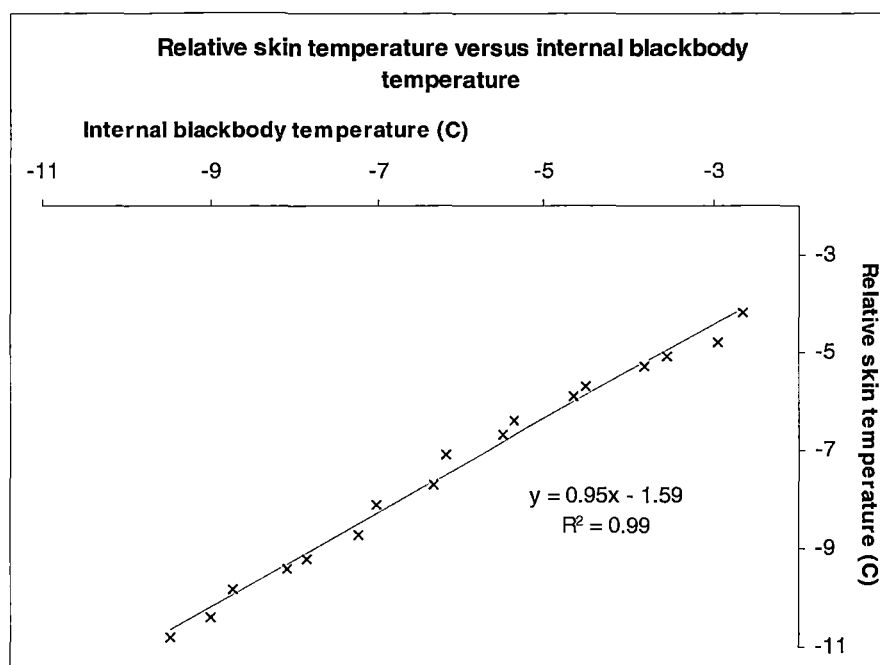


Figure 5.15. Relative blackbody skin brightness temperature plotted against the internally-measured blackbody temperature.

A plot of the relative skin temperature against the internal temperature revealed a very slight divergence between the two over the same measurement set. The plot is shown in Figure 5.15, with a linear trendline fitted to the data. The divergence – most likely not evident in Figure 5.14 due to the accuracy of the trendline equations – translated to approximately 0.05°C per 30 minutes, which was well within the expected accuracy limits of the instrument. The cold calibration was performed during a nine-day period in June 2002. Measurements were made in six runs, described in Table 5.3 below.

The temperature plane coverage achieved by the set of cold calibrations is shown below in Figure 5.16. The data from the cold calibration are shown in red and the data from the warm calibration (see Figure 5.10) are shown in black for reference. The extension of the calibrated range that was achieved by the cold calibration is immediately obvious.

Calibration run	Initial Blackbody temperature (°C)	Initial Internal Instrument temperature (°C)	Number of measurement sequences
1	-9.2	22.1	15
2	-8.8	27.8	33
3	-16.9	27.8	33
4	-9.3	13.7	463
5	-17.0	12.8	404
6	16.7	12.7	342

Table 5.3. Description of data-gathering sequences or ‘runs’ for the instrument’s cold calibration. The final calibration run was a test of a “cold” instrument temperature measuring a “warm” or ambient temperature target. The total number of measurement sequences was 1290.

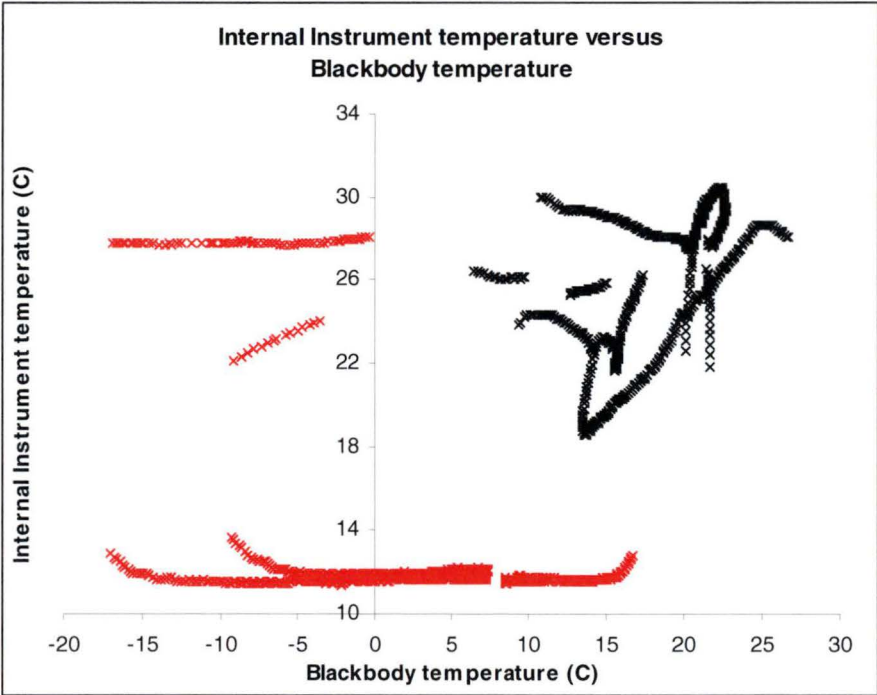


Figure 5.16. Additional coverage achieved by the cold calibration runs is shown in red, while the black marks indicate the coverage achieved by the warm calibration (see Figure 5.10).

The cold calibration was intended to be an addition to the warm calibration, not an alternative. For that reason, the data from both cold and warm calibrations was combined for final analysis. The cold calibration data were not analysed separately. The warm calibration

included sufficient coverage for use in particular circumstances – warm ambient temperatures and surfaces ranging from 6 to 27 °C. However, the cold calibration alone did not achieve sufficient coverage for any intended purpose and was therefore not considered for use prior to combination with the warm calibration data.

5.9 Calibration of the instrument – combined calibration results

The data sets from the warm and cold calibrations were combined and treated as a single data set. The first step taken in processing the data was to remove all data points that corresponded to instrument-blackbody temperature differentials of 1°C or less. The temperature differential was defined as

$$\Delta T = T_{i_1} - T_{blackbody} \quad (5.4)$$

The reason for removing these points was poor response from the instrument when the internal instrument temperature was at or near the blackbody temperature.

The reason for the poor response was most likely the shape of the waveform produced by the detector. The sample and hold circuitry was designed to detect a peak (local maximum) value within a particular period of time. The choice of that period of time was made based on the location of the local maximum when the instrument was pointed at a target with a temperature less than its own internal temperature. If the target is warmer than the instrument's internal temperature, the shape of the detector response changes, producing a local minimum rather than a maximum.

The explanation above would justify removing points that corresponded to instrument-blackbody temperature differentials of 0°C or less. The criterion was adjusted to 1°C based on examination of the data. This is a valid change because the instrument thermocouples measure the instrument's internal temperature at two positions within the instrument, neither of which necessarily represents the exact absolute brightness temperature of the detector's reference radiation level. While the measured internal temperatures provide values for use in the instrument's calibration, it was not expected that a difference of 0°C between the blackbody and instrument temperature would yield exactly zero response from the detector.

145 of 2343 data points met the condition on ΔT and were removed. The remaining 2198 calibration data were then sorted by ΔT_{i_1} , the difference in internal instrument temperature

between one measurement sequence and the next. A multiple linear regression was then run on the data, based on the form of equation (5.3). The regressions were applied to subsets of the data, each subset corresponding to the data that would remain if data points were removed based on their corresponding value of $\Delta T_{i,2}$.

The aim was to identify an optimum condition on the change in the internal instrument temperature that yielded a low standard error without compromising the conditions under which the instrument could be considered reliable. The underlying assertion was that the calibration process had subjected the instrument to much faster temperature changes than would be experienced in a field environment. The standard errors in the resulting multiple linear regressions are shown in Figure 5.17 below.

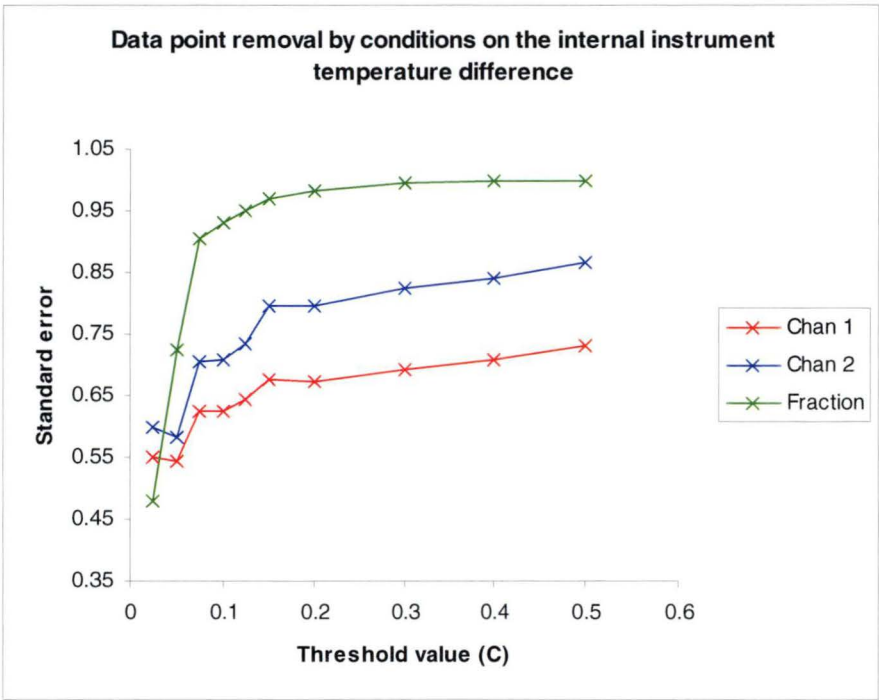


Figure 5.17. The standard error in the temperature predicted from the calibration data set that remains after a threshold condition is applied to the change in the internal instrument temperature between one measurement and the next. The standard error decreases obviously as the threshold is lowered.

The plot shows the standard error in each channel for the remaining data points if the threshold value were to be applied to the data set. It also shows (in green) the fraction of the total number of data points that would remain if the threshold value were applied. The number of remaining data points dropped sharply for threshold values of 0.075°C and below. 90.6% of the calibration data points had values of $\Delta T_{i,2}$ less than 0.075°C. Any decrease in

standard error for threshold values less than 0.075°C would have been strongly influenced by the decrease in the amount of data.

However for threshold values of 0.1°C and above, particularly between 0.1 and 0.15 °C, the standard error decreases with threshold value more strongly than the fraction of remaining data points.

A threshold value of 0.125°C was chosen as a candidate value for further testing.

Application of this threshold resulted in a decrease in standard error of 0.086°C (from 0.73 to 0.644 °C) for channel one and 0.131°C (from 0.866 to 0.735°C) for channel two. 2086 of 2198 data points remained after the threshold criterion on $\Delta T_{i,2}$ was applied.

A similar analysis was performed on the remaining data using a threshold condition on $\Delta T_{Blackbody}$, the difference in blackbody temperature from one measurement sequence to the next. For a varying threshold level, measurements corresponding to a change in $T_{Blackbody}$ that exceeded the threshold were removed, and the standard deviation in the resulting calibration equation was calculated. The results are shown in Figure 5.18 below. In this plot the standard errors follow the trend in the number of remaining data points more closely than in Figure 5.17. There was little to be gained in applying a threshold condition to the data without removing a large proportion of the data points.

Such a condition on $\Delta T_{Blackbody}$ would also have proved more restrictive for the instrument's eventual application. Fluctuations in the target temperature or shifts from one target to another would produce large changes in the target temperature. If a condition on the target temperature only guaranteed the instrument's correct calibration under conditions of slow change, many of the desired applications for the instrument would be restricted. For these reasons no threshold condition was applied to the data based upon $\Delta T_{Blackbody}$.

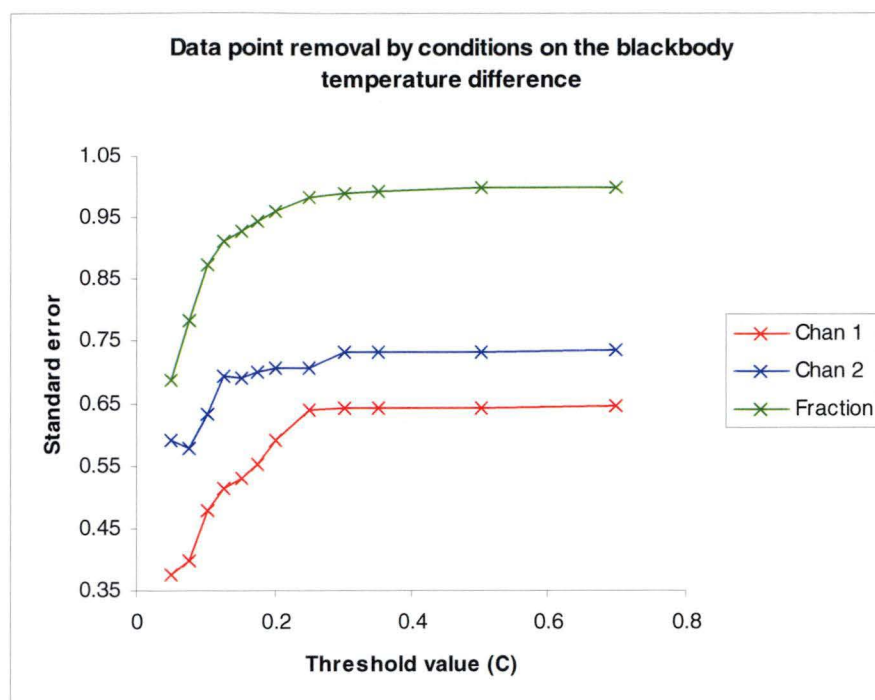


Figure 5.18. The standard error in the temperature predicted from the calibration data set that remains after a threshold condition is applied to the rate of change of the blackbody target temperature. The standard error decreases obviously as the threshold is lowered.

The instrument’s insulation and self-heating properties guarantee slow internal temperature fluctuations under normal field conditions, so that a threshold condition can be applied to $\Delta T_{i,2}$ without restricting its potential applications in the same way.

The standard errors in the predicted target temperature for the refined data set were 0.64 and 0.74 °C for channels one and two respectively. These were well in excess of the values obtained for the warm calibration (0.128 and 0.106 °C respectively) and also in excess of 0.5°C, set as a target value of the accuracy during the instrument development.

An attempt was made to further reduce the standard error values by modification of the form of the calibration equation. The values above were obtained by applying a multiple linear regression fit to the data using an equation of the form of equation (5.3).

Many potential forms of the calibration equation were assessed, including variations of polynomials in instrument signal and internal temperature. These polynomials ranged up to and including the fourth order. Many of these yielded little improvement in the standard error values. Notably, little or no improvement was made through the inclusion of powers

higher than the second power for all variables. Also, it was found that the inclusion of a term that multiplied the instrument's signal output by the internal temperature gave significant gains.

The results also showed a strong dependence on the internal temperature measured by the second instrument thermocouple, relative to the internal instrument temperature measured by the first thermocouple. This dependence is reflected in the final instrument calibration equation, which took the form

$$T_i = c_{i,8}S_i^2 + c_{i,7}S_i + c_{i,6}\sqrt{S_i} + c_{i,5}S_iTi_{i,2} + c_{i,4}Ti_{i,2}^2 + c_{i,3}Ti_{i,2} + c_{i,2}Ti_{i,1} + c_{i,1} \quad (5.5)$$

The coefficients calculated by the multiple linear regression analysis are shown in Table 5.4 below. The standard error values were 0.428°C for channel one and 0.390°C for channel two. Plots of the values predicted by the calibration equation against the measured blackbody temperature are shown in Figures 5.19a and 5.19b. An analysis of the multiple linear regression fit to only the cold calibration data yielded standard errors of 0.415 and 0.347 °C – an improvement, but not sufficient to warrant the use of a second calibration equation for exclusively ‘cold’ applications. This justified the choice to analyse the warm and cold calibration data in combination. An analysis of the errors introduced into the predictive equations by errors of this magnitude in the temperature inputs is detailed in Appendix C.

Coefficient	Channel 1 (i=1)	Channel 2 (i=2)
$c_{i,1}$	-2.481	0.8741
$c_{i,2}$	-2.978	-2.632
$c_{i,3}$	3.429	3.419
$c_{i,4}$	1.702×10^{-3}	-5.266×10^{-3}
$c_{i,5}$	4.502×10^{-3}	2.131×10^{-3}
$c_{i,6}$	2.588	-1.309×10^{-2}
$c_{i,7}$	-0.4444	-8.174×10^{-2}
$c_{i,8}$	5.497×10^{-6}	-5.713×10^{-5}

Table 5.4. List of empirically-derived coefficients in both channels for equation (5.5).

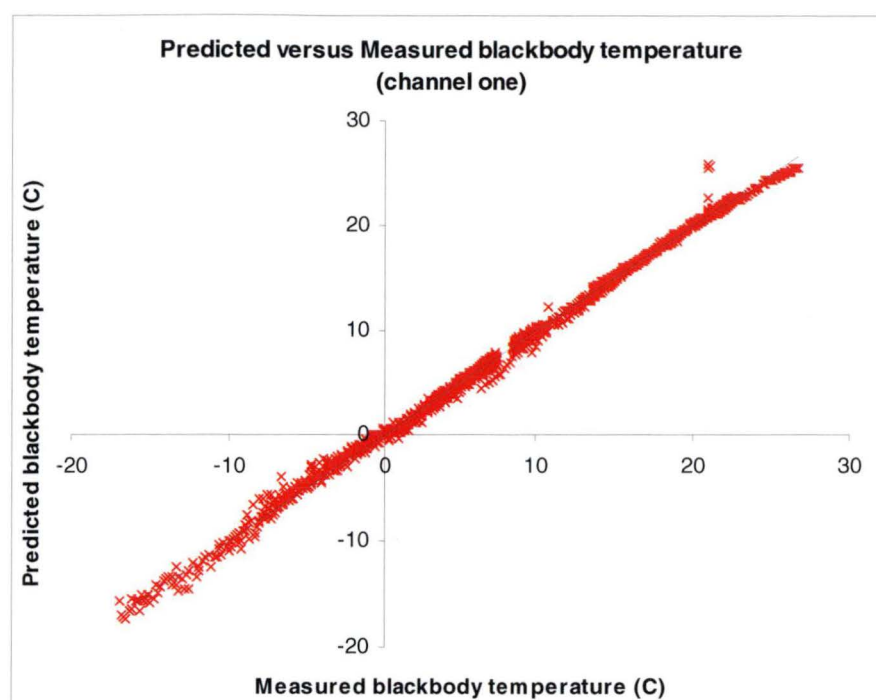


Figure 5.19a. Blackbody source temperature predicted by equation (5.5) from channel one, plotted against the measured blackbody source temperature.

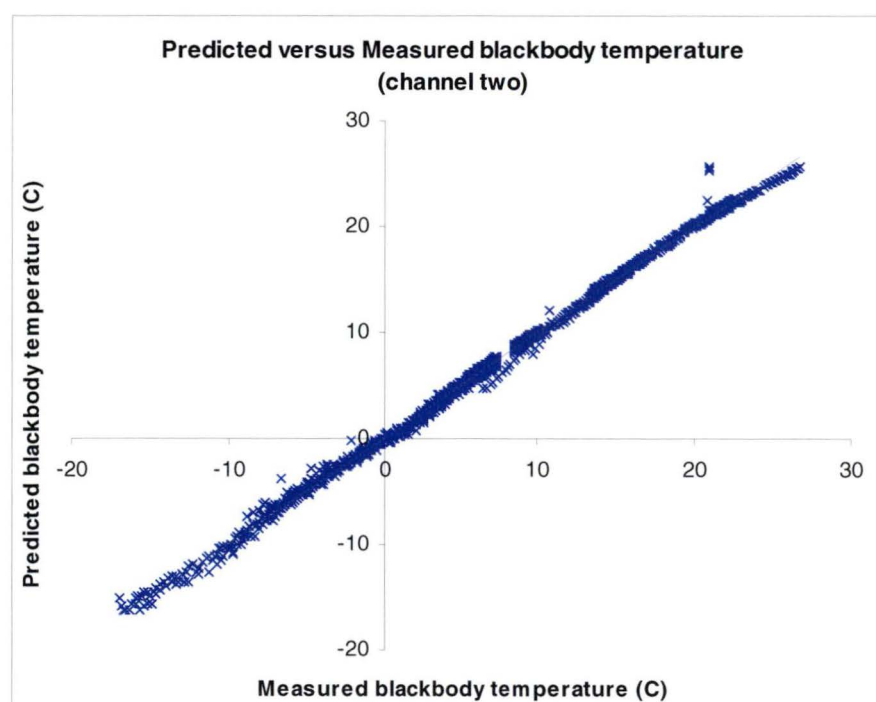


Figure 5.19b. Blackbody source temperature predicted by equation (5.5) from channel two, plotted against the measured blackbody source temperature.

The residual values (the difference between the predicted and measured target temperatures) were analysed in an attempt to discover any trends that may have existed in the data. This

analysis was performed for channel one only, as any genuine trends present in the residual values should be present for both channels. To verify this hypothesis, the residuals for the channel two data were plotted against those for the channel one data. The resulting plot, with a linear trendline and its equation, are shown in Figure 5.20 below. It can be seen in Figure 5.20 that although there is some scatter about the trendline, the residuals on channel two are essentially correlated with those on channel one.

The residual values from channel one were then plotted against five different quantities for which trends within the data may be expected. These are summarised in Table 5.5 below. The R^2 correlation values for a linear trendline fit to each plot are also presented in the table. The plots of the channel one residual values against the various quantities are shown in Figures 5.21a, b, c, d and e.

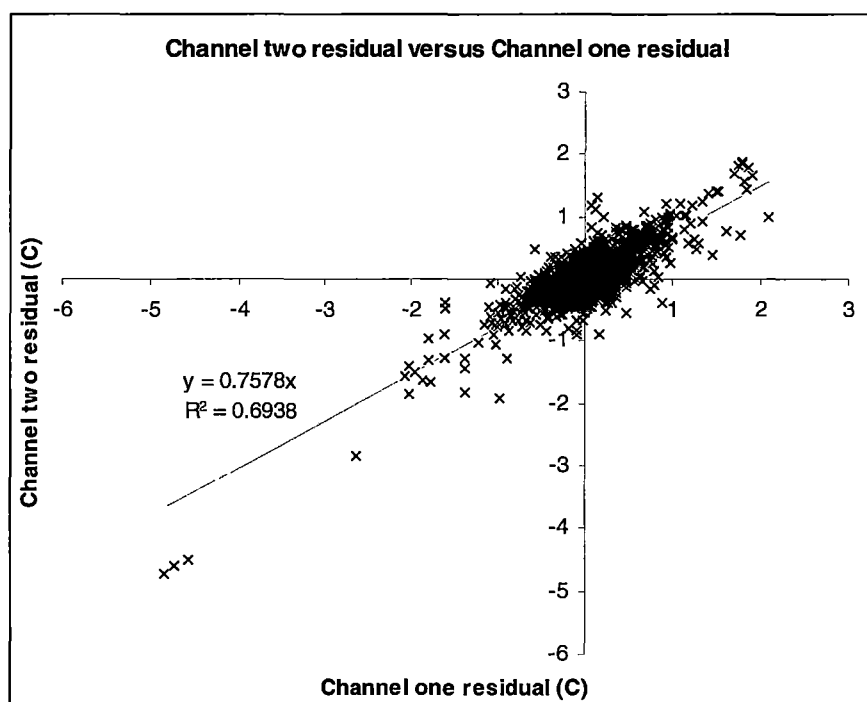


Figure 5.20. Residual values (predicted temperature minus measured temperature) for channel two plotted against the residual values for channel one.

Quantity	Correlation R^2 value
$T_{Blackbody}$	2.1×10^{-3}
$Ti_{1,2}$	1.0×10^{-24}
$T_{Blackbody} - Ti_{1,2}$	4.0×10^{-3}
$\Delta T_{Blackbody}$	1.1×10^{-3}
$\Delta Ti_{1,2}$	2.3×10^{-4}

Table 5.5. Correlation indices for the correlation between channel one's residual values and the indicated quantities.

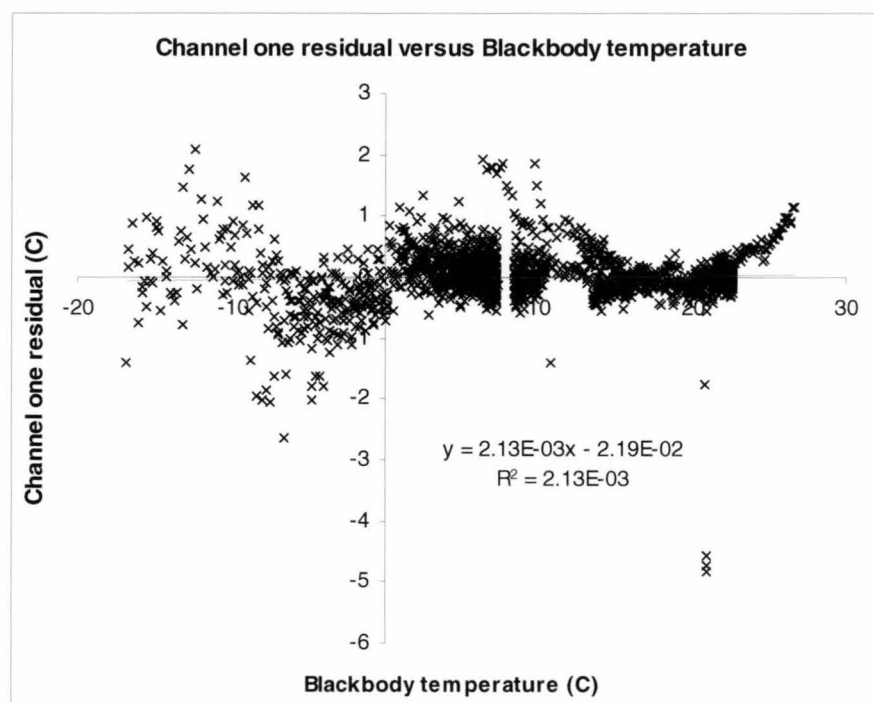


Figure 5.21a. Residual values (predicted temperature minus measured temperature) for channel one, plotted against measured blackbody source temperature.

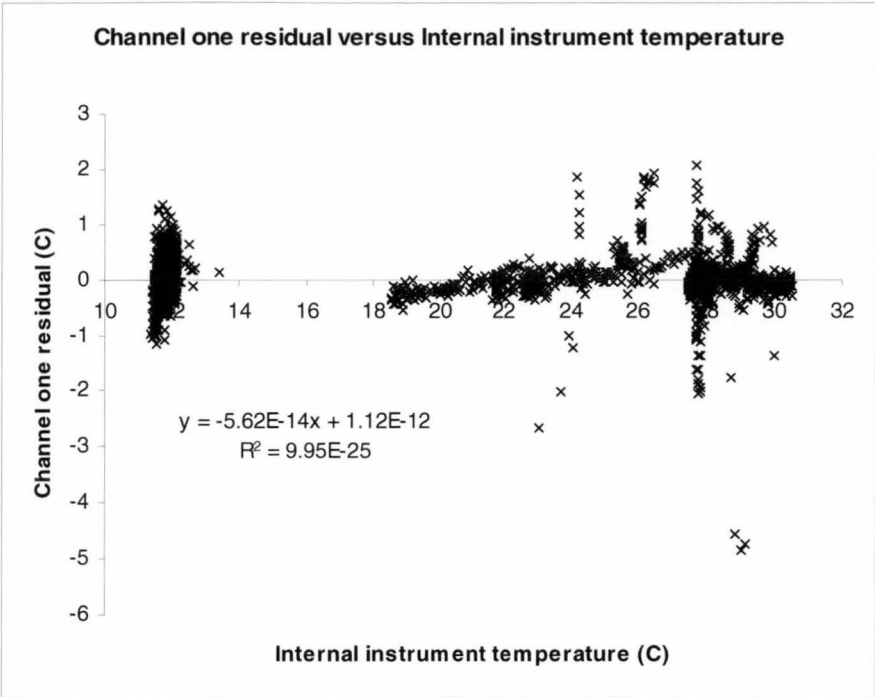


Figure 5.21b. Residual values (predicted temperature minus measured temperature) for channel one, plotted against internal instrument temperature.

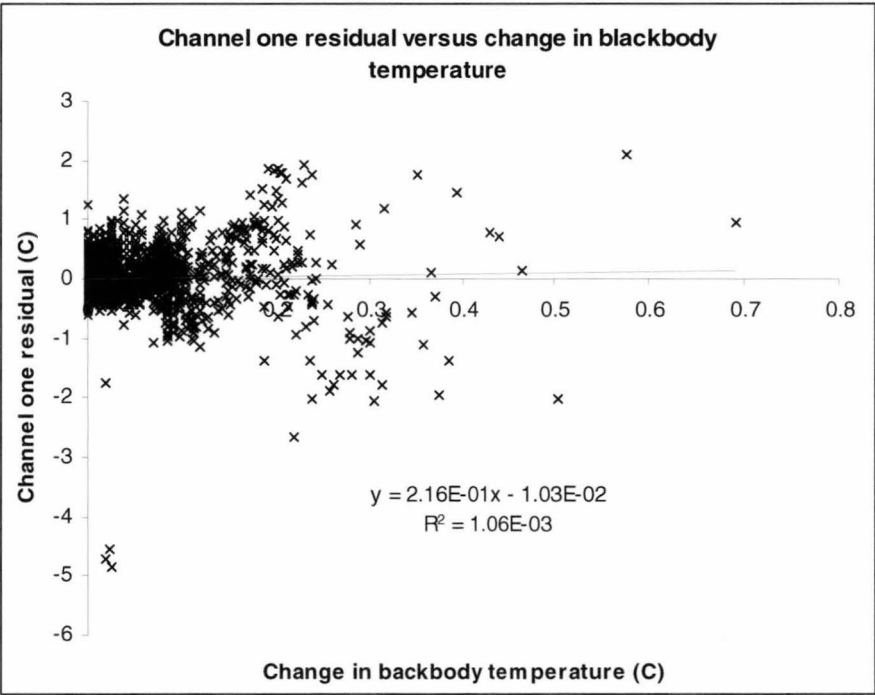


Figure 5.21c. Residual values (predicted temperature minus measured temperature) for channel one, plotted against the temporal inter-measurement change in blackbody source temperature.

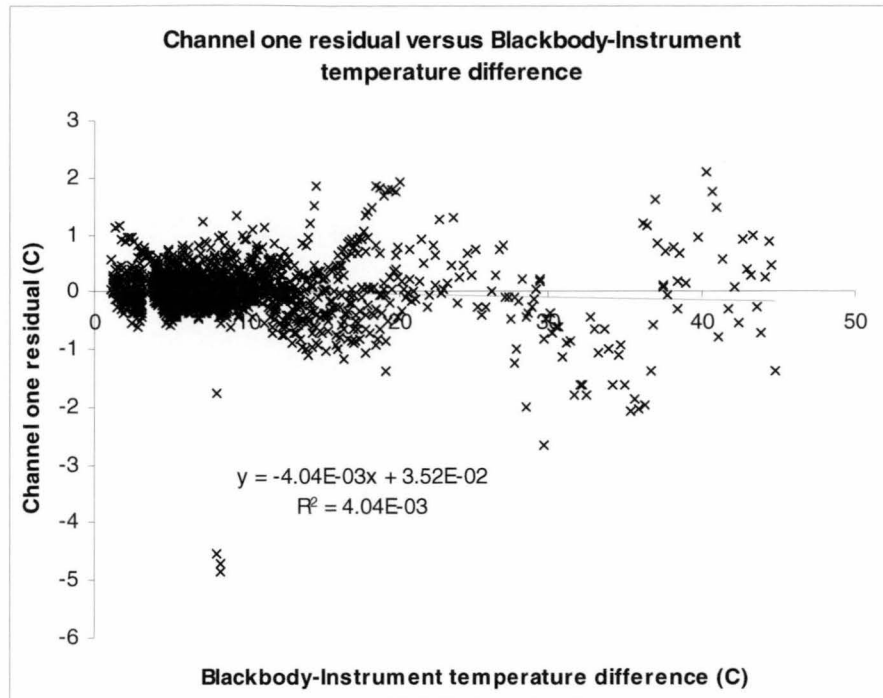


Figure 5.21d. Residual values (predicted temperature minus measured temperature) for channel one, plotted against the difference between blackbody source temperature and internal instrument temperature.

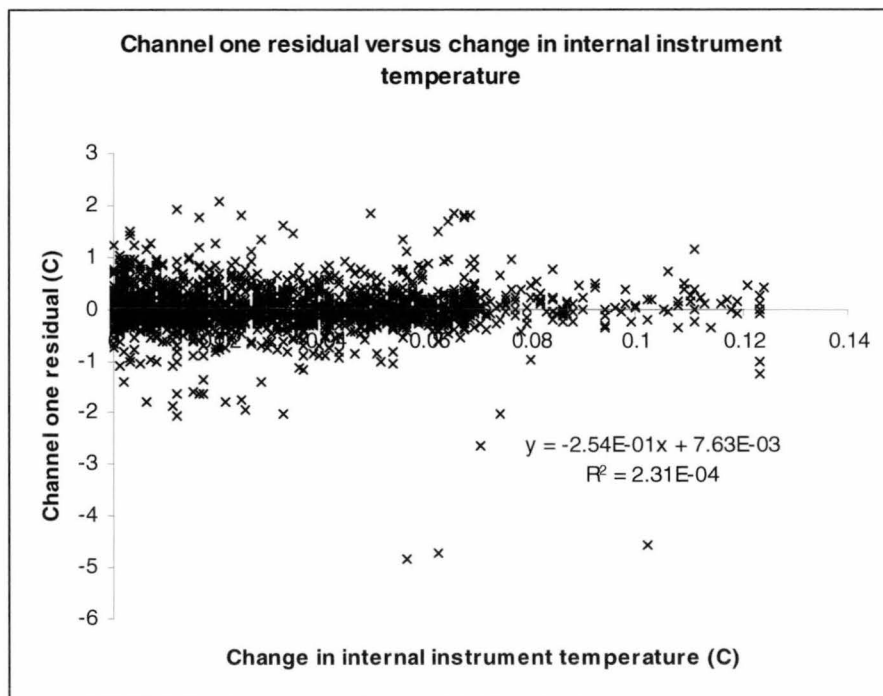


Figure 5.21e. Residual values (predicted temperature minus measured temperature) for channel one, plotted against the inter-measurement change in internal instrument temperature.

This analysis showed that there was little if anything to be gained through further elimination of calibration data or addition of parameters to the calibration equation. Examination of the data from a qualitative perspective yielded one significant issue. There are two series of data points, between 6 and 10 °C target temperature (see Figures 5.19a and 5.19b) that obviously correspond to high residual values. These series correspond to periods in the calibration when the instrument was used immediately after being turned on. They do not meet the threshold criterion for the change in instrument temperature, most likely because the instrument was used in a cold room for the corresponding calibration runs and the coldness of the room countered the instrument's self-heating somewhat.

While any additional threshold criteria would reduce the size of the calibration data set and limit the instrument's range of application, a qualitative condition for the instrument's use was based upon this observation. This condition (which was applied in all field use of the instrument) was that the instrument had been powered for at least one hour before measurements began.

The instrument calibration resulted in an equation that could be used to convert the instrument's outputs into the brightness temperature of its target. The resulting brightness temperatures can be used in the equations described in Chapter 2 to determine directional radiance, hemispherical irradiance (through integration) and divergence of both radiance and irradiance. The conversion was accurate to better than 0.5°C in both channels and may be applied over an internal instrument temperature range of 10 to 30 °C and target temperature range of -18 to 28 °C.

5.10 Summary

This chapter has described the testing and calibration of the final instrument design. These tests were designed to ensure that the implementation of the instrument design had produced the required capabilities and also to measure and fine-tune instrument parameters such as the field of view and chopping speed.

For the sake of usefulness and brevity the chapter has not detailed the preliminary testing and calibration processes that were used throughout the evolution of the instrument. These were used to provide feedback of the instrument's performance and in most cases prove a requirement for further work on the design. A brief example is shown in Figures 5.22a and

5.22b below. The figures show a 3D calibration curve plotting instrument response against internal instrument and target temperatures. Figure 5.22a shows the calibration curve before the replacement of the LIS 114 detector (discussed in Section 3.3). This plot provided the motivation for changing the detector. Figure 5.22b shows the same plot, after the LIE 307 replaced the LIS 114. Although used only qualitatively, the plots clearly justify the change.

This type of feedback-driven evolution applied to both the instrument and the testing processes, which also developed in complexity and improved as the instrument was developed. In detailing the final forms of the testing and calibration processes, this chapter has itself been a brief summary of the work done to develop, test and calibrate the instrument.

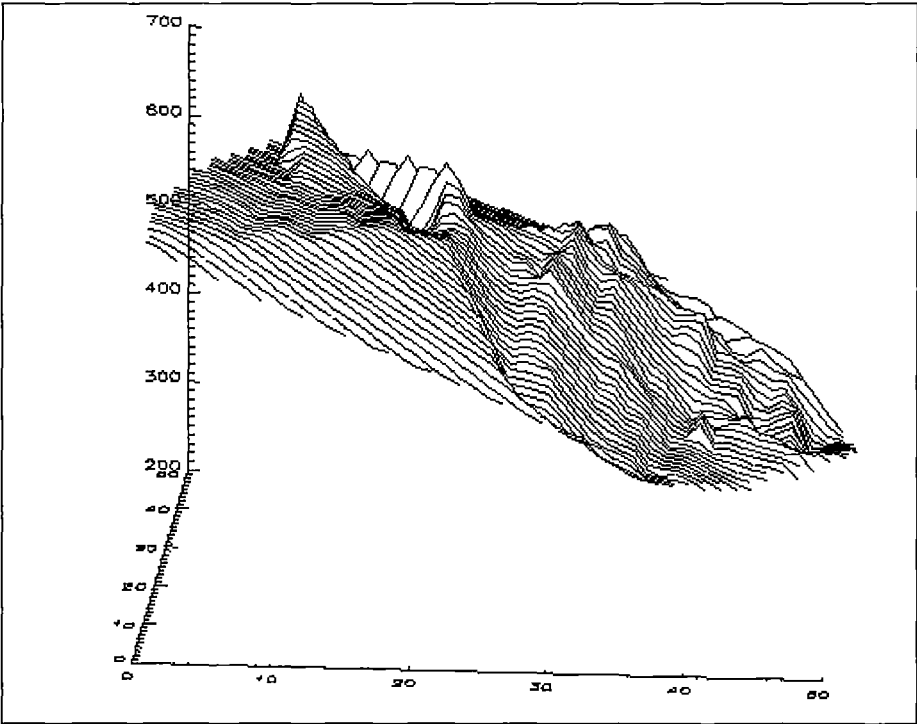


Figure 5.22a. (x,y,z) plot corresponding to instrument response in mV versus the blackbody source and internal instrument temperatures. This plot depicts data gathered during early calibration runs using the LIS114 pyroelectric detector. The x-axis and y-axis correspond to blackbody source and internal instrument temperatures (both in °C) and the z-axis corresponds to the instrument response in mV.

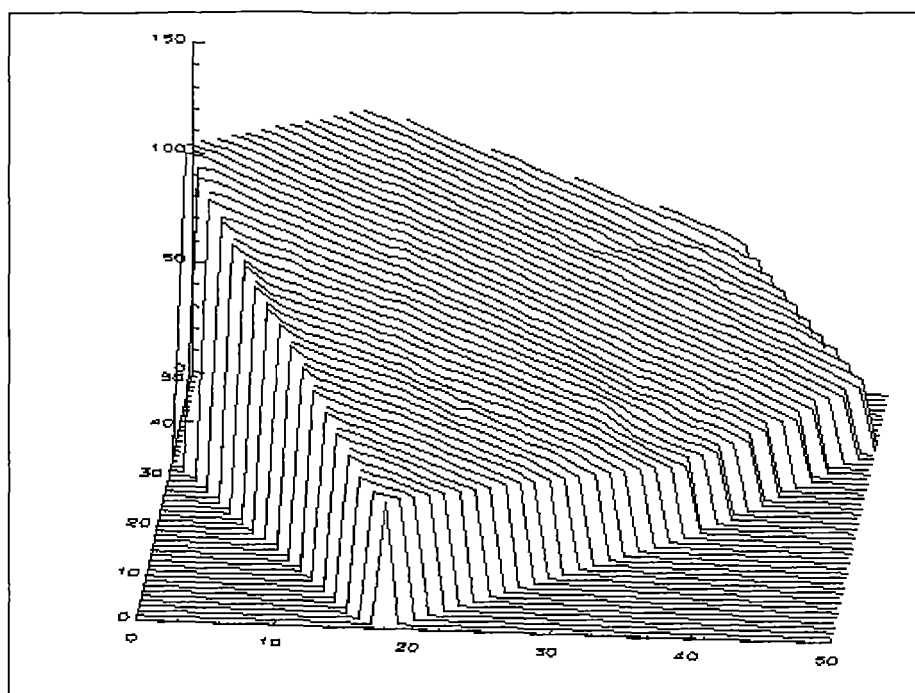


Figure 5.22b. This figure shows the same plot as shown above in Figure 5.22a, but depicts data gathered during calibration runs conducted after the LIS114 detector was replaced by the LIE307 detector. The x-axis and y-axis correspond to blackbody source and internal instrument temperatures (both in °C) and the z-axis corresponds to the instrument response in mV.

Chapter 6

Field Measurement program

6.1 Introduction

The field measurement program was conducted between April and July 2002. There were two motivations for the field measurement program. One was to test the various instrument capabilities described in Chapter 2. The second was to use the results to study the impact of infrared divergence on the cooling rate of the nocturnal boundary layer (NBL) near the ground at night.

The analysis of the gathered data will be detailed in Chapters 7, 8 and 9. This chapter will describe the field sites at which data was gathered, the equipment used, its installation and the measurement configurations that were used to gather the data.

6.2 Field sites

Data were gathered at two field sites. The first site was intended to provide measurements of brightness temperatures from both the ground and the sky for infrared divergence calculations, while the second site was used only to gather sky brightness temperature data. The intended use for the gathered data determined the properties required of each site and the equipment that was installed.

The first site was chosen based on the likelihood of easily measurable infrared divergence occurring there. The infrared divergence calculations also imposed several requirements on the choice of site. Flat, uniform ground was required with low, homogeneous ground cover in the close vicinity of the measurement site. Flatness of the surrounding terrain was also desirable, as it would reduce the likelihood of terrain-related airflow near or through the measurement site.

As measurements were required at several different heights, the choice of the first field site was also subject to the practical considerations of erecting a tower on the site. The primary consideration was the ability of the underlying ground to support such a structure. Vehicle access and the need for permission to erect the tower were also taken into account.

A site was chosen at the Hobart International Airport, approximately fifteen kilometers from Hobart's CBD. The runway part of the airport complex is approximately three metres above sea level, the airport itself being close to large waterways to the north (Barilla Bay) and east (Pitt Water) and the ocean to the south (Frederick Henry Bay).

Permission was granted by the airport authorities for the erection of a scaffold tower within the perimeter fence. The perimeter fence ran approximately forty metres to the southwest and northwest of the site. The main runway was approximately 300 metres to the northeast of the site, and part of the tarmac apron was approximately 125 metres to the southeast of the site. Approximately 250 metres directly to the west of the site, the airport control tower and Bureau of Meteorology observation station were situated atop a small hill (height approximately 22 metres). The hill was the only topographical feature of any significant height within two kilometers of the site. The hill was approximately seven hundred metres long and 250 metres wide at its ten-metre elevation contour. Photographs of the terrain near the field site in two directions are presented in Figures 6.1a and 6.1b (looking south and north respectively).

The field site provided the ideal location for measurements of infrared divergence. A homogeneous high-emissivity surface such as the short grass at the site was essential for infrared temperature readings. The open, flat and uniform terrain provided ideal conditions for strong and easily measured infrared divergence. The proximity of the site to the Bureau of Meteorology's airport observation site also allowed seamless integration of the Bureau's sonde-measured upper-atmosphere profiles.

A local scaffolding contractor erected the measurement tower in February 2002. The tower was designed to allow access to its highest platform for ease of installation and retrieval of the instrument and its data logger. The tower's highest platform was at ten metres height, with handrails at 10.5 metres. The footprint of the tower was three metres by three metres, uniform over its height. Scaffold outrigging with a five by five metre footprint was used to stabilise the tower. There was a second platform at five metres height, with ladders from the ground to the second platform and from the second to the top platform. A photograph of the tower is shown in Figure 6.2 below.



Figure 6.1a. View to the south from the base of the tower.



Figure 6.1b. View to the north from the base of the tower.



Figure 6.2. Measurement tower at the airport site.

Various additional measuring instruments were attached to the tower to provide additional data. These instruments and the data they provided will be discussed later in this chapter. The tower provided a stable and flexible platform for the instruments used, in a location perfectly suited to the desired environmental conditions.

The second site used for field measurements was the roof of the Geography and Environmental Studies building at the University of Tasmania's Sandy Bay campus. As only measurements of sky brightness temperature were required from this site, there were few site requirements other than a relatively unobstructed view of the night sky.

The roof site provided such a view in most directions, obscured only by the university buildings and far-lying terrain up to 30° elevation to the south. The intended measurement direction was north to northeast, which was completely clear from obstruction. The roof site provided a clear, flat space for installation of the instrument's tripod mount and a purpose-built platform for the accompanying pyrgeometer. The installation at the roof site will be discussed further later in this chapter.

6.3 Equipment installation at field sites

The equipment installed at the airport tower site was intended to provide infrared temperature measurements of ground and sky, together with a temperature and relative humidity profile of the nocturnal boundary layer over the height interval of the tower. Additional radiometric measurements were also made through the use of a pyrgeometer and net radiometer. Ground temperature measurements were also required, to provide a reference for the ground brightness temperature.

The radiometric instruments were installed on the top platform of the tower. Their arrangement is shown in Figure 6.3 below. The instruments were attached at the level of the top platform, 10 metres above the ground.

The mount for the dual channel radiometer (DCR) was permanently attached to the tower, while the radiometer itself could be installed or removed in seconds using the mount head's quick-release shoe. The pyrgeometer was permanently mounted on a steel bracket and the net radiometer's arm was also attached to the scaffolding. The measurement process for the radiometric instruments will be discussed in further detail in the next section.

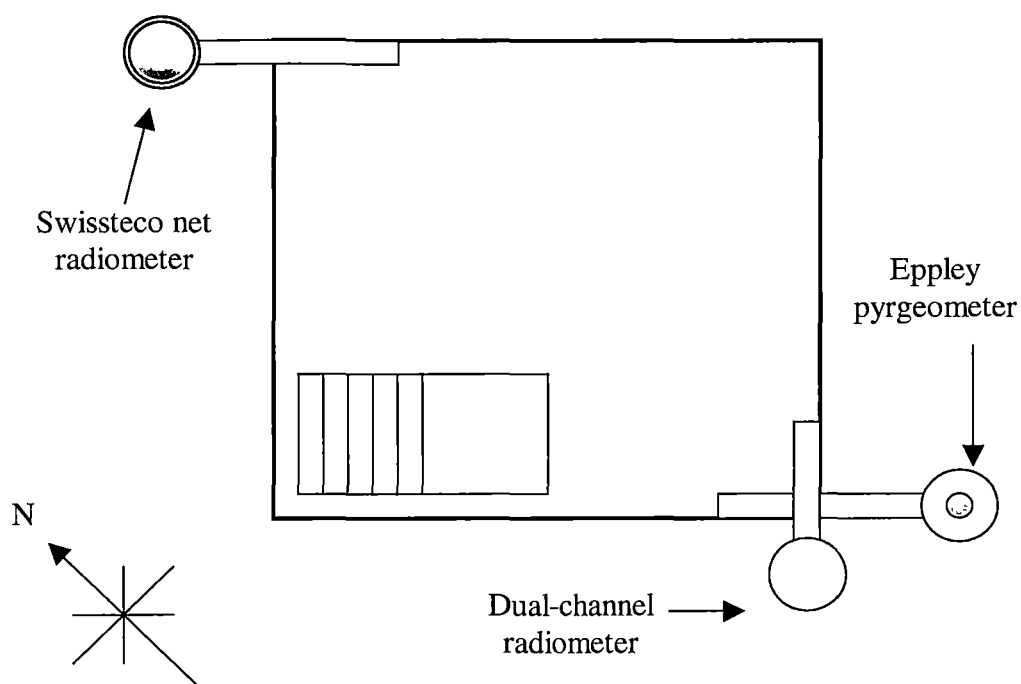


Figure 6.3. Schematic diagram of instrument positions on the top platform of the tower.

The installation was designed so that the DCR and its data logger could be installed and removed quickly and easily. This was an important requirement, as the DCR was not proofed against rain or excessive atmospheric moisture. The pyrgeometer output was logged by the same data logger program as the DCR and was therefore wired into the same data logger. Its removable plug allowed the cable – which was permanently wired into the data logger - to be removed when the DCR and data logger were removed.

A single car battery was used to power the DCR when it was installed at the tower site. The battery remained on the top platform throughout the field measurement program and was recharged regularly by a solar panel at the base of the tower. A separate motorcycle battery was used to power the data logger because the DCR needed to be powered exclusively.

A separate data logger (Campbell 21X) was used to log data from the net radiometer and profile-measuring instruments. This allowed the profile-measuring instruments to be logged independently of the DCR and pyrgeometer. The CR21X was permanently installed at the tower site. The instruments used to measure the atmospheric profile and their configurations are shown in Figure 6.4. The diagram shows only the northern corner pillar of the tower for clarity.

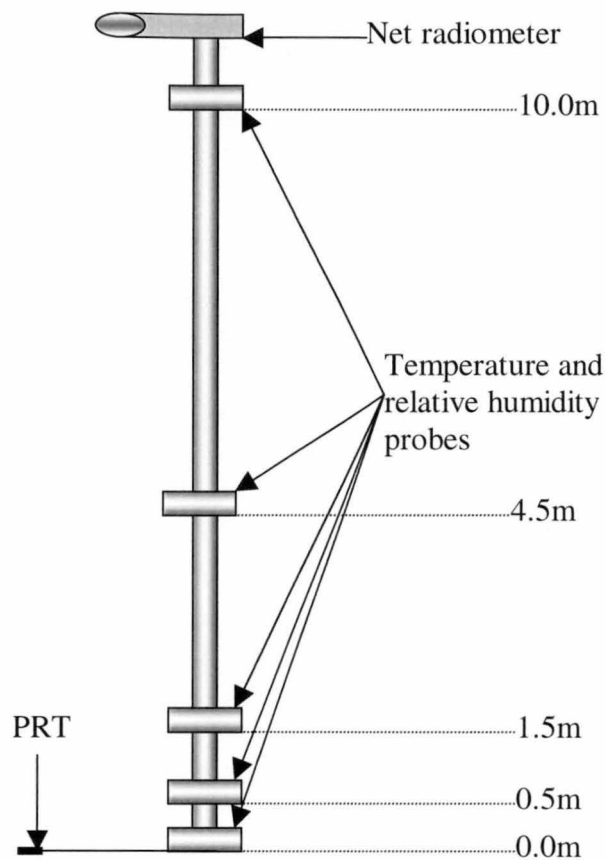


Figure 6.4. Temperature and RH probe positioning on the northern corner of the tower.

A platinum resistance thermometer (PRT) was used to measure the ground temperature. This was required in order to provide a reference for comparison with the DCR-measured ground brightness temperature. The PRT was gently inserted just inside the ground surface, lying parallel to the ground. The PRT was expected to give only a rough reference for the surface brightness temperature, for two reasons. Firstly, the grass overlying the ground would dominate the DCR's view, while the PRT was arranged to measure the temperature of the underlying soil. There could be no guarantee that the two temperatures would be the same. Secondly, the emissivity of the grass, while uniform and close to one, could not be guaranteed to be exactly one. For these reasons it was expected that the ground PRT temperature and ground brightness temperature as measured by the DCR would not be exactly the same. Difficulties in the use of measured ground temperature as a reference for ground brightness temperature are well documented (Robinson 1950).

The temperature and relative humidity probes were installed as shown in Figure 6.4. Campbell CS500 probes were used in four of the installations and a Vaisala HMP45C for the fifth (at ground level). While the Vaisala unit requires a different set of logger instructions

for interpreting its temperature measurement and a different calibration procedure, once installed and calibrated the units are indistinguishable in terms of their function.

Both units measured air temperature using a 1000Ω PRT and relative humidity using an INTERCAP© capacitive humidity sensor. Both contained signal-conditioning circuitry for the humidity sensor, providing a 0 to 1000 mV output that related linearly to the measured relative humidity (0 to 100 % at 10mV/1%). The CS500 units contained similar circuitry for the temperature sensor, providing a 0 to 1000 mV output that related linearly to the measured temperature with a range of -40 to 60°C . The HMP45C unit provided direct connection to the PRT and was therefore be used in combination with additional circuitry (temperature-independent resistors) in a bridge configuration. The data logger was programmed to measure the resistance of the PRT and calculate the temperature from the resistance value.

The tips of all of the probes were mounted in tubes approximately 280 mm long and 60 mm in diameter. The entry point of the probe into the tube was sealed and both the probe and the tube were wrapped in aluminized Mylar to prevent radiative warming or cooling of the tube or the probe body. Fans were then mounted at the end of the tube, oriented so that they would blow air from the tube and thereby draw fresh air into the tube. This arrangement prevented any possible heating of the air by the fan until after the air had passed the probe. Assuming full efficiency the fans drew air through the tubes at a rate of 2.8 litres per second.

A marine battery with a 109 Amp-hour capacity powered the fans, probes and the aquarium pump that was used to pump dried air into the dome of the net radiometer. A motorcycle battery was used to power the data logger whenever the large battery was disconnected. The large battery was also connected to the solar panel used to recharge the DCR's battery – plugs allowed the solar panel to be switched between the batteries. To conserve power, the probes, fans and aquarium pump were switched on using relays one minute before measurements began. They were then switched off once measurements had ceased – the full measurement process will be discussed in the next section.

Instrument installation on the roof site at the University consisted only of the DCR and the Eppley pyrgeometer. The pyrgeometer was mounted on an instrument bank used specifically for radiometric instruments. The DCR was mounted on a large tripod using the tripod attachments described in Chapter 5. The DCR was installed approximately three metres from the pyrgeometer at the same height. Once the tripod and pyrgeometer were installed, the DCR, its battery and the data logger could easily be installed and removed in the same way

as for the tower site. The measurement process used for the roof site installation will be discussed further in the next section.

6.4 Field measurement programs

For all measurement sets from the airport tower site, the instruments on the tower yielded air temperature, relative humidity, ground temperature and net radiation data at five-minute intervals. These data were the product of an average of data logged at two-second intervals over the last minute of each five-minute interval. As mentioned in the previous section, the fans, probes and net radiometer's dry air pump were switched on one minute before sampling began.

The net radiometer's millivolt output was converted to W/m^2 using a linear calibration function. The resistance of the ground-based PRT was measured using an external four-way bridge and then converted to temperature using a standard PRT conversion function. The relative humidity output of all of the probes was adjusted using linear calibration equations, derived from a standard wet/dry salt calibration process. The temperature measurement from the Vaisala probe was also calibrated using a standard linear calibration equation, derived from a comparison with the 'standard' PRT used for the ground temperature measurements. The CS500 probes were likewise calibrated for temperature but found to be accurate to within their specified limits, and so no correction was applied.

For all DCR measurements, a measurement of the hemispherical longwave irradiance from the sky was also made using the Eppley pyrgeometer. These data therefore occurred at the same frequency as the DCR measurements. Five minutes was used as the base unit of time for DCR measurements, allowing 130 seconds for the measurement sequence to occur (see Chapter 4) and a further 170 seconds for positioning of the DCR by rotation of the instrument mount. The instrument mount was rotated in intervals of five degrees - 139 steps of the stepper motor. For each measurement set the data logger program was adjusted to scan through the desired sequence in five-degree intervals, scanning back to the mount's reference position regularly to ensure accurate positioning. The various scanning sequences used will be detailed in the next section.

The DCR's outputs of signal voltage and internal temperature were initially converted to brightness temperatures by the logger program, using the warm calibration equation. As the calibration equation was later updated after the cold calibration was performed, the

calibration was reversed to calculate the original signal voltage and internal temperature values. The procedure for reversing the calibration is detailed in Appendix A.

The Eppley pyrgeometer operated in passive mode, without any internal correction for the case temperature. The Bureau of Meteorology’s instrument calibration personnel recommended this mode of operation as a means of avoiding inaccuracies due to decay with time of the pyrgeometer’s internal battery voltage. The case temperature was measured using the case thermistor output which was wired directly into the data logger. No correction was made for dome temperature as the measurements were made after sunset and before sunrise, when differential heating of the dome (usually due to solar radiation absorption) is negligible. The data logger used the calibration constant to scale the measured thermopile voltage and calculated the thermistor case temperature using the appropriate thermistor (YSI44031) equation. These values were logged and the final conversion to downwelling hemispherical irradiance was performed in post-processing.

6.5 Field data set description

Once the primary field installations and testing were complete, measurements were conducted at the field sites over eight nights between April and July 2002. Measurements were conducted whenever clear-sky conditions were experienced for lengthy periods during the night. The measurement program for each measurement set is shown in Table 6.1 below.

The ‘AP’ abbreviation denotes the airport site while ‘RF’ denotes the roof site. ‘Time begin’ and ‘time end’ denote the time stamps of the first and last DCR measurements in the set, respectively. ‘DCR nadir angles’ denotes the angles (in degrees) at which down-looking DCR measurements were made. Likewise, ‘DCR zenith angles’ denotes the angles at which up-looking DCR measurements were made. For each of these, the corresponding ‘Interval’ denotes the time interval between measurements.

‘21:00 BOM sonde profile’ denotes the availability of the Bureau of Meteorology’s nightly profile of temperature and relative humidity. These will be discussed in more detail later in this section. ‘Y’ denotes that the sonde profile was available, ‘N’ that it was not. ‘N/A’ denotes that the sonde profile was not applicable to the measurement set because measurements were not made after 18:22 and the sonde profile was therefore meaningless.

Date	29/04	01/05	10/05	13/05	14/05	18/06	29/06	30/07
Site	AP	AP	AP	AP	AP	AP	RF	RF
Time begin	15:00	12:47	20:07	17:07	14:12	15:37	21:17	16:22
Time end	18:22	16:07	09:47	09:32	10:27	10:27	10:52	09:57
DCR nadir angles (°)	0	0	0	0	20,35, 50	15,30, 45,60, 75	N/A	N/A
Frequency (mins)	5	5	5	5	15	30	N/A	N/A
DCR zenith angles (°)	0	0	N/A	N/A	N/A	N/A	0, 15, 30,45, 60, 75	0, 15, 30,45, 60, 75
Interval (mins)	60	60	N/A	N/A	N/A	N/A	30	30
21:00 BOM sonde profile	N/A	Y	Y	Y	Y	Y	N	N

Table 6.1. Measurement program summary for all measurement nights.

Additional information was also purchased from the Bureau of Meteorology's Hobart Airport observation site. The records included wind speed and direction, visibility, cloud cover, temperature and pressure. The wind and cloud information was used primarily to verify the existence of favorable conditions during measurement periods. The other information was not used. The judgment of favorable conditions was a qualitative one – the ideal conditions were zero wind and no cloud cover at all. A summary of the relevant data is presented in Chapter 7.

6.6 Summary

Analysis of the gathered data sets will be described in Chapters 7, 8 and 9. The purpose of this chapter has been to describe the sites at which measurements were made, the processes that produced the data sets and the conditions under which the data was gathered. In the following chapters these data sets will be referenced by the date upon which measurements were made. This chapter then serves as a reference for the conditions under which those measurements were made and the configuration of the gathered data set.

Chapter 7

Fieldwork results I – data set descriptions and metadata

7.1 Introduction

This Chapter details the local meteorological conditions corresponding to each set of measured data. The conditions were assessed based on data measured by the DCR, data measured by the tower-mounted instruments and further data provided by the Bureau of Meteorology's Hobart Airport and Battery Point observation sites. The data gathering process and measurement details are included in each section as appropriate.

Values of the relevant measurements at the start and end of each measurement set and the average of those values over the whole measurement set are presented in tables on a per-quantity basis. These tables are followed by sets of charts of the quantities for which time series were available over the course of the measurement set. These charts are presented on a per-night basis together with a description of the meteorological conditions on each measurement night and a brief qualitative analysis of the available data where appropriate.

7.2 Net radiation

The net radiation was measured by the tower-mounted Swissteco net radiometer – see Chapter 6 for details of this instrument and its installation. The start and stop times for all data sets were based upon the net radiation's transition from positive to negative and negative to positive respectively. The positive to negative transition indicated that the effect of shortwave solar radiation on the net radiation was minimised as the time approached sunset. The reverse is true for the negative to positive transition, just after sunrise. Net radiation measurements were made only at the airport site and therefore no data was available for the roof site measurement sets.

Charts of the measured net radiation over the measurement period defined in Table 7.1 are shown on a per-night basis in sections to follow.

Date	Net radiation transition to negative	Net radiation transition to positive	Average net radiation (W/m²)
01/05/02	16:00	08:00	-57.3
10/05/02	19:20*	08:15	-56.2
13/05/02	19:05*	08:55	-62.1
14/05/02	15:30	07:50	-46.8
18/06/02	16:00	08:30	-48.1

Table 7.1. Times of net radiation transitions from positive to negative, negative to positive and average net radiation between those times. Times indicated by an asterisk (*) are the measurement start time – the time of the positive to negative transition was not measured. Measurements were made at five-minute intervals, each measurement was the average of 60 samples taken at one-second intervals over the final minute in the five-minute interval.

7.3 Downwelling longwave irradiance

Downwelling longwave irradiance was measured at five-minute intervals by the tower-mounted Eppley pyrgeometer (see Chapter 6). Table 7.2 below gives the downwelling longwave irradiance measured at the start and end of the data set (see Table 7.1 for the start and end times) and the average downwelling longwave irradiance over that time. The Eppley pyrgeometer was used at both the airport and roof sites and hence data is available for the two measurement sets made at the roof site.

Date	Downwelling longwave irradiance at start time (W/m²)	Downwelling longwave irradiance at end time (W/m²)	Average downwelling longwave irradiance (W/m²)
01/05/02	305.6	276.1	279.7
10/05/02	293.1	292.5	292.2
13/05/02	278.2	330.8	271.0
14/05/02	284.3	263.1	276.6
18/06/02	313.9	266.0	259.6
29/06/02	261.7	265.8	257.3
30/07/02	287.8	250.9	261.3

Table 7.2. Downwelling longwave irradiance at the start and end of each measurement set, and the average value for each measurement set. Individual measurements consisted of an average of 30 samples at two-second intervals, during the fourth minute of every five-minute interval. For the data set gathered 29/06/02, the start and end times were 21:20 and 07:00 respectively. For the data set gathered 30/07/02, the start and end times were 16:25 and 07:00 respectively. These start and end times were chosen based on the net radiation characteristics of the previous measurement sets. In the case of the 29/06/02, measurements did not commence until 21:20.

Charts of the measured downwelling longwave irradiance over the measurement period defined in Table 7.1 are shown on a per-night basis in sections to follow.

7.4 Average air temperature (0.0 to 10.0 metres)

The tower-mounted Campbell CS500 probes measured the air temperature at the airport site, over the height interval from 0.1 to 10.0 metres. A weighted average (based on the height of each probe) was calculated to represent the average air temperature over the height interval. The average air temperature at the start and end time are shown with the average air temperature, temporally averaged over the measurement period, in Table 7.3 below.

Air temperature data was also available for the data measured at the roof site, although this data was provided by the Bureau of Meteorology. The Bureau's measurements were made at the Battery Point meteorological station in Hobart, approximately one kilometer from the

roof site. Half-hourly measurements were provided, each an average of 30 measurements made at one-minute intervals.

Date	Average air temperature at start time (°C)	Average air temperature at end time (°C)	Average air temperature, averaged with time (°C)
01/05/02	16.7	9.0	8.2
10/05/02	11.3	11.3	10.2
13/05/02	9.9	4.1	6.5
14/05/02	15.0	4.6	6.3
18/06/02	9.9	3.1	2.8
29/06/02	7.9	4.1	5.6
30/07/02	12.5	3.4	6.6

Table 7.3. Air temperatures measured by tower-mounted probes, averaged over the height interval of the tower. Tower measurements were made at five-minute intervals, each measurement was the average of 60 samples taken at one-second intervals over the final minute in the five-minute interval. Data corresponding to nights on which data was gathered at the roof site were provided by the Bureau of Meteorology.

Charts of the averaged air temperature over the measurement periods defined in Table 7.1 are shown on a per-night basis in sections to follow.

7.5 Air temperature stability index (0.1 to 10 metres)

Measurements from the tower-mounted probes were used to calculate an index of the air temperature stability. For each five-minute interval, the temperature measured by the Vaisala probe at approximately 0.1 metres was subtracted from the temperature measured by the CS500 probe at 10.0 metres. The temperature difference served to represent the inversion strength and hence the air temperature stability over the tower’s ten metre height interval. The value of the air temperature stability index at the measurement set’s start and end times, together with the average value over the measurement set, are given in Table 7.4 below. As an air temperature profile was not available for the roof site, air temperature stability indices were not available for the roof measurement nights.

Charts of the air temperature stability index over the measurement periods defined in Table 7.1 are shown on a per-night basis in sections to follow.

Date	Air temperature stability index at start time (°C)	Air temperature stability index at end time (°C)	Average air temperature stability index (°C)
01/05/02	1.5	-1.5	1.8
10/05/02	4.2	-0.8	1.5
13/05/02	5.4	0.5	1.7
14/05/02	0.6	1.2	1.7
18/06/02	-0.3	0.8	0.8

Table 7.4. Air temperature stability index, calculated by subtracting the air temperature at 0.1 metres from the air temperature at 10.0 metres. The air temperature values were measured at five-minute intervals as described in Table 7.3.

7.6 Relative humidity

The tower-mounted probes also measured relative humidity at five heights over the height interval of the tower at the airport site. The relative humidity values were averaged over the height interval 0.0 to 10.0 metres using the same weighted average used to calculate the average air temperature in Section 7.2.3. The average relative humidity at the start and end of each measurement set together with the average over the measurement set, are given in Table 7.5 below. Relative humidity measurements were not available for nights on which measurements were made at the roof site.

Date	Average relative humidity at start time (%)	Average relative humidity at end time (%)	Average relative humidity for full measurement set (%)
01/05/02	58.6	83.6	89.0
10/05/02	71.9	78.2	81.4
13/05/02	68.4	92.0	84.4
14/05/02	60.0	98.5	92.0
18/06/02	64.0	84.0	90.2

Table 7.5. Relative humidity measured by tower-mounted probes, averaged over the height interval of the tower. Measurements were made at five-minute intervals, each measurement was the average of 60 samples taken at one-second intervals over the final minute in the five-minute interval.

Charts of the average relative humidity over the measurement periods defined in Table 7.1 are shown on a per-night basis in sections to follow.

7.7 DCR-measured ground brightness temperature

The difficulties associated with an accurate measurement of ground temperature using a PRT were discussed in Chapter 6. These difficulties and the resulting inaccuracies were avoided by using the DCR’s window-channel measurement (from ten metres) as the ground brightness temperature. This application of the instrument-measured brightness temperature was ideally suited to the ground temperature required in the MODTRAN model profiles, as the model normally requires input of both absolute ground temperature and broadband emissivity in order to calculate a ground brightness temperature.

The ground brightness temperature provided the truest possible measurement of the upwelling radiance as it includes any emissivity or surface reflection effects. This assumes that the ground emissivity is constant across the relevant portion of the infrared spectrum. This same assumption is crucial if measuring absolute ground temperature along with downwelling irradiance and using a broadband emissivity value to calculate upwelling radiance.

The start and end time values as well as the average ground brightness temperature are shown for each night in Table 7.6. Charts of the DCR-measured ground brightness temperature over the measurement periods defined in Table 7.1 are shown on a per-night basis in sections to follow. Ground brightness temperature measurements were not made at the roof site.

The frequency of ground brightness temperature measurements depended on the measurement night. This variation depends on the measurement sequence used for each night, which will be discussed further in Section 7.19 to follow.

Date	Ground brightness temperature at start time (°C)	Ground brightness temperature at end time (°C)	Average ground brightness temperature for full measurement set (°C)
01/05/02	14.3	9.0	4.9
10/05/02	6.6	9.6	6.7
13/05/02	3.8	8.0	3.8
14/05/02	14.3	1.9	4.1
18/06/02	9.2	4.4	2.9

Table 7.6. Ground brightness temperature measured from 10 metres in the DCR’s window channel.

7.8 Average wind speed

Wind speed data was obtained from the Bureau of Meteorology’s Hobart Airport and Battery Point observation sites. The airport site data are routinely gathered by the Bureau from an anemometer at approximately ten metres height. The tower upon which the anemometer is mounted is located approximately five hundred metres from the observation tower upon which the DCR and auxiliary instruments were placed. The Battery point site has the majority of its instruments mounted at 50.5 metres elevation, with anemometers mounted on a pole 20 metres above the other instruments.

Each ‘average’ wind speed measurement is the mean of the instantaneous wind speed over half an hour – the sampling rate used for the instantaneous measurements was one sample per second. The average wind speed at the start and end times for each night are presented in

Table 7.7 below. The half-hourly measurements throughout the course of each night are shown on a per-night basis in sections to follow.

Date	Average wind speed at start time (knots)	Average wind speed at end time (knots)	Mean of the average wind speed for full measurement set (knots)
01/05/02	5	5	4.0
10/05/02	5	8	6.4
13/05/02	5	5	6.5
14/05/02	6	3	3.4
18/06/02	6	8	7.1
29/06/02	2.1	2.4	2.3
30/07/02	1.8	5.4	3.8

Table 7.7. Average wind speed for the airport and roof sites, supplied by the Bureau of Meteorology’s Hobart Airport observation station and Battery Point meteorological station.

7.9 Maximum wind speed

Together with the half-hourly mean wind speed, the Bureau of Meteorology also provided the half-hourly maximum wind speed. These maxima were the maximum value contributing to the mean wind speed. As mentioned in the previous section, the frequency of the instantaneous wind speed sampling was one sample per second. The maximum wind speed at the start and end time as well as the mean of these maxima is presented for each night in Table 7.8 below.

Date	Maximum wind speed at start time (knots)	Maximum wind speed at end time (knots)	Mean of the maximum wind speed for full measurement set (knots)
01/05/02	7	8	6.0
10/05/02	6	12	9.7
13/05/02	7	7	8.7
14/05/02	8	7	5.2
18/06/02	9	13	9.8
29/06/02	4.1	4.1	4.0
30/07/02	3.6	8.7	6.0

Table 7.8. Half-hourly maximum wind speed for the airport and roof sites, supplied by the Bureau of Meteorology’s Hobart Airport observation station and Battery Point meteorological station.

7.10 Wind direction

The Bureau of Meteorology also supplied half-hourly measurements of mean wind direction at the airport site. The mean wind direction at the start and end time as well as the mean of the half-hourly directions is presented for each night in Table 7.9 below.

Date	Mean wind direction at start time (°)	Mean wind direction at end time (°)	Mean of the mean wind direction for full measurement set (°)
01/05/02	140	330	308
10/05/02	330	330	325
13/05/02	290	320	315
14/05/02	140	310	300
18/06/02	320	330	315

Table 7.9. Half-hourly mean wind direction for the airport site, supplied by the Bureau of Meteorology’s Hobart Airport observation station.

7.11 Cloud amount

The Bureau of Meteorology supplied half-hourly estimates of cloud cover and dominant cloud type for each measurement night at the airport site. Three-hourly cloud cover information was available for the roof site. Table 7.10 below shows the cloud cover at the start and end times for each night, as well as the mean of the cloud cover between these times.

Date	Cloud coverage at start time (octas)	Cloud coverage at end time (octas)	Mean of the cloud coverage for full measurement set (octas)
01/05/02	1	0	0.12
10/05/02	0	1	0.77
13/05/02	0	6	0.79
14/05/02	1	1	1.3
18/06/02	6	4	2.8
29/06/02	3	3	2.3
30/07/02	0	2	0.4

Table 7.10. Half-hourly cloud coverage for the airport site, supplied by the Bureau of Meteorology’s Hobart Airport observation station. Three-hourly cloud coverage for the roof site was measured at the Battery Point meteorological station.

Charts of the cloud coverage for each night are shown on a per-night basis in sections to follow.

7.12 Nightly data for the 1st of May 2002

This section contains charts of the data described in the preceding sections, as well as brief additional data and analysis. The Mean Sea-Level Pressure (MSLP) chart at 22:00 is shown in Figure 7.1a below and an infrared satellite image made at 21:30 is shown in Figure 7.1b.

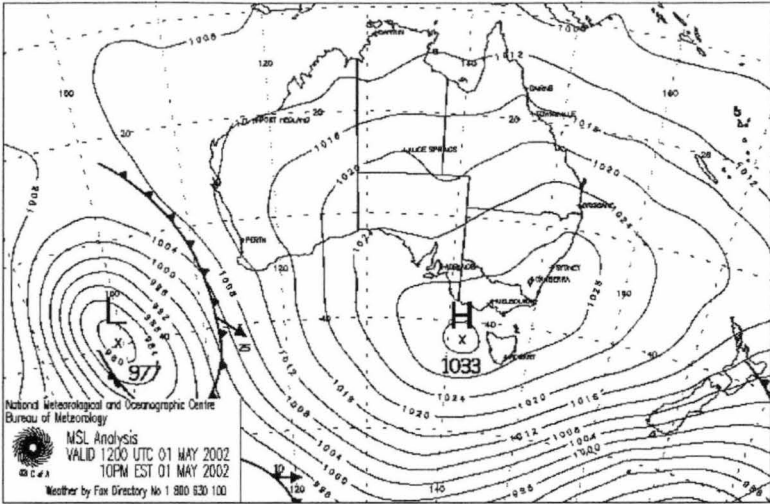


Figure 7.1a. MSLP chart, 22:00, 1st of May.

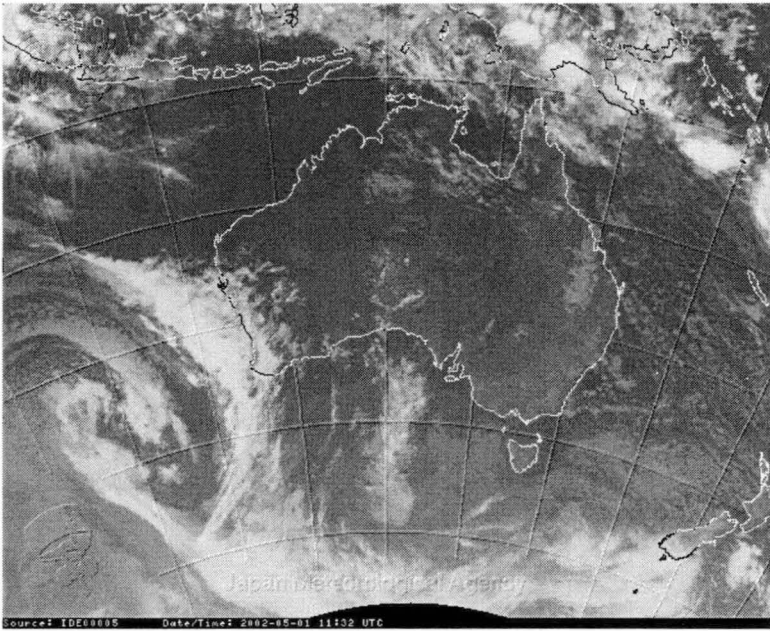
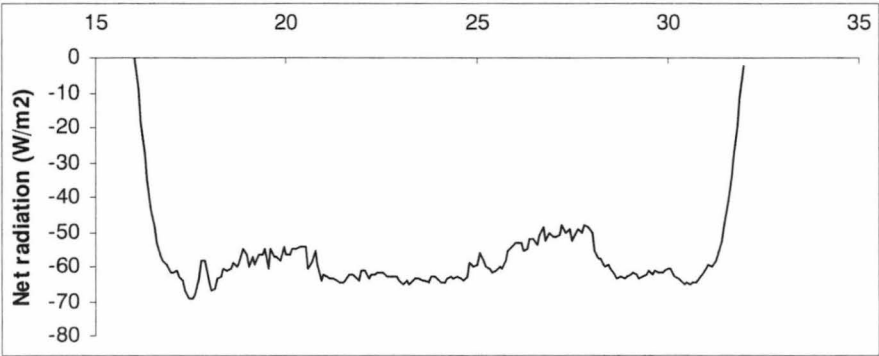
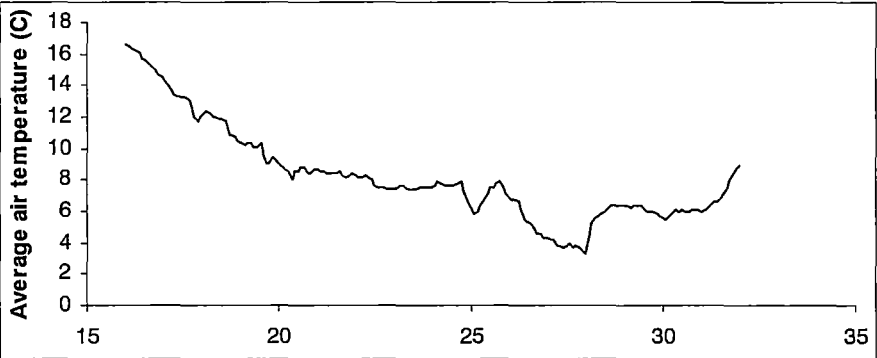
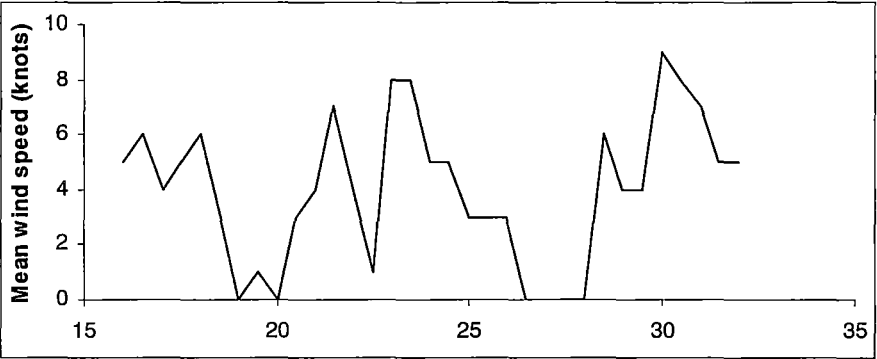
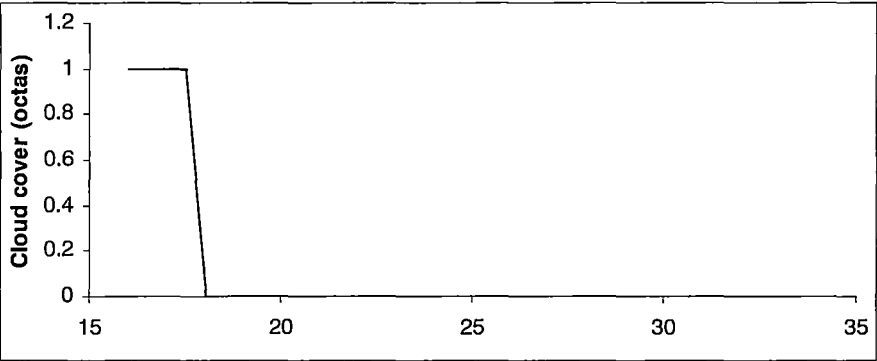
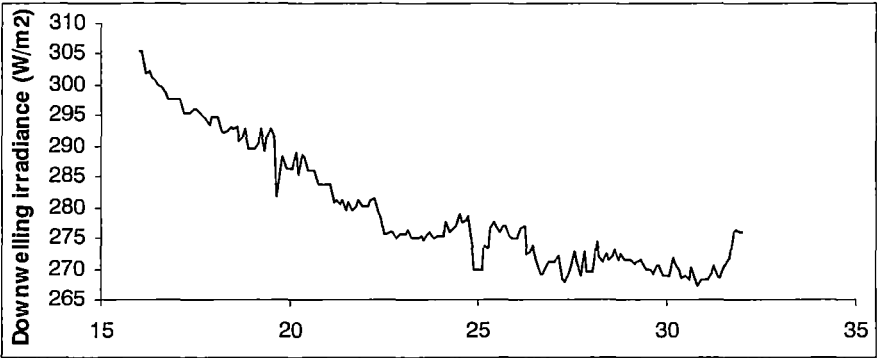
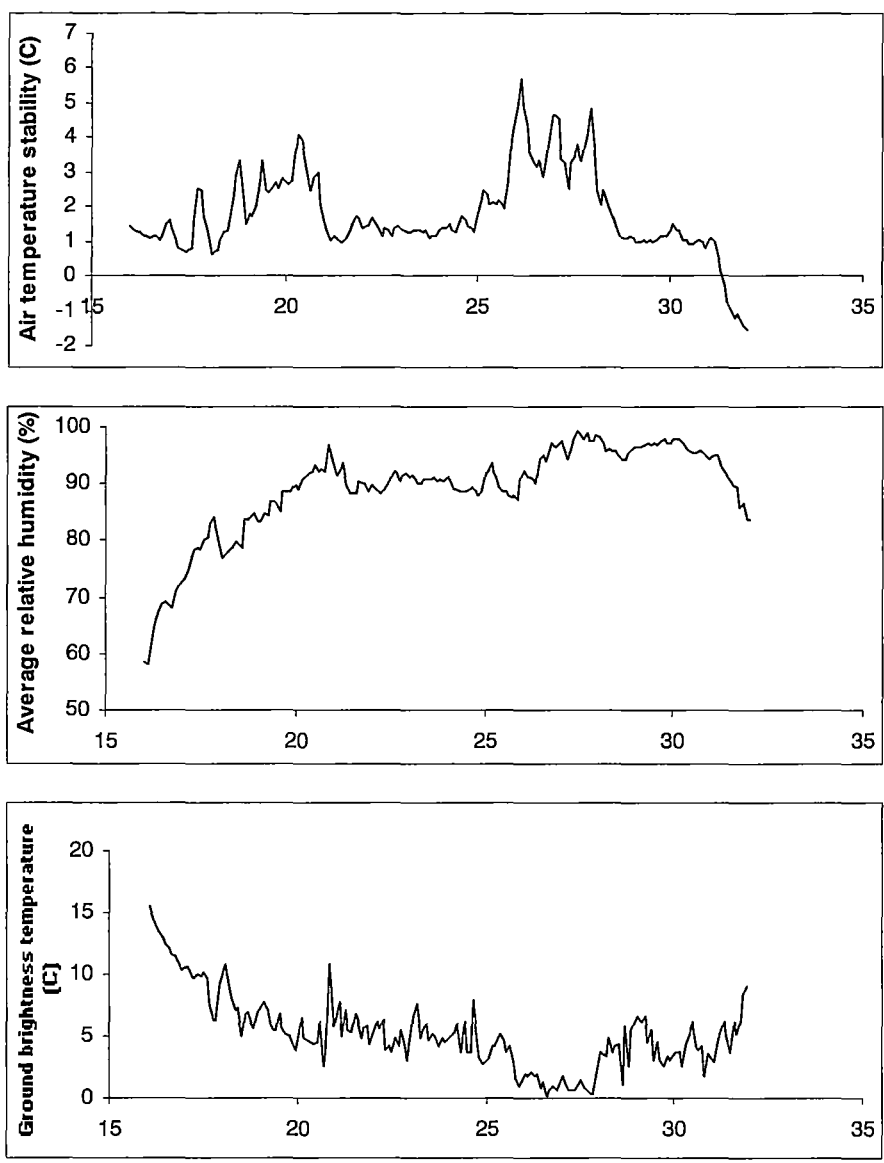


Figure 7.1b. Infrared satellite image, 21:30, 1st of May.







Figures 7.1c – 7.1j. Each chart shows the trend in the indicated quantity with time, expressed as hours after 0:00 on the 1st of May.

The Mean Sea Level Pressure (MSLP) chart showed a high-pressure system to the West of Tasmania at 22:00 on the 1st of May, also slightly north of Hobart. The high-pressure zone moved only slightly north-east during the twelve hours to 10:00 on the 2nd of May. The satellite image shows very clear skies over Tasmania, with only a very small amount of light cloud to the southeast and no cloud over Hobart, also evidenced in the plot of cloud amount. There was little change in the cloud patterns overnight.

The net radiation remained essentially flat during the night at approximately -60 W/m^2 . Two periods of slightly elevated net radiation (approximately $5 - 10 \text{ W/m}^2$ increase between 18:00 and 21:00, 25:00 and 28:00) were coincident with similar increases in the

downwelling irradiance, which otherwise followed a smooth downward trend throughout the night. The wind speed was consistently low during the night, although periods of lowest wind speed corresponded to the increases in net radiation and downwelling irradiance mentioned above.

The average air temperature showed steady cooling between 16:00 and 20:00, followed by a period of essentially constant temperature until 26:00, followed by strong cooling between 26:00 and 28:00. The average air temperature began to increase after 28:00. These periods of cooling are matched in time by periods of relatively high air temperature stability index, which indicated the existence of a relatively strong temperature inversion at those times. The average relative humidity showed a tendency to increase during periods of cooling and remained flat during periods of stable or increasing air temperature. The ground brightness temperature followed the trends evident in the average air temperature.

7.13 Nightly data for the 10th of May 2002

This section contains charts of the data described in the preceding sections, as well as brief additional data and analysis. The Mean Sea-Level Pressure (MSLP) chart at 22:00 is shown in Figure 7.2a below and an infrared satellite image made at 20:25 is shown in Figure 7.2b.

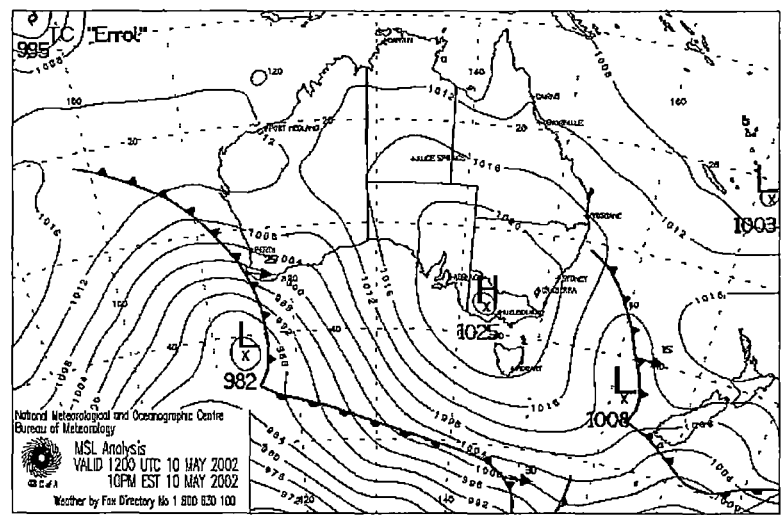


Figure 7.2a. MSLP chart, 22:00, 10th of May.

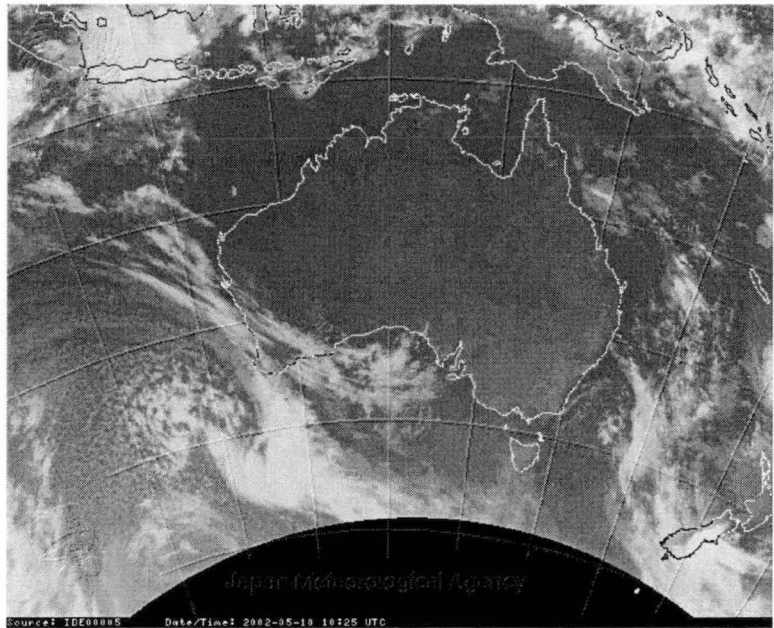
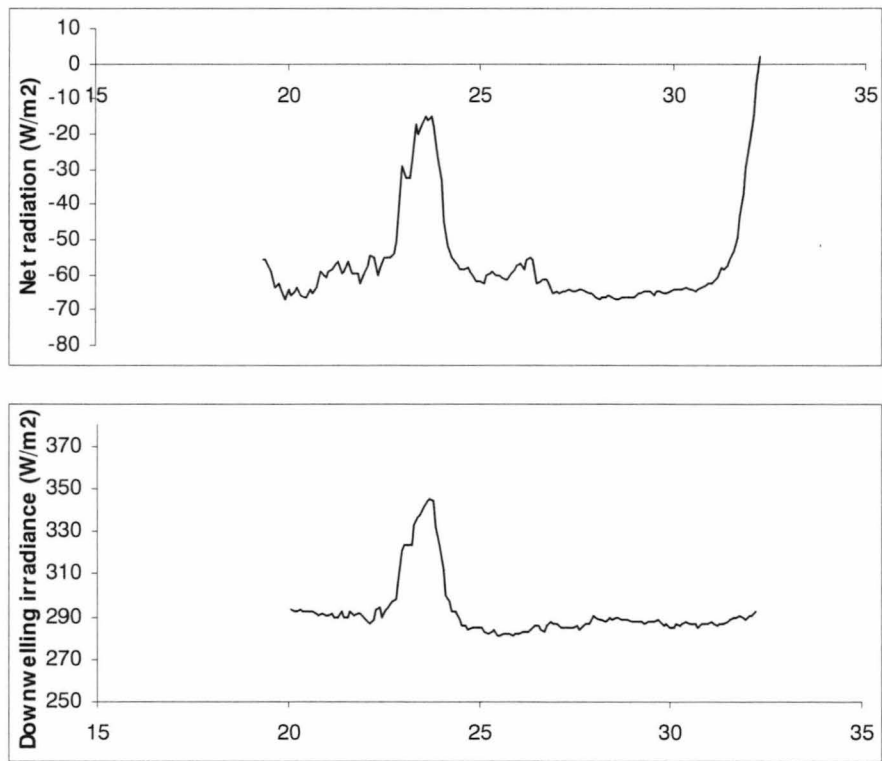
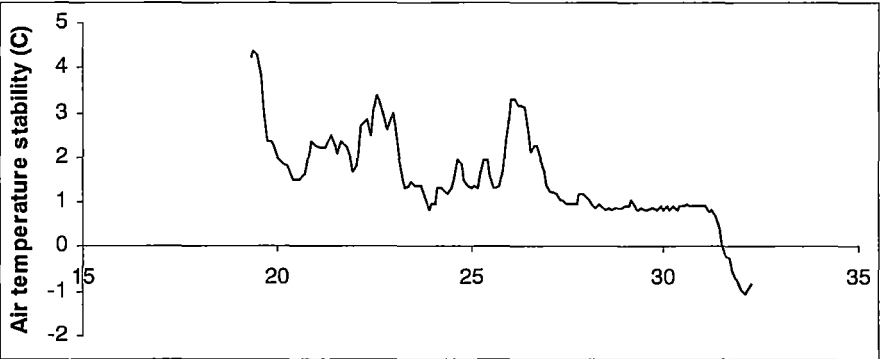
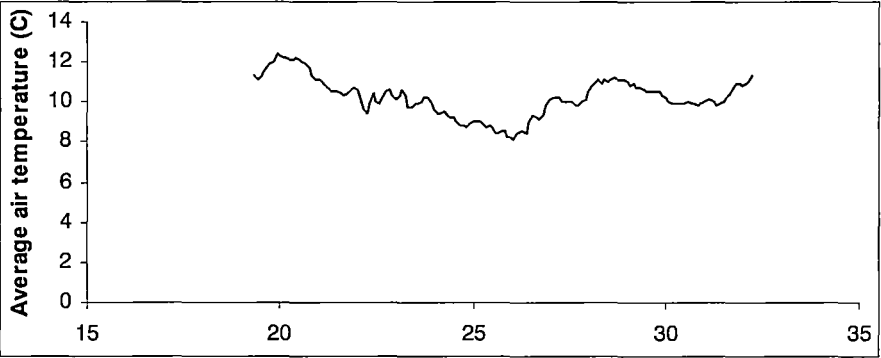
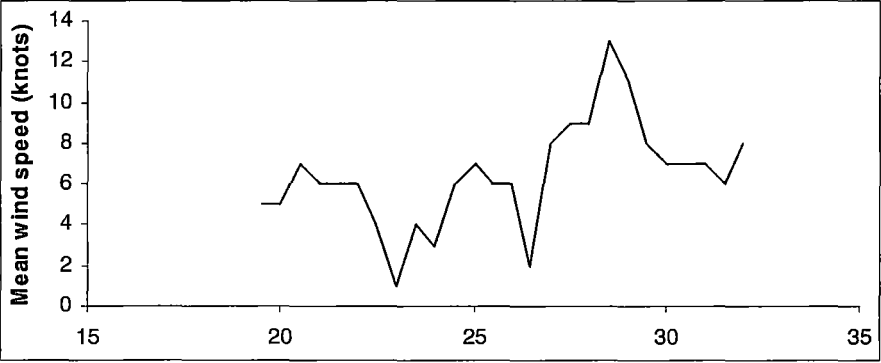
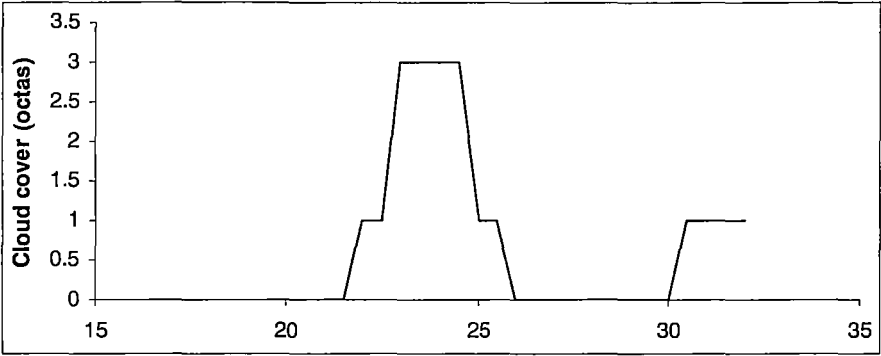
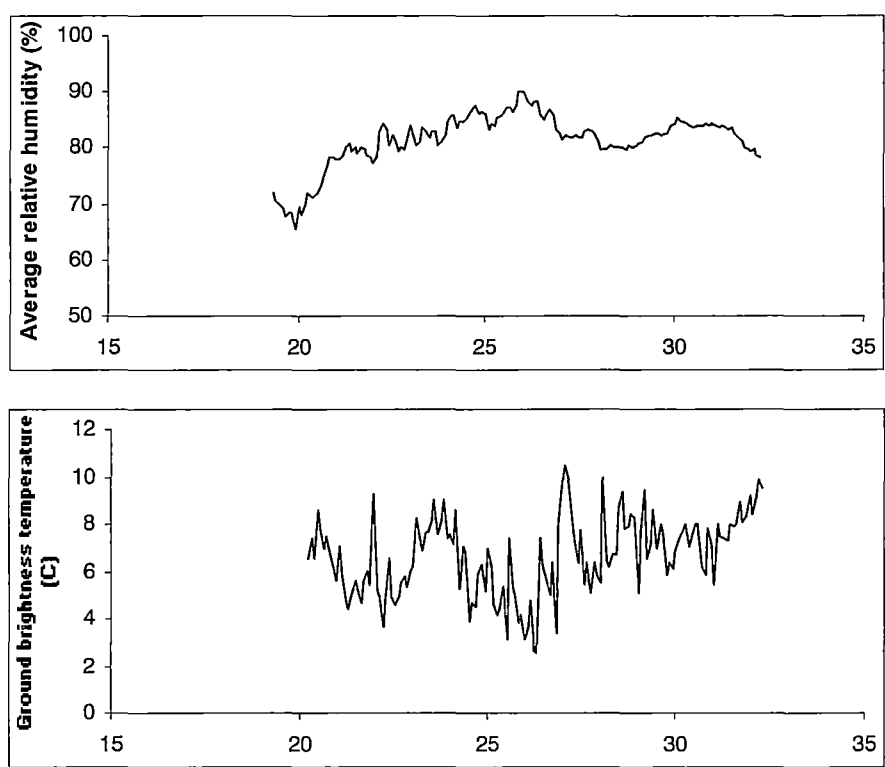


Figure 7.2b. Infrared satellite image, 20:25, 10th of May.







Figures 7.2c – 7.2j. Each chart shows the trend in the indicated quantity with time, expressed as hours after 0:00 on the 10th of May.

The MSLP chart shows a moderate (1025 hPa) high-pressure system centred over western Victoria, north-northwest of Hobart at 22:00. The centre of the system moved directly east overnight and was directly north of Hobart at 10:00 a.m the next day. The satellite image shows a cloud band cloud extending north towards Tasmania at 20:25, which passed to the east during the night. The passage of this cloud band is evident in the chart of cloud cover, which shows cloud coverage increasing to three octas between 21:30 and 23:00, the decreasing back to zero between 24:30 and 26:00. The cloud began to increase again just before dawn.

The net radiation chart displays the expected behaviour, with a large peak of approximate magnitude 45 W/m² developing and subsiding during the period between 22:30 and 25:00. The downwelling irradiance mirrors this peak as expected. The wind speed was essentially stable at approximately 6 knots between 19:30 and 22:00, dropping to a minimum at 23:00. A local maximum at 25:00 was followed by a further minimum at 26:30, the cloud coverage then increasing as dawn approached.

The average air temperature was very stable during the night, with a very slight downward trend between 19:00 and 26:00 followed by an upward trend after 26:00. The air temperature

stability index was relatively low throughout the night, although it reached and then maintained a minimum value after 26:00. The relative humidity increased slowly from 22:00 to 26:00 and was either stable or slightly increasing thereafter. Any trends in the ground brightness temperature were almost completely swamped by short-term variations, although a slight downward trend appears to become a slight upward trend at 26:00.

7.14 Nightly data for the 13th of May 2002

This section contains charts of the data described in the preceding sections, as well as brief additional data and analysis. The Mean Sea-Level Pressure (MSLP) chart at 22:00 is shown in Figure 7.3a below and an infrared satellite image made at 21:30 is shown in Figure 7.3b.

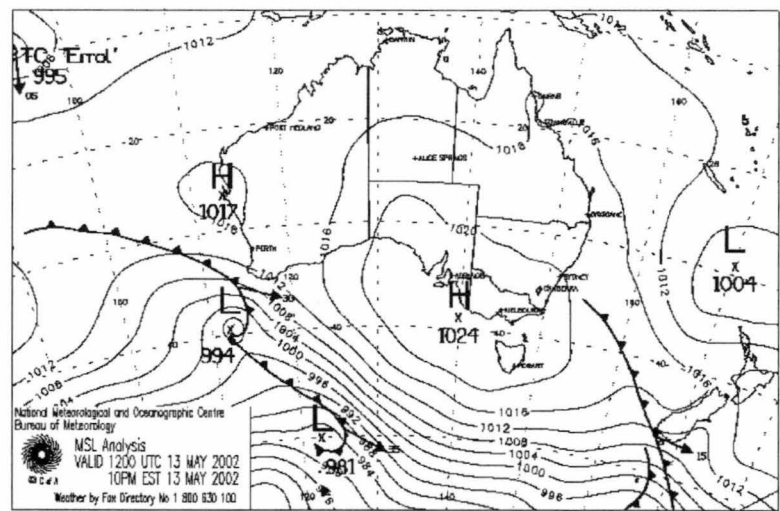


Figure 7.3a. MSLP chart, 22:00, 13th of May.

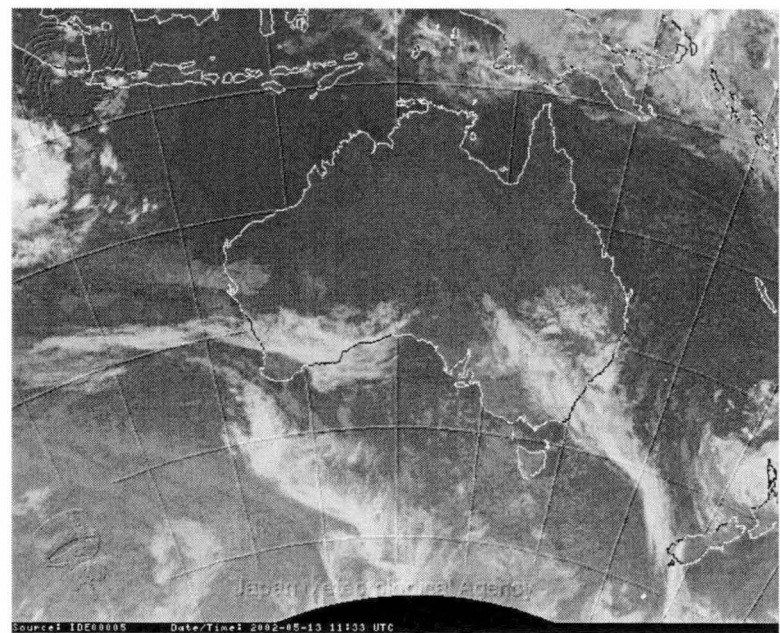
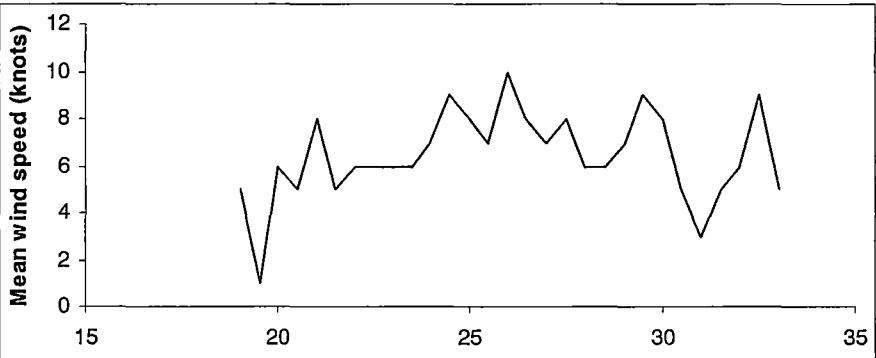
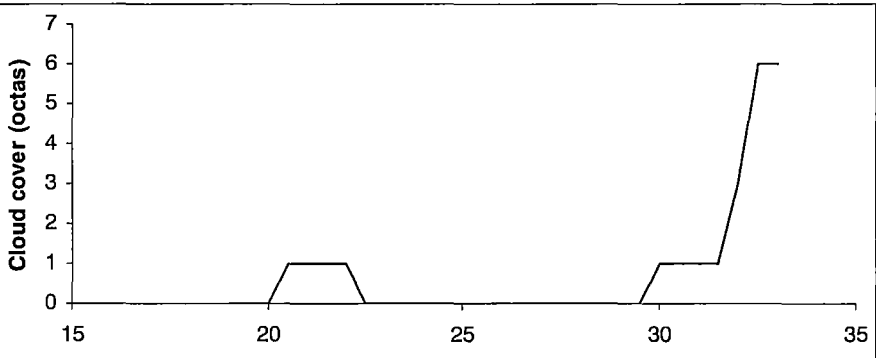
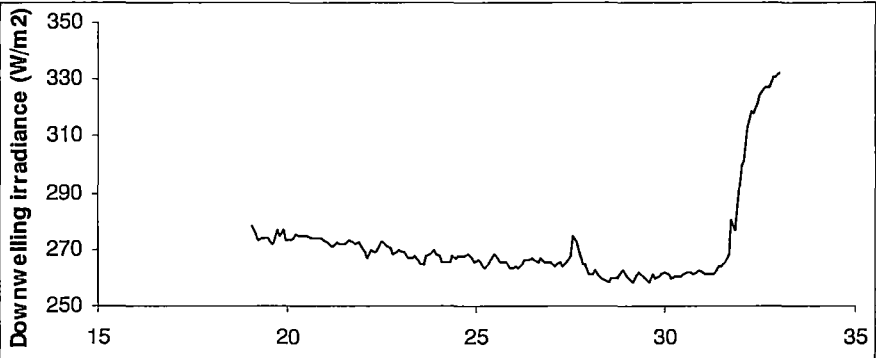
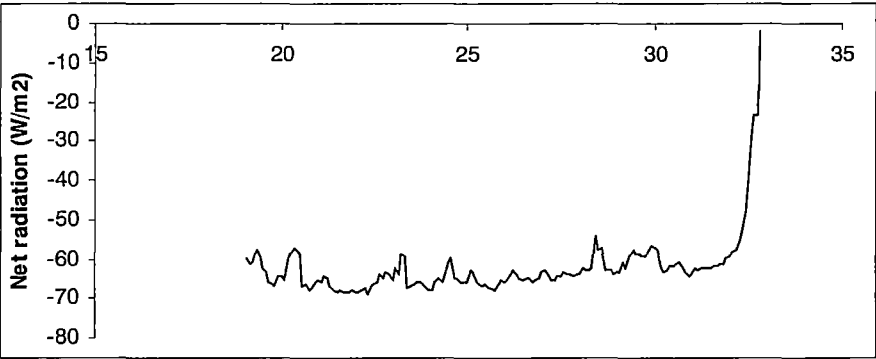
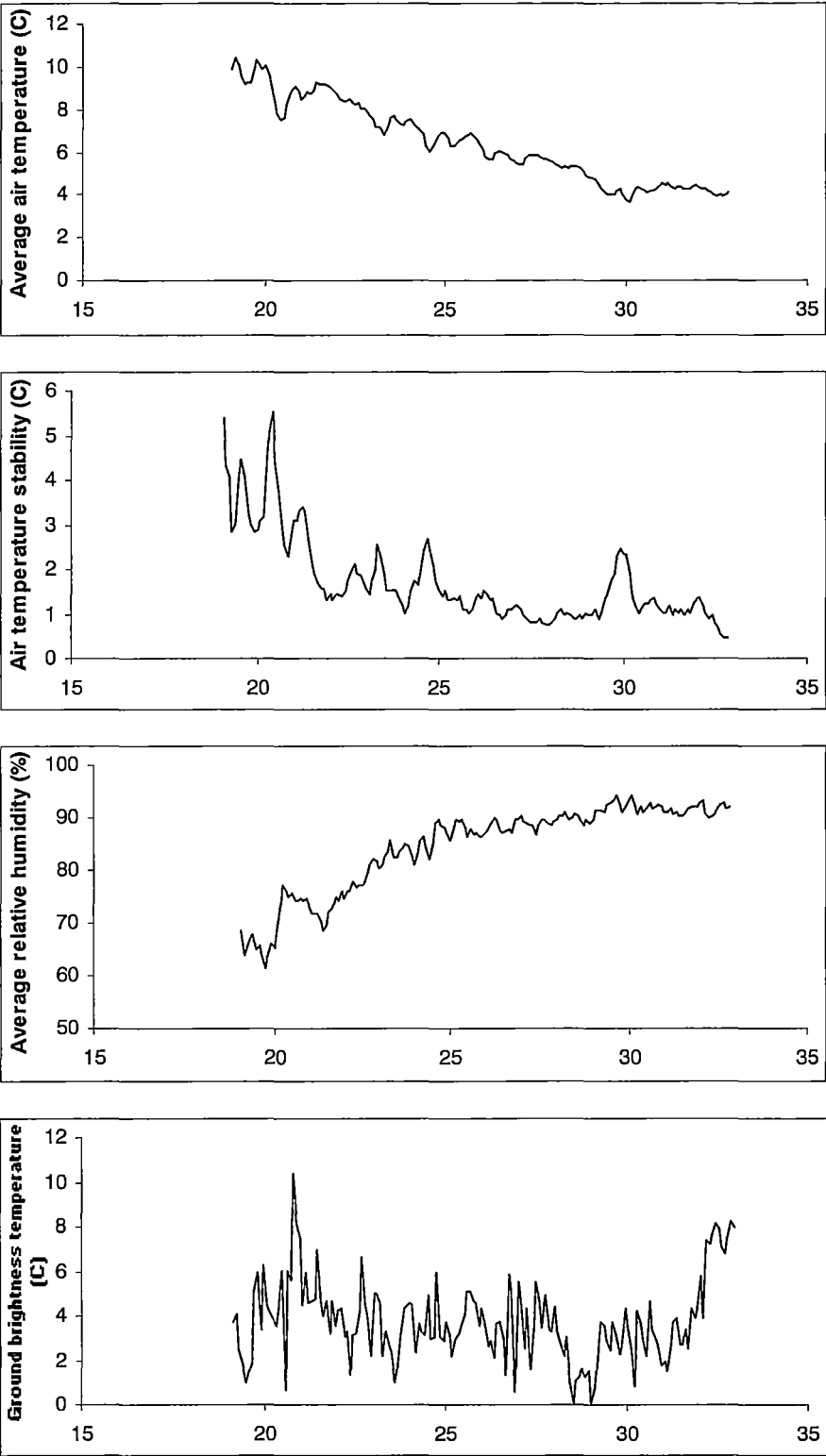


Figure 7.3b. Infrared satellite image, 21:30, 13th of May.





Figures 7.3c – 7.3j. Each chart shows the trend in the indicated quantity with time, expressed as hours after 0:00 on the 13th of May.

The MSLP chart shows a moderate (1024 hPa) high-pressure system northwest of Hobart and directly south of Adelaide at 22:00. This system moved east during the night, bringing

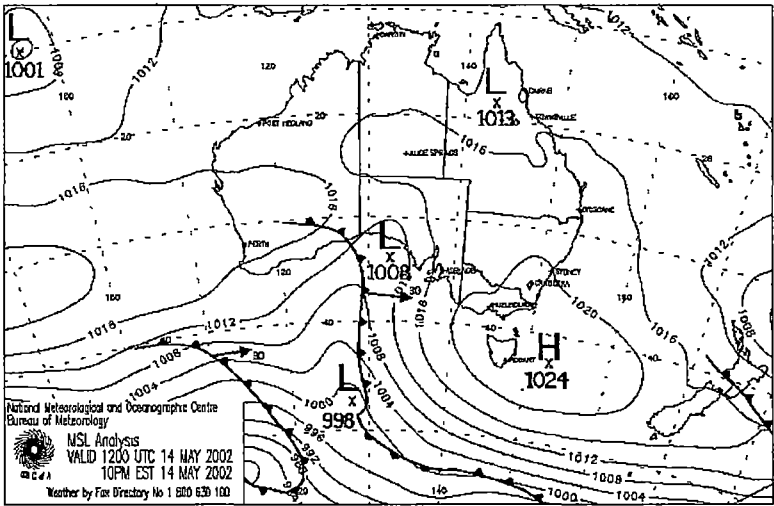
rain to Victoria. It then moved south and was centred directly above Hobart at 10 a.m the next day. The satellite image shows scattered high cloud to the west and south of Hobart at 21:30, although the locally clear sky remained throughout the night. This is reflected in the chart of cloud coverage, which has a small peak between 20:30 and 22:00 but otherwise indicates clear skies until 29:30.

The net radiation was essentially constant at approximately -60 W/m^2 throughout the night. The downwelling longwave irradiance displayed a very slight decrease (from approximately 275 W/m^2 to approximately 260 W/m^2 throughout the night. The mean wind speed remained consistent at approximately 6 to 7 knots over the measured period.

The average air temperature cooled smoothly from approximately 10°C at 20:00 to approximately 4°C at 30:00. The air temperature stability index was relatively high for the first hours of the night, dropping after 22:00 and staying relatively low (1 to 2°C) for the remainder of the night. The relative humidity increased throughout the night, rapidly at first and then more slowly after 25:00. The ground brightness temperature fluctuated between approximately 3 and 4°C for the majority of the night. There was a brief minimum at 29:00 before it increased again.

7.15 Nightly data for the 14th of May 2002

This section contains charts of the data described in the preceding sections, as well as brief additional data and analysis. The Mean Sea-Level Pressure (MSLP) chart at 22:00 is shown in Figure 7.4a below and an infrared satellite image made at 21:30 is shown in Figure 7.4b.



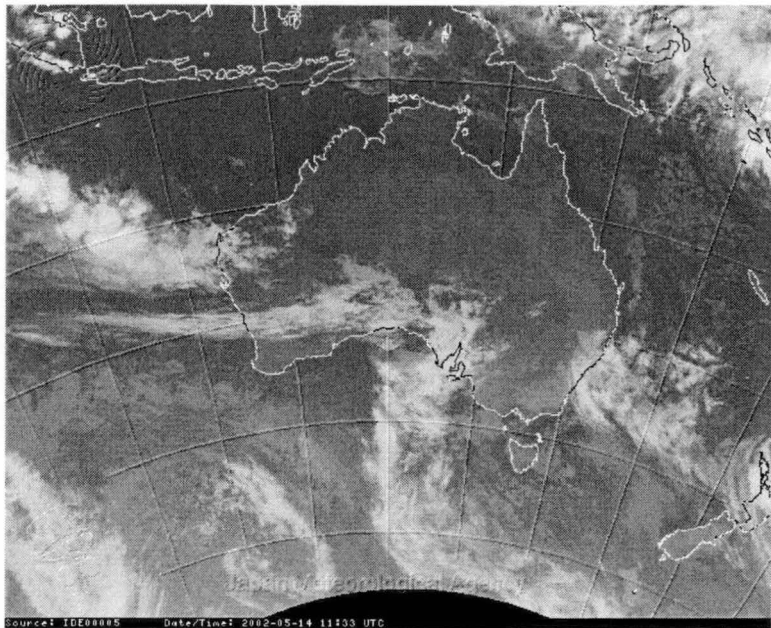
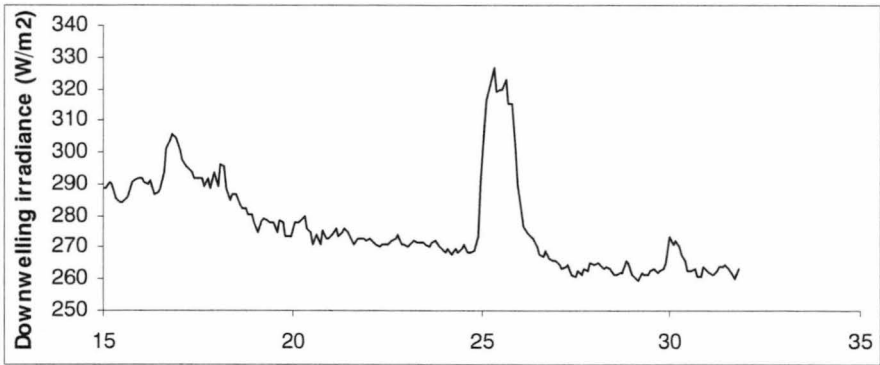
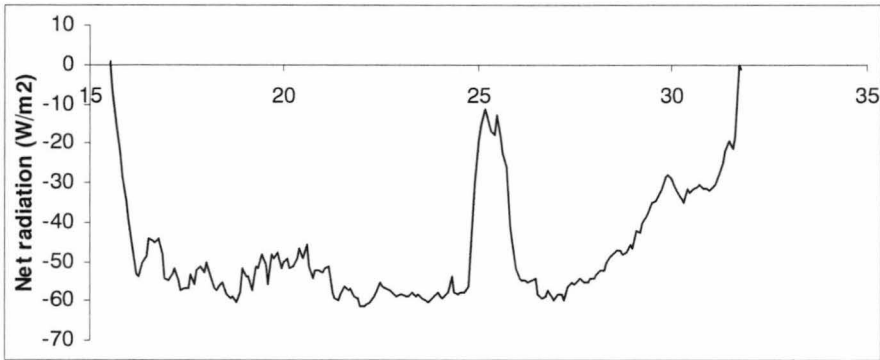
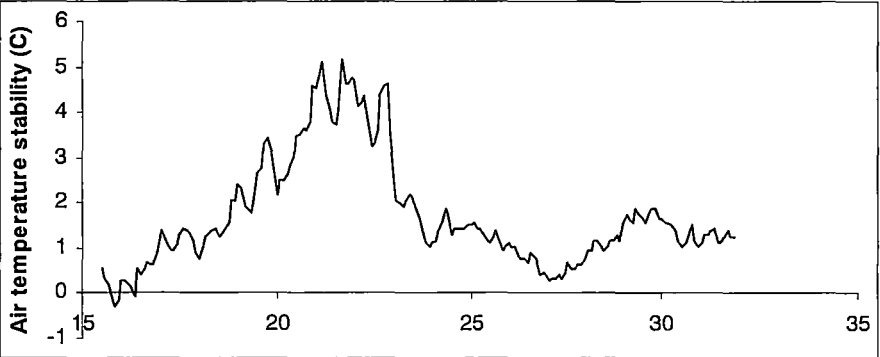
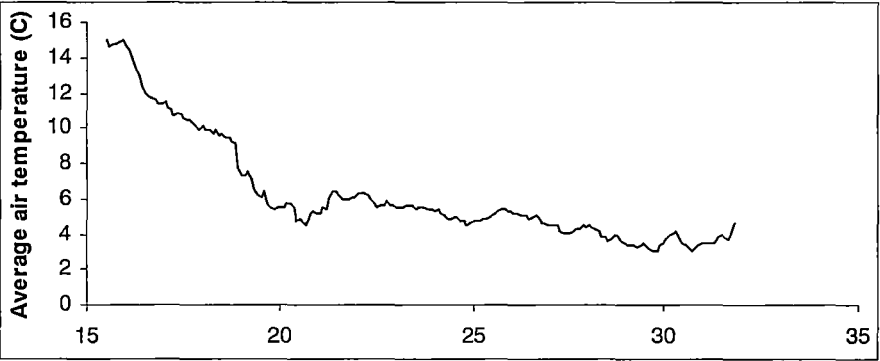
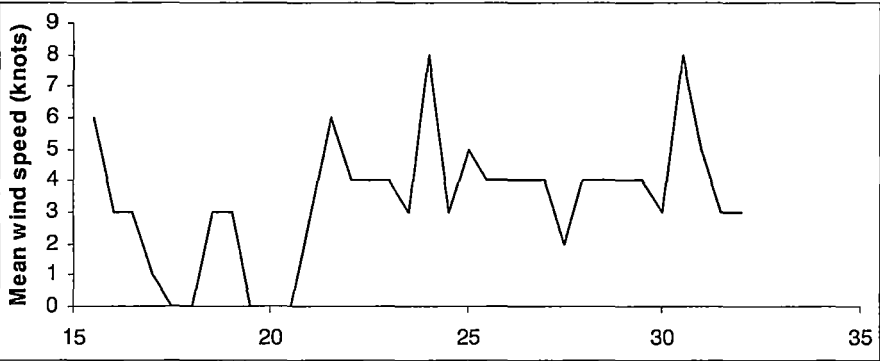
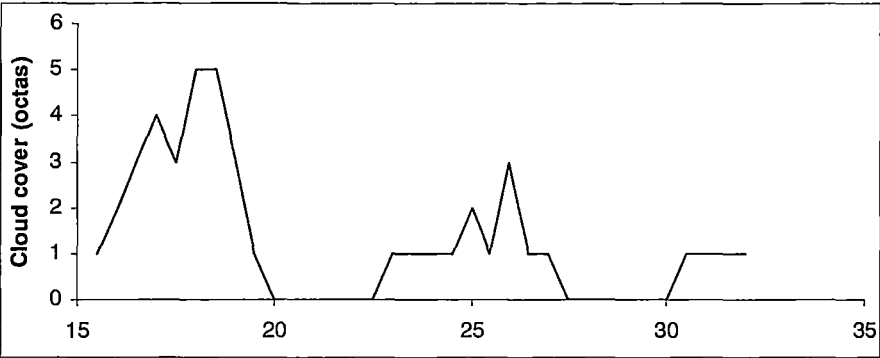
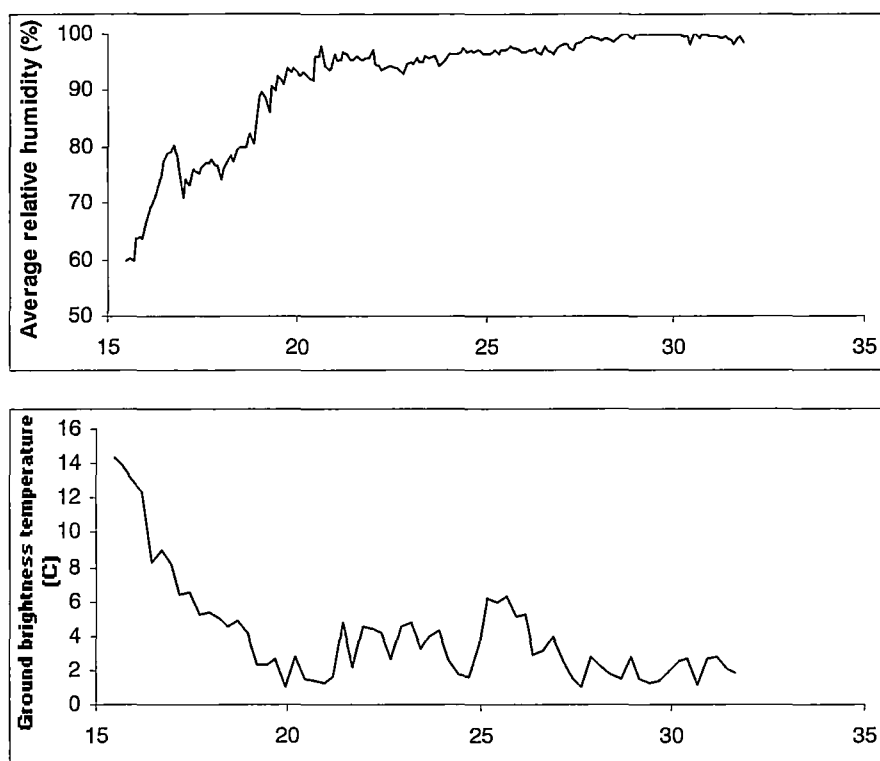


Figure 7.4b. Infrared satellite image, 21:30, 14th of May.







Figures 7.4c – 7.4j. Each chart shows the trend in the indicated quantity with time, expressed as hours after 0:00 on the 14th of May.

The MSLP chart shows a moderate (1024 hPa) high-pressure system directly east of Hobart at 22:00 and an advancing cold front to the west. There was minimal eastward movement by both features during the night. The satellite image shows scattered light cloud over Tasmania in general, although locally clear over Hobart at 21:30. The cloud coverage chart shows significant cloud cover before 20:00, clearing thereafter until 22:30. There was light cloud coverage (up to 3 octas) between 22:30 and 27:30, after which the sky remained clear until 30:00.

The early (pre-20:00) cloud has little visible effect on the net radiation, while the cloud during the night caused an obvious peak. This peak was reflected in the downwelling longwave irradiance, which also showed evidence of the effect of cloud cover early in the evening. Winds were very light in the early part of the night, strengthening to approximately 4 knots at 20:30 and remaining at approximately 4 knots thereafter, with some short-term maxima up to 8 knots.

The air temperature dropped quickly between 16:00 and 20:00, followed by a period of slow but steady cooling. A high air temperature stability index existed during the period of rapid cooling, but dropped to approximately one to two °C after 23:00 and remained low for the

remainder of the night. The relative humidity increased rapidly between 16:00 and 20:00, and continued to increase less rapidly thereafter with saturation occurring just before dawn. The ground brightness temperature dropped rapidly between 16:00 and 20:00. It remained essentially stable thereafter, with some short-term fluctuations.

7.16 Nightly data for the 18th of June 2002

This section contains charts of the data described in the preceding sections, as well as brief additional data and analysis. The Mean Sea-Level Pressure (MSLP) chart at 22:00 is shown in Figure 7.5a below and an infrared satellite image made at 21:30 is shown in Figure 7.5b.

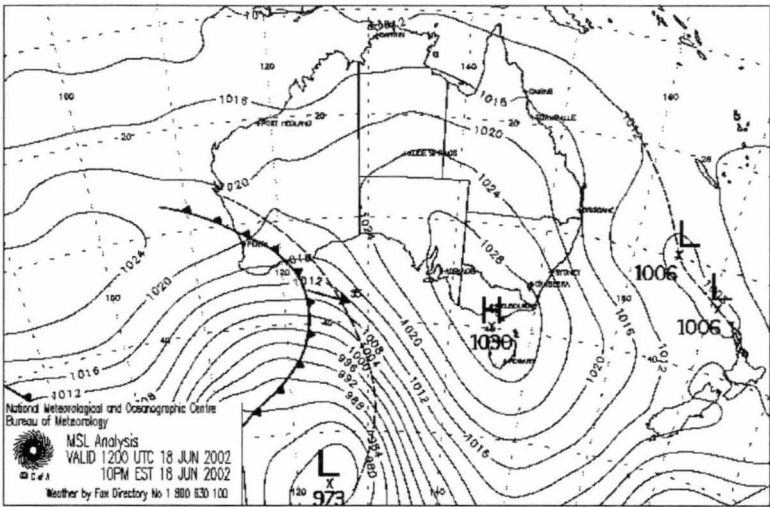


Figure 7.5a. MSLP chart, 22:00, 18th of June.

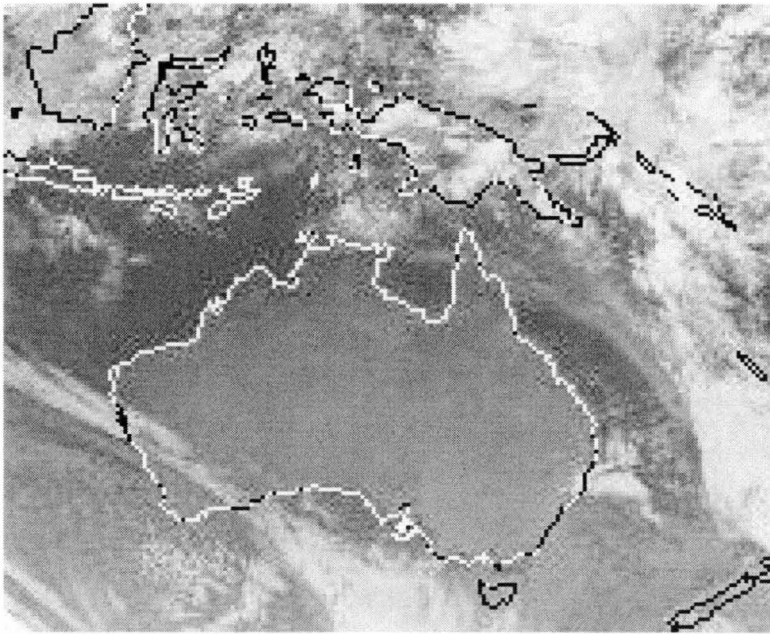
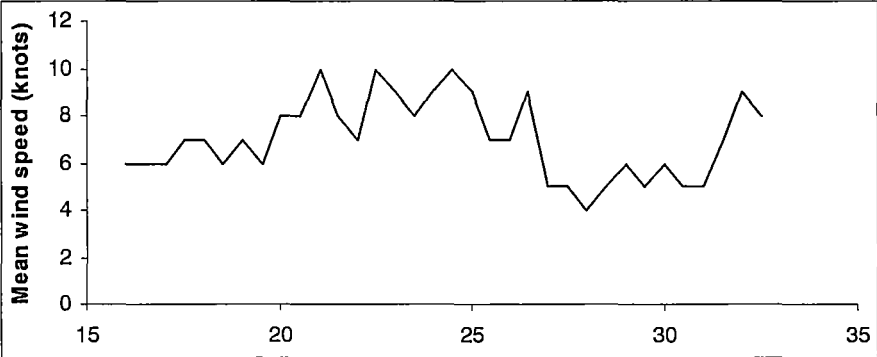
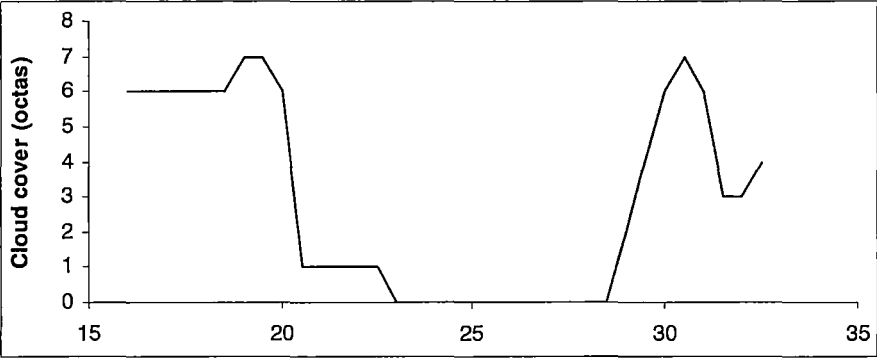
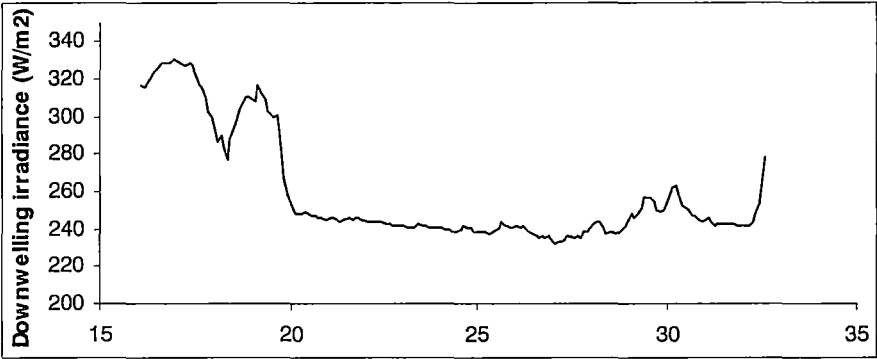
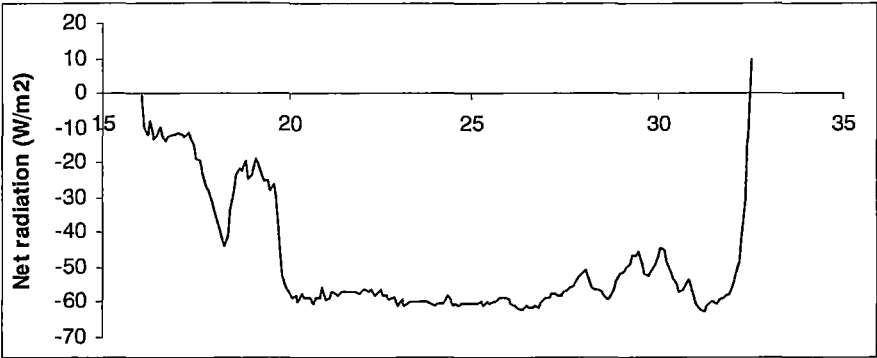
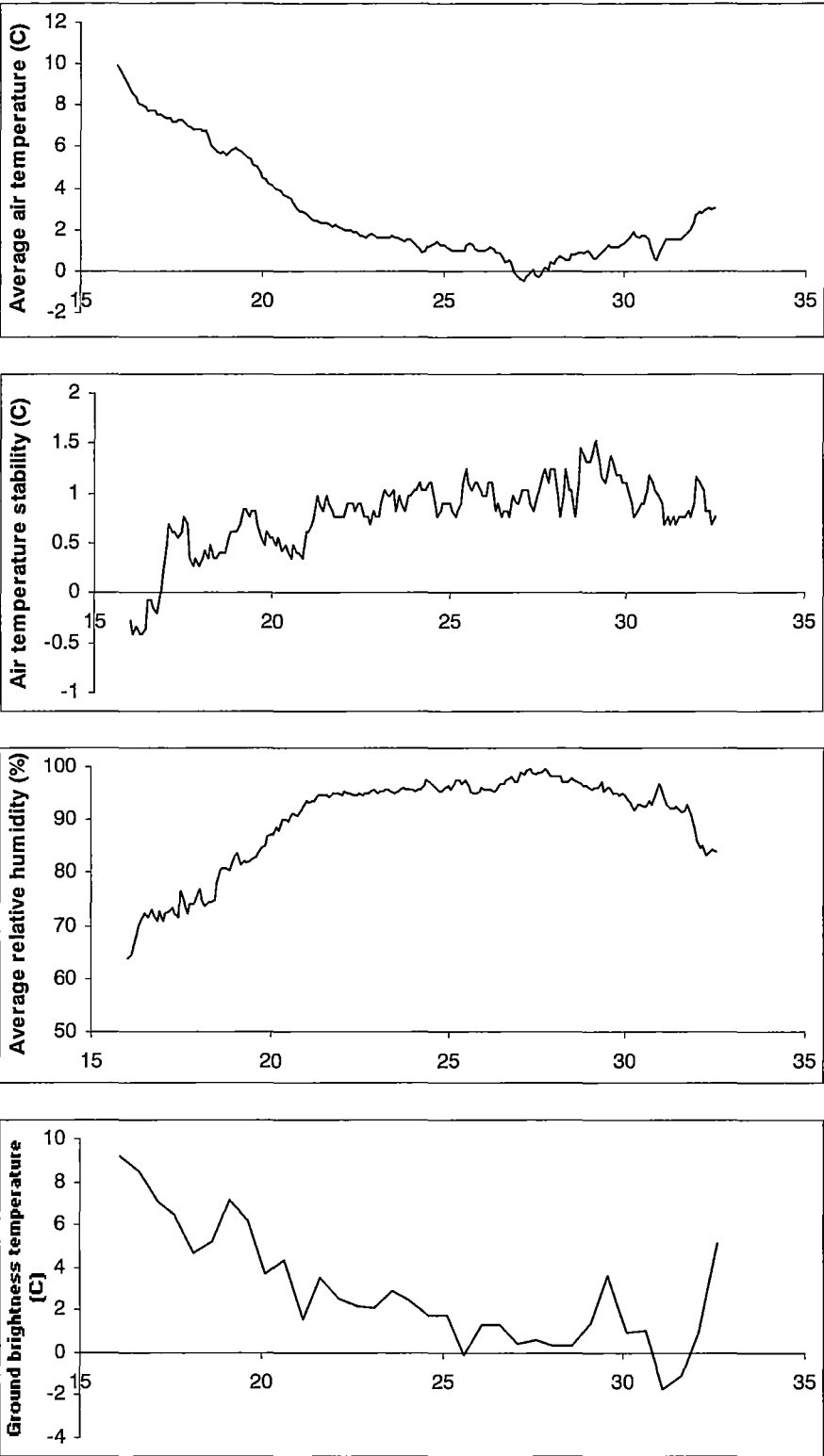


Figure 7.5b. Infrared satellite image, 21:00, 18th of June.





Figures 7.5c – 7.5j. Each chart shows the trend in the indicated quantity with time, expressed as hours after 0:00 on the 18th of June.

The MSLP chart shows a strong (1030 hPa) high-pressure system centred over Bass Strait, north-northwest of Hobart at 22:00. It moved towards the northeast during the night,

bringing rain to much of mainland Australia's southeast coast. The satellite image shows a cloud band to the west of Tasmania, associated with an approaching cold front. There was also extensive cloud to the south and scattered cloud to the west of Hobart. The chart of cloud coverage shows extensive cloud coverage (6 to 7 octas), dropping to one octa at 20:30 and then to clear sky at 23:00. Clear sky conditions remained until extensive cloud cover developed again after 28:30. This pattern was consistent with eastward passage of the cloud bands observed in the satellite image.

The early cloud cover significantly impacted both net radiation and downwelling longwave irradiance. The re-emergence of cloud as the morning approached had a visible but less dramatic effect. The wind speed remained consistently between five and ten knots, with some short-term fluctuations within that range.

The average air temperature dropped smoothly and steadily between 16:00 and 24:00 and remained essentially constant thereafter. The air temperature stability index rose slightly from negative at 16:00, but never exceeded 1.5 °C. The relative humidity increased rapidly between 16:00 and 22:00 and changed little after 22:00. The ground brightness temperature showed a general decreasing trend between 16:00 and 25:00, and remained essentially constant thereafter.

7.17 Nightly data for the 29th of June 2002

This section contains charts of the data described in the preceding sections, as well as brief additional data and analysis. The Mean Sea-Level Pressure (MSLP) chart at 22:00 is shown in Figure 7.6a below and an infrared satellite image made at 21:30 is shown in Figure 7.6b.

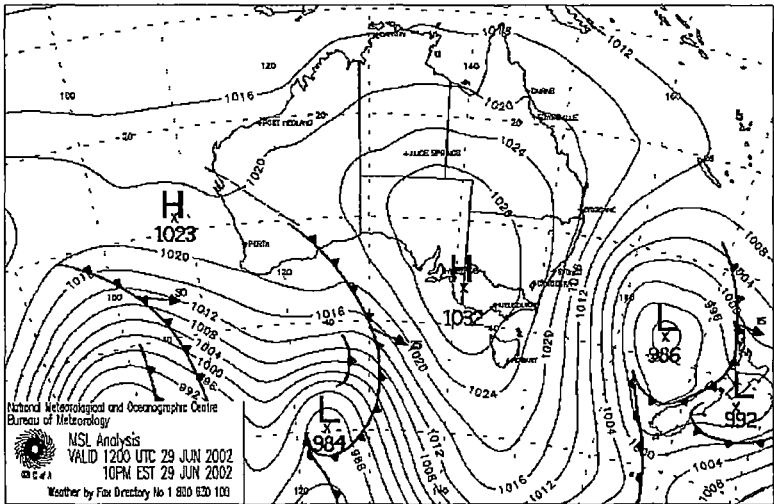


Figure 7.6a. MSLP chart, 22:00, 29th of June.

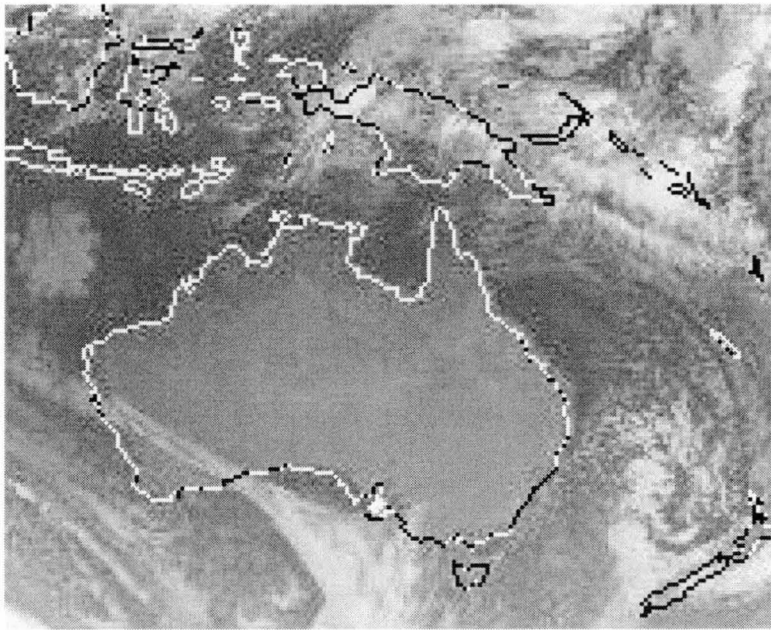
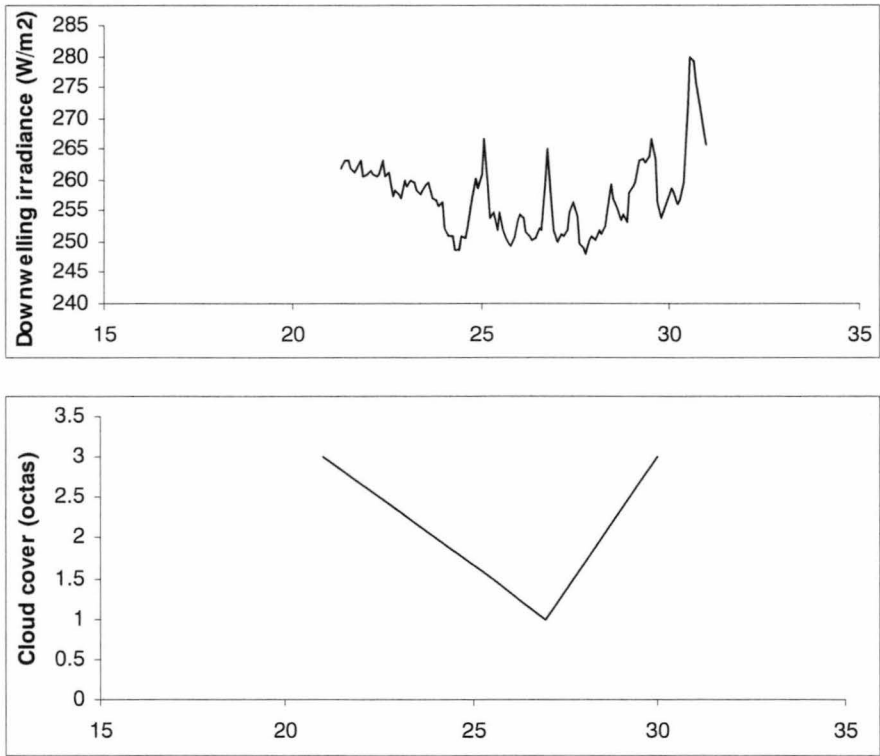
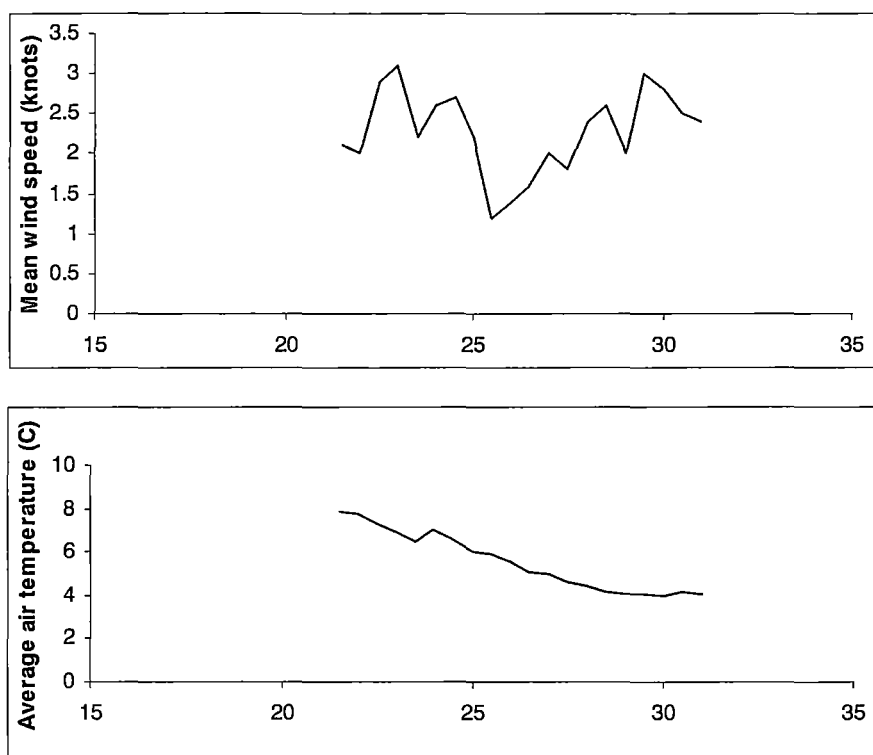


Figure 7.6b. Infrared satellite image, 21:00, 29th of June.





Figures 7.6c – 7.6f. Each chart shows the trend in the indicated quantity with time, expressed as hours after 0:00 on the 29th of June.

The MSLP chart shows a strong (1032 hPa) high-pressure system to the northwest of Tasmania, centred over the South Australia – Victoria border. A cold front in the Great Australian Bight was approaching Tasmania from the west. The cold front advanced significantly during the night, pushing the high-pressure system slightly to the east. The satellite image shows the cloud band associated with the approaching front to the west of Tasmania, as well as some extensive cloud coverage to the south. The cloud coverage chart shows cloud decreasing slowly from three to one octa between 21:00 and 27:00, then increasing as dawn approached.

The downwelling longwave irradiance was essentially constant throughout the night, despite large short-term fluctuations. Winds were very light, between one and three knots throughout the night, while the average air temperature decreased gradually but steadily through the night.

Charts for the net radiation, relative humidity, air temperature stability index and ground brightness temperature were not available because measurements were made at the roof site on this date.

7.18 Nightly data for the 30th of July 2002

This section contains charts of the data described in the preceding sections, as well as brief additional data and analysis. The Mean Sea-Level Pressure (MSLP) chart at 22:00 is shown in Figure 7.7a below and an infrared satellite image made at 21:30 is shown in Figure 7.7b.

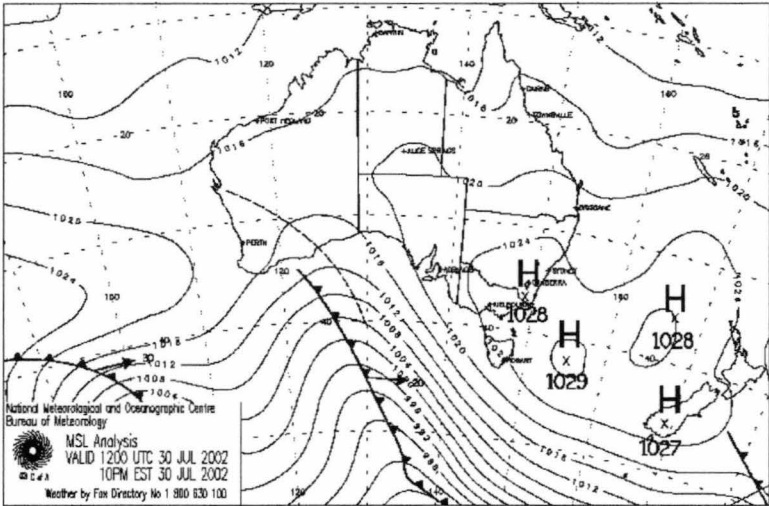


Figure 7.7a. MSLP chart, 22:00, 30th of July.

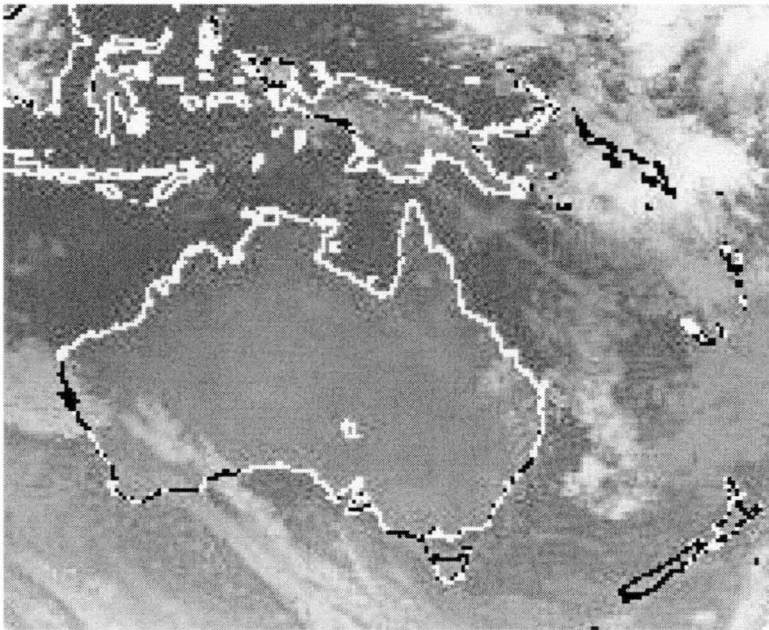
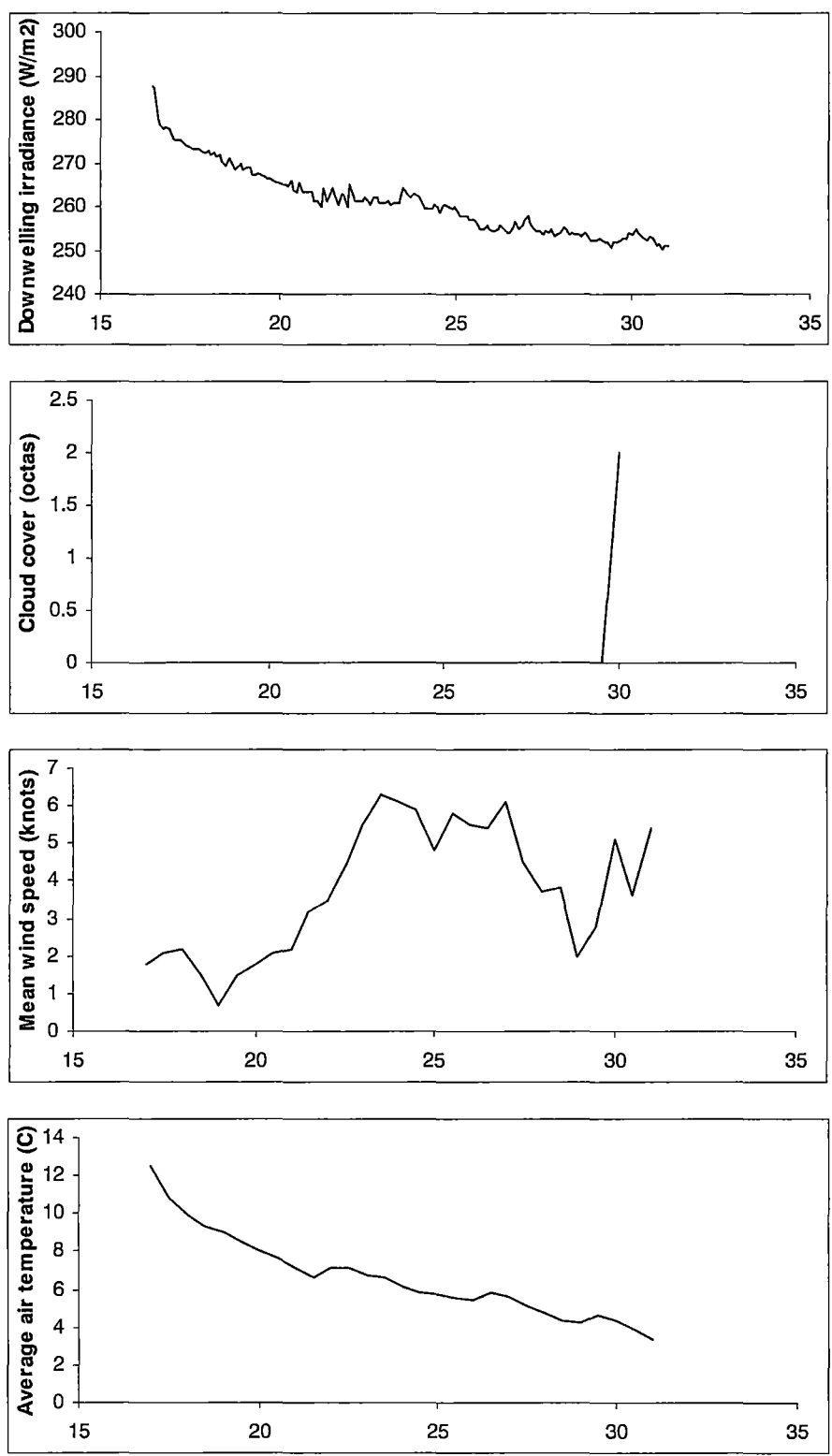


Figure 7.7b. Infrared satellite image, 21:00, 30th of July.



Figures 7.7c – 7.7f. Each chart shows the trend in the indicated quantity with time, expressed as hours after 0:00 on the 30th of July.

The MSLP chart shows a complex high-pressure system to the north and east of Tasmania. A cold front was positioned to the west of Tasmania at 22:00 and advanced rapidly to the east

during the night. The satellite image shows the obvious cloud band associated with the cold front to the west, with clear skies over Tasmania. The cloud coverage chart shows clear-sky conditions until some cloud develops at 29:30.

The downwelling longwave irradiance decreased very smoothly throughout the night, dropping from approximately 280 W/m^2 at 16:00 to approximately 250 W/m^2 at 30:00. The wind speed increased from approximately one knot at 17:00 to approximately six knots at 24:00. The wind speed remained essentially constant between 24:00 and 27:00, decreasing again after that. The air temperature decreased rapidly until 22:00, declining smoothly but less rapidly after that.

Once again, the measurements of net radiation, air temperature stability index, relative humidity and ground brightness temperature were not available as the DCR was employed at the University roof site on the 30th July.

7.19 DCR measurement sequences

DCR brightness temperature measurements were gathered using different measurement regimes for each night. These measurement regimes were summarised briefly in Table 6.1. A variety of measurement regimes were used so that the gathered data sets could be applied to a variety of the available calculation options detailed in Chapter 2. The measurement sequences will be described in further detail here and the justification for the employment of each will be examined in the following Chapter.

Table 7.11 below describes the DCR measurement sequence used for each measurement night at the airport site. The lowest angle of measurement was 165 degrees from the zenith (15 degrees from the nadir) – no measurements were made looking directly downwards. This angle was chosen in order to avoid including the tower in the instrument’s field of view without significantly affecting the data. This was verified in theory by an examination of MODTRAN–derived radiances based on model profiles from all of the five airport measurement nights. The average difference between radiances modeled at 0 and 15 degrees nadir measurement angle, down-looking from ten metres, was less than $0.001 \text{ W/m}^2/\text{steradian}$ in channel one and less than $0.0001 \text{ W/m}^2/\text{steradian}$ in channel two.

	Date				
	01/05/02	10/05/02	13/05/02	14/05/02	18/06/02
Time after the hour (mins)	DCR orientation (degrees from zenith)				
0	0	165	165	165	-
5	165	165	165	150	165
10	165	165	165	135	150
15	165	165	165	165	135
20	165	165	165	150	120
25	165	165	165	135	105
30	165	165	165	165	-
35	165	165	165	150	165
40	165	165	165	135	150
45	165	165	165	165	135
50	165	165	165	150	120
55	165	165	165	135	105

Table 7.11. DCR measurement regimes for each measurement night at the airport site. The measurement regime used at the roof site (29th of June and 30th of July) was a half-hourly cycle consisting of measurements at five-minute intervals at 0, 15, 30, 45, 60 and 75 degrees from the zenith.

MODTRAN results from the analyses presented in Chapter 2 also confirmed the insignificance of the difference between measurements at zero degrees and fifteen degrees nadir angle. For the 192 test cases described in Section 2.7, the percentage differences between radiance values at fifteen and zero degrees nadir angle were 0.005%, 0.02% and 0.0002% for broadband radiance, channel one (active channel) radiance and channel two (window channel) radiance respectively. These differences fall easily within the expected error boundaries for the DCR brightness temperature measurements.

The DCR-measured rightness temperatures therefore provide ground brightness temperatures effectively measured at the vertical for input to all relevant calculations. The angular measurements – those measured away from the vertical - provide angular brightness temperatures that, upon conversion to radiance or radiance divergence, can be integrated over the hemisphere.

The use of angular brightness temperatures eliminates angular emissivity effects as a potential source of error, as the radiances are measured directly. Angular effects are known to cause differences in radiative temperature of up to 5°C (Chehbouni *et al.* 2001), mostly due to angular emissivity variations. These variations have been measured as being up to 8% over a semi-arid sandy soil site (McAtee *et al.* 2003). The direct measurement of the window channel brightness temperature accounts for these variations because the measured brightness temperature is used directly as ground temperature input to the model. This relied on the previously noted assumption – that the emissivity can be considered uniform across the relevant portion of the infrared spectrum.

7.20 MODTRAN profiles for data analysis and results comparison

A useful tool in the examination of the measured results was the MODTRAN radiative transfer model. As noted in Section 6.5, the Bureau of Meteorology supplied nightly radiosonde-gathered profiles of pressure, temperature and relative humidity. These profiles were measured at approximately 21:00 each night, starting at the Bureau’s Hobart Airport observation site at height 22m. These profiles were supplemented with data from the tower-mounted instruments to complete the profile down to ground level.

The Campbell CS500 probes provided temperature and relative humidity data at 0.5, 1.5, 4.5 and 10.0 metres. As mentioned in the previous section, the DCR’s window channel was used to measure the ground brightness temperature for input to the model. The use of a ground brightness temperature circumvented the need to input an accurate ground temperature and emissivity to the model, as discussed in the previous section.

For the data sets gathered on the 1st, 10th and 13th of May, only a single profile was used for MODTRAN input, corresponding to the DCR’s ground temperature measurement and tower profile measured at the time closest to 21:00. For the data sets gathered on the 14th of May and 18th of June, multiple profiles were necessary because multiple DCR measurements were made at different nadir angles. For each of the considered measurements, the same profile was used from 22.0 metres to the top of the atmosphere. However the supplementary tower and DCR ground temperature data used to supplement the upper profile were taken from the measurements made at the same time as the relevant DCR measurement. This approach allowed for changes in the profile over the initial ten metres that may have occurred during the time taken for a DCR measurement sequence.

For example, the five angular measurements made in the half hour between 21:00 and 21:30 on the 18th of June each had a corresponding MODTRAN input profile consisting of the DCR-measured ground temperature at 21:05, 21:10, 21:15, 21:20 and 21:25, the tower-measured temperature and relative humidity (0.5 to 10.0 metres) at those times and the Bureau of Meteorology's sonde profile from 22.0 metres to the top of the atmosphere.

Where relevant, these profile sets were used as a set to generate time-dependent radiances that were then used in further analysis. This process reduced any negative effects that may have been introduced by changes in the ground temperature or the low-level profile during the DCR's measurement sequence.

The MODTRAN parameters unrelated to the profiles of temperature, pressure and relative humidity are described in Appendix B. These settings were used for all input files except where explicitly indicated otherwise.

7.21 Summary

This Chapter has provided additional information about the nights upon which DCR measurements were made.

Metadata from the Bureau of Meteorology has included Mean Sea Level Pressure (MSLP) charts and satellite imagery that provide useful knowledge about the weather patterns that produced and affected the conditions on each of the measurement nights.

Other data sourced from the BoM included local (site-specific) cloud cover, half-hourly mean and maximum wind speeds and air temperature data for the roof site where temperature probes were not employed with the DCR.

These additional data were combined with data measured by instruments at the measurement site. In the case of the roof site, the Eppley pyrgeometer and the DCR were used. At the tower site, the data from these instruments was supplemented by data from a vertical array of temperature and relative humidity probes and a net radiometer.

The data from all of these sources has been summarised and presented in this Chapter in order to provide the context in which DCR measurements were made. In some cases the additional data was used to test or categorise the results from the DCR's measurements. In other cases the data was used to indicate the presence or otherwise of ideal or expected

measurement conditions. These data were then used to filter the candidate data for further comparisons and examination.

These processes will be discussed and detailed as necessary in the following Chapters.

Chapter 8

Fieldwork results II – instrument and model performance

8.1 Introduction

This Chapter describes the results of tests comparing DCR-predicted values of downwelling irradiance and upwelling irradiance divergence (initially measured as brightness temperature) against modeled and measured values. The formulae described in Chapter 2 were used to convert the DCR's brightness temperature outputs into the relevant quantities where required. The measured quantities were compared directly with modeled values of brightness temperature (or radiance) generated by the MODTRAN radiative transfer model, based on measured atmospheric profiles where available. In some cases measured values were available from auxiliary instrumentation, in particular the Eppley pyrgeometer.

The purpose of these tests was to appraise the fitness of the instrument and the formulae described in Chapter 2 for measuring such quantities as radiance and irradiance divergence. The measured values provided a reference, while the modeled values provided an intermediate step, used as a guide to the reliability of the instrument's measurements. The data used for each comparison depended on the availability of the relevant parameters for calculation of the required quantities. A description of the available data will be provided for each individual comparison. Chapter 7 provided detailed information of the measurement sequences used and the additional data gathered on each measurement night.

For all uses of the MODTRAN radiative transfer model throughout this Chapter, the essential input file is described in Appendix B. That description details the settings used commonly for all input files, except where it is explicitly indicated that the settings were varied.

8.2 Calculation of downwelling irradiance L_{\downarrow} extrapolated from vertical downwelling radiance $R_{\downarrow}(0^{\circ})$ - results

Equation (2.34) calculates downwelling irradiance L_{\downarrow} from vertically downwelling narrowband radiance in two channels. In this equation brightness temperatures $T_{\downarrow 1}$ and $T_{\downarrow 2}$ directly represent the vertically incident narrowband radiances in channels 1 (active) and 2 (window) respectively. Equation (2.34) has the following form:

$$L_{\downarrow} = 2.514T_{\downarrow 1} + 3.238T_{\downarrow 2} + 416.67$$

Relevant data were available from three measurement nights. The relevant data consisted of DCR brightness temperature measurements made with the instrument pointing vertically upwards and concurrent Eppley pyrgeometer measurements. The available data is summarised in Table 8.1 below. The full measurement sequences for each night are described in Table 7.11.

Measurement date	DCR data span	DCR data frequency	Eppley data span	Eppley data frequency
01/05/02	18:02 - 07:02	Once hourly	16:59 - 07:04	Every 5 minutes
29/06/02	21:47 – 06:47	Once every 30 minutes	21:44 – 10:49	Every 5 minutes
30/07/02	17:22 – 06:52	Once every 30 minutes	17:19 – 09:54	Every five minutes

Table 8.1. Availability and frequency of DCR brightness temperature measurements at zero degrees zenith angle and Eppley pyrgeometer-measured downwelling irradiance. Chapter 7 details further meteorological data associated with each measurement night.

For each available set of two brightness temperature measurements, L_{\downarrow} was calculated using equation (2.34). The two Eppley measurements made before and after each pair of brightness temperatures were averaged to give a measured value of L_{\downarrow} . These values were then compared for each measurement date. The results of these comparisons are shown in Figures 8.1a, 8.1b and 8.1c below.

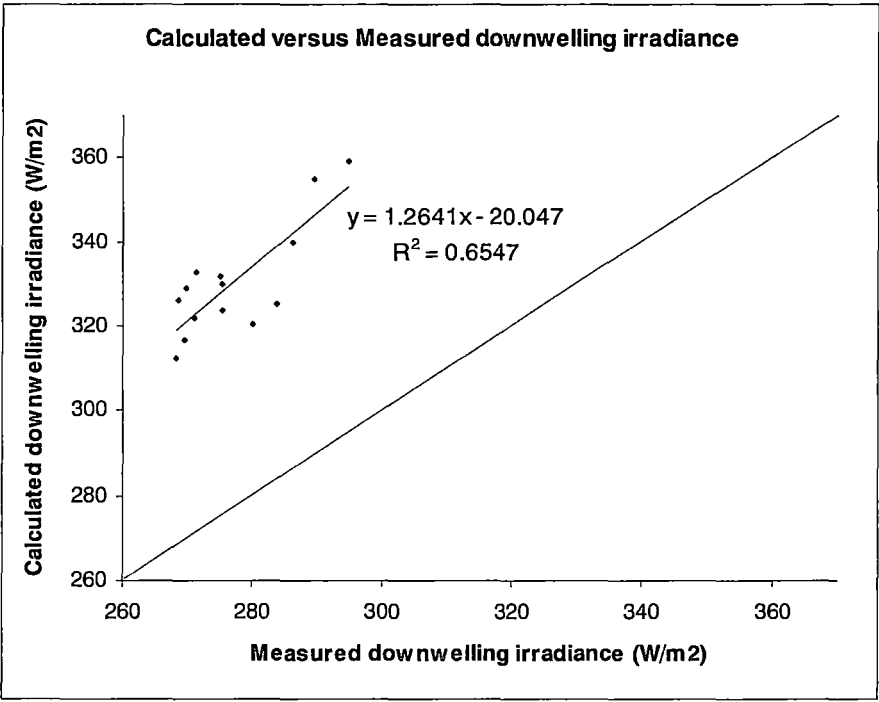


Figure 8.1a. Downwelling irradiance calculated from DCR brightness temperatures using equation (2.34) versus downwelling irradiance measured by the Eppley pyrgeometer, 1st of May. N=14, RMS ($x_i - y_i$) error is 53.7 W/m².

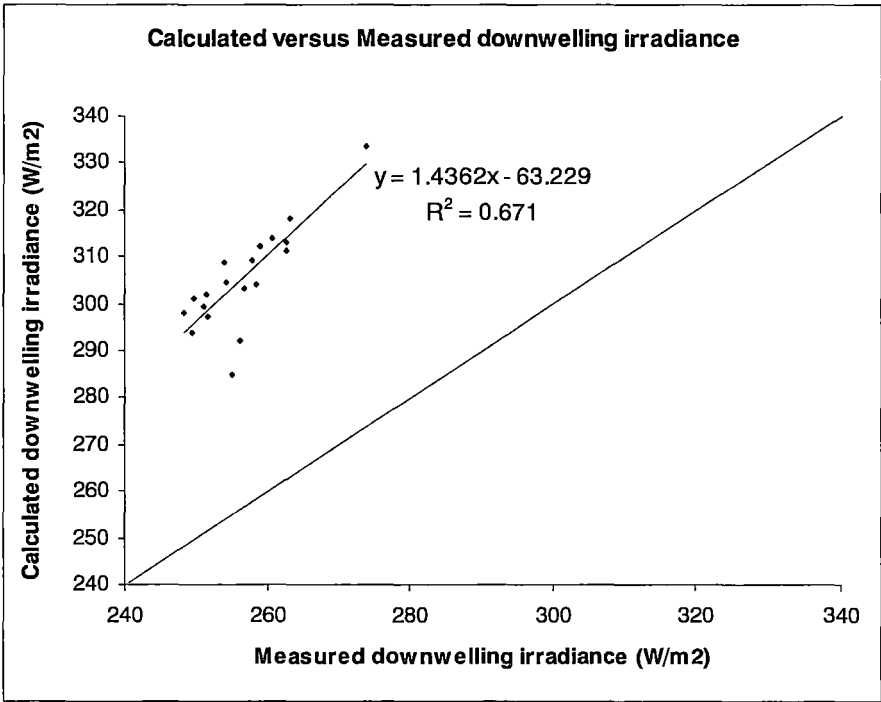


Figure 8.1b. Downwelling irradiance calculated from DCR brightness temperatures using equation (2.34) versus downwelling irradiance measured by the Eppley pyrgeometer, 29th of June. N=19, RMS ($x_i - y_i$) error is 49.2 W/m².

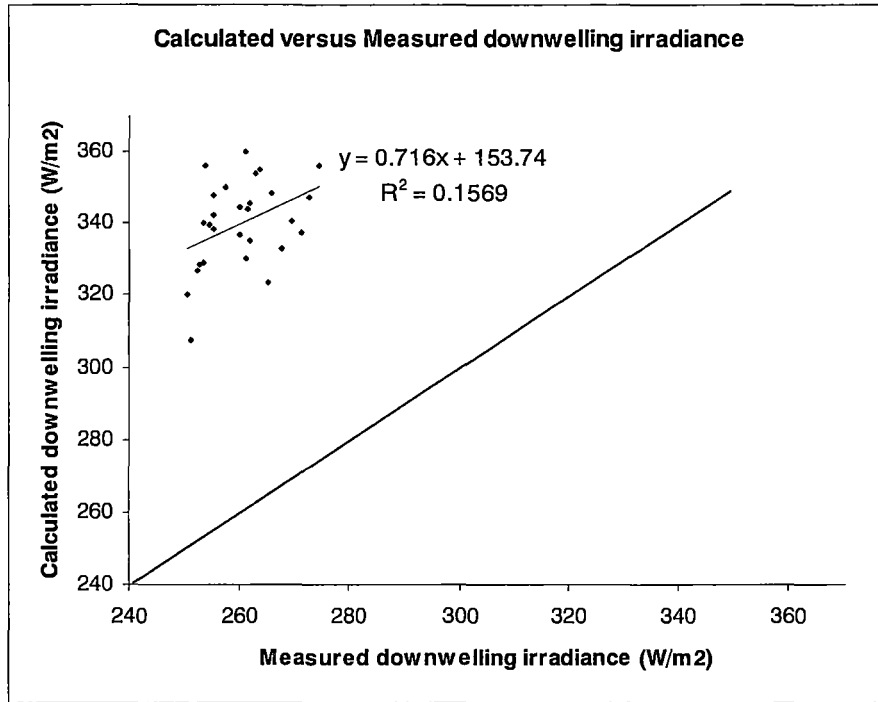


Figure 8.1c. Downwelling irradiance calculated from DCR brightness temperatures using equation (2.34) versus downwelling irradiance measured by the Eppley pyrgeometer, 30th of July. N=28, RMS (x_i, y_i) error is 80.6 W/m².

These figures show that the downwelling irradiance calculated from the DCR's brightness temperature measurements is substantially over-predicting the downwelling irradiance measured by the Eppley pyrgeometer. The data from the first and second measurement dates display a stronger correlation with the Eppley-measured data and are essentially consistent with each other. However the data from the third measurement night is very poorly correlated and further is inconsistent with the data from the previous two measurement dates.

The data from the three measurement dates was then combined to give an overall assessment of the comparison between calculated and measured values of L_{\downarrow} . A plot of the combined data is shown in Figure 8.2 below. The correlation and the linear trend in the combined data is essentially the same as the worst-case correlation and trend in the data from the 30th of July.

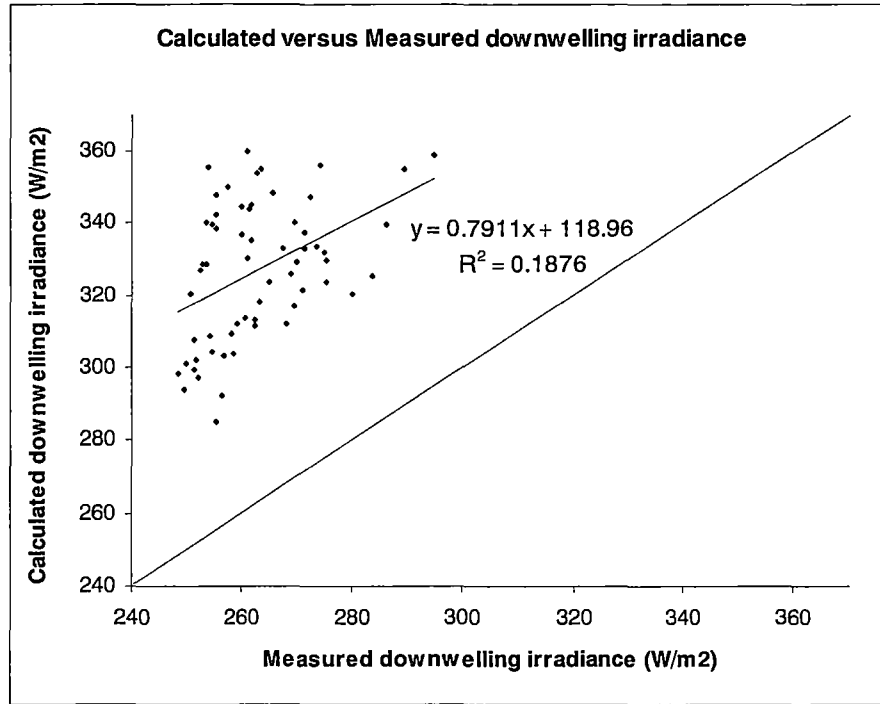


Figure 8.2. Downwelling irradiance calculated from DCR brightness temperatures using equation (2.34), versus downwelling irradiance measured by the Eppley pyrgeometer. Combined data from three nights. N=61, RMS ($x_i - y_i$) error is 66.3 W/m².

The plots above revealed an obvious positive offset in the downwelling irradiance values predicted from the measured brightness temperatures. In the data from the 1st of May and 29th of June the offset appears to be reasonably systematic, much less so in the data from the 30th July. Downwelling irradiance values calculated by integrating predicted radiance show many of the same characteristics as the data above. These values will be examined in the next section, with analysis common to both sets detailed thereafter.

8.3 Downwelling irradiance L_{\downarrow} from integration of directional radiance $R_{\downarrow}(\theta)$ - results

Equation (2.33) calculates downwelling broadband radiance R_{\downarrow} from downwelling narrowband radiance in two channels, independently of the direction. In the equation brightness temperatures $T_{\downarrow 1}$ and $T_{\downarrow 2}$ directly represent the narrowband radiances in channels one (active) and two (window) respectively, measured at the angle of incidence. The equation takes the form:

$$R_{\downarrow} = 0.8194T_{\downarrow 1} + 0.6493T_{\downarrow 2} + 103.44.$$

Directional broadband radiances calculated by this equation were integrated over the hemisphere to give the downwelling irradiance, which was then compared with downwelling irradiance measured by the Eppley pyrgeometer.

Six measurements of directional radiance were made, one at each of 0, 15, 30, 45, 60 and 75° zenith angle. These measurements were spaced in time by five minutes, yielding half an hour per ‘cycle’. The data available for this analysis was the same as that detailed for the measurement dates 29/06/02 and 30/07/02 in Table 8.1 in the previous section.

For each ‘cycle’ of six directional measurements (and hence for each integrated value of the downwelling irradiance), the corresponding six Eppley-measured values were averaged to give a single value for comparison. These were then compared directly with the calculated values. The results of these comparisons are plotted in Figures 8.3a and 8.3b below.

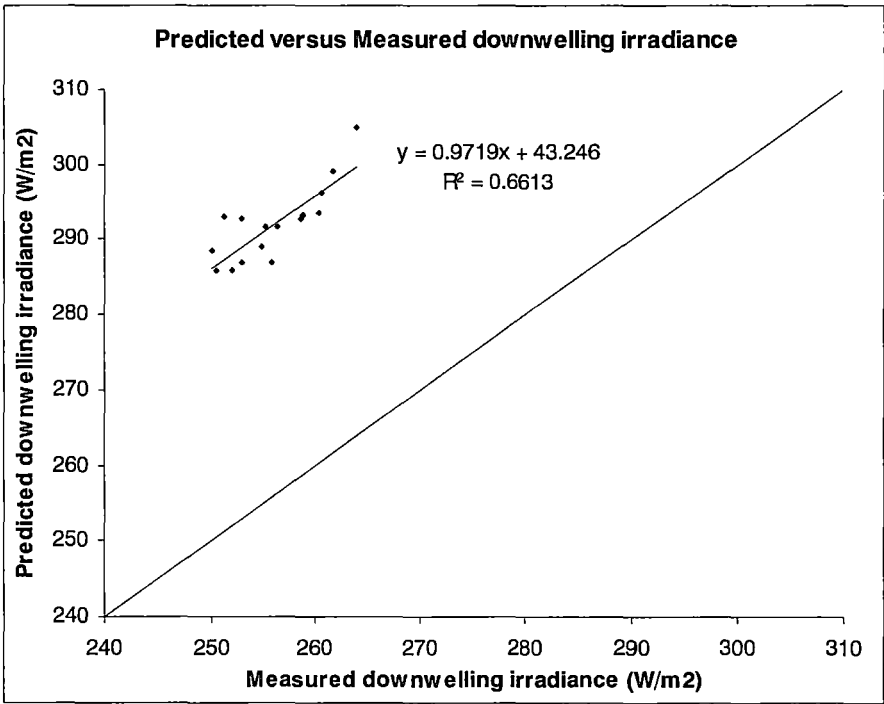


Figure 8.3a. Downwelling irradiance calculated from integrated DCR-derived broadband radiance, versus Eppley-measured downwelling irradiance, 29th of June. N=16, RMS ($x_i - y_i$) error is 36.2 W/m².

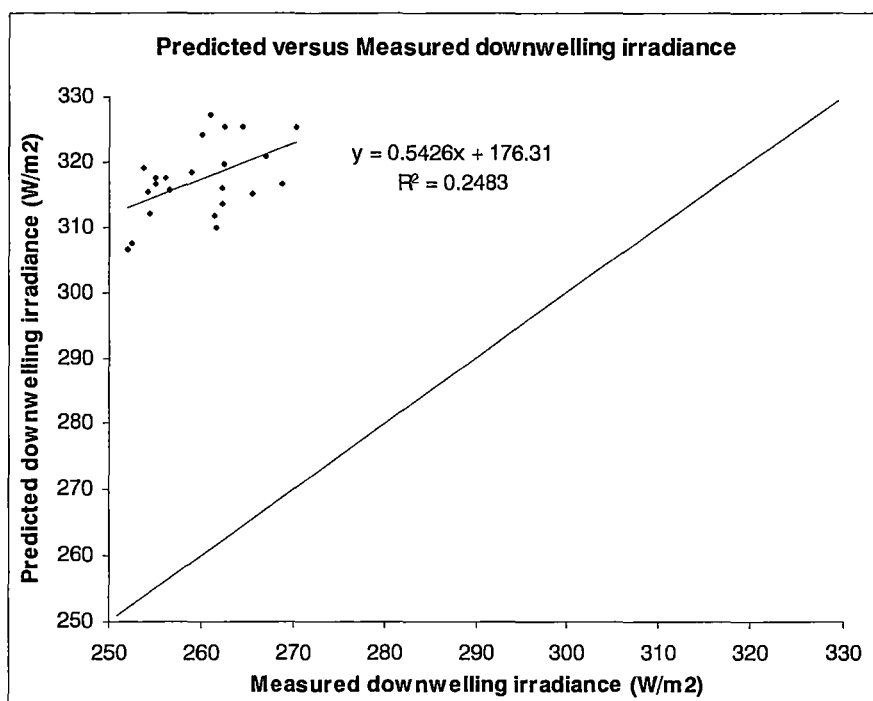


Figure 8.3b. Downwelling irradiance calculated from integrated DCR-derived broadband radiance, versus Eppley-measured downwelling irradiance, 30th of July. N=23, RMS ($x_i - y_i$) error is 57.7 W/m².

The data from the 29th June gave a close match in slope between the predicted and measured values, with a trendline slope of 0.97 and a moderate correlation index of 0.66. As with the extrapolated values in the previous section however, the data were offset substantially. Again, the data from the 30th July gave a weaker match between predicted and measured values (trendline slope 0.54) and a much weaker correlation index of 0.25. The combined data gave a different result entirely, not closely related to either of the individual data sets, with a linear trendline slope of 1.48 and an R^2 value of 0.32. A plot of the combined data set is shown in Figure 8.4.

These data exhibited the same behaviour as the extrapolated data in the previous section – a strong positive offset in the predicted values. Again the correlation of the values based on DCR measurements with the Eppley-measured data was stronger for the 29th of June than for the 30th of July. The RMS error for the 29th of June was significantly lower than for the 30th of July, and in both cases the RMS errors were approximately 30% lower for the integrated values than for the extrapolated. These differences and similarities in behaviour are explored in detail in the next section.

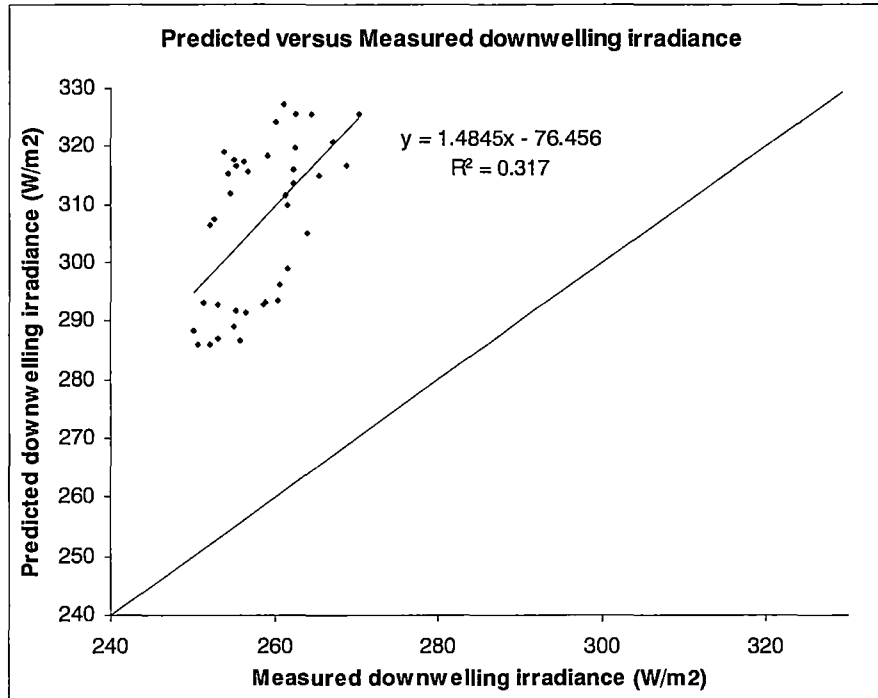


Figure 8.4. Downwelling irradiance calculated from integrated DCR-derived broadband radiance, versus Eppley-measured downwelling irradiance, combined data from two nights. N=39, RMS $(x_i - y_i)$ error is 50.0 W/m².

8.4 Downwelling irradiance L_d from DCR-measured brightness temperatures – data quality analysis

The first step in analysing the downwelling irradiance values was to investigate the relative difference between the performances of the prediction from one night to the next. All three data sets exhibited an unacceptably high RMS error in the comparison between Eppley-measured and DCR-derived downwelling irradiance. However the charts above indicate that for both the extrapolation and integration methods, the DCR-derived data from the 30th of July had a greater RMS error than the other night(s) and the departure from the Eppley-measured values was significantly less systematic.

The data measured on the 30th of July were excluded from further analysis for several reasons. Of primary concern was an observed variability in visibility during the course of the night. The Bureau of Meteorology's three-hourly visibility measurements dropped from 40km at 18:00 to 30km at 21:00 and further to 25km at 0:00. The visibility then increased to 35km at 03:00 on the 31st of July, remained at 35km at 06:00 and decreased to 20km at 09:00. While the final decrease was outside the time period in which measurements were

made, the general variability throughout the night decreased the level of confidence in the data.

Another discrepancy in the data gathered on the 30th of July related to the difference between measured air temperature and the DCR-measured active channel brightness temperature. Because the atmosphere is almost opaque in the active channel, it was reasonable to expect that the active channel brightness temperatures would match the air temperature at the instrument level. For the 1st of May, the air temperatures were measured by the tower-mounted temperature and relative humidity probe at 10 metres. For the other two measurement nights the Bureau of Meteorology provided the air temperature. While there was no basis for expecting that the two temperatures should match exactly, it can be seen in Figure 8.5 below that the behaviour of the active-channel brightness temperature on the 30th of July departed from the behaviour observed on the 1st of May and 29th of June.

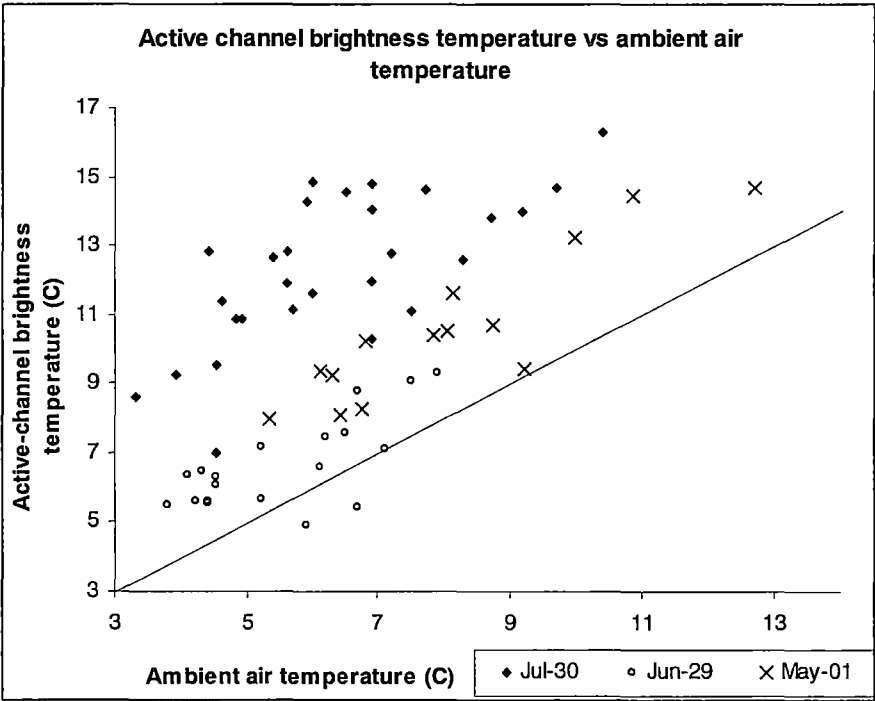


Figure 8.5. DCR-measured active-channel brightness temperature versus air temperature for three measurement nights. For the 1st of May, N=14 and the RMS ($x_i - y_i$) error is 2.7°C. For the 29th of June, N=19 and the RMS ($x_i - y_i$) error is 1.5°C. For the 30th of July, N=28 and the RMS ($x_i - y_i$) error is 6.2°C.

A final experiment was performed to establish the non-validity of the data gathered on the 30th of July. If the departure from the Eppley-measured values was systematic in some way then the values predicted by the two methods - extrapolation and integration – should have

been consistent to some degree. If the data from the 30th of June were indeed affected by the factors mentioned above in some non-systematic way, the effect should be evident in a comparison between extrapolated and integrated values.

The integrated values were plotted against the extrapolated values for the two nights for which both were available, with the resulting plots shown in Figures 8.6a and 8.6b below. The difference in the correlation between the integrated and extrapolated values for the two nights is evident in the slope and R^2 values for the plots. The RMS error was lower for the 29th of June than for the 30th of July, but the RMS error was strongly dependent on the absolute offset. The data from the 29th of June has slope 0.49 and R^2 0.46, while the data from the 30th July has slope 0.08 and R^2 0.03.

This comparison serves as verification that the data gathered on the 30th July was affected by the factors detailed earlier, and further that it was affected in some non-systematic fashion. For this reason the data set gathered on that night was excluded from further analysis.

The two sections that follow describe methods used to explain and counteract the obvious overestimation of the downwelling irradiance by the DCR-derived values. The possibility of an underestimation of L_{\downarrow} by the Eppley pyrgeometer was considered but rejected for two reasons. A first test compared the integrated downwelling broadband irradiance from the MODTRAN model with the Eppley-measured irradiance at 21:00 on the 1st of May, the only time for which a full atmospheric profile was available. The integrated modeled values gave L_{\downarrow} as 285.8 W/m² while the Eppley measured 283.7 W/m². This result can reasonably be interpreted as validation of both the MODTRAN model and the Eppley pyrgeometer. The MODTRAN model result came from an independently measured atmospheric profile and the Eppley instrument had recently been calibrated and so a close match between the two independent results was at least a validation of further comparison between MODTRAN model results and the Eppley measurements.

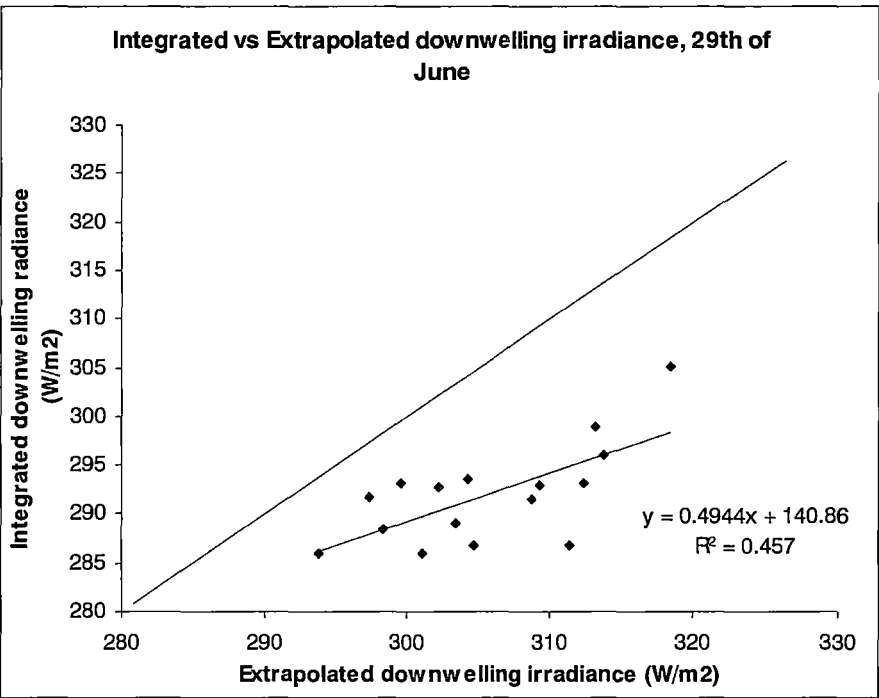


Figure 8.6a. Integrated DCR-derived downwelling irradiance values plotted against extrapolated DCR-derived downwelling irradiance values for the 29th of June. N=16, RMS (x_i-y_i) error is 14.6 W/m².

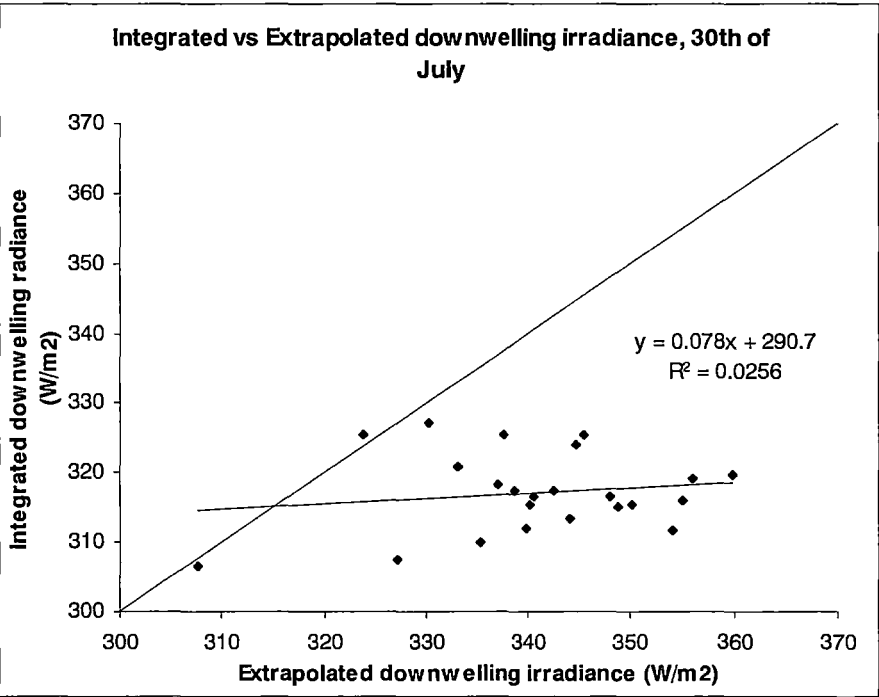


Figure 8.6b. Integrated DCR-derived downwelling irradiance values plotted against extrapolated DCR-derived downwelling irradiance values for the 30th of July. N=23, RMS (x_i-y_i) error is 26.4 W/m².

Beyond that comparison the values were considered in absolute terms and compared with measured values from the literature. Sky emissivity studies (Prata, 1996) typically yield a simplified result of the form

$$L_{\downarrow} = \varepsilon_{sky} \sigma T_0^4,$$

where T_0 is the screen-level air temperature and ε_{sky} is a grey-body sky ‘emissivity’.

Values for the emissivity range typically from 0.65 to 0.85. This formula was inverted to yield the sky emissivity and applied to the Eppley-measured and DCR-derived downwelling irradiances. It was found that for the extrapolated values from the 1st of May and 29th of June, the Eppley-measured values of L_{\downarrow} yielded ε_{sky} in the range 0.72 to 0.81 while the DCR-derived values of L_{\downarrow} yielded ε_{sky} in the range 0.85 to 0.99. This served to further confirm that the difference between the Eppley-measured and DCR-derived values was due to an overestimation of L_{\downarrow} in the DCR-derived values rather than an underestimation by the Eppley.

8.5 Downwelling irradiance L_{\downarrow} from DCR-measured brightness temperatures - reparameterisation of formulae

One possible explanation for the DCR-derived measurement’s overestimation of the downwelling irradiance was an excessively strong dependence of the equations for R_{\downarrow} (2.33) and L_{\downarrow} (2.34) on the window-channel brightness temperature $T_{\downarrow 2}$. The window-channel brightness temperature is typically strongly negative for measurements made at night, and any overestimation of its effect will yield an overestimation of the downwelling irradiance.

The MODTRAN profiles used to generate equations (2.33) and (2.34) in Section 2.13 were assigned a default visibility of 23km (‘RURAL’), corresponding to an atmosphere relatively clear of aerosols. However, measurements on the 29th of June were made in an urban setting at the roof site, and while measurements were made in a remote setting on the 1st of May (at the airport), the proximity of the site to the city of Hobart and to air and road traffic means that a clean ‘rural’ atmosphere was unlikely.

It was hypothesized that an increase in the aerosol content of the atmosphere (and hence a decrease in visibility) would strongly affect $T_{\downarrow 2}$ while only moderately affecting the broadband quantities L_{\downarrow} and R_{\downarrow} . $T_{\downarrow 1}$ is strongly affected by air temperature near the instrument and was therefore likely to be only weakly affected by the visibility over

distances on the scale of kilometers. The expected effect of decreased visibility on the brightness temperature was an overestimation of L_{\downarrow} .

Rather than attempting to estimate or derive a visibility value for each measurement on each of the two nights, the parameterisations for L_{\downarrow} and R_{\downarrow} were revised to account for varying visibility. This was achieved by re-running the original model sets that were used to derive equations (2.33) and (2.34). The original model sets are described in detail in Section 2.13.

Visibility was incorporated into the models by a cyclic set of visibility values: 35.0, 25.0, 15.0, 5.0 and 1.0km. These values were added to the 192 MODTRAN input files in order, creating a pseudo-random variation in visibility across the set of profiles. The models were then run and the broadband radiance R_{\downarrow} and modeled brightness temperatures $T_{\downarrow 1}$ and $T_{\downarrow 2}$ were extracted for each measurement angle in each test. The angular R_{\downarrow} values were then integrated to give L_{\downarrow} for each test.

The extracted values were then used to recreate equations (2.33) and (2.34). The original form of these equations was:

$$R_{\downarrow} = 0.8194T_{\downarrow 1} + 0.6493T_{\downarrow 2} + 103.44 \quad (2.33)$$

with N=1152, $R^2=0.996$ and RMS (x_i-y_i) error 0.37 W/m²/steradian and

$$L_{\downarrow} = 2.514T_{\downarrow 1} + 3.238T_{\downarrow 2} + 416.67 \quad (2.34)$$

with N=192, $R^2=0.999$ and RMS (x_i-y_i) error 0.35 W/m².

The revised equations that resulted from the inclusion of a variable visibility in the parameterisation took the form:

$$R_{\downarrow} = 0.8847T_{\downarrow 1} + 0.5611T_{\downarrow 2} + 94.131 \quad (8.1)$$

with N=1152, $R^2=0.993$ and RMS (x_i-y_i) error 0.59 W/m²/steradian and

$$L_{\downarrow} = 3.181T_{\downarrow 1} + 1.943T_{\downarrow 2} + 335.31 \quad (8.2)$$

with N=192, $R^2=0.995$ and RMS (x_i-y_i) error 1.41 W/m².

The difference in the predicted (DCR-derived) downwelling irradiance due to the revision of these equations is evident in the plots shown in the figures below. Figures 8.7a and 8.7b illustrate the improvement in the extrapolated values that is gained by using equation (8.2) in place of equation (2.34). A similar comparison for the integrated values – using equation (8.1) in place of equation (2.33) is shown in Figure 8.8 below. This figure can be compared

directly with Figure 8.3a. As angular measurements were not made on the 1st of May, no comparison of the integrated values can be made for that date.

Table 8.2 below summarises the improvements made by the revision of equations (2.33) and (2.34) to include the effects of variable visibility. While the RMS errors in the new parameterisations were slightly higher than in the originals (0.59 W/m²/steradian versus 0.37 W/m²/steradian for equations (2.33)/(8.1) and 1.41 W/m² versus 0.35 W/m² for equations (2.34)/(8.2)), these were far outweighed by the reductions in RMS error in the DCR-derived versus Eppley-measured downwelling irradiances. The parameterisations were also strengthened by the inclusion of variable visibility – the range of conditions over which the input model profiles could be applied was greatly increased.

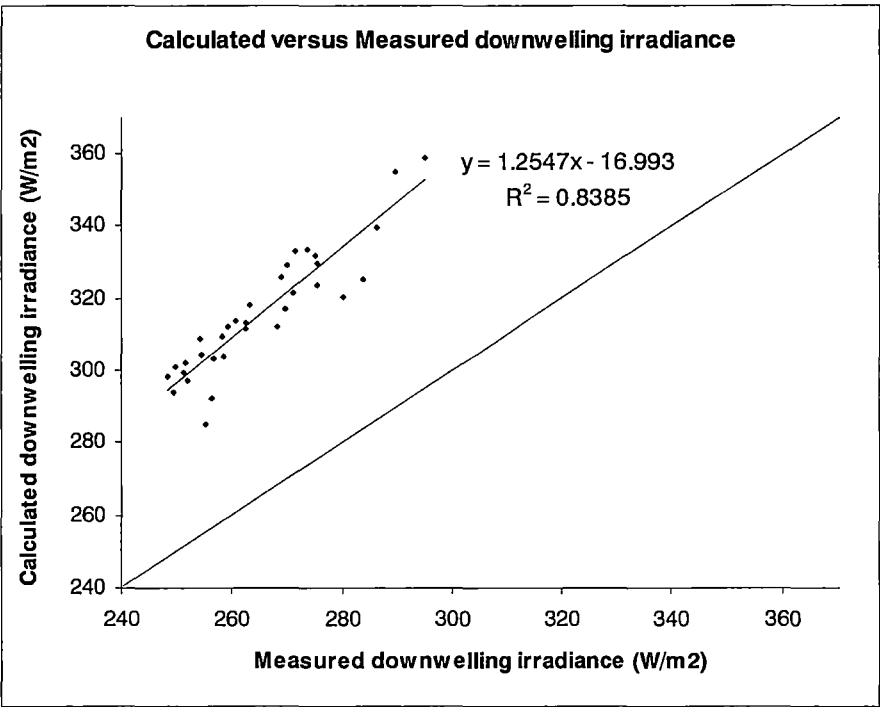


Figure 8.7a. DCR-derived downwelling irradiance extrapolated from $T_{\downarrow 1}$ and $T_{\downarrow 2}$ using equation (2.34) versus Eppley-measured downwelling longwave irradiance. Combined data from the 1st of May and 29th of June. N=33 and RMS ($x_i - y_i$) error is 51.1 W/m².

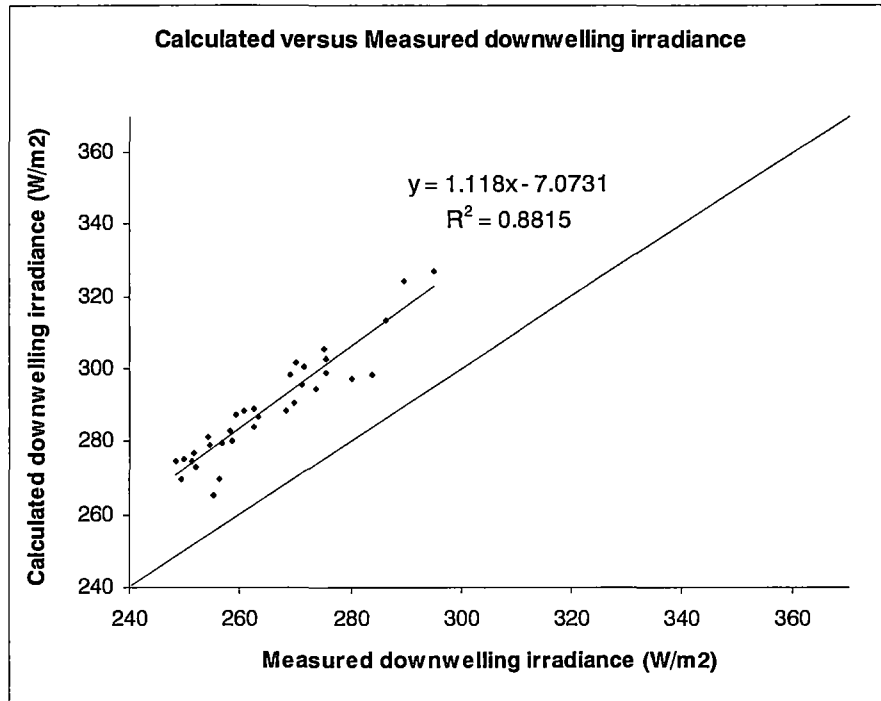


Figure 8.7b. DCR-derived downwelling irradiance extrapolated from $T_{\downarrow 1}$ and $T_{\downarrow 2}$ using equation (8.2) versus Eppley-measured downwelling irradiance. Combined data from the 1st of May and 29th of June. N=33 and RMS ($x_i - y_i$) error is 24.8 W/m².

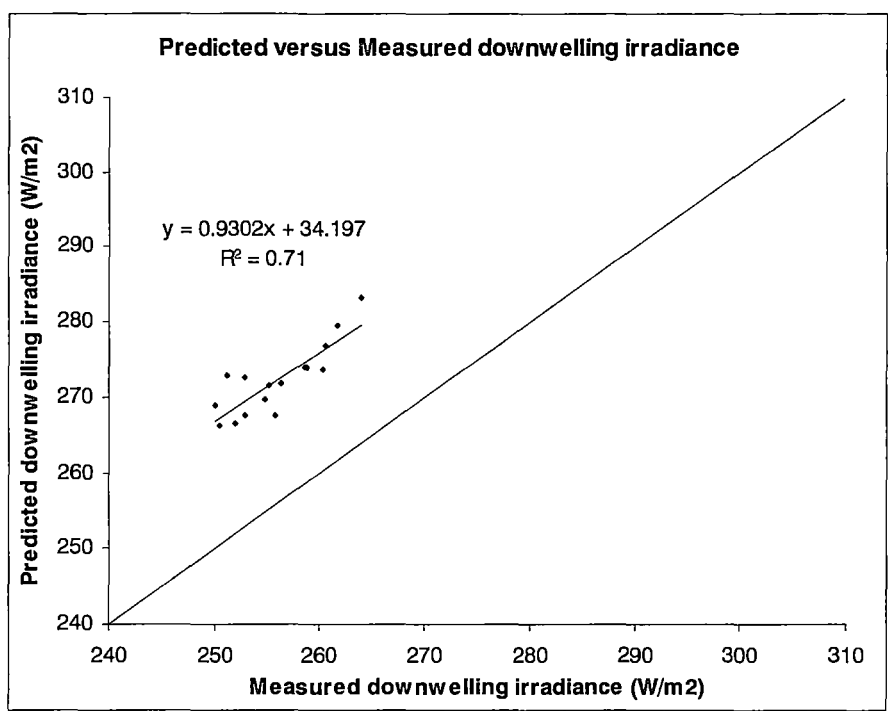


Figure 8.8. DCR-derived downwelling irradiance calculated by integrating angular values of R_{\downarrow} derived from $T_{\downarrow 1}$ and $T_{\downarrow 2}$ using equation (8.1). $N=16$ and RMS (x_i-y_i) error is 16.5 W/m^2 .

Extrapolated values	Original (2.34)	Revised (8.2)
01/05/2002	53.7	26.5
29/06/2002	49.2	23.4
Combined	51.1	24.8
Integrated values	Original (2.33)	Revised (8.1)
29/06/2002	36.2	16.5

Table 8.2. RMS (x_i-y_i) error values for DCR-derived versus Eppley-measured downwelling irradiance. All values in W/m^2 .

8.6 Downwelling irradiance L_{\downarrow} from DCR-measured brightness temperatures - recalibration of window-channel temperature

A further avenue was explored in order to explain the difference between the DCR-derived and Eppley-measured downwelling irradiance. The results from the MODTRAN test based on the atmospheric profile at 21:00 on the 1st of May were examined and compared with both the Eppley's and DCR's measurements at that time.

The measured brightness temperature in the active channel (9.4°C) closely matched the modeled value (9.6°C), but in the window channel the measured and modeled values were –34.6°C and –48.3°C respectively. With a close match between the active-channel brightness temperatures, this difference in the window-channel temperatures is implicated as a partial cause of the observed discrepancy in values of L_{\downarrow} .

The most likely cause of an incorrect reading of the window channel brightness temperature was the instrument calibration. While the cold calibration extended the calibrated target temperature range down to -18°C, the expected brightness temperature of the sky in this channel - output by the MODTRAN model - was minus 48.3°C for the test profile at 21:00 on the 1st of May. Any deviation of the instrument's response from the calibrated response curve over this 30°C extension beyond the calibrated range would result in a large difference in the measured temperature. In this case, the resulting difference was approximately 13.7°C.

This difference accounts for a large portion of the observed difference between calculated and measured values of L_{\downarrow} . It can be seen immediately from the form of Equation (2.34) that a difference of 13.7°C in T_{b2} will yield a difference of 44.4 W/m² in L_{\downarrow} . The observed difference between calculated and modeled values was 43.8 W/m². The original calibration values down to -18°C gave no indication of possible significant deviations below -18°C due to the fitted nature of the calibration equation.

Further evidence of the instrument's inability to accurately measure extremely low temperatures was the improved performance of the integrated L_{\downarrow} against the extrapolated L_{\downarrow} . In all comparisons between DCR-derived and Eppley values, the integrated values yielded a lower RMS error than the extrapolated values. This made sense if the instrument's low-temperature calibration were at fault. The extrapolated values were based solely on the brightness temperature measurements made by the DCR at 0° nadir. These were invariably the lowest temperatures in each angular set, with T_{b2} typically below -30°C.

For the integrated L_{\downarrow} values the brightness temperatures were measured at 0, 15, 30, 45, 60 and 75° nadir. The brightness temperature values increased with nadir angle, and those at 60 and 75° were typically within the calibrated range of the instrument. Therefore the effect of an overestimation of extremely low brightness temperatures was mitigated with increasing nadir angle. Since the integrated L_{\downarrow} was the weighted sum of R_{\downarrow} across a range of nadir angles, this mitigation was carried into the final L_{\downarrow} value.

To test the validity of this hypothesis and in attempt to further improve the results, the instrument was 'recalibrated' for brightness temperatures below -18°C . Unfortunately only one additional calibration point was available due to the lack of atmospheric profiles for times other than 21:00 on the 1st of May. This point – $(-34.6^{\circ}\text{C}, -48.3^{\circ}\text{C})$ was added to a set of points describing a 1:1 relationship between minus 18°C and 20°C . A plot of the resulting set of points is shown in Figure 8.9 below. The curve fitted to the data has an equation of the form:

$$T_{\downarrow 2\text{New}} = 3.47 \times 10^{-4} T_{\downarrow 2\text{Old}}^3 - 2.06 \times 10^{-3} T_{\downarrow 2\text{Old}}^2 + 0.912 T_{\downarrow 2\text{Old}} + 0.244 \quad (8.3)$$

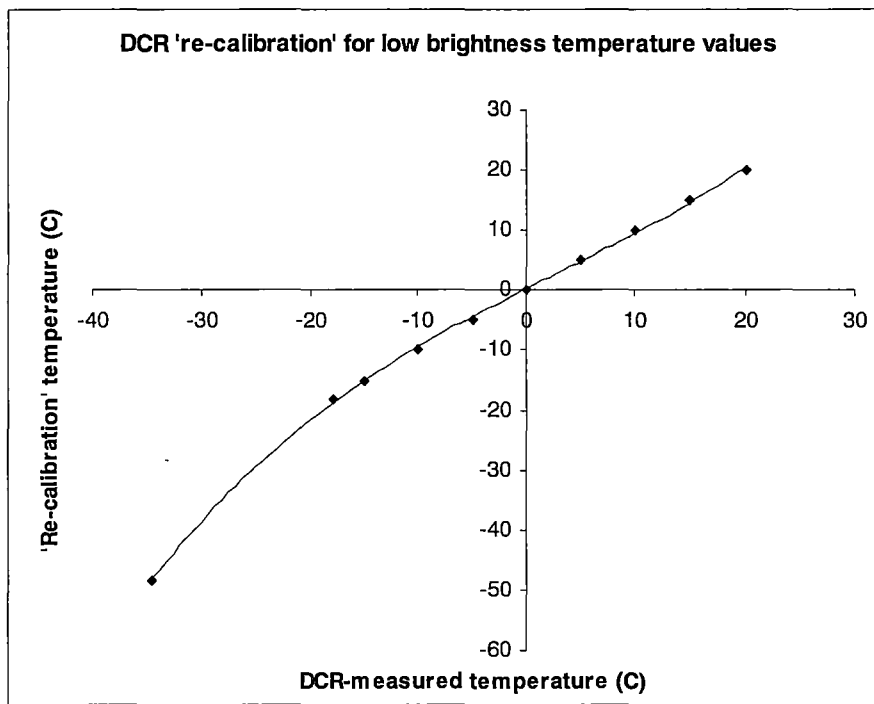


Figure 8.9. Re-calibration curve using 1:1 points within the instrument's calibrated range and a single additional point at $(-48.3^{\circ}\text{C}, -34.6^{\circ}\text{C})$, corresponding to the MODTRAN-predicted and instrument-measured brightness temperatures in channel 2 at 21:00 on the 1st of May.

The availability of only one point for the re-calibration weakened the re-calibration in two ways. Obviously only a single point was less reliable than many. Also, the single point corresponded to a single value for the instrument's internal temperature, a critical value in the original calibration along with the instrument signal in millivolts and the target temperature (see Chapter 5). This in turn meant that the re-calibration was most valid at or

very near the corresponding value for the internal instrument temperature. Ideally, a full re-calibration would take the form:

$$T_{\downarrow 2New} = f(T_{\downarrow 1Old}, Ti)$$

with Ti some simplified form of the internal instrument temperatures $Ti_{t,1}$ and $Ti_{t,2}$. For this reason it was expected that the re-calibration would be most effective for the data gathered on the 1st of May around 21:00, when the instrument’s internal temperature was close to the value implicitly included in the re-calibration equation.

To test the re-calibration, it was applied to values of $T_{\downarrow 2}$ before they were used in the calculation of L_{\downarrow} and R_{\downarrow} . Equations (2.33) and (2.34) were used initially in order to test the re-calibration independently of the re-parameterisation. The results are shown in Figures 8.10a and 8.10b below, and the effect of the re-calibration on the RMS errors in the DCR-derived versus Eppley-measured comparisons is summarised in Table 8.3 below.

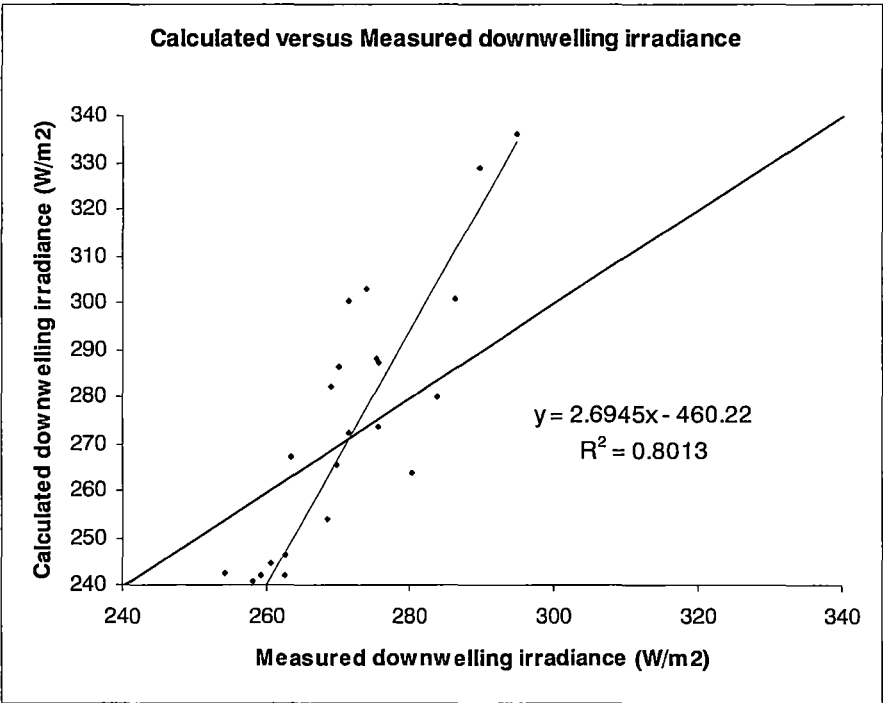


Figure 8.10a. DCR-derived downwelling irradiance extrapolated from $T_{\downarrow 1}$ and $T_{\downarrow 2}$ using equation (2.34) and re-calibrated values of $T_{\downarrow 2}$, versus Eppley-measured downwelling irradiance. Data is from the 1st of May and 29th of June. N=33 and RMS error is 28.7 W/m².

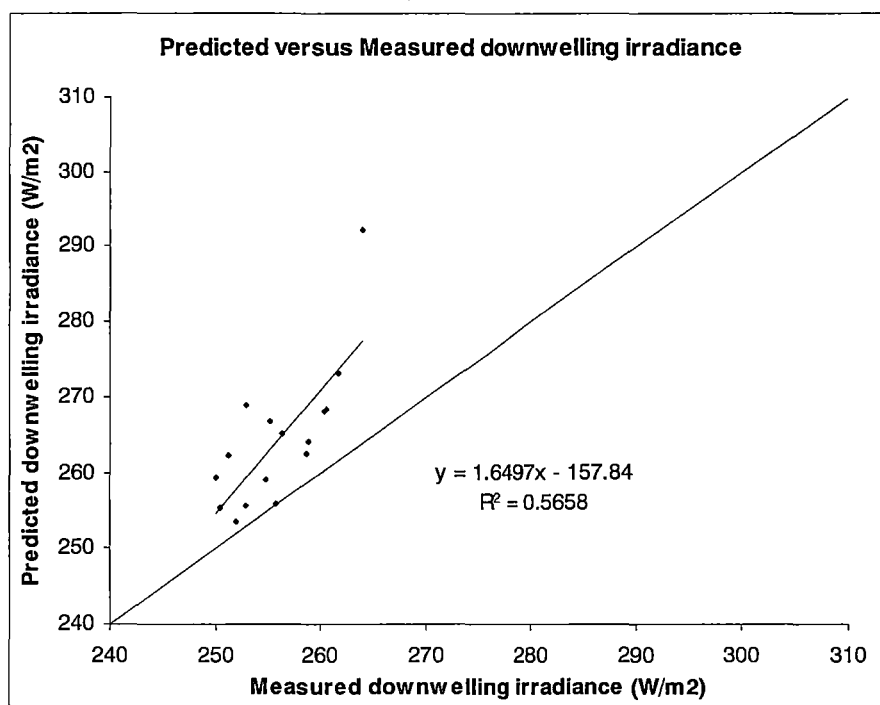


Figure 8.10b. DCR-derived downwelling irradiance integrated R_d values which were calculated from $T_{\downarrow 1}$ and $T_{\downarrow 2}$ using equation (2.33) and re-calibrated values of $T_{\downarrow 2}$ versus Eppley-measured downwelling irradiance. Data is from the 29th of June. N=16 and RMS error is 10.7 W/m².

Extrapolated values	Original	Re-calibrated
01/05/2002	53.7	19.9
29/06/2002	49.2	33.7
Combined	51.1	28.7
Integrated values	Original	Re-calibrated
29/06/2002	36.2	10.7

Table 8.3. RMS error values for DCR-derived versus Eppley-measured downwelling irradiance. All values are in W/m².

As anticipated, the re-calibration was most effective for the extrapolated data on the 1st of May, the date corresponding to the data point used to generate the revised calibration. Also as anticipated, it was very effective for the integrated data although no comparison could be made across dates due to the lack of angular data for integration on the 1st of May.

8.7 Downwelling irradiance L_{\downarrow} from DCR-measured brightness temperatures – combination of reparameterisation and recalibration

The re-calibration and revised parameterisations were combined in order to assess their combined effect on the data. Plots of the resulting DCR-derived versus Eppley-measured comparison are shown in Figures 8.11a and 8.11b below, and the RMS errors are summarised in Table 8.4. The combined modifications resulted in a marginal but consistent improvement over the re-calibrated values alone.

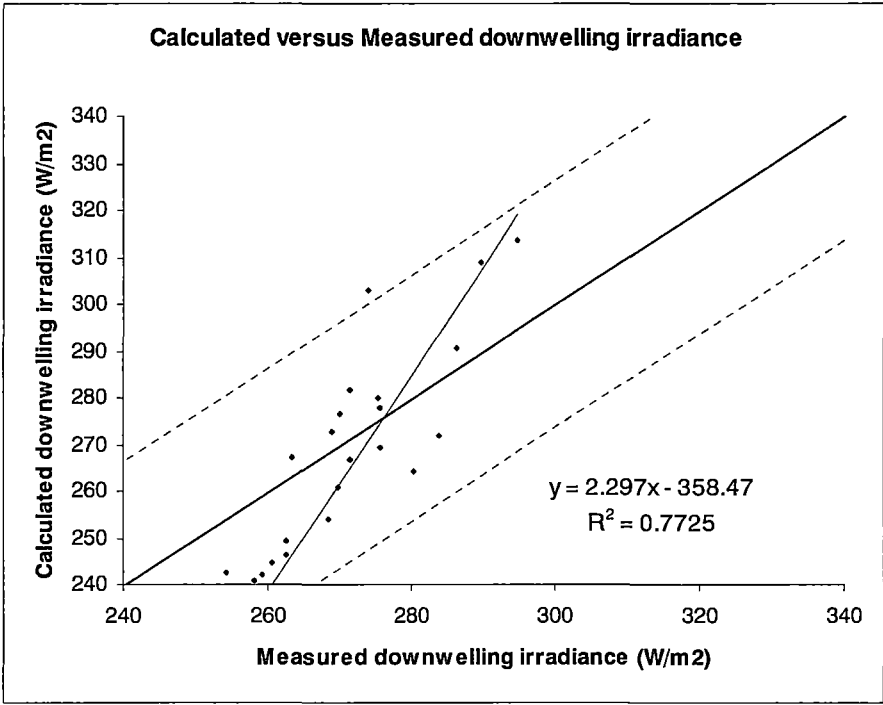


Figure 8.11a. DCR-derived downwelling irradiance extrapolated from $T_{\downarrow 1}$ and $T_{\downarrow 2}$ using equation (8.2) and re-calibrated values of $T_{\downarrow 2}$, versus Eppley-measured downwelling irradiance. Data is from the 1st of May and 29th of June. $N=33$ and RMS $(x_i - y_i)$ error is 26.4 W/m². Dashed trendlines indicate the 1:1 line \pm the RMS $(x_i - y_i)$ error and the error in the slope is 0.22.

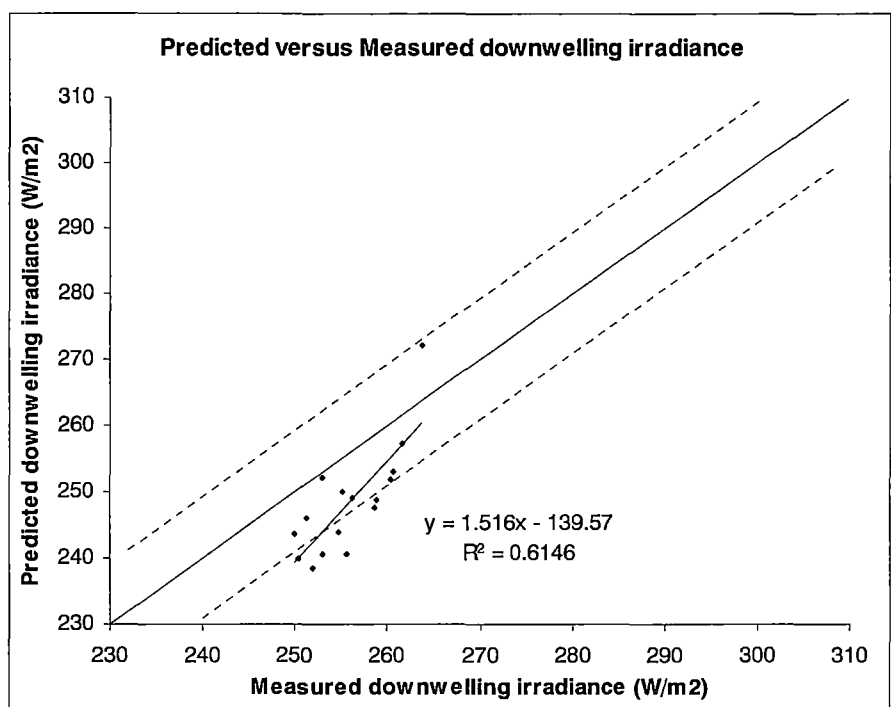


Figure 8.11b. DCR-derived downwelling irradiance from integrated R_{\downarrow} values which were calculated from $T_{\downarrow 1}$ and $T_{\downarrow 2}$ using equation (8.1) and re-calibrated values of $T_{\downarrow 2}$ versus Eppley-measured downwelling irradiance. Data is from the 29th of June. $N=16$ and RMS $(x_i - y_i)$ error is 9.3 W/m^2 . Dashed trendlines indicate the 1:1 line \pm the RMS $(x_i - y_i)$ error and the error in the slope is 0.32.

Extrapolated values	Original	Revised
01/05/2002	53.7	10.9
29/06/2002	49.2	33.5
Combined	51.1	26.4
Integrated values	Original	Revised
29/06/2002	36.2	9.3

Table 8.4. RMS error values for DCR-derived versus Eppley-measured downwelling irradiance. All values are in W/m^2 .

It can be seen from these results that both the re-parameterisation of equations (2.33) and (2.34) and the re-calibration of the window-channel brightness temperatures yielded strong improvement in the comparison between DCR-derived and Eppley-measured values of downwelling irradiance. The combined modifications yielded RMS errors significantly lower than those for the re-parameterisation alone and marginally lower than those for the re-calibration alone.

While the combined revision of the equations and recalibration had very positive effects on the RMS error values, the effect of the recalibration had a degrading effect on the slopes of the linear relationships between the predicted and Eppley-measured values.

For the extrapolated data the original comparison (without recalibration) had a slope of 1.12 for combined data from the 1st of May and 29th of June. For the integrated data the slope was 0.93 for data from the 29th of June. The slopes of the corresponding relationships post-recalibration were 2.30 and 1.52 respectively.

This effect was most likely due to the nature of the recalibration, which relied upon a single point beyond the range of the original calibration. The recalibration curve was a smooth curve that essentially retained the values within the original calibration range and accommodated the additional point. It has already been mentioned that this single point did not accurately represent the effects of changing internal instrument temperature. However in addition the calibration curve (Figure 8.9) spanned a gap of almost 15°C across which there were no additional reference points.

Since the majority of measured window-channel brightness temperatures fall within or beyond the range corresponding to the gap, it was likely that the cubic nature of the calibration correction curve across the gap contributed to an under-correction of temperatures lower than -34.6° and an over-correction of temperatures between -34.6 and -18°C. The prediction of the irradiance depended proportionally on these predicted temperatures, and so this bias in the temperature correction would yield a similar bias in the predicted downwelling irradiance. This bias was manifested as an increase in the slope of the linear relationship between the predicted and Eppley-measured irradiance values.

Figure 8.12 below shows the effect of the recalibration bias on extrapolated irradiance values. The difference between predicted and Eppley-measured values was plotted against the difference between the window-channel brightness temperature and the recalibration reference temperature. A linear fit to the plotted data is also shown, and serves very well to validate the hypothesis discussed above. The RMS ($x_i - y_i$) error in the linear regression is 7.4 W/m².

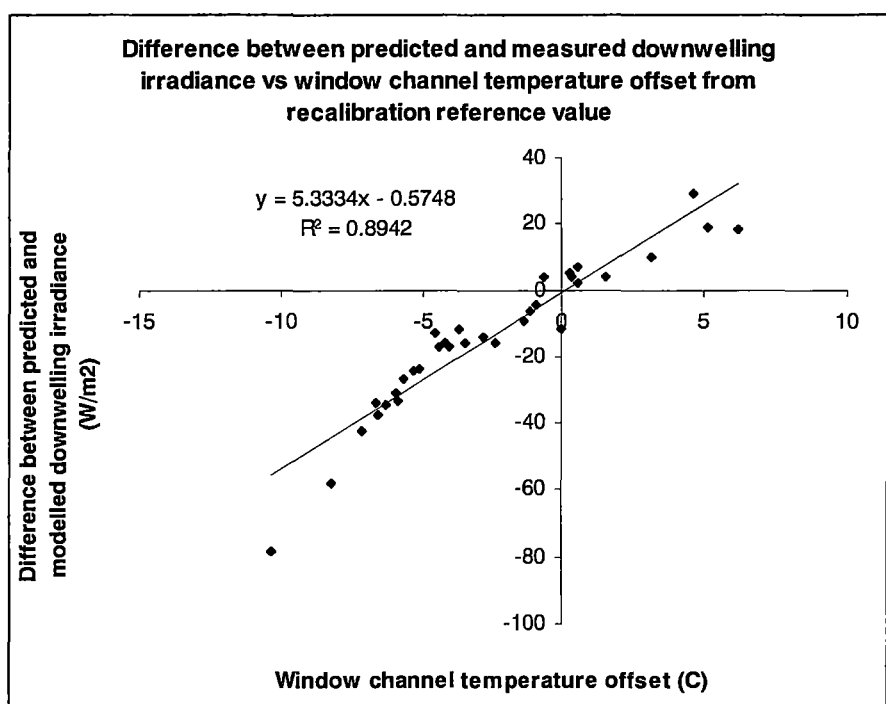


Figure 8.12. Difference between predicted and Eppley-measured downwelling irradiance values versus the difference between the window-channel brightness temperature and the recalibration reference temperature (-34.6°C). Plotted data is from the re-parameterised predictions by extrapolation, 1st of May and 29th of June combined. N=33.

While the plotted data indicated that the recalibration curve was the source of the observed increase in slope, the lack of further reference points prevented further analysis. If more reference points had been available, both to fill the gap in the recalibration data and to span a suitable range of internal instrument temperatures, the recalibration curve could have been more accurately modeled. The predicted values could then be more appropriately corrected to yield improvement in both the RMS error and the slope of the relationship between DCR-predicted and Eppley-measured data.

Individually, each modification to the prediction was justified by the resulting improvement in RMS error values for the predicted data, and their combination presents a substantially strengthened case for the use of the sky brightness temperatures in two channels to characterize the downwelling irradiance.

8.8 Brightness temperatures T_1 and T_2 calculated from upwelling radiance

Equations (2.24) and (2.25) calculate brightness temperatures T_1 and T_2 from narrowband radiance in active and window channels respectively, independently of the direction of incidence. These equations are repeated for reference below:

$$T_1 = 0.78249 \cdot R_a^3 - 8.1286 \cdot R_a^2 + 41.707 \cdot R_a - 55.076 \quad (2.24)$$

$$T_2 = 10.531 \cdot R_w^3 - 47.808 \cdot R_w^2 + 112.34 \cdot R_w - 67.474. \quad (2.25)$$

Brightness temperatures measured by the DCR were compared with brightness temperatures calculated using these equations with modeled directional narrowband radiances as inputs. The modeled values were generated by the MODTRAN radiative transfer model based on profiles constructed via the means described in Section 7.13.

Full sonde profiles were available for all nights, describing the atmosphere at approximately 21:00. These were supplemented with data from the tower-mounted temperature and relative humidity probes. The atmospheric profile above ten metres had no effect on the modeled values for upwelling radiance, and so for the purpose of modelling upwelling radiance, profiles were available at five-minute intervals throughout the measurement period.

Profiles were constructed using temperature and relative humidity data at half-hourly intervals between 6:00 pm and 6:00 am (where available) for each measurement night at the tower site. As discussed in Chapters 6 and 7, the DCR-measured window-channel brightness temperature at 15° nadir was used as the ground surface temperature input to the model. This avoided problems associated with obtaining an accurate ground temperature measurement and also accounted for any reflection of downwelling radiance by the ground.

The start and end times for these half-hourly profiles was determined to some extent by the availability of data. The start and end times and number of profiles for each night are presented in Table 8.5 below.

These profiles were run in MODTRAN v3.7 with the ‘virtual’ instrument positioned at ten metres, looking directly downwards. From the resulting files, the broadband radiance and the radiances in each channel were extracted and converted to brightness temperatures using equations (2.24) and (2.25). These modeled brightness temperatures were then compared with DCR-measured brightness temperatures from the corresponding half-hourly DCR measurement.

Date	Start time	End time	Number of profiles
01/05/2002	18:00	06:00	25
10/05/2002	20:30	06:00	20
13/05/2002	19:30	06:00	22
14/05/2002	18:00	06:00	25
18/06/2002	18:00	06:00	25

Table 8.5. Start and end times and the number of half-hourly atmospheric profiles between 0 and 10 metres available for each measurement night.

The correspondence between the measured window-channel brightness temperature $T_{\uparrow 2DCR}$ and the modeled window-channel brightness temperature $T_{\uparrow 2MOD}$ was tested. These two brightness temperatures were expected to be tightly coupled through the use of $T_{\uparrow 2DCR}$ as the ground surface temperature in the model.

As discussed in Section 2.8, the maximum absolute difference between the two should be less than or equal to 0.06°C . For the analysed values the maximum absolute difference was found to be 0.02°C . From a linear fit based on the 117 available values of each, it was found that the standard error in the fit was 0.006°C , well within the expected range. The slope of the linear fit was 1.00, the intercept 0.004°C and R^2 was 1.00. This level of correspondence was deemed sufficient that $T_{\uparrow 2MOD}$ and $T_{\uparrow 2DCR}$ are used interchangeably in this analysis when represented by $T_{\uparrow 2}$.

The correspondence between the measured active-channel brightness temperature $T_{\uparrow 1DCR}$ and the modeled active-channel brightness temperature $T_{\uparrow 1MOD}$ was also tested. Both of these were expected to deviate from $T_{\uparrow 2}$ as a result of atmospheric emission in the active channel spectrum. Testing their correspondence was therefore a test of the correspondence between the measured and modeled radiance in the active channel.

A linear regression fit was used for the comparison, and was performed on the data set for each night as well as for the data combined across all available nights. The slope, intercept, correlation index R^2 and standard error for each of these comparisons are presented in Table 8.6 below. The comparison of the combined data is plotted in Figure 8.13.

Date	N	Slope	Intercept (°C)	Standard error (°C)	R ²	RMS ($x_i - y_i$) error (°C)	Mean bias error (°C)
01/05/02	25	0.90	0.15	0.60	0.93	0.76	-0.46
10/05/02	20	0.83	0.72	0.63	0.67	1.01	-0.80
13/05/02	22	0.64	1.11	1.29	0.36	1.62	-0.92
14/05/02	25	0.91	-0.49	0.56	0.85	1.13	-0.99
18/06/02	25	0.97	-0.62	0.76	0.84	1.03	-0.72
Combined	117	0.94	-0.45	0.83	0.89	1.14	-0.77
Combined, excluding 13 th May	95	0.96	-0.53	0.66	0.94	0.99	-0.74

Table 8.6. Slope, intercept, correlation index R² and standard error for the linear regression fit of $T_{\uparrow MOD}$ to $T_{\uparrow DCR}$. Also included are the RMS ($x_i - y_i$) error and the Mean bias error between the modeled and measured values.

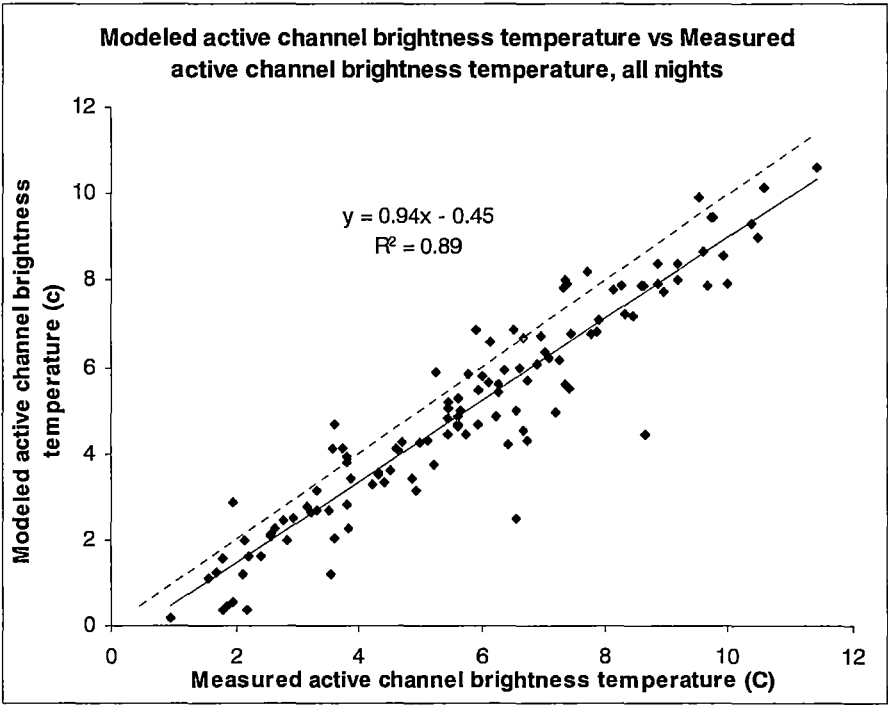


Figure 8.13. MODTRAN-modeled versus DCR-measured active channel (channel 1) brightness temperature, all nights combined.

The comparison showed reasonably uniform characteristics of the parameters of the linear regression fit across most of the measurement nights, with the exception of the 13th of May. Across the other four nights, the slope ranged from 0.83 to 0.93, the intercept from –0.62 to 0.72 °C, the RMS error from 0.76 to 0.1.13 °C and R^2 from 0.67 to 0.93. The same parameters from the data gathered on the 13th of May were outside all of these ranges. Table 8.6 therefore also contains the values of the linear regression fit parameters for the fit to all of the data, excluding the 13th of May. It can be seen that the mean bias error is consistently negative and makes a substantial contribution to the RMS error in every case.

Excluding the data from the 13th of May yielded only a slightly more favourable comparison between values of $T_{\uparrow l}$ measured by the DCR and those predicted by MODTRAN based on model profiles and so the data from the 13th of May were retained. The linear regression fit for the combined data from all nights yielded slope 0.94, intercept –0.45 °C, RMS error 1.14 °C and R^2 0.89. The RMS errors in the direct comparison are in excess of a combination of the instrument’s expected accuracies of 0.43°C in the active channel and 0.35°C in the window channel (see Section 5.8). However the value of the intercept is evidence that the source of a large proportion of the RMS error is a negative bias in the fit. The effect of that bias on further calculations involving the brightness temperatures is investigated in the following section. A later section explores several possible sources for the observed bias.

8.9 Upwelling radiance divergence $divR_{\uparrow}$ predicted from brightness temperatures

Equation (2.28) calculates upwelling broadband radiance divergence $divR_{\uparrow B}$ from brightness temperatures $T_{\uparrow 1}$ and $T_{\uparrow 2}$. It is based on MODTRAN-derived results as detailed in Section 2.9. Equation (2.28) is presented here for reference:

$$divR_{\uparrow B} = 7.128 \times 10^{-3} T_{\uparrow 1}^2 - 7.008 \times 10^{-3} T_{\uparrow 2}^2 + 0.6974 T_{\uparrow 1} - 0.6984 T_{\uparrow 2} + 2.162 \times 10^{-3} \quad (2.28)$$

The standard error in the formulation of the equation from modeled results was 0.02 W/m²/ster. While the equation was formulated from values calculated at 0° nadir incidence angle, it was shown in Section 2.15 to predict radiance divergence at a range of incident angles (0°, 15°, 30°, 45°, 60°, 75° nadir) with a standard error of 0.15 W/m²/ster.

For each of the model profiles discussed in Section 8.8, results were obtained from MODTRAN that provided the upwelling broadband radiance at ten and zero metres. The

height of zero metres was approximated by one millimetre to provide a negligible column height – MODTRAN will not calculate a result for a non-existent air column.

This provided three avenues for the calculation of the upwelling radiance divergence $divR_{\uparrow}$:

- a) $divR_{\uparrow} = R_{\uparrow}(10m) - R_{\uparrow}(0m)$,
- b) $divR_{\uparrow} = f_{2.28}(T_{\uparrow 1DCR}, T_{\uparrow 2DCR})$ and
- c) $divR_{\uparrow} = f_{2.28}(T_{\uparrow 1MOD}, T_{\uparrow 2MOD})$,

with $T_{\uparrow nMOD}$ and $T_{\uparrow nDCR}$ the modeled and measured brightness temperatures examined in the previous section, and $f_{2.28}$ representing equation (2.28).

An excellent correlation was expected between the upwelling radiance divergences obtained via methods a) and c) above, because the parameterisation expressed by equation (2.28) was derived from MODTRAN results as discussed in Chapter 2. A comparison of these values confirmed that expectation, with a linear regression fit across that data from all nights yielding a slope of 1.09, an intercept of 0.00 W/m²/steradian, R² of 1.00 and standard error in the regression of 0.03 W/m²/steradian. The RMS error between values of $divR_{\uparrow}$ predicted by method c) and the modeled values (method a)) was 0.08 W/m²/steradian.

This comparison served to establish that the conditions reflected by the modeled profiles were suitable for the application of equation (2.28), by virtue of the close match between predicted and modeled values. While this result was not unexpected, it was important to establish that the values predicted for the modeled profiles did not depart significantly from the values predicted by equation (2.28). Any significant departure would introduce doubt as to the suitability of the modeled values for comparison with those derived from DCR measurements.

The next step was to examine the values predicted using method b), using equation (2.28) and the DCR-measured brightness temperatures. These predicted values were compared to the modeled values obtained via method a). The results of linear regression fit and RMS error are presented in Table 8.7 below, and a plot of the combined data is shown in Figure 8.14.

Date	N	Slope	Intercept (W/m ² /ster)	Standard error (W/m ² /ster)	R ²	RMS error ($x_i - y_i$) (W/m ² /ster)	Mean bias error (W/m ² /ster)
01/05/02	25	1.91	-0.44	0.40	0.79	0.69	0.46
10/05/02	20	1.80	-0.07	0.47	0.68	0.95	0.78
13/05/02	22	1.69	0.13	1.04	0.41	1.30	0.78
14/05/02	25	0.96	0.89	0.43	0.67	0.92	0.83
18/06/02	25	2.76	0.62	0.37	0.77	0.76	0.53
Combined	117	1.32	0.44	0.64	0.62	0.94	0.67

Table 8.7. Slope, intercept, correlation index R^2 and standard error for the linear regression fit of predicted to modeled values of $divR_{\uparrow}$. Also included are the RMS ($x_i - y_i$) error and mean bias error between the predicted and modeled values.

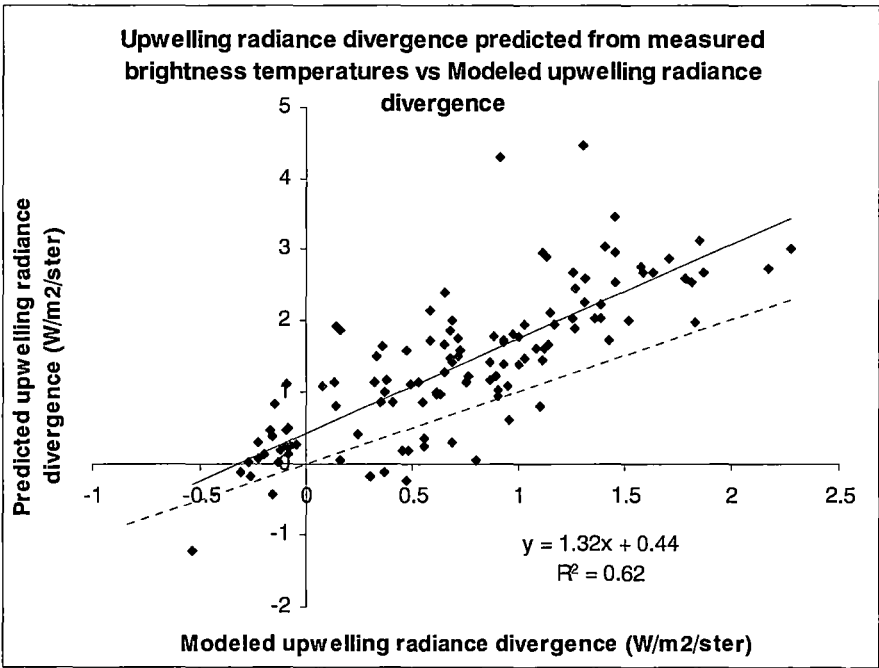


Figure 8.14. Upwelling radiance divergence $divR_{\uparrow}$ predicted from DCR measurements using equation (2.28) versus upwelling radiance divergence calculated from MODTRAN-derived broadband radiance, data from all nights combined. Standard, RMS ($x_i - y_i$) and mean bias errors are listed in Table 8.7.

It is evident in Table 8.7 that the predicted radiance divergence values inherit significant effects from the mean bias errors present in the brightness temperatures, as was expected. An effort was made to discriminate between errors in the radiance divergence introduced by the

observed errors in the brightness temperatures and the inherent variation in the DCR-measured brightness temperatures.

DCR-measured values for $T_{\uparrow l}$ were corrected based on the linear relationship that was established in the previous section between the modeled and DCR-measured values. The correction took the form:

$$T_{\uparrow lDCR(corrected)} = 0.94 \times T_{\uparrow lDCR(original)} - 0.45.$$

The effect of the active-channel brightness temperature correction is evident in a plot of the resulting upwelling radiance divergence values, shown in Figure 8.15 below.

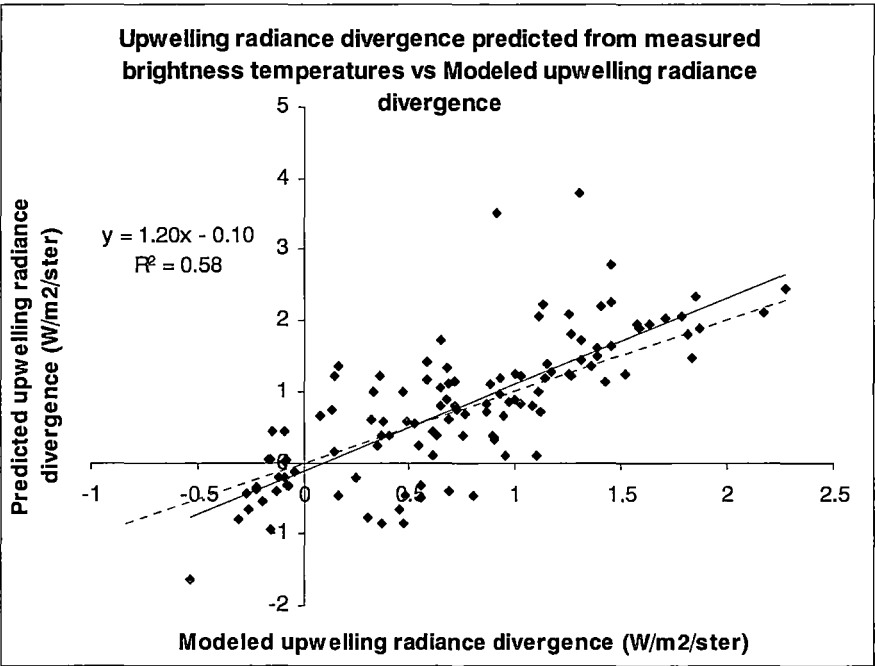


Figure 8.15. Upwelling radiance divergence $divR_{\uparrow}$ predicted from corrected DCR measurements using equation (2.28), versus upwelling radiance divergence calculated from MODTRAN-derived broadband radiance, data from all nights combined. $N=117$, standard error is $0.63 \text{ W/m}^2/\text{steradian}$ and RMS $(x_i - y_i)$ error is $0.64 \text{ W/m}^2/\text{steradian}$.

The improvements gained by correction of the DCR’s measurements of $T_{\uparrow l}$ were immediately evident. Compared with the original plot in Figure 8.14, the slope decreased from 1.32 to 1.20, the intercept from 0.44 to $-0.10 \text{ W/m}^2/\text{steradian}$. The decrease in the RMS error from 0.94 to $0.64 \text{ W/m}^2/\text{steradian}$ was also significant.

Quantitatively the plot in Figure 8.15 demonstrates the effects of the expected random variation in the DCR's measurements, with little or no evidence of significant systematic bias. It also demonstrates the suitability of the use of an equation such as equation (2.28) for calculation of upwelling radiance divergence from brightness temperatures in two channels.

8.10 Upwelling radiance divergence $divR_{\uparrow}$ at angles away from the vertical

Equation (2.28), provided in the previous section for reference, was tested in Chapter 2 using modeled values of $divR_{\uparrow}$, $T_{\uparrow 1}$ and $T_{\uparrow 2}$ at nadir angles 0, 15, 30, 45, 60, and 75 degrees. DCR measurements were made at multiple angles on the 14th of May and 18th of June, and this section describes an analysis of modeled and measured results on the 18th of June. If directional predictions of the upwelling radiance divergence were valid, integration of the angular radiance divergence values provides a path to calculation of the upwelling irradiance divergence $divL_{\uparrow}$.

A test was performed using data from two sets of angular measurements on the 18th of June, at 21:00 and 3:00. Since the DCR measurements were made at five-minute intervals, the corresponding atmospheric profiles were adjusted using the temperature and relative humidity measurements corresponding exactly to the time of each DCR measurement. Values measured by the tower-mounted probes were used for temperature and relative humidity, and the DCR's window channel brightness temperature was used for the ground temperature. This yielded five different profiles for each set of angular measurements, which were input to the MODTRAN model.

Broadband radiances at ten and zero metres ($R_{\uparrow}(10m)$ and $R_{\uparrow}(0m)$) were extracted from the model's results, along with modeled brightness temperatures $T_{\uparrow 1}$ and $T_{\uparrow 2}$ at ten metres. The directly modeled broadband radiance divergence $divR_{\uparrow}$ was then calculated via

$$divR_{\uparrow} = R_{\uparrow}(10m) - R_{\uparrow}(0m)$$

for each modeled profile.

An initial comparison between modeled and brightness temperatures in the window channel showed that the RMS error between them was 0.0058°C. This was expected given the measured value's role as ground temperature input to the model, but this comparison addressed any doubts that the close match between the two might be undone by the very long measurement path length at large nadir angles.

At 75° measurement angle, the DCR's field of view contained some portion of sky view because its field of view half-angle was greater than 15°. This view of the clear night sky had a powerful influence on the DCR-measured brightness temperature in the window channel. In turn, this had a strong influence on the modeled active-channel brightness temperature but seemed to have little if any effect on the DCR-measured active channel brightness temperature. The data at 75° were excluded from the calculation of radiance divergence due to this uncertainty.

Equation (2.28) was then used to calculate upwelling radiance divergences from the modeled and corrected measured brightness temperatures. The DCR's active-channel brightness temperatures were corrected as detailed in the previous section. The predicted values were then compared with the directly modeled radiance divergences. The results are plotted in Figure 8.16 below. The RMS error in the model-predicted values was 0.01 W/m²/steradian compared with 0.59 W/m²/steradian for the DCR-predicted values.

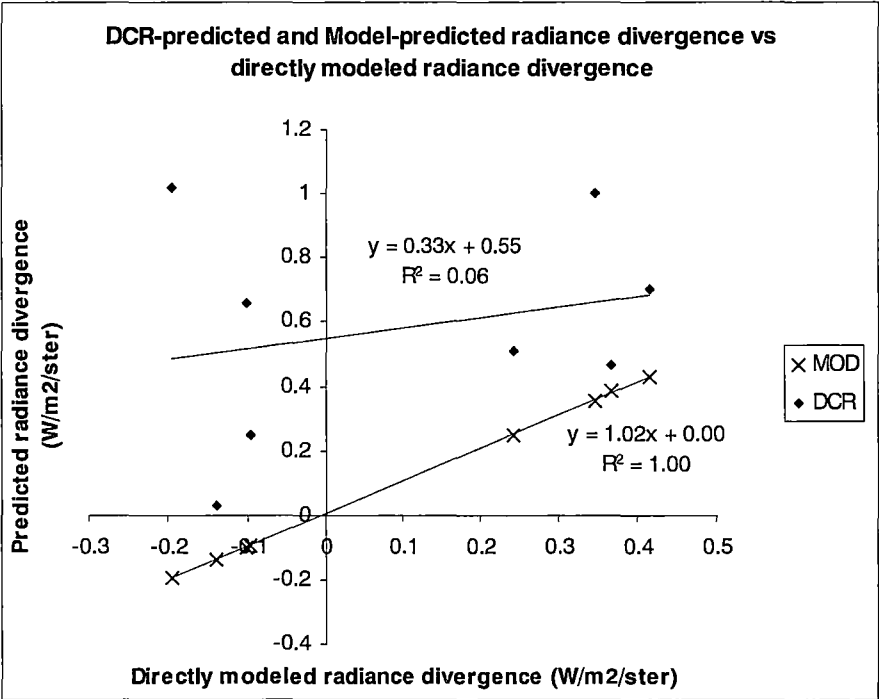


Figure 8.16. DCR-predicted (DCR) and model-predicted (MOD) radiance divergence versus directly modeled radiance divergence. Data corresponding to measurements at 75° nadir angle have been excluded.

The RMS error of 0.01 W/m²/steradian for the model-predicted values validates the use of equation (2.28) for the modeled profiles. The RMS error of 0.59 W/m²/steradian for the DCR-predicted values is similar to the RMS error of 0.64 W/m²/steradian for the data

corresponding to 15° measurement angle. Slope, intercept and correlation index values were affected by the small magnitude of the radiance divergence relative to the expected RMS error.

Integration of angular radiance divergences to give irradiance divergence is the only suitable approach under conditions where the viewed surface is non-uniform or inhomogeneous or both. However under the measurement conditions at the airport site where the ground was flat and uniform, the alternative approaches discussed in Section 2.11 are also valid methods for calculating the upwelling irradiance divergences. These methods, embodied in equations (2.31) and (2.32), use brightness temperature measurements at or near 0° nadir angle (necessarily 15° in this case) to predict the upwelling irradiance divergence. The validity and performance of these models is analysed in the next section.

8.11 Upwelling irradiance divergence $divL_{\uparrow}$

The parameterisations in Chapter 2 provided two methods for calculation of upwelling irradiance divergence $divL_{\uparrow}$ from brightness temperatures measured at or close to the vertical. The corresponding equations are presented below for reference:

$$divL_{\uparrow} = -1.1263divR_{\uparrow}^3 - 0.01052divR_{\uparrow}^2 + 4.2583divR_{\uparrow} \quad (2.31)$$

$$divL_{\uparrow} = 3.211 \times 10^{-3} T_{\uparrow 1}^2 - 2.410 \times 10^{-3} T_{\uparrow 2}^2 + 3.127 T_{\uparrow 1} - 3.138 T_{\uparrow 2} - 1.143 \times 10^{-2} \quad (2.32)$$

Equation (2.31) calculates $divL_{\uparrow}$ based on $divR_{\uparrow}$, the upwelling radiance divergence at or close to the vertical. $divR_{\uparrow}$ can in turn be calculated from $T_{\uparrow 1}$ and $T_{\uparrow 2}$ measured at or close to the vertical, using equation (2.28). While the standard error in the parameterisation used to generate equation (2.31) was 0.081 W/m², it was noted in Chapter 2 (Section 2.11) that based on the plot of predicted versus modeled values there was expected to be more significant error when the predicted values exceeded the range of values included in the parameterisation.

Equation (2.32) calculates $divL_{\uparrow}$ based directly on brightness temperatures $T_{\uparrow 1}$ and $T_{\uparrow 2}$ measured at or close to the vertical. The standard error in the parameterisation used to generate the equation was 0.034 W/m².

This section examines the performance of these equations when applied to the model profiles and DCR-measured brightness temperatures from the airport measurement nights. The

analysis was performed in two steps. First, the accuracy of the equations in predicting the modeled $divL_{\uparrow}$ from modeled brightness temperatures was tested in order to establish the validity of their use under these conditions. This was achieved by generating MODTRAN input files corresponding to the atmospheric profile at hourly intervals. These files were constructed using temperature and relative humidity data from the tower-mounted probes as detailed in previous sections. MODTRAN was instructed to produce broadband radiance values at 0, 15, 30, 45, 60 and 75° nadir angle and at 0 and 10 metres height. These were then integrated using the method described in Section 2.10 to give the upwelling irradiance L_{\uparrow} at 0 and 10 metres. The upwelling irradiance divergence was then calculated simply via:

$$divL_{\uparrow} = L_{\uparrow}(10m) - L_{\uparrow}(0m)$$

Brightness temperatures at 10 metres and 0° nadir angle were then extracted from MODTRAN's spectral output tables using the method described in Section 2.7 and used in previous sections. This yielded modeled values of $L_{\uparrow}(10m)$, $L_{\uparrow}(0m)$, $T_{\uparrow 1}$ and $T_{\uparrow 2}$ for each hourly input profile.

Equations (2.31) and (2.32) were then used to calculate values of $divL_{\uparrow}$ for each 'measurement' and the resulting values were compared with the values of $divL_{\uparrow}$ derived by direct subtraction of $L_{\uparrow}(0m)$ from $L_{\uparrow}(10m)$. The comparison is plotted in Figure 8.17 below. Equation (2.28) was used to calculate values of $divR_{\uparrow}$ for input to equation (2.31).

It was evident immediately that equation (2.31) was unsuitable for further use for prediction of $divL_{\uparrow}$. The comparison was reasonably favourable within the range of modeled values used to generate the prediction (see Figure 2.8), but degenerated significantly outside that range. This degeneration is a result of the equation used, which was produced based only on a range of values that lie within the linear portion of the plotted data. Outside that range, the results produced by the prediction equation obviously deviates significantly from the behaviour of the directly modelled values. In contrast, equation 2.32 produces values that are consistently related to the directly modelled values.

It was possible that re-generating the parameterisation might improve the predicted values. However given the unreliability already present in the prediction of $divR_{\uparrow}$ as discussed in the previous two sections, the more direct route provided by equation (2.32) was preferable in order to minimise the accumulation of errors.

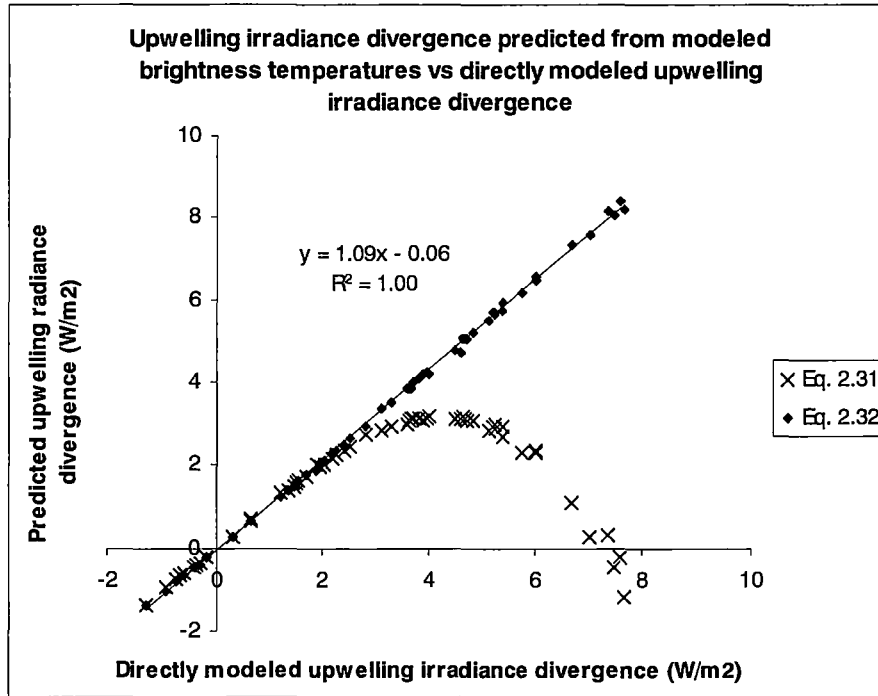


Figure 8.17. Upwelling irradiance divergence $divL_{\uparrow}$ predicted from modeled brightness temperatures, plotted against values calculated from modeled irradiance via subtraction of $L_{\uparrow}(0m)$ from $L_{\uparrow}(10m)$.

In contrast, the prediction of $divL_{\uparrow}$ by equation (2.32) compared very favourably with the directly modeled values across the whole range. The linear relationship plotted in Figure 8.17 had a slope of 1.09, intercept -0.06 W/m^2 , R^2 of 1.00 and RMS error 0.32 W/m^2 . This proved the validity of equation (2.32) under the conditions in which measurements were made.

In the second step of the analysis, equation (2.32) was used to predict $divL_{\uparrow}$ using DCR-measured brightness temperatures as inputs. The DCR's active-channel brightness temperatures were corrected prior to the calculation, as in the previous and earlier sections. The results of the comparison between these and the directly modeled values are plotted in Figure 8.18 below.

These results showed the positive bias that was expected given the already-noted bias in the DCR-measured brightness temperatures. A linear fit between the predicted and modeled values gave slope of 1.22, intercept -0.44 W/m^2 , R^2 of 0.56 and RMS error 2.69 W/m^2 . The mean bias error between predicted and modeled values was also calculated as an indication of the bias and was found to be 0.23 W/m^2 . This indicated that the major proportion of the RMS error was due to the variation in the DCR's brightness temperature measurements.

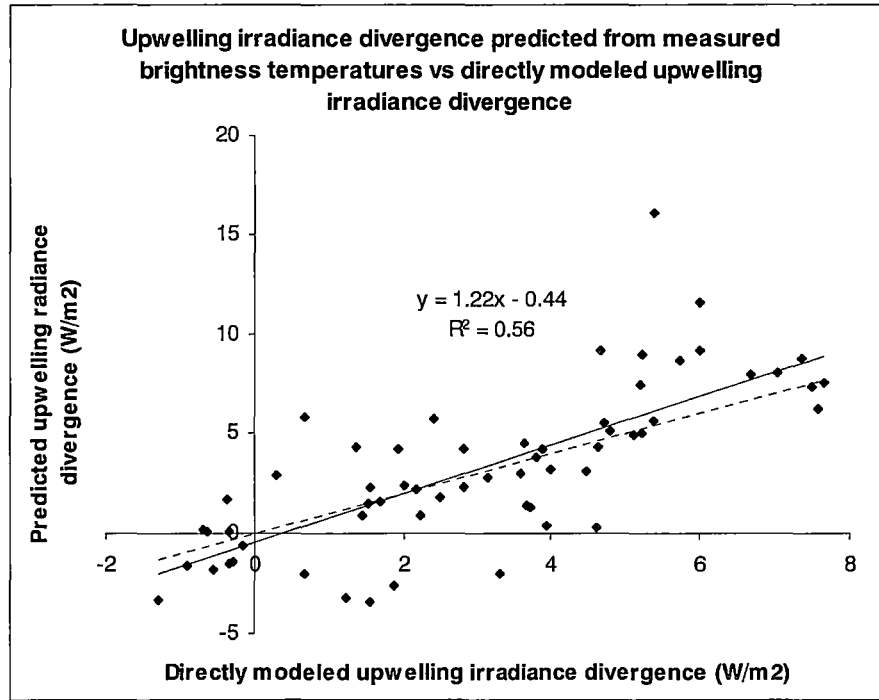


Figure 8.18. Upwelling irradiance divergence $divL_{\uparrow}$ predicted from corrected DCR-measured brightness temperatures, plotted against values calculated from modeled irradiance via subtraction of $L_{\uparrow}(0m)$ from $L_{\uparrow}(10m)$.

Given the excellent performance of equation (2.32) in predicting $divL_{\uparrow}$ from modeled brightness temperatures and assuming that the model accurately predicts relative values of $divL_{\uparrow}$ and brightness temperature, it is likely that a more accurate instrument than the DCR would yield much more accurate predictions of the upwelling irradiance divergence from a suitable parameterisation. However the DCR-predicted values did provide a measure of the upwelling irradiance divergence suitable for use in calculation of the total divergence.

8.12 Downwelling irradiance divergence $divL_{\downarrow}$

Once the upwelling irradiance divergence $divL_{\uparrow}$ had been measured or predicted, the downwelling irradiance divergence $divL_{\downarrow}$ was required for calculation of the net irradiance divergence $divL^*$. Section 2.14 described the form and derivation of equation (2.35), which calculates the downwelling irradiance divergence from four brightness temperatures – measurements in both channels and both upwelling and downwelling directions. Equation (2.35) is presented below for reference:

$$\begin{aligned} \text{div}L_{\downarrow} = & -1.4165 \times 10^{-3} T_{\uparrow 1}^2 - 1.3690 \times 10^{-2} T_{\uparrow 2}^2 + 9.0305 \times 10^{-3} T_{\downarrow 1}^2 + 1.1248 \times 10^{-2} T_{\downarrow 2}^2 \\ & - 7.2250 \times 10^{-2} T_{\uparrow 1} - 0.52877 T_{\uparrow 2} + 0.68433 T_{\downarrow 1} + 1.1257 T_{\downarrow 2} + 27.654 \end{aligned} \quad (2.35).$$

The form of this equation – in that it included brightness temperature values measured in both directions – was due to the positioning of the instrument above the air column of interest. Essentially, the upwelling brightness temperatures provide a measure of the absorptive or emissive activity in that air column, while the downwelling brightness temperatures provide a measure of the downwelling irradiance L_{\downarrow} .

The downwelling brightness temperatures also provide a spectral characterisation of L_{\downarrow} in the two measurement channels, which will be shown to be a crucial aspect of the downwelling irradiance divergence prediction.

In Section 2.14, equation (2.35) was shown to predict the downwelling irradiance divergence with a standard error of 0.1026 W/m² over the modeled data set used to create the equation (described in Section 2.10).

Two tests were performed to test the validity of the original approach (equation (2.35)) to prediction of the downwelling irradiance divergence. Modeled values of $T_{\uparrow 1}$, $T_{\uparrow 2}$, $T_{\downarrow 1}$ and $T_{\downarrow 2}$ were used with equation (2.35) to predict $\text{div}L_{\downarrow}$. The predicted values were then compared to those calculated from MODTRAN-derived values of L_{\downarrow} at ten and zero metres. The results are shown in Figure 8.19 below.

It was clear from the plot that equation (2.35) was overestimating the absolute values and underestimating the slope. The availability of ‘real’ profiles provided the opportunity for a revision of equation (2.35) based on real profile data. The profiles used to generate equation (2.35) had no fine structure within the first ten-metre layer above the ground, which was a likely cause for the prediction’s failure. The equation was revised by a multiple regression fit to the available data and had the form:

$$\begin{aligned} \text{div}L_{\downarrow} = & -5.468 \times 10^{-2} T_{\uparrow 1}^2 + 3.871 \times 10^{-2} T_{\uparrow 2}^2 - 25.40 T_{\downarrow 1}^2 + 909.6 T_{\downarrow 2}^2 - 1.664 T_{\uparrow 1} \\ & + 0.8172 T_{\uparrow 2} + 143.0 T_{\downarrow 1} - 314.4 T_{\downarrow 2} + 27.654 \end{aligned} \quad (8.4)$$

A plot of the resulting predictions is shown in Figure 8.20 below.

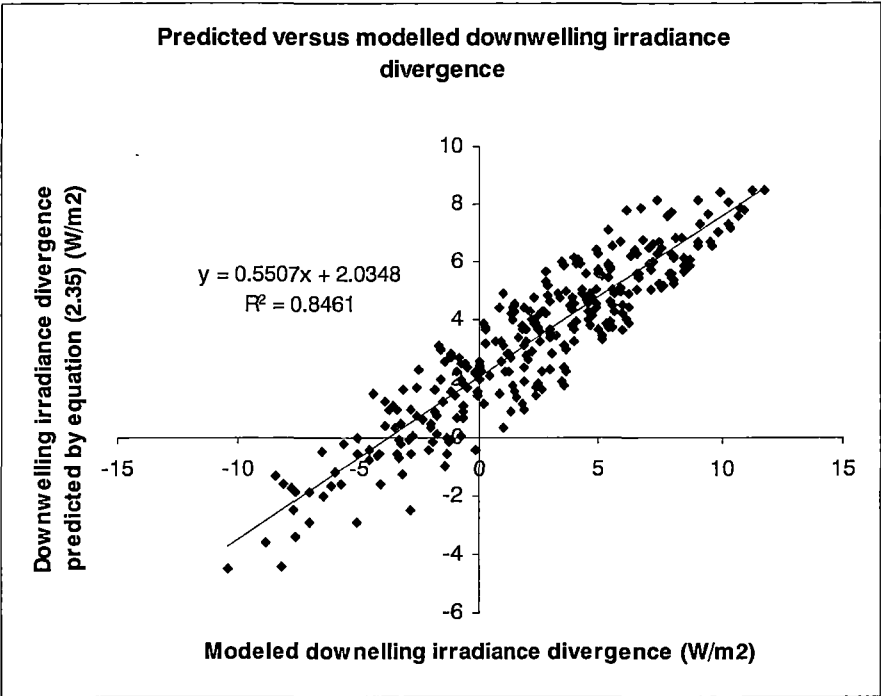


Figure 8.19. $divL_{\downarrow}$ predicted by equation (2.35) versus directly modeled $divL_{\downarrow}$. $N=300$, RMS $(x_i - y_i)$ error is 2.48 W/m^2 .

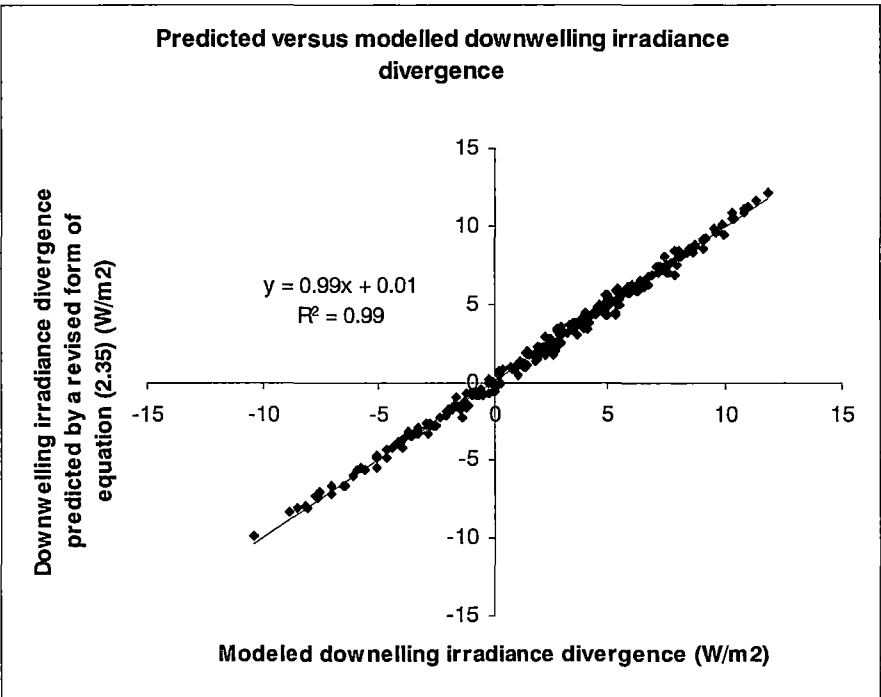


Figure 8.20. $divL_{\downarrow}$ calculated via equation (8.4), a revised form of equation (2.35) versus directly-modeled $divL_{\downarrow}$. $N=300$, RMS $(x_i - y_i)$ error is 0.32 W/m^2 .

The plot shown in Figure 8.20 demonstrates a vast improvement over equation (2.35) in the accuracy of the prediction. In doing so it provides validation of the concepts introduced in Chapter 2 for prediction of $divL_{\downarrow}$ from two-channel brightness temperature measurements.

There were very few measurements of downwelling brightness temperatures $T_{\downarrow 1}$ and $T_{\downarrow 2}$ made during the airport field measurement program - hourly measurements were made on the 1st of May. Further, those measurements that were made were subject to the same errors discussed in Sections 8.2 to 8.7 - specifically, the inability of the instrument to accurately measure the window-channel brightness temperature due to the unknown nature of its calibration curve beyond -18°C.

This lack of data and the known problems with the existing data yielded a requirement for an alternative means of predicting $divL_{\downarrow}$. The aim was to characterise the divergence produced by the temperature profile below ten metres as a function of the downwelling irradiance at ten metres, resulting in a linear function of the form

$$divL_{\downarrow} = c_1 L_{\downarrow} + c_0$$

for each instance of the temperature profile. The Eppley-measured values of L_{\downarrow} could then be used to calculate $divL_{\downarrow}$ for each individual case.

The 60 hourly temperature profiles measured by the tower-mounted instruments and described in the previous section were used as the profile “bases” between zero and ten metres. The BoM’s sonde-measured atmospheric profiles at 21:00 each night were then used to provide five alternative profile “caps” from 22 metres to TOA.

Every combination of these 60 profile bases and five caps were then fed to the MODTRAN code as input profiles. From the resulting files, directional radiances at 0, 15, 30, 45, 60 and 75° zenith angle were extracted and integrated to give the downwelling irradiance at ten and zero metres. The downwelling irradiance divergence was then calculated for each case by subtraction.

To test the validity of the modeled values of L_{\downarrow} that were used in the calculation of regressions for each profile base, the values corresponding to each profile cap were compared to the corresponding Eppley measurements at 21:00 on each night. The results are presented in Table 8.7 below. The results validate MODTRAN’s predicted downwelling irradiance values.

Date	MODTRAN-predicted L_{\downarrow} (W/m^2)	Eppley-measured L_{\downarrow} (W/m^2)
01/05/2002	283.4	283.6
10/05/2002	293.8	290.4
13/05/2002	274.7	272.9*
14/05/2002	274.7	274.1
18/06/2002	247.3	245.6*

Table 8.7. MODTRAN-predicted and Eppley-measured L_{\downarrow} at 21:00 on each measurement night. RMS ($x_i - y_i$) error is 1.90 W/m^2 . ‘*’ denotes measurements for which 1 octa of cloud was present.

An example plot of $divL_{\downarrow}$ against L_{\downarrow} is shown in Figure 8.21 below. This plot corresponds to the profile base at 0:00 on the 2nd of May.

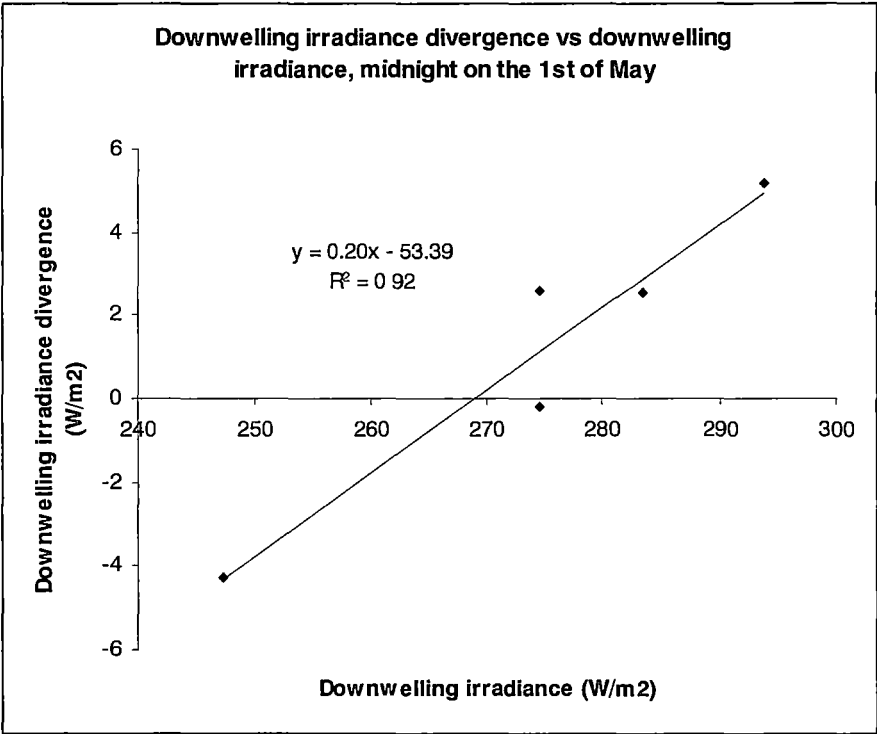


Figure 8.21. Downwelling irradiance divergence versus downwelling irradiance, midnight on the 1st of May. N=5, RMS ($x_i - y_i$) error is 1.15 W/m^2 .

A linear regression fit of the type shown in Figure 8.19 was applied to the set of five values for each profile base. Across the full set of 60 profile bases, the RMS error in the regression fit was consistent, with minimum, maximum and average values of 1.02, 1.19 and 1.12 W/m^2 respectively.

For comparison, the RMS error in a similar regression fit across the data from all of the 60 profile bases simultaneously was 3.36 W/m². A further attempt at linear regression of the form:

$$divL_{\downarrow} = c_2L_{\downarrow} + c_1divL_{\uparrow} + c_0$$

across all of the data yielded an RMS error of 2.65 W/m². These relatively high values reinforced the choice of prediction method for *divL_↓*.

The response of the profile bases to *L_↓* also reinforced the benefits of spectral characterisation of *L_↓* in equation (2.35). Table 8.8 below is an example of the results from a single profile base and shows the effect of the spectral nature of *L_↓* on the resulting value of *divL_↓*. Data are from the same set plotted in Figure 8.19, with the modeled values for *T_{↓1}* and *T_{↓2}* also listed.

Profile cap:	21:00, 13 th May	21:00, 14 th May
<i>L_↓</i> (W/m ²)	274.71	274.69
<i>T_{↓1}</i> (°C)	9.5	7.7
<i>T_{↓2}</i> (°C)	-51.3	-50.1
<i>divL_↓</i> (W/m ²)	2.59	-0.17

Table 8.8. Illustration of the effect of the spectral character of the downwelling irradiance on the downwelling irradiance divergence. Profile base is from 0:00, 1st of May.

It can be seen in Table 8.7 that the value of *L_↓* is almost identical in each case. However the spectral character - as evidenced by the brightness temperatures in window and active channels - differs significantly. The downwelling irradiance divergence also differs significantly, indicating that the spectral character of the downwelling irradiance is an important contributor to the downwelling irradiance divergence. Data from the other 59 profile bases exhibited the same behaviour.

It was this differentiation (and therefore significant accuracy) that was lost in the choice of prediction method for *divL_↓*. However with Eppley-measured *L_↓* values as the only trustworthy downwelling data available, the choice was borne out of necessity.

The method described above yielded hourly values of $divL_{\downarrow}$ for use in calculation of values of the net irradiance divergence $divL$. These are analysed and discussed in the next chapter. The dependence of this method on MODTRAN results and Eppley-measured downwelling flux is a weakness but was required due to the measurement program and the problems associated with measurement of window-channel sky brightness temperatures. This section has also addressed the suitability of the original proposed method and found much to reinforce its validity.

8.13 Examination of the discrepancy between measured and predicted upwelling radiance R_{\uparrow}

In Section 8.8 the instrument's active-channel brightness temperatures were shown to be systematically higher than the MODTRAN-predicted brightness temperatures, with an offset in the linear fit between the two of approximately 0.5 °C.

The effects of this offset were minimised throughout the other sections by linear correction of the DCR's active-channel brightness temperature. However the cause for the discrepancy was not immediately obvious. The early sections of this chapter dealt with various revision strategies for overestimation of the DCR-predicted downwelling irradiance, but in that case the fault was immediately identifiable as that of the prediction equations, given that the MODTRAN results showed excellent agreement with the Eppley pyrgeometer. In the case of upwelling radiances however, there was no reference instrument with which to compare the MODTRAN and DCR results.

A further complication was the coupling between the modeled and DCR-measured results due to the use of the DCR's window-channel brightness temperature measurement as the ground brightness temperature in the MODTRAN input profile. This left no avenue for detection of possible discrepancies in the DCR's window-channel measurements. However there was no reason to suspect that the discrepancies existed in these measurements, as the instrument was operating within its calibrated range both for the measured brightness temperatures and the internal instrument temperature.

Assuming that the instrument's window-channel temperature measurements were valid, there were two remaining hypotheses:

1. That the instrument was somehow overestimating the active-channel brightness temperature.

2. That the MODTRAN results were somehow underestimating the active-channel brightness temperature, either due to model itself or to missing or incorrect parameters in the input profiles.

Hypothesis 1 was the less likely of the two, given that (as mentioned above) the instrument was operating within its calibrated range. Active-channel brightness temperatures had also been shown to agree well with the modeled active-channel brightness temperatures for downwelling irradiance (see Section 8.6). Another possibility was a difference in surface emissivity in the two channels, although tests before and after the measurement program showed that the two channels read the same surface brightness temperature to within their expected error limits at negligible distance from the surface. While unlikely, a systematic instrument error could not be ruled out due the absence of a radiometric comparison.

Hypothesis 2 above had two possible sources: either the model was failing to fully represent the absorption and emission in the air column, or that the atmospheric conditions were not being correctly represented by the model input conditions. The former of these was not verifiable without additional measuring instruments or a published test of the model's performance over very short (10 metre) path lengths.

The second possible source was explored in an attempt to establish its likelihood. The desired result in the various tests performed was to achieve a divergence in the modeled brightness temperatures. Since there was no absolute reference for the window-channel brightness temperature, the effect on both temperatures of varying conditions was considered.

In the case that variation in conditions that caused an increase or decrease in the window-channel brightness temperature, it was assumed that the effect would be replicated in the DCR-measured brightness temperature. As that change would then be fed back into the model via the surface brightness temperature, only a divergence of the two brightness temperatures could cause an effective increase in the modeled active-channel brightness temperature.

The input variables that were considered in these studies were temperature, relative humidity, aerosol content (via the visibility input parameter) and liquid water droplet content.

Temperature and relative humidity variations were quickly discounted for two reasons. Firstly, a reliable profile of measured quantities was available from the tower data and so there was no reason to suspect that the input values did not represent the atmospheric conditions at any given time. Secondly, variations in these quantities were found not to be able to produce the required level of divergence between the brightness temperatures.

The aerosol content of the atmosphere was then considered. This was particularly relevant given the impact of the inclusion of variable visibility in the downwelling irradiance models (Section 8.5). Counter to this relevance was the fact that the variable aerosols in the downwelling irradiance models produced an increase in the window-channel brightness temperature over long path lengths, as opposed to the increase in active-channel brightness temperature over short path lengths that was sought in these tests. For that reason the predictive equations for short path length quantities were not revised for aerosol content in the same way as the downwelling irradiance equation was revised in Section 8.5.

A test was conducted using the model profile from 21:00 on the 1st of May. Ten models were run, with the visibility parameter ranging from 25.0 km down to 0.5 km. Brightness temperatures were then extracted from the modeled results. It was found that the difference in brightness temperatures across the full range of visibility values was 0.0095 °C in the active channel and 0.024 °C in the window channel. This was sufficient evidence to discount atmospheric aerosols as the cause of the observed temperature discrepancies.

The final test involved simulating liquid water droplet condensation in the atmosphere using a cloud layer between zero and ten metres. The relevant parameter in the MODTRAN input was the liquid water droplet density in grams per m³. The input profile for 21:00 on the 10th of May was used as a base to create six model inputs with liquid water droplet density ranging from zero to 16.64 g/m³. Broadband radiances and brightness temperatures in both channels at zero and ten metres were extracted from the results.

The behaviour of the difference between active and window channel brightness temperatures at 10 metres is shown in Figure 8.22 below. Figure 8.23 shows the active and window channel brightness temperatures that contribute to the difference.

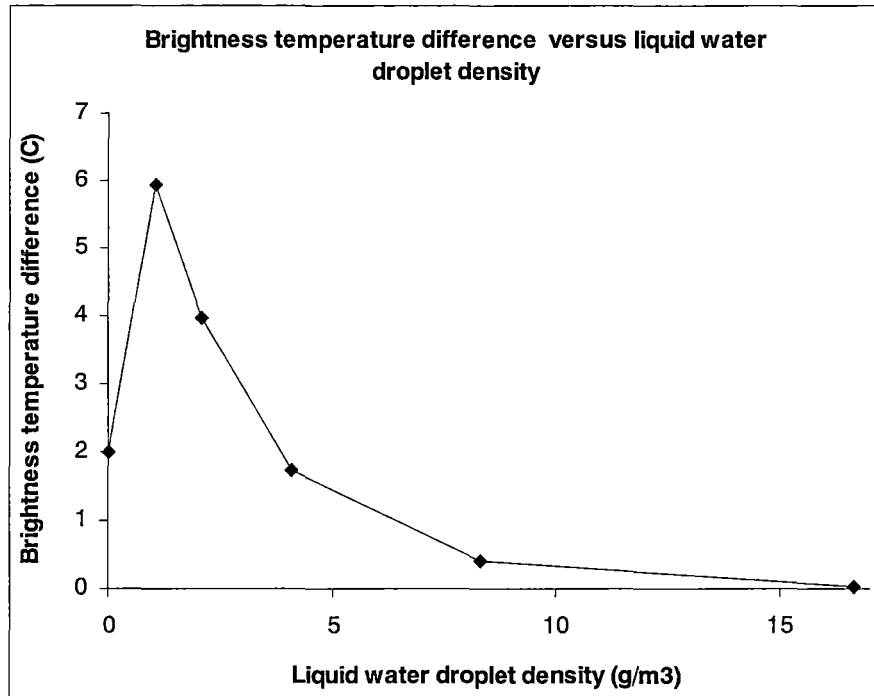


Figure 8.22. Difference between modeled upwelling active and window channel brightness temperatures versus liquid water droplet density in a layer between 0 and 10 metres.

Examining the difference between the window- and active-channel temperatures in Figure 8.23 reveals the sources of the divergence and convergence evident in Figure 8.22. The active-channel brightness temperature increases quickly with increasing liquid water droplet density, reaching a saturation point at approximately 4 g/m^3 . The window-channel brightness temperature, however, drops to a minimum at 1.02 g/m^3 before increasing in the same fashion but less rapidly than the active-channel brightness temperature. It shows evidence of approaching saturation at the maximum modeled 16.64 g/m^3 .

The initial drop in the window-channel brightness temperature is impossible to explain given that the surface temperature is 5.8°C and that minimum air temperature in the ten-metre profile is 9.49°C . Both values tend towards a value of approximately 10.9°C at saturation, which is central to the air temperatures at 4.5 metres (10.5°C) and 10 metres (11.4°C).

These effects on both window and active-channel brightness temperature have strong implications for this study. Their practical effects on the field measurements are unknown due to the lack of an independent measure of the liquid water droplet density. The divergence of the brightness temperatures could be used to explain the discrepancy in the modeled and measured active-channel temperatures, although the dependence of the existence of the

temperature divergence on the density would weaken the argument. Further, they are an unlikely cause for the consistent underestimation by the model, as this would require a reasonably consistent liquid water droplet density across all measurements on all nights, which is an unlikely scenario.

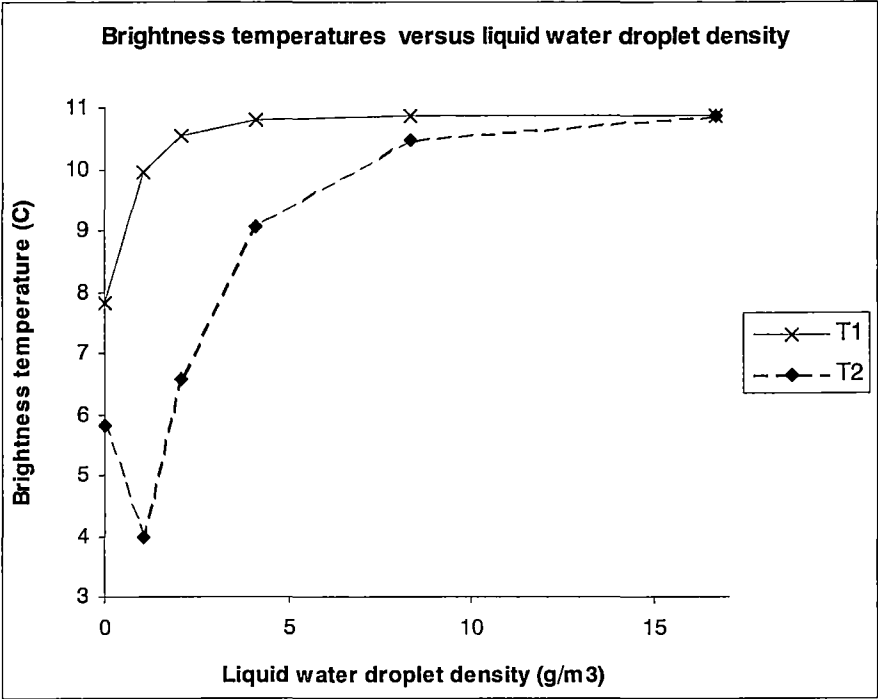


Figure 8.23. Modeled upwelling active-channel (T1) and window-channel (T2) brightness temperatures versus liquid water droplet density.

The potential effect of the liquid water droplets – if present – on the predictive equations and the related assumptions is much greater. The most fundamental assumption in the predictions of radiance and irradiance divergence is that the window-channel brightness temperature measured at ten metres accurately represents the window-channel brightness temperature at zero metres (equation (2.9) and Section 2.3). This behaviour was consistently observed for all modeled parameters other than the liquid water droplet content.

The radiance divergence is essentially a function of the active-channel temperature at zero and ten metres. The active-channel brightness temperature at zero metres is represented in the predictive equations by the window-channel brightness temperature at ten metres. If this assumption of equality (to within the specified accuracy) is not present, the validity of the predictive equations is compromised. The window-channel temperature variation described above breaks the assumption that the window-channel brightness temperature at ten metres accurately represents the active-channel brightness temperature at zero metres.

It is unlikely that these liquid water droplet effects had an impact on the measured field data – condensation was not noted during the measurement period and would likely have resulted in a highly variable visibility during the night, which was also not recorded by the BoM for any of the measurement nights. However this exploration yielded an important caveat for future use of the predictive equation method.

This result also has important implications for remote sensing applications – a very thin condensation layer at the surface could conceivably cause window-channel surface temperature variations of -2 to $+5$ K (based only this single test). Many remote sensing models allow for the removal of the atmosphere's effects via the use of models such as MODTRAN, but this effect may need to be considered as a possible source of large errors.

This result, although important, left the active-channel brightness temperatures unexplained. It is suspected that the differences observed were due to a failure of the MODTRAN model to predict the full effects of the atmosphere on the active-channel radiance over such a short path length, but additional measurements would be required to test that hypothesis. In this case the model profiles were available and were used to revise the brightness temperatures based on MODTRAN's predictions.

For the future intended application of the DCR as a stand-alone instrument for measuring radiance divergence, this hypothesis will need to be proved or replaced with an alternative. Improvement of the accuracy of the instrument would quickly establish the true cause of the discrepancy. The observed offset of 0.45 °C in the active channel brightness temperatures was within the standard error expected in the DCR's active-channel measurements. Measurements with an accuracy of 0.1 °C or better would indicate whether the offset was genuinely systematic or due to random (internal instrument effects) or pseudo-random (unmeasured atmospheric effects) variation.

8.14 Summary

This Chapter has described the conversion of measured brightness temperatures in two narrow band channels into the various quantities described in Chapter 2. A comparison between longwave downwelling irradiance predicted from narrow band measurements and measured by an Eppley pyrgeometer initially yielded poor results, with RMS errors of 66.3

W/m^2 for predictions using equation (2.34) and 50.0 W/m^2 for predictions using equation (2.33).

The results were improved by rejecting the data from the 30th July and further by reparameterisation of equation (2.34) based on new model profiles that included variable visibility. Even further improvement was gained by adjusting the window-channel brightness temperatures for a suspected change in the calibration curve below the calibration range of -18°C . These changes together yielded improvements in the RMS errors: 26.4 W/m^2 for the values predicted by the revised form of equation (2.34) and 9.3 W/m^2 for those predicted by the revised form of equation (2.33).

In Section 8.9, upwelling radiance divergence $\text{div}R_\uparrow$ was predicted by equation (2.28) from the original DCR-measured brightness temperatures. The RMS error between the predicted and modeled values was $0.94 \text{ W/m}^2/\text{steradian}$. Using equation (2.28) to calculate $\text{div}R_\uparrow$ from the modeled brightness temperatures yielded an RMS error of $0.08 \text{ W/m}^2/\text{steradian}$. The linear correction of the DCR's active-channel brightness temperature reduced the RMS error between the predicted and modeled values of $\text{div}R_\uparrow$ from 0.94 to $0.64 \text{ W/m}^2/\text{steradian}$. Comparison of predicted and modeled values of $\text{div}R_\uparrow$ at angles away from the vertical (see Section 8.10) yielded an RMS error of $0.59 \text{ W/m}^2/\text{steradian}$.

Prediction of the upwelling irradiance divergence $\text{div}L_\uparrow$ was possible via equation (2.31), which uses $\text{div}R_\uparrow$ predicted by equation (2.28), and equation (2.32), which uses the brightness temperatures directly. Equation (2.31) failed to properly predict $\text{div}L_\uparrow$ from modeled brightness temperatures and was therefore excluded from consideration with the measured brightness temperatures. Equation (2.32) predicted $\text{div}L_\uparrow$ from modeled brightness temperatures with an RMS error of 0.32 W/m^2 , justifying its use with the measured brightness temperature data. The values predicted from corrected brightness temperatures gave an RMS error of 2.69 W/m^2 when compared with directly modeled values.

The downwelling irradiance divergence $\text{div}L_\downarrow$ was calculated by necessity from a combination of Eppley-measured L_\downarrow and MODTRAN-derived relationships between $\text{div}L_\downarrow$ and L_\downarrow (see Section 8.12). However a revised form of equation (2.35) was shown to be able to calculate $\text{div}L_\downarrow$ from modeled brightness temperatures with an RMS error (against directly modeled values) of 0.32 W/m^2 , compared with an RMS error of 2.48 W/m^2 when the original form of equation (2.35) was used.

Chapter 9

Fieldwork results III – radiative divergence and cooling

9.1 Introduction

This Chapter details and examines the behaviour of irradiance divergence and observed cooling rates with time, during the course of each night.

The net longwave radiative flux divergence $divL$ was calculated by addition of the downwelling and upwelling components $divL_{\downarrow}$ and $divL_{\uparrow}$ that were derived in Sections 8.12 and 8.11 respectively.

Longwave radiative cooling rates were then calculated from $divL$ via:

$$\frac{\Delta T}{\Delta t} = \frac{divL_{\uparrow} - divL_{\downarrow}}{\rho C_p H}$$

as discussed in section 2.2. For this study, the following values were used:

Δt , the period of time over which the change occurs: 3600 seconds

ρ , the density of the air mass (at 10°C): 1.246 kg/m³

C_p , the specific heat of the air mass: 1010 J/kg/°C

H , the height interval over which the divergences are measured: 10 metres

The density of the air mass was taken as its value at 10°C. The value at 0°C is 1.292 kg/m³, and the difference between these was well within the expected error in the measured quantities. The use of height rather than a volume in this equation relied on the assumption of horizontal homogeneity in the ground surface and atmospheric structure. This equation yields a cooling rate per square metre of the bounding surfaces above and below. This did not affect the results because the cooling rates calculated directly from measured temperatures were treated in the same manner. The quantities described above were used to calculate a set of hourly values for the predicted cooling rate in °C per hour.

The measured cooling rate was calculated by subtraction of hourly averages of the vertically averaged air temperature. The temperatures measured by each tower-mounted probe were weighted by the height interval represented by each probe and then averaged over the total ten-metre column height. This yielded an average value for every five-minute interval during the measurement period. These were then further averaged over each hour to give an hourly

average temperature on the half-hour. The measured cooling rate on the hour was then the difference between the hourly temperatures on the preceding and following half-hours. This yielded an hourly value for the measured cooling rate.

Both sets of cooling rate data were presented as positive cooling rates – positive values represent the cooling rate in °C per hour and negative values represent warming. The final data consisted of two sets (predicted radiative cooling and observed total cooling) hourly values between 18:00 and 06:00 and were filtered for times when the cloud cover was rated by the BoM at 0 octas. The behaviour of these data is explored for each night in the following section.

9.2 Radiative divergence and cooling of the air layer

Several plots are presented for each night. The first shows the behaviour of the following quantities with time:

- upwelling irradiance divergence,
- downwelling irradiance divergence,
- total irradiance divergence,
- air temperature stability index.

These quantities are displayed as hourly averages, calculated as detailed in the previous chapter.

The second plot resolves the air temperature stability index into its two components, the air temperatures at ground level (0.1m) and ten metres. The data, initially measured at five-minute intervals, were also averaged to give an hourly value. The data corresponding to cloud-free intervals were then selected for display so that the second plots would match the first.

Charts are also presented showing the radiative cooling and overall cooling with time – these values are calculated as detailed in the previous section. In addition, the average relative humidity over the layer (calculated via a height-weighted average) is also presented as a trend against time. Further charts of high temporal and spatial resolution data are also presented where valuable.

These charts are presented and discussed in this section for each night. The following section discusses the common elements in the nightly data and develops and interpretation of the data.

1st of May 2002

The 1st of May was the only night for which a full series (18:00 to 06:00) of hourly measurements were available. These are presented in Figures 9.1a, b, c, d, e and f below.

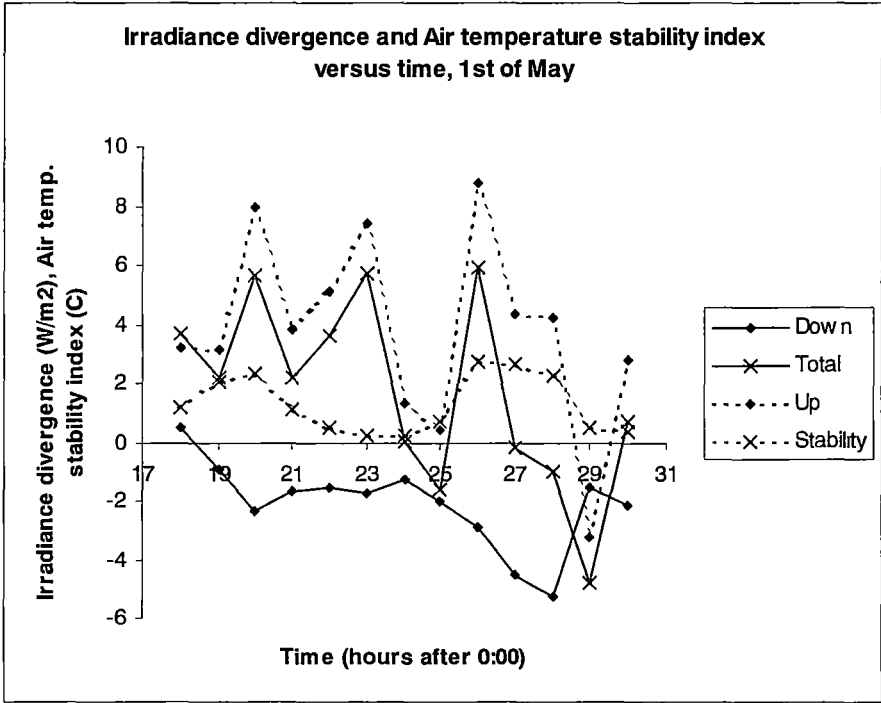


Figure 9.1a. Total and up/down component irradiance divergences and air temperature stability index, 1st of May.

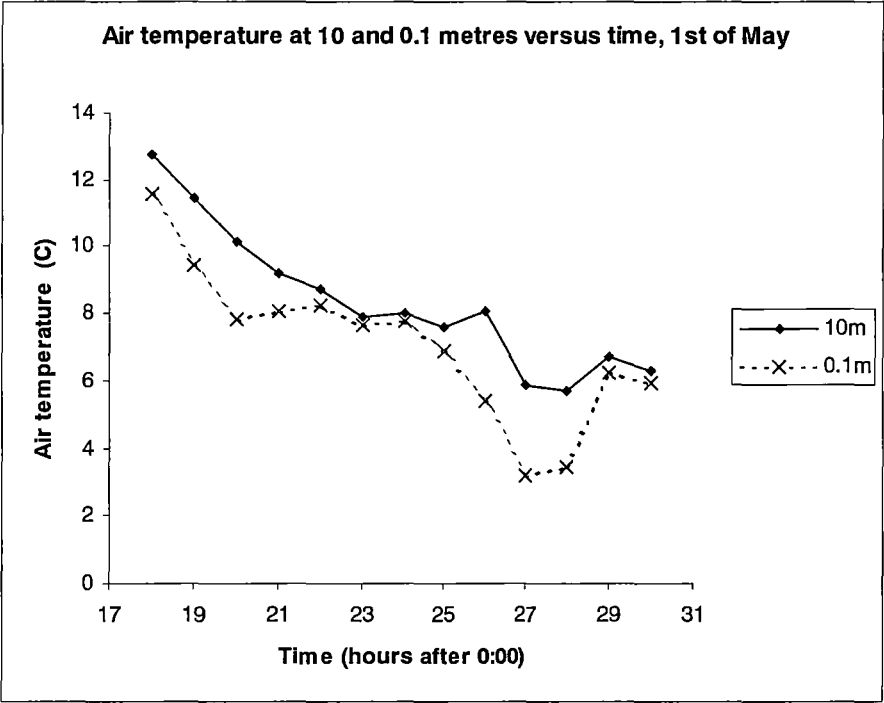


Figure 9.1b. Air temperature stability index components, 1st of May.

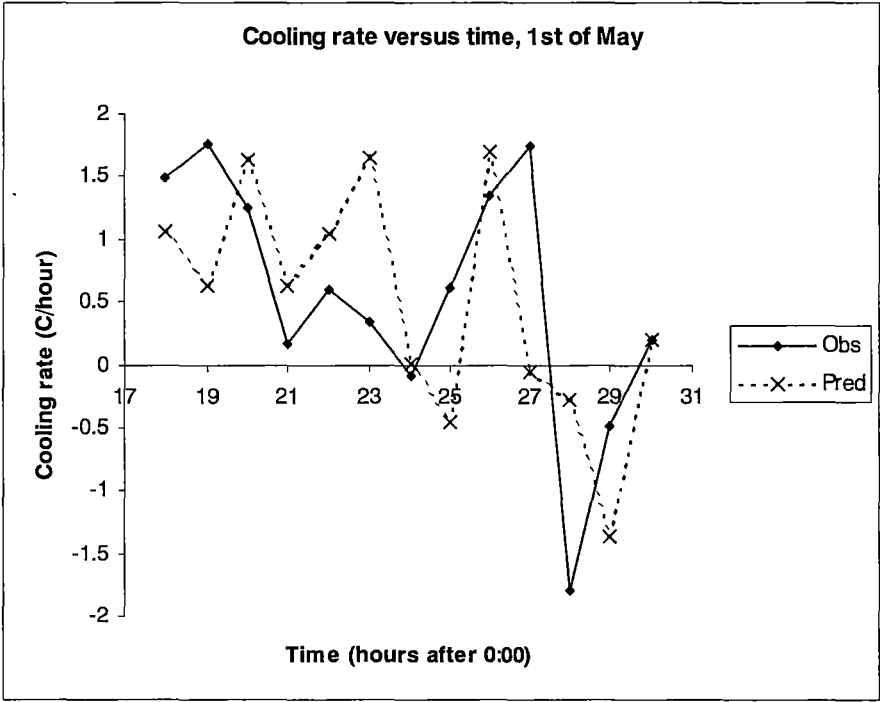


Figure 9.1c. Observed total hourly cooling rate ('Obs') and predicted radiative hourly cooling rate ('Pred'), 1st of May.

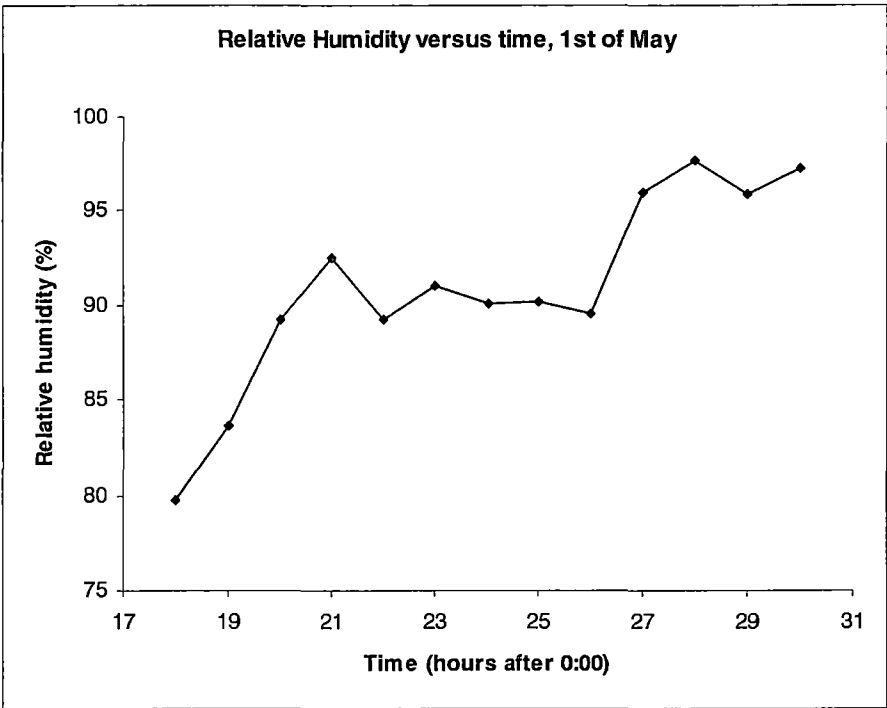


Figure 9.1d. Average hourly relative humidity over the ten-metre layer, 1st of May.

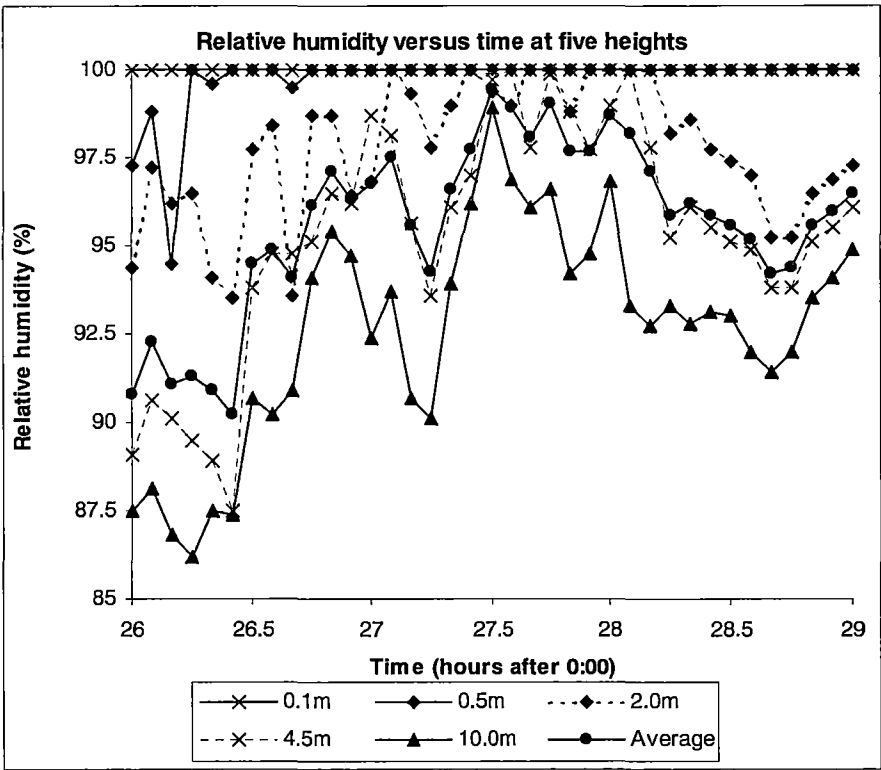


Figure 9.1e. Relative humidities at five heights and their height-weighted average, presented at five-minute temporal resolution. 26 – 29 hours, 1st of May.

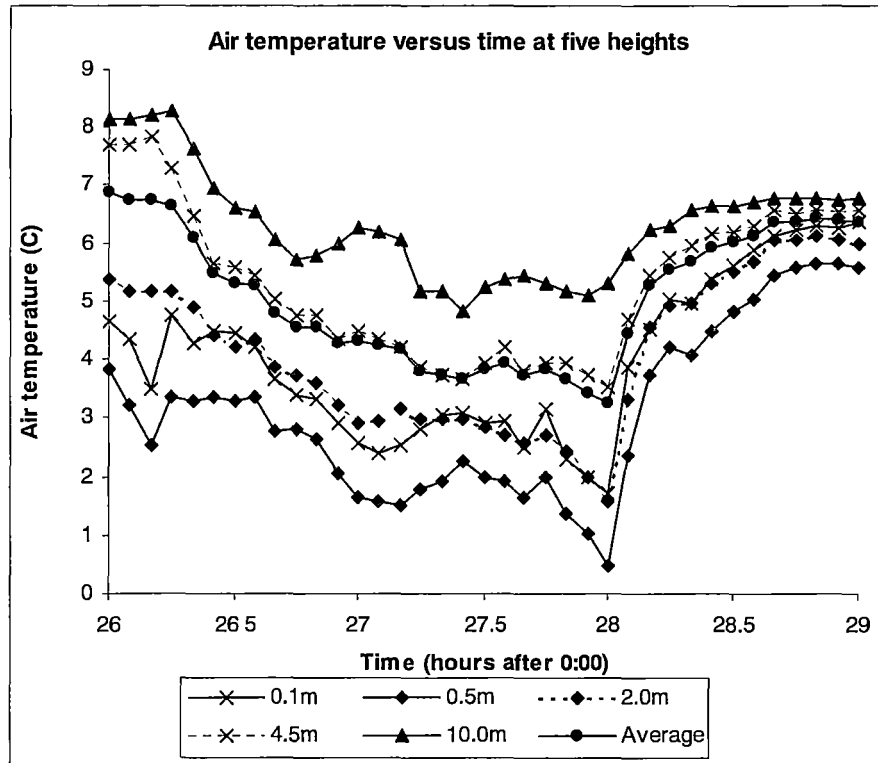


Figure 9.1f. Air temperatures at five heights and their height-weighted average, presented at five-minute temporal resolution. 26 – 29 hours, 1st of May.

Figure 9.1a shows that the general trend in the upwelling divergence was a decrease from a maximum at 18 hours to a minimum at 25 hours, followed by a sudden increase and a further period of gradual decrease. The magnitude of the negative downwelling divergence increased throughout the night. One noticeable feature is the strongly negative radiative divergence, occurring in both incoming and outgoing fluxes, at 20 hours. The stability index shows maximum values of around 2°C, but had near-zero values between 22 and 25 hours.

Further insight may be gained by examining the two temperature components of the air temperature stability index, shown in Figure 9.1b. A generally smooth decrease of the temperature at 10 metres was offset by two periods of stronger cooling at 0.1 metres, which yielded divergence of the two temperatures and therefore an increase in the stability index. It is likely that the effects of wind dominated the decreased cooling during the middle period of the night. Figure 7.1f shows an increase from near-zero mean wind speed at 20 hours to maximum values of 8 knots at 23 hours. A period of dead calm between 26.5 and 28 hours corresponds to the redevelopment of the cooling. Under medium to high wind speeds, turbulent mixing is considerable, resulting in near-isothermal conditions in the layer.

Figure 9.1c shows the importance of the effect of radiative cooling on the total cooling rate. The observed cooling followed the general trend of the radiative cooling early in the night. However after midnight the transition from strong cooling to strong warming was more rapid for the observed cooling rate than for the radiative cooling rate.

The behaviour of the relative humidity during the night is shown in Figure 9.1d. There were two periods of more rapid increase in the relative humidity, corresponding to the periods of most rapid cooling. The relative humidity reached saturation at some heights during the peak at 28 hours, as shown in Figure 9.1e. The relative humidity reached 100% at 0.5 metres at 26.25 hours and remained at 100% thereafter. It was also at or close to saturation level at 2.0 metres at 27 hours and on numerous occasions thereafter. The relative humidity at all heights increased rapidly between 27.25 and 27.5 hours. Figure 9.1f shows that temperatures at all heights increased rapidly immediately after 28 hours.

It is likely that the period of saturation at 28 hours is related to the strong warming that occurred at all levels after 28 hours. The release of latent heat during condensation of liquid water droplets is likely to produce near-isothermal conditions, causing increased mixing in the atmospheric column. Concurrent with latent heat liberation the increased mixing would transport warmer air from layers aloft down into the layer. It is likely that the observed warming is a combination of these two processes.

In summary then, these figures illustrate the expected cooling behaviour before midnight – a gradual decrease in the radiative cooling mirrored by a decrease in the observed total cooling. They also indicate a rapid change from strong cooling to strong warming at 28 hours, apparently due to the release of latent heat following the occurrence of saturation. The sudden warming had an immediate stabilizing effect, which gradually reduced the radiative cooling rate and yielded radiative warming. The condensation associated with the occurrence of saturation reduced the relative humidity from its maximum at 28 hours. There were no indications of the development of radiative fog in the BoM's visibility measurements or 'Present weather' records for that night.

10th of May 2002

The data for the 10th of May were significantly affected by cloud cover. Data between 22 and 25 hours inclusive were unsuitable for inclusion. The remaining data are plotted in Figures 9.2a, b, c, d, e and f below.

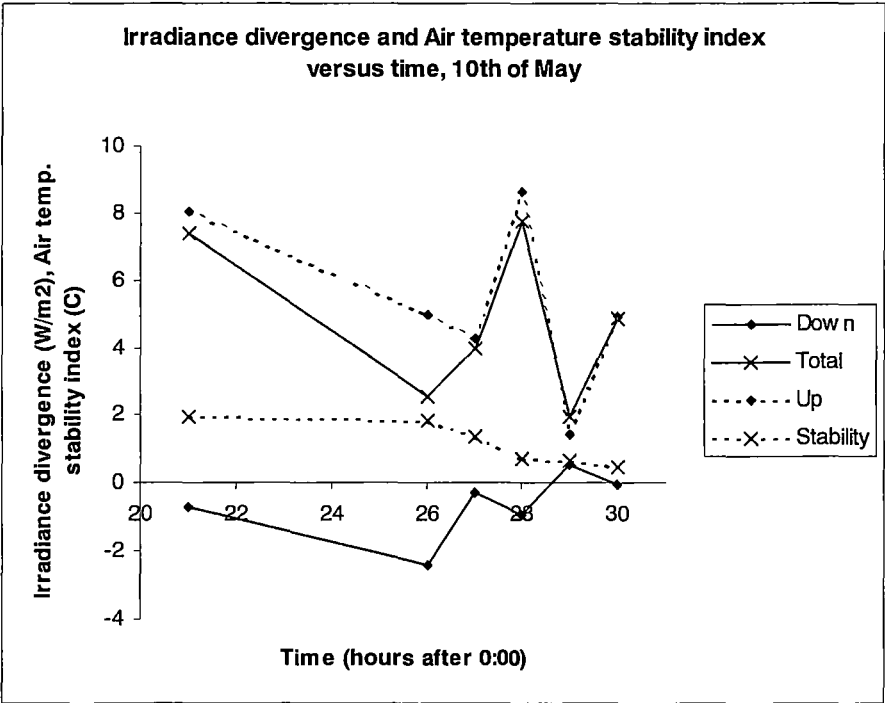


Figure 9.2a. Total and up/down component irradiance divergences and air temperature stability index, 10th of May.

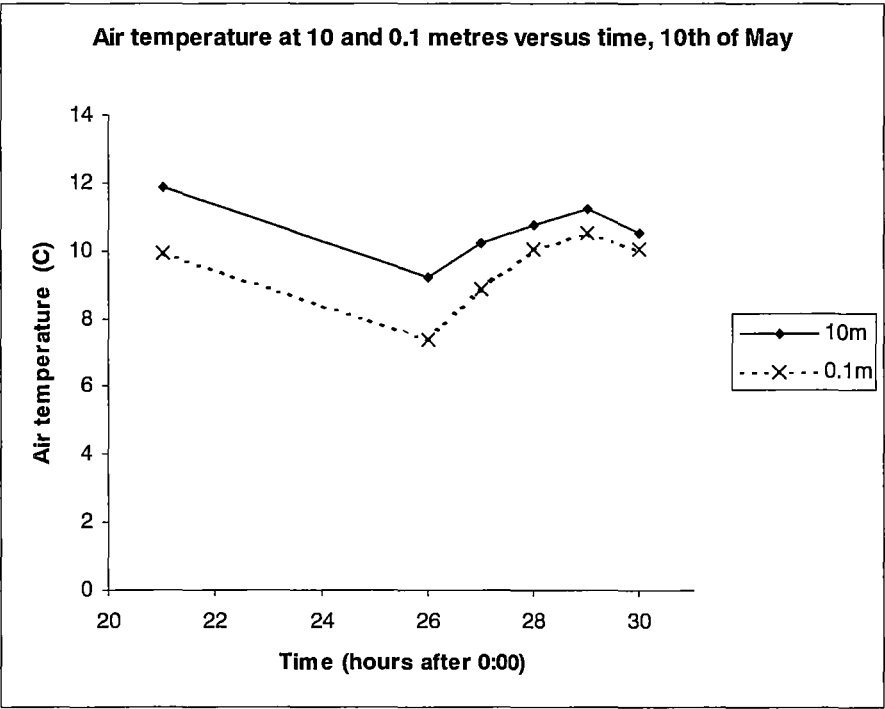


Figure 9.2b. Air temperature stability index components, 10th of May.

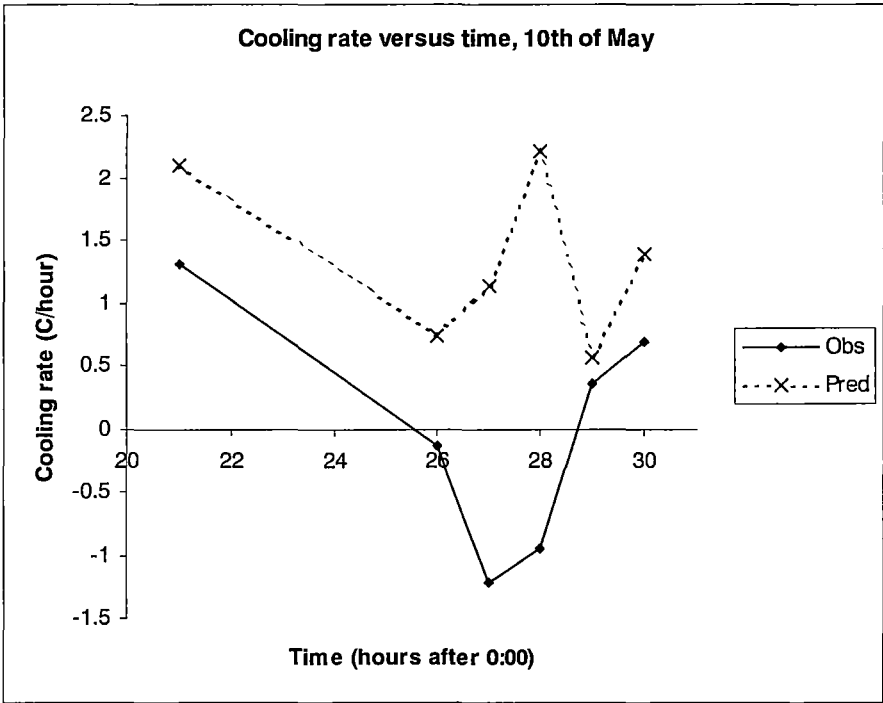


Figure 9.2c. Observed total hourly cooling rate (‘Obs’) and predicted radiative hourly cooling rate (‘Pred’), 10th of May.

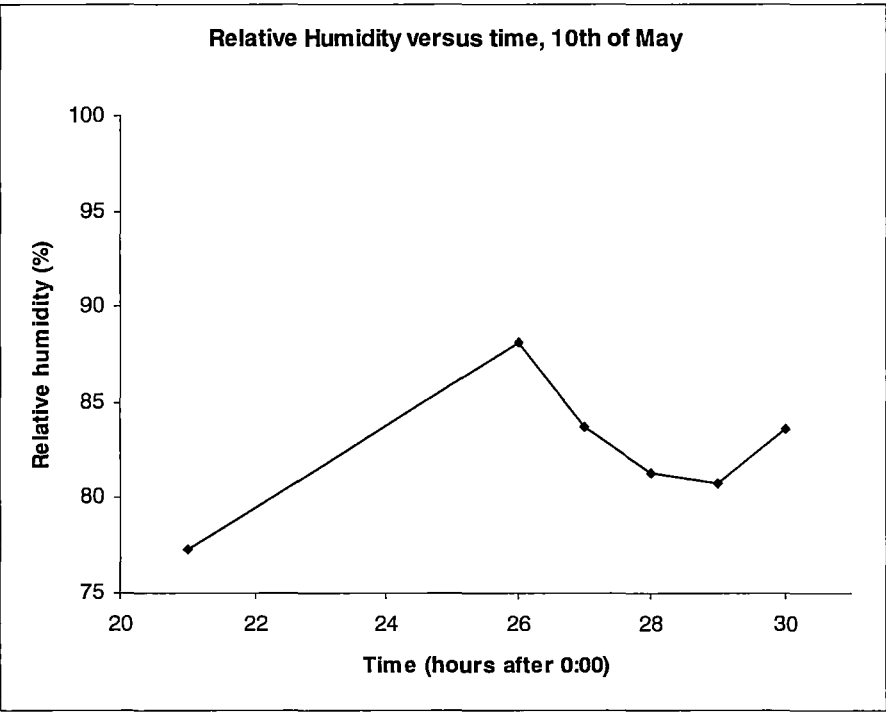


Figure 9.2d. Average hourly relative humidity over the ten-metre layer, 10th of May.

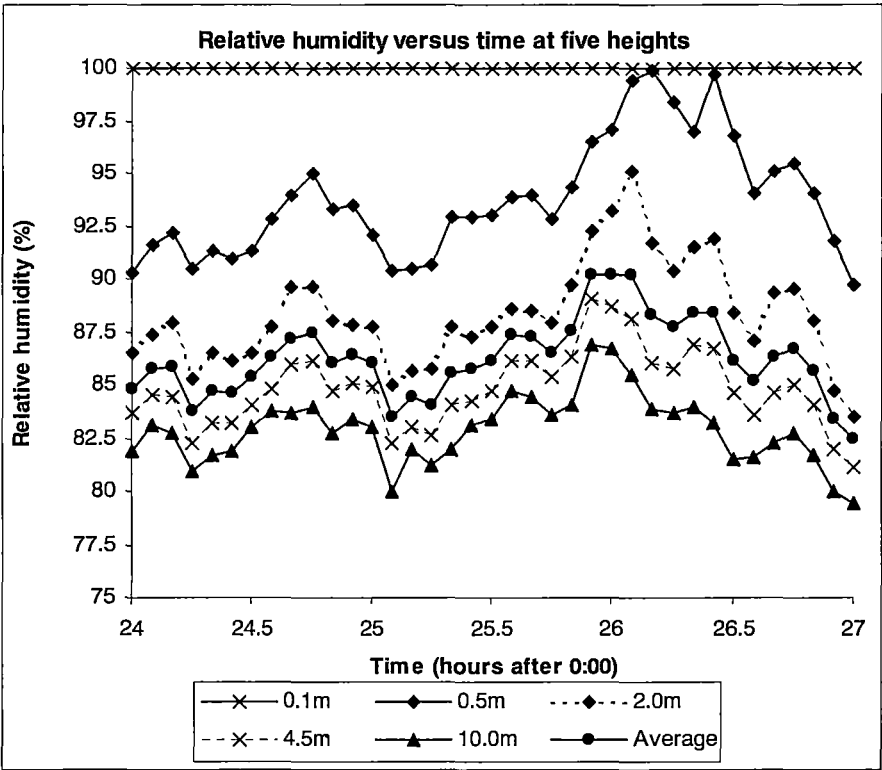


Figure 9.2e. Relative humidities at five heights and their height-weighted average, presented at five-minute temporal resolution. 24 – 27 hours, 10th of May.

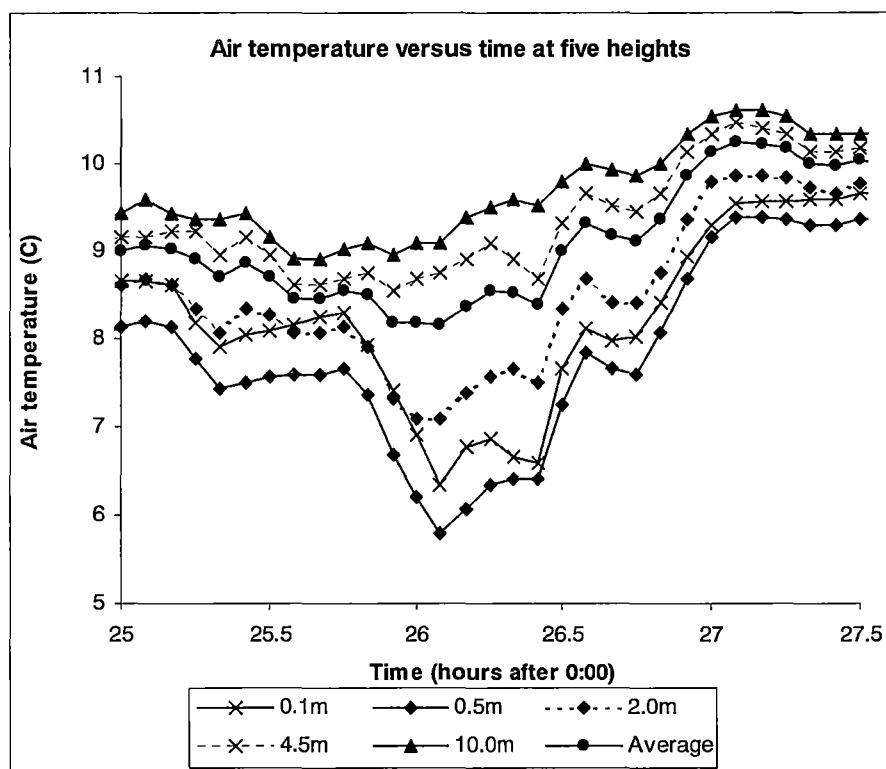


Figure 9.2f. Air temperatures at five heights and their height-weighted average, presented at five-minute temporal resolution. 25 – 27.5 hours, 10th of May.

Figure 9.2a shows that despite the missing data between 21 and 26 hours, there was evidence of an overall decrease in the upwelling and net longwave divergence. This was followed by a period of increase between 26 and 28 hours, followed by a further decrease. The downwelling convergence was minimal by comparison and had little impact on the total. The stability decreased gradually after 26 hours, corresponding to an increase in the half-hourly mean wind speed from 2 knots at 26 hours to 13 knots at 29 hours.

The air temperature stability index components plotted in Figure 9.2b indicate that the gradual decrease in the stability index was due to convergence of the two temperatures, which follow the same trend. Both temperatures demonstrated warming after 26 hours.

Examining the observed total cooling and predicted radiative cooling (Figure 9.2c), the overall trend across the two values at 21 and 26 hours indicated a decrease in both radiative and total cooling. Beyond 26 hours the radiative and total cooling are in complete disagreement, diverging between 26 and 28 hours and converging thereafter. The radiative cooling rate indicates strong cooling between 26 and 28 hours, while the observed total cooling rate indicates warming.

An overall increase in the relative humidity (plotted in Figure 9.2d) between 21 and 26 hours is followed by a steady decrease between 26 and 29 hours and a slight increase between 29 and 30 hours. None of these values indicated saturation. However the high-resolution values plotted in Figure 9.2e indicated brief saturation at 0.5 metres between 26 and 26.5 hours. The relative humidity increased rapidly at all heights between 25.75 and 26 hours and decreased gradually thereafter. The corresponding high-resolution temperature values plotted in Figure 9.2f indicated a sudden increase in temperature at all heights at approximately 26.5 hours.

In essence the behaviour of the temperature and relative humidity at approximately 26 hours mirrored their behaviour at approximately 28 hours on the 1st of May. A rapid increase in the relative humidity to saturation level was followed within half an hour by a transition from neutral cooling (strong cooling on the 1st of May) to moderate warming (strong warming on the 1st of May). This indicated again that the warming was likely to be due to the effects of the release of latent heat, which in turn was due to condensation caused by saturation.

In this case all of the effects were less prominent than on the 1st of May, possibly due to the damping effect of higher wind speeds. Table 7.7 shows that the mean wind speed for the entire night was 6.4 knots for the 10th of May, compared to 4.0 knots for the 1st of May. The wind was also more consistently strong. There was no data available before 26 hours to provide evidence for the role of radiative cooling in the initial transition to saturation. Again the BoM's visibility and 'Present weather' records did not indicate radiative fog.

13th of May 2002

The data for the 13th of May were slightly affected by cloud cover, with cloud recorded at 21 and 22 hours. The remainder of the night was unaffected. Plots of the available data are shown in Figures 9.3a, b, c and d below.

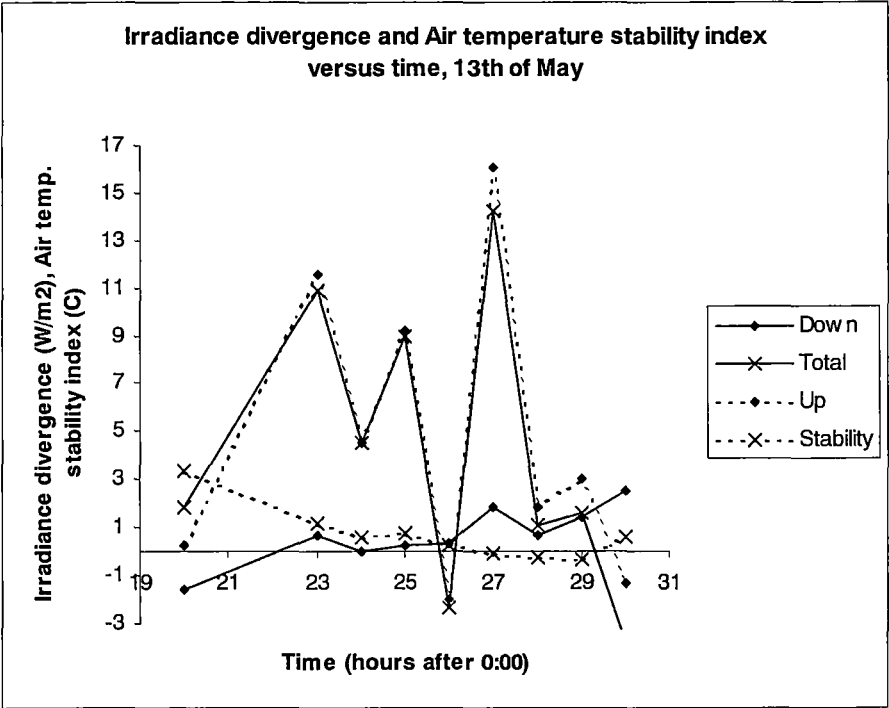


Figure 9.3a. Total and up/down component irradiance divergences and air temperature stability index, 13th of May.

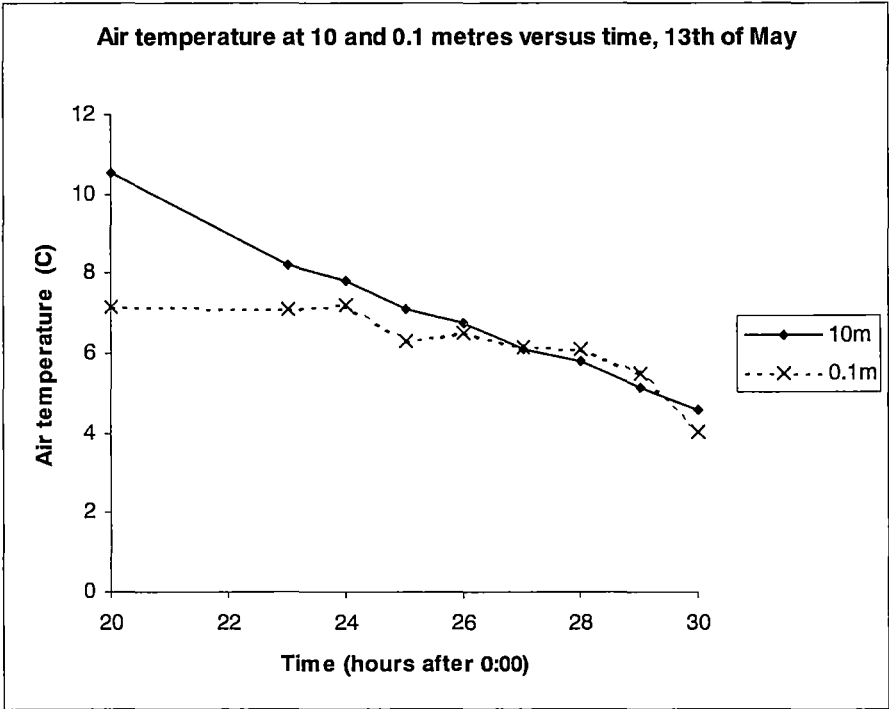


Figure 9.3b. Air temperature stability index components, 13th of May.

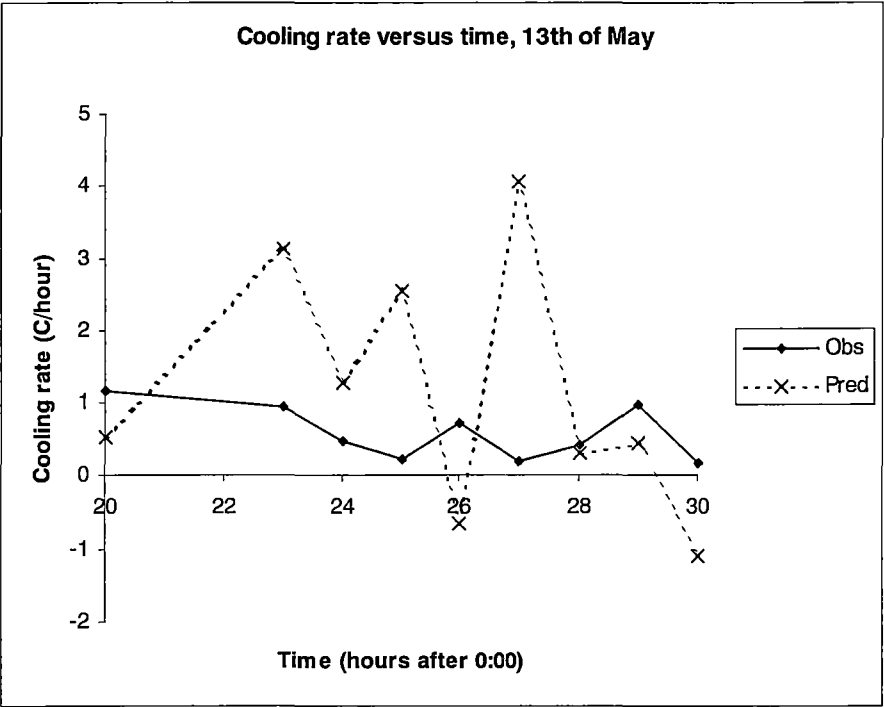


Figure 9.3c. Observed total hourly cooling rate ('Obs') and predicted radiative hourly cooling rate ('Pred'), 13th of May.

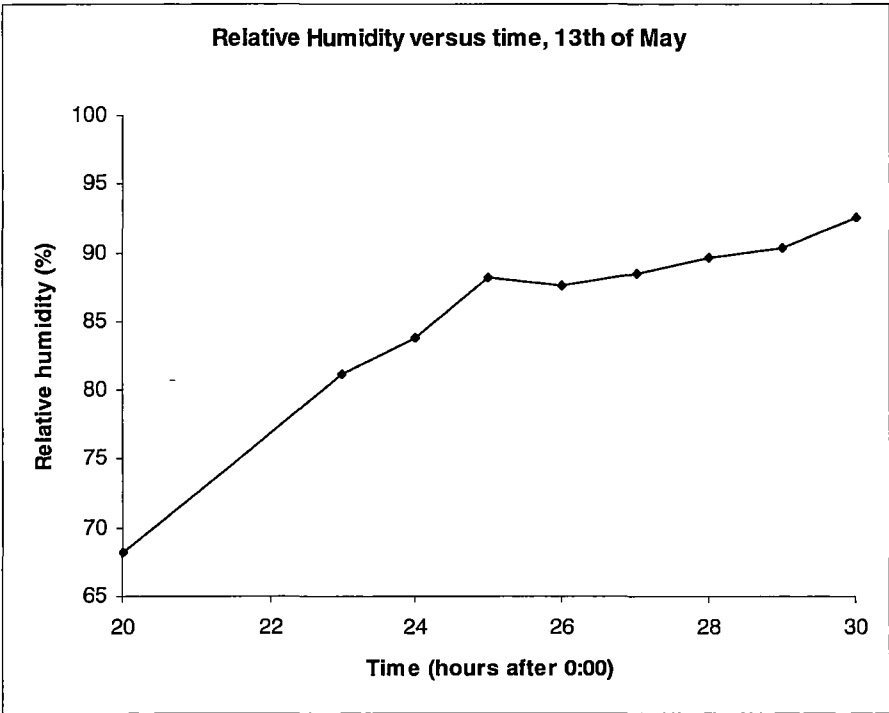


Figure 9.3d. Average hourly relative humidity over the ten-metre layer, 13th of May.

The divergence data plotted in Figure 9.3a was dominated by very large peaks in the upwelling divergence that were matched by large peaks in the total divergence, with the downwelling divergence making only a small contribution to the total as it increased steadily from weak negative divergence to weak divergence during the course of the night. The total divergence increased initially over the period from 20 hours to 23 hours, then decreased to a minimum at 26 hours, followed by the largest peak at 27 hours and a rapid decline to weak divergence at 28 hours and beyond. The air temperature stability index decreased steadily from strong stability at 20 hours to a minimum at 29 hours, increasing slightly between 29 and 30 hours.

The air temperature stability index components plotted in Figure 9.3b show the source of the steady decrease in the stability index. The temperature at 10 metres decreased more quickly than the temperature at 0.1 metres, yielding gradual convergence of the two.

The peaks in the net radiative divergence were evident in Figure 9.3c as peaks in the predicted radiative cooling rate. These are not reflected in the observed total cooling rate. While the cooling rate slowed gradually between 20 hours and 25 hours – consistent with the previous nights – there was no change to warming after 25 hours. The rate of cooling increased between 25 and 26 hours, and weak to moderate cooling was maintained thereafter.

The steady increase in the relative humidity (Figure 9.3d) throughout the night reflects the steady observed total cooling. At no time during the night was there an indication of the occurrence of saturation.

The data from the 13th of May showed moderate consistent observed cooling throughout the night. The inversion was strong initially but decayed steadily throughout the night. This moderate behaviour was not reflected in the predicted radiative cooling rates, which varied significantly with time and contained large peaks corresponding to the strongest predicted radiative cooling for all nights. It is likely that the effects of wind significantly countered the strong radiative cooling on this night. While the 13th of May was not on average the windiest night (see Table 7.7), the wind speed was consistently above 6 knots between 21 and 30 hours (Figure 7.3f). This wind would have decreased the stability index by mixing, and generated downward sensible heat flux to counter the radiative divergence.

14th of May 2002

The data from the 14th of May were very significantly affected by cloud cover, with data between 22 and 28 hours unusable due to cloud coverage rated between 1 and 3 octas. Plots of the available data are shown in Figures 9.4a, b, c, d and e below.

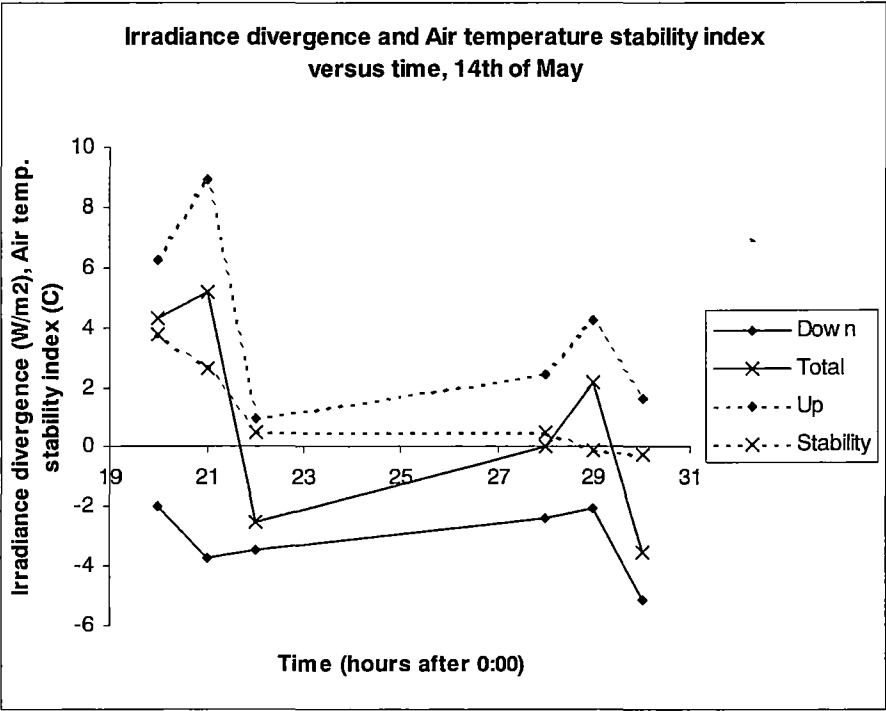


Figure 9.4a. Total and up/down component irradiance divergences and air temperature stability index, 14th of May.

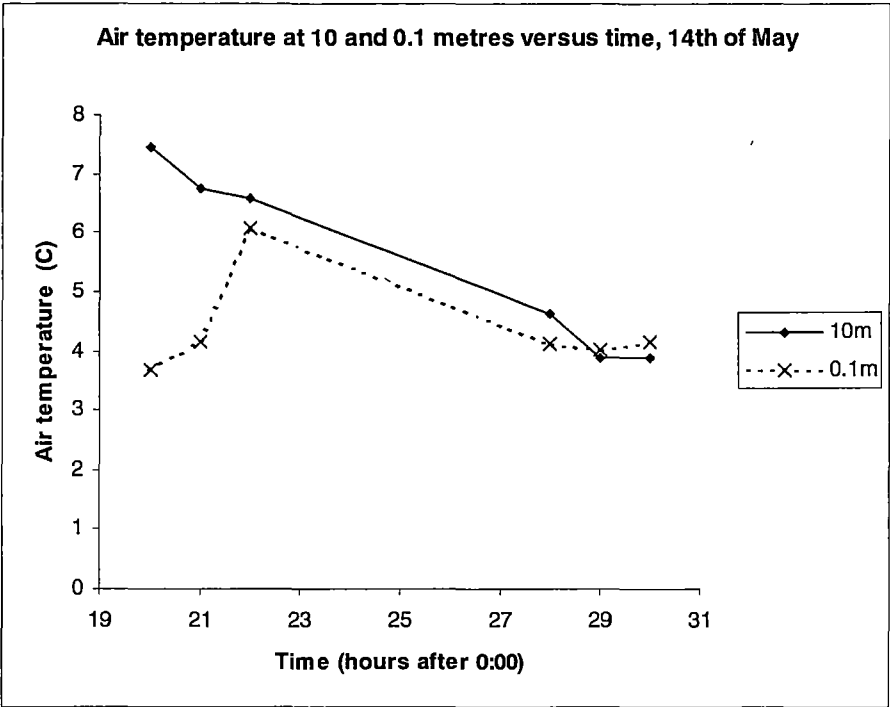


Figure 9.4b. Air temperature stability index components, 14th of May.

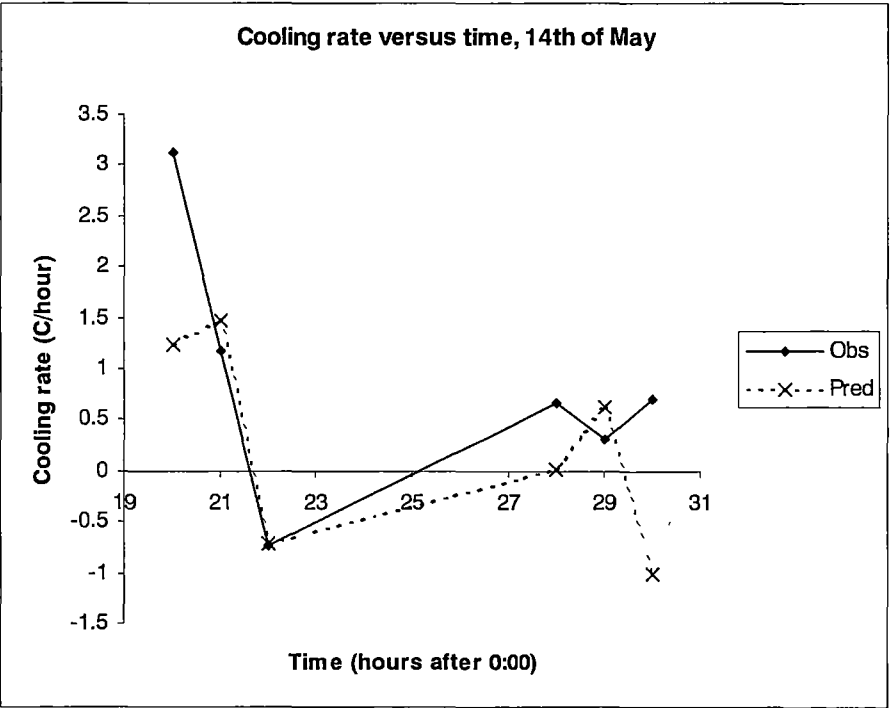


Figure 9.4c. Observed total hourly cooling rate ('Obs') and predicted radiative hourly cooling rate ('Pred'), 14th of May.

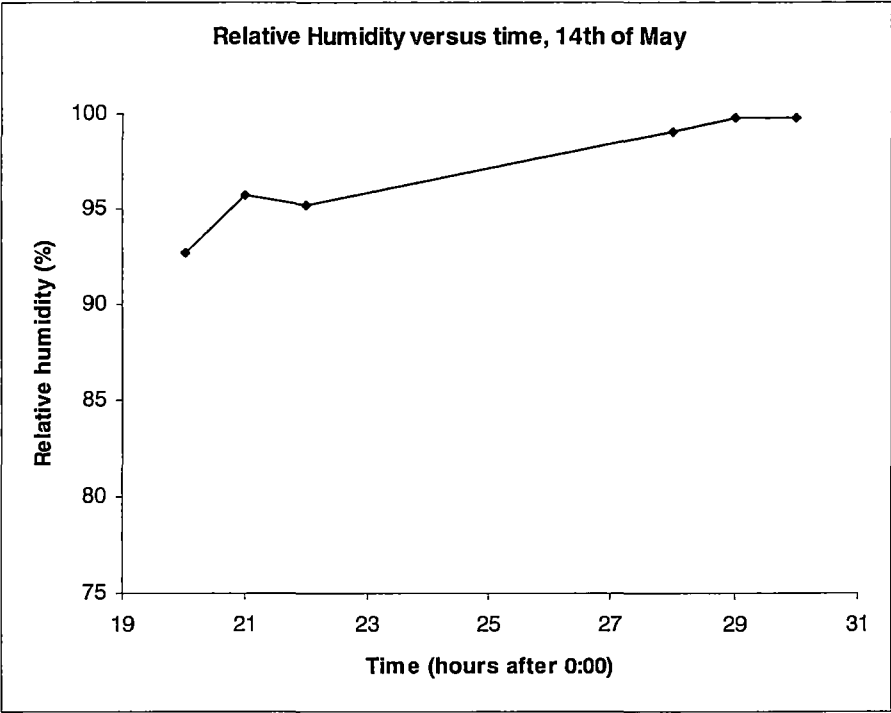


Figure 9.4d. Average hourly relative humidity over the ten-metre layer, 14th of May.

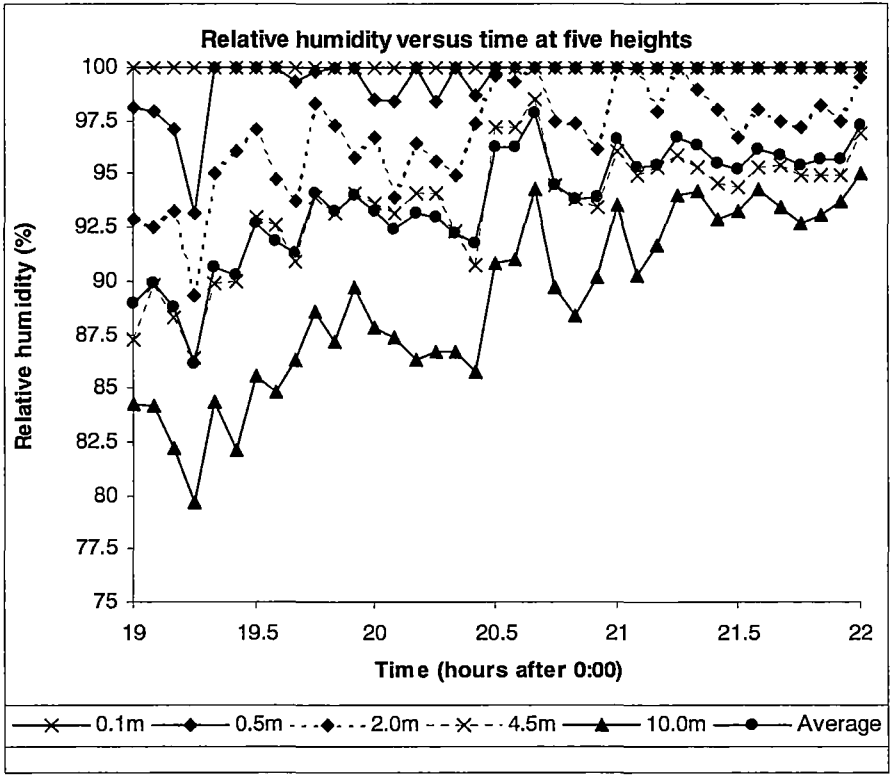


Figure 9.4e. Relative humidity at five heights and their height-weighted average, presented at five-minute temporal resolution. 19 – 22 hours, 14th of May.

Figure 9.4a shows that in this case the net longwave divergence was affected in equal measure by its up and downwelling components due a stronger downwelling convergence than was seen for other nights. The key feature in the total divergence was a sudden drop from moderate divergence to moderate convergence between 21 and 22 hours, preceded by a slight increase. Incidentally, this behavioral trend was repeated in the three hours of available data at the end of the night. In both cases the change was accompanied by a reduction in the air temperature stability index.

The source of the decreases in the stability index are evident in Figure 9.4b. In the early case, the temperature convergence was mainly due to strong warming at 0.1 metres. In the later case the temperature at 10 metres dropped, bringing it below the essentially constant temperature at 0.1 metres.

Figure 9.4c shows that the rapid change from cooling to warming between 21 and 22 hours was present in both the radiative and total cooling. The observed total cooling also exhibited a rapid decrease between 20 and 21 hours that was not reflected in the predicted radiative cooling. The radiative and total cooling rates were similar in magnitude at 28 and 29 hours. At 30 hours the predicted radiative rate had changed to moderate warming while the observed rate remained at light cooling.

The relative humidity was relatively high throughout the night (Figure 9.4d), however the high frequency data in Figure 9.4e shows frequent occurrences of saturation at 0.5 metres and multiple occurrences at 2.0 metres. The first instances of saturation precede the first dramatic decrease in observed cooling by approximately half an hour.

Despite the limited number of valid data for the 14th of May, there was evidence again to suggest that a dramatic decrease in the cooling rate was due to the release of latent heat during condensation. This event occurred much earlier in the night than similar events observed on the 1st and 10th of May. In this case the large magnitude of the initial cooling and the high relative humidity at the beginning of the night most likely combined to yield the rapid onset of condensation and therefore a corresponding rapid decrease in the cooling rate. The mean wind speed (Figure 7.4f) was favourable towards strong radiative cooling early in the night, with light or no wind between 18 and 21 hours. After 21 hours the wind speed became consistently moderate at approximately 4 knots. Overall the 14th of May had the lowest mean wind speed for the whole night (Table 7.7), of all the nights for which measurements were taken at the airport site.

The data in the early morning did not have any interesting features. The magnitude of the cooling or warming for both total and radiative cooling rates was small, and the relative humidity was at saturation levels. It is worthy of note that the Bureau of Meteorology's 'Present weather' records noted the occurrence of fog at 6:30 a.m. on the 15th of May (30.5 hours), accompanied by a decrease in the minimum visibility from 30km to 6km.

18th of June 2002

Cloud cover interrupted the data from the 18th of June in the early part of the night (before 23 hours) and the early part of the morning (after 28 hours). The remaining data are shown in Figures 9.5a, b, c, d and e below.

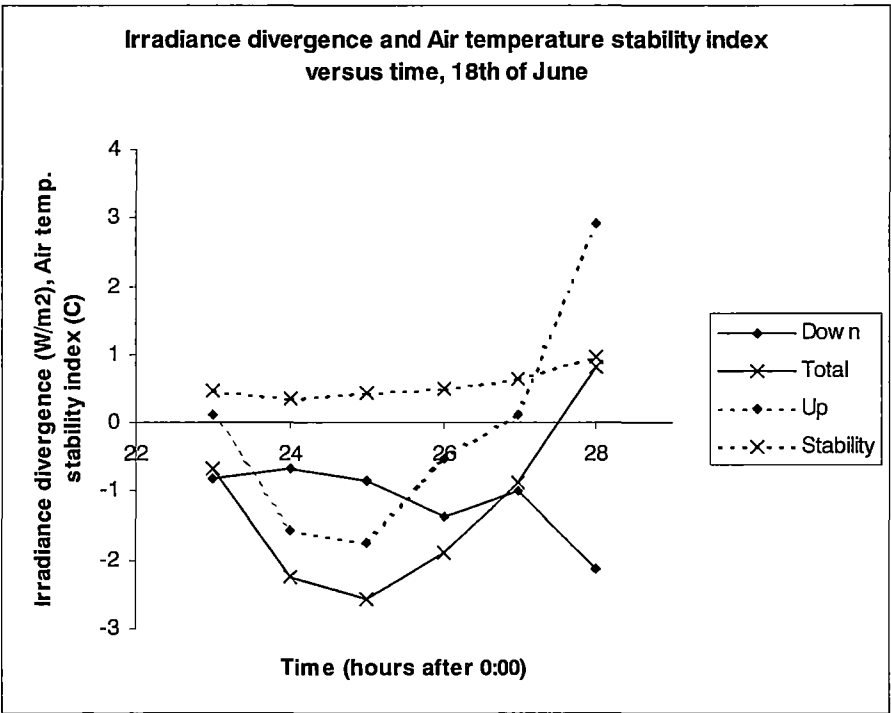


Figure 9.5a. Total and up/down component irradiance divergences and air temperature stability index, 18th of June.

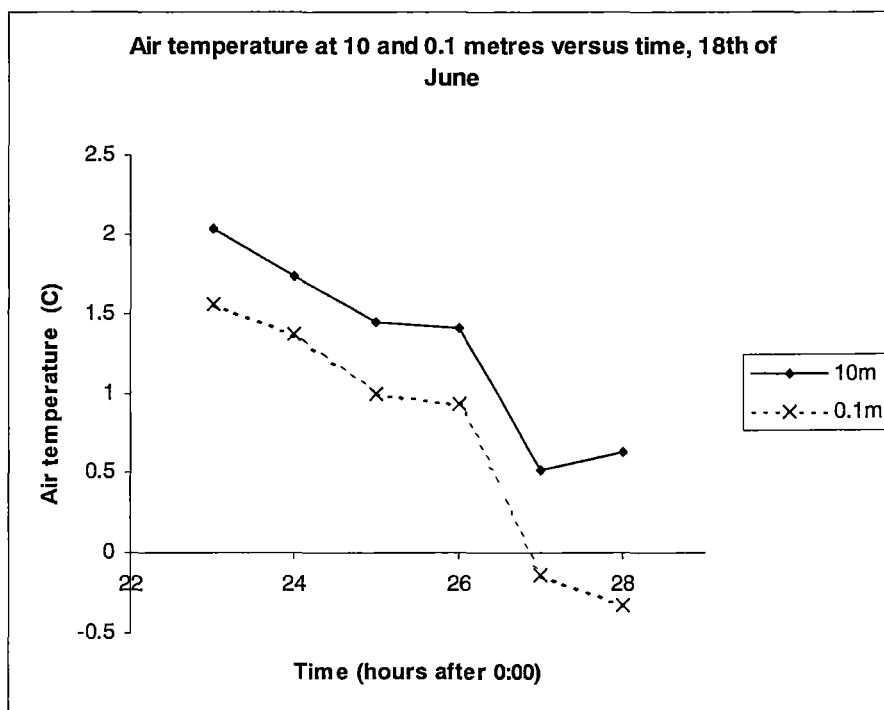


Figure 9.5b. Air temperature stability index components, 18th of June.

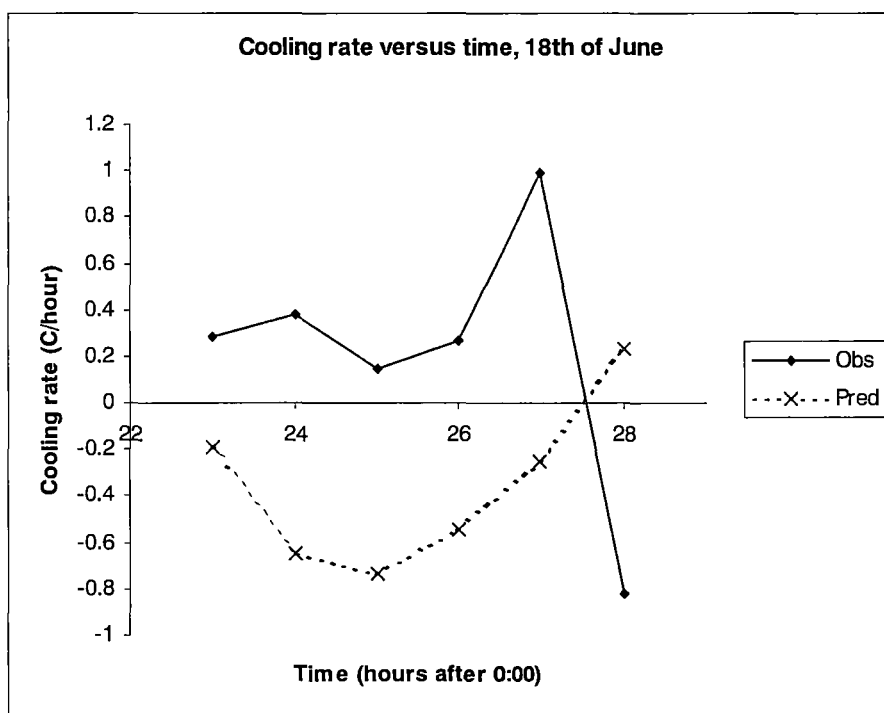


Figure 9.5c. Observed total hourly cooling rate ('Obs') and predicted radiative hourly cooling rate ('Pred'), 18th of June.

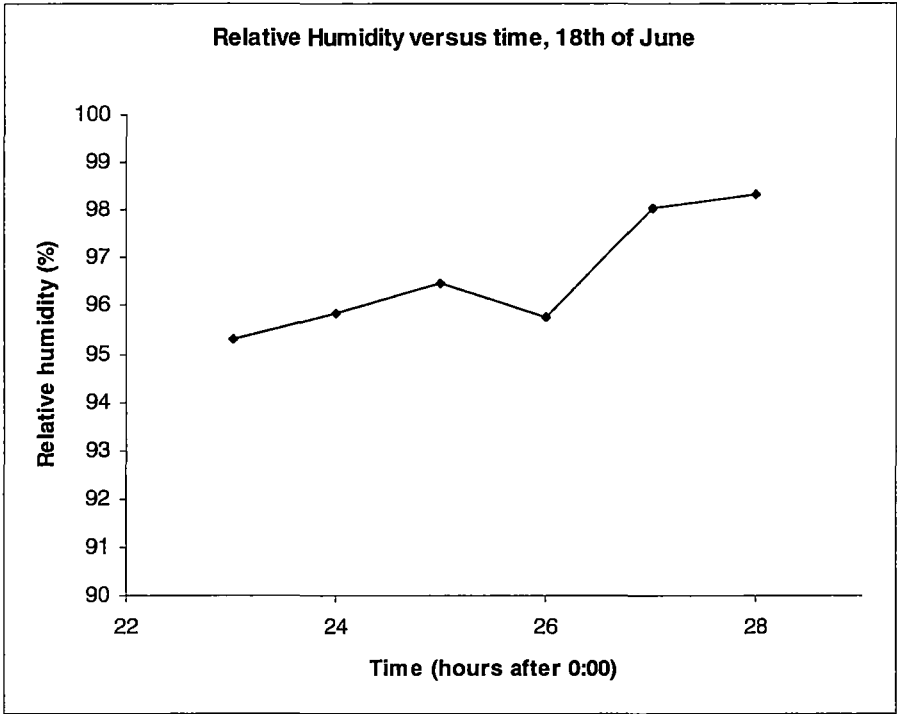


Figure 9.5d. Average hourly relative humidity over the ten-metre layer, 18th of June.

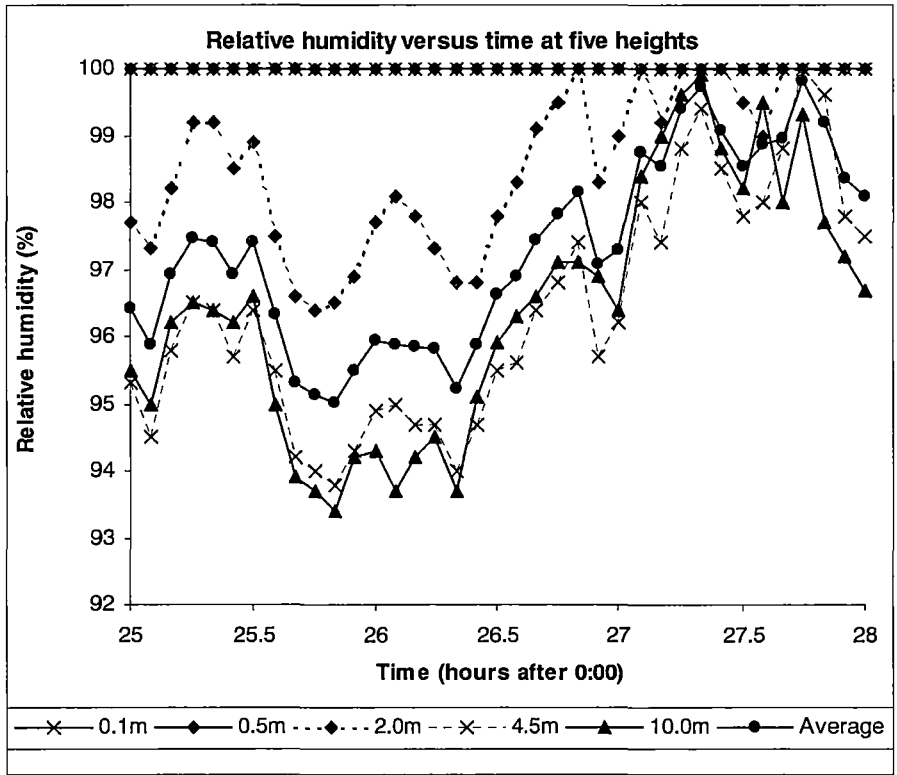


Figure 9.5e. Relative humidity at five heights and their height-weighted average, presented at five-minute temporal resolution. 25 – 28 hours, 18th of June.

Figure 9.5a shows that the upwelling divergence decreased between 23 and 25 hours and then increased steadily between 25 and 28 hours. The downwelling convergence increased slowly between 23 and 28 hours. The net divergence was initially weakly negative, becoming more strongly negative before increasing again and reaching a positive value at 28 hours. The air temperature stability index was small and consistent, increasing slightly during the course of the measurements. The component temperatures of the air temperature stability index (Figure 9.5b) followed the same trend with time, explaining the consistency in the air temperature stability index.

In Figure 9.5c it can be seen that the radiative divergence yielded weak to moderate predicted radiative warming between 23 and 27 hours and weak cooling at 28 hours. The total observed cooling was weak and consistent between 23 and 26 hours before increasing suddenly between 26 and 27 hours and then decreasing even more suddenly between 27 and 28 hours. Warming was observed at 28 hours.

The average relative humidity (Figure 9.5d) was essentially constant between 23 and 26 hours before increasing suddenly between 26 and 27 hours. Values were relatively high throughout the measurement period. The high-resolution data plotted in Figure 9.5e show that saturation was maintained at 0.1 and 0.5 metres throughout the plotted three-hour period, while occurring occasionally at other heights after 26.5 hours. A sudden increase in the relative humidity at all heights occurred at approximately 26.3 hours and again at 27 hours.

In summary, the data for the 18th of June demonstrated a sudden change from cooling to warming, corresponding to an increase in the relative humidity to saturation level. As with the 14th of May, the relative humidity was very high throughout the measurement period. In this case however, the cooling that drove the increase of the relative humidity was not radiative, as the radiative flux divergence indicated radiative warming at the time. As with the 13th of May, only low rates of actual cooling or warming were seen at all stages during the night and the stability index was very small. Also consistent with observations on the other nights, the Bureau of Meteorology's visibility and 'Present weather' records did not indicate the presence of fog or visible condensation.

The wind speed data for the 18th of June indicated that wind speeds were above six knots for the majority of the night, dropping to between 4 and 6 knots after 27 hours. As with other nights, the wind was likely to have had a destabilising effect and minimised the net radiative divergence by mixing the air layer and therefore weakening the inversion.

9.3 Synthesis of cooling mechanisms

This section summarises and explains the cooling and warming phenomena that were present on the various measurement nights. These were as follows:

1. The ground surface cooled rapidly in the early hours of the evening. Radiative heat loss to the sky caused the ground surface to cool rapidly in the absence of shortwave solar forcing. The shallow air layer nearest the ground was cooled by conduction, creating a sharp but shallow inversion close to the surface. This is consistent with published observations (Funk 1960, Elliot 1964). The inversion resulted in upwelling radiative divergence and downwelling convergence. Of these two, the upwelling divergence dominated, yielding net longwave divergence that cooled the ten-metre layer nearest the ground surface. This behaviour is in agreement with previous measurements under clear and calm conditions (Funk 1962). Turbulent and sensible heat fluxes played a role in mixing the air in the layer, somewhat countering the radiative cooling effect (Funk 1960, Nkemdirim 1978). Diminished radiative cooling was often coincident with increased horizontal half-hourly mean wind speed at ten metres, consistent with published observations (Funk 1962).
2. As the evening progressed, there was an overall decreasing trend in the net longwave radiative divergence. Such a decrease has been observed throughout the whole night in cross-axis measurements made in an urban canyon (Nunez and Oke 1976), where the decrease continued throughout the whole night. Along-axis measurements in the same study are more likely to correspond with measurements made over open ground, and showed an initial strong decrease, followed by a brief recovery at approximately 22 hours and then a further decrease. Recent measurements over open ground (Burns *et al* 2000) show the divergence decreasing from a maximum at 16 hours to a minimum at 20 hours, followed by a gradual increase between 20 hours and dawn. In this study, on all nights for which data were available, the net longwave divergence decreased from a maximum early in the night to a local minimum in the two hours between midnight and 02:00. On every night for which data was available at midnight and the early morning (1st, 10th, 13th of May and 18th of June), a local maximum was reached after this initial decline. For those nights with the required data (1st, 10th, 13th of May), the net longwave divergence again decreased to a minimum as daylight approached. Early measurements (Funk 1962)

showed that the magnitude and behaviour of the radiative cooling is highly sensitive to the thickness and position of the measured air layer.

3. In the early part of the night (before midnight), the cooling rate predicted by the radiative divergence generally corresponded well with the measured total cooling rate. During these hours the radiative divergence generally also corresponded to a moderate or strong inversion, measured by the air temperature stability index. Both of these observations are consistent with previous observations (Funk 1960) and with the theory (Mahrt *et al* 1998). In most cases however, increases in the radiative divergence after midnight were not reflected in the observed total cooling rate and also did not correspond to a moderate or strong inversion. In three cases (1st and 13th of May and 18th of June), destabilisation was accompanied by an increase in the horizontal wind speed at ten metres. Increased wind mixed the air mass, causing the destabilisation and generating downward sensible heat flux convergence that countered the cooling effect of the radiative divergence.
4. Steady cooling of the air layer increased the relative humidity and in some cases led to saturation of the layers nearest the ground. Saturation yielded condensation, which resulted in the release of latent heat that warmed the air. This warming effect was independent of the radiative divergence, which was considerably lessened by the destabilisation caused by the warming event. Warming due to the occurrence of condensation was observed on the 1st, 10th, and 14th of May and the 18th of June. In each case the condensation event followed a period of increased radiative cooling. This is consistent with observations (Funk 1962) that radiative fog formation was preceded by radiation cooling in the lowest ten metres and the occurrence of saturation in that layer. However the actual onset of fog in that case was dependent on the existence of stronger radiative cooling after the saturation event in the lowest layer. This behaviour was not observed on any night in this study, explaining the lack of full development of radiative fog. On the 13th of May, the effects of relatively strong wind countered the radiative cooling. The resulting total cooling rate was consistently small throughout the night, and saturation was never reached.

9.4 Summary

This chapter presented the results of nightly comparisons between radiative cooling rates and observed total cooling rates. The radiative cooling rates were based on the DCR's measurements and the 'virtual instrument' equations that were developed in Chapter 2 and

tested in Chapter 8. Further insight into the behaviour of the total cooling and its relationship with the radiative cooling was provided by measurements of relative humidity and temperature at five heights over the ten-metre layer closest to the ground.

Section 9.2 presented the results for each night and provided explanations for the observed behaviour. Section 9.3 detailed the common or consistent elements of that behaviour across all of the nights. The most striking of the results was the effect of the occurrence of saturation in generating condensation and therefore warming of the layer.

The key factors contributing to the occurrence of condensation were strong radiative cooling and high initial relative humidity. Strong radiative cooling served to advance the onset of condensation by increasing the relative humidity to saturation level. The resulting warming destabilised the layer and decreased both the radiative cooling and the relative humidity. It would be unsurprising to observe several occurrences of this cycle during a single night under conditions for strong radiative cooling and high relative humidity, such as the 14th of May. While radiative cooling data were not available between 22 and 28 hours on the 14th of May, the cooling rates and relative humidity during that night (plotted in Figures 9.6a and b below) indicate that there have indeed been multiple condensation events during that night. These plots include the data excluded from Figures 9.4c and d.

It is anticipated that further study could test a hypothesis regarding the relationship between the strength of the radiative cooling effect and the frequency of condensation events for a given night. It is proposed that strong radiative cooling and high relative humidity would yield a higher frequency of occurrence. Early measurements (Funk 1960) showed relatively high frequency (1 hour^{-1}) transitions between radiative cooling and warming, although these were not linked to the occurrence of condensation in that study.

The Bureau of Meteorology's 'present weather' records and visibility measurements did not record a decrease in visibility or a radiative fog event for any of the condensation events proposed above. An inquiry into the nature of the visibility measurements revealed that these were performed visually using distant landmarks as reference. The measuring position is at 22 metres elevation, at least 20 metres above the ground at the tower site. So it may be that either condensation did not occur at a sufficient level to yield visible droplets, or that visible droplets appeared near the ground but did not affect the line-of-sight to the distant landmarks used for visibility estimation.

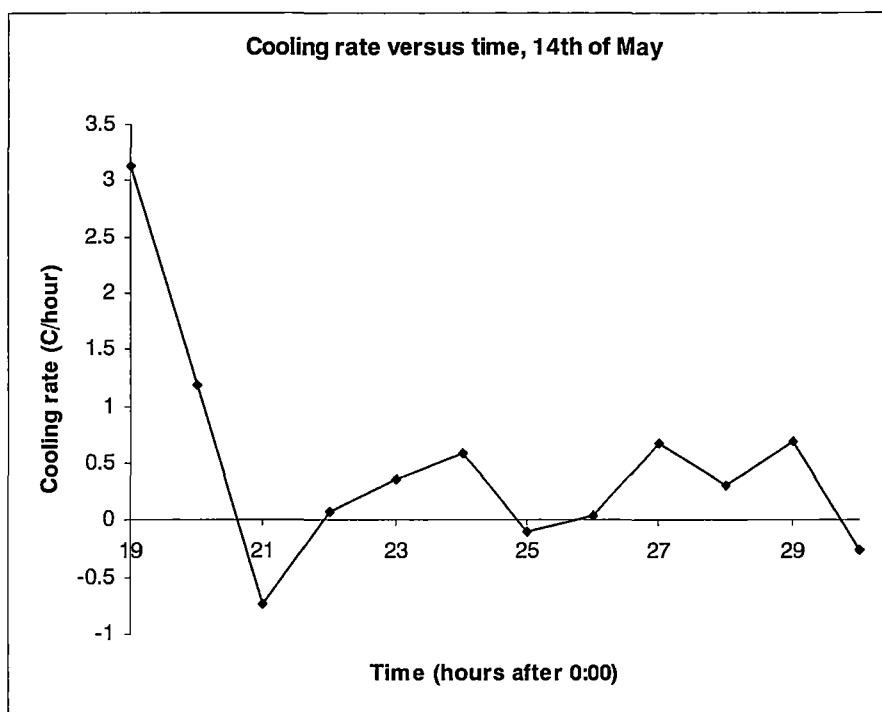


Figure 9.6a. Observed total cooling rate versus time, 14th of May. There is evidence of at least two sudden transitions from cooling to warming, between 19 and 21 hours and between 24 and 25 hours. In each case there is a slow recovery of the cooling rate following the warming event.

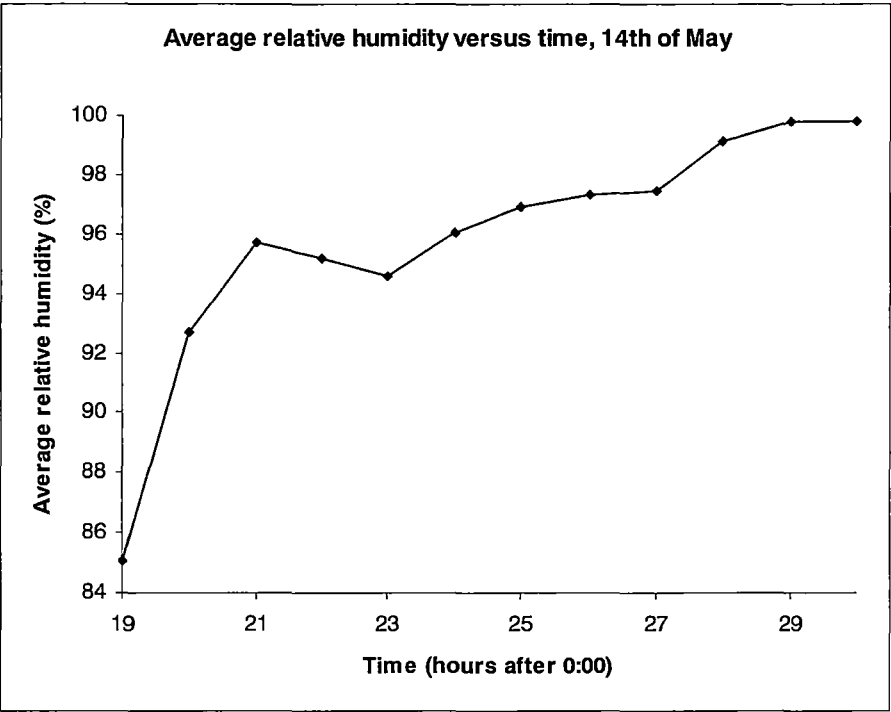


Figure 9.6b. Average relative humidity versus time, 14th of May. There is evidence of the decrease in relative humidity following the transition to warming at 21 hours, and a slowed increase after the transition to warming at 25 hours. In each case the increase resumes as the cooling rate recovers.

Chapter 10

Discussion and Conclusion

10.1 Virtual instrument

Chapter 2 described the development of a ‘virtual instrument’, a set of equations for the conversion of brightness temperature measurements into various radiative quantities. That development was based essentially on the concept that the majority of the atmospheric radiative activity in the longwave is represented by the activity in a narrow channel containing multiple active spectral bands. A measurement in such a channel could be contrasted or combined with a measurement in a channel containing few (if any) active spectral bands, yielding a unique estimate of the required quantity.

The accuracy of the ‘virtual instrument’ in predicting the required quantities would prove the case for the development of a real instrument for measuring brightness temperatures in two channels, and its use for prediction of real radiative quantities. The virtual instrument, if realised, would provide numerous advantages over traditional measurement methods, in particular overcoming the need to make measurements of longwave radiative flux at multiple heights in order to determine the radiative flux divergence.

The virtual instrument was developed using ensembles of input parameters and the MODTRAN radiative transfer model. The model produced values for quantities such as radiance, radiance divergence, irradiance and irradiance divergence. The model results were also converted to the expected measured brightness temperatures in the instrument’s two channels. Multiple linear regressions were then used to generate the equations that best predicted the final quantities from the modeled brightness temperatures. A summary of the accuracy of the various equations in subsequent testing is presented in Table 10.1 below (these were originally presented in Table 2.14).

Quantity	Equation	RMS error of prediction for test profiles (%)
Upwelling broadband radiance $R_{\uparrow B}$	(2.28)	10.1%
Upwelling irradiance divergence $divL_{\uparrow}$	(2.29)	10.0%
Downwelling broadband radiance $R_{\downarrow B}$	(2.33)	12.3%
Downwelling irradiance L_{\downarrow}	(2.34)	0.17%
Downwelling irradiance divergence $divL_{\downarrow}$	(2.35)	48.7%
Net irradiance divergence $divL^*$	(2.36)	25.3%

Table 10.1. The accuracy of the virtual instrument’s prediction equations for various quantities.

For most quantities the accuracy of prediction was of the order of 10% - significantly better for the prediction of downwelling irradiance L_{\downarrow} . The exception was the downwelling radiative divergence $divL_{\downarrow}$, which yielded an RMS error of 48.7%. The combination of that error with the RMS error of 10.0% for the upwelling radiative divergence yielded an RMS error in the net longwave radiative divergence $divL^*$ of 25.3%.

A revised form of equation (2.35) in Section 8.12 yielded a much lower RMS error of 7.7%. The revision was based on the measured profiles across five measurement nights. While not a conclusive reparameterisation, this indicated that the unrealistic nature of the profiles used to generate equation (2.35) in Chapter 2 was a significant contributor to the large errors. This reinforced the suitability of the method and indicated that the prediction could be further improved by the use of a more realistic ensemble of model profiles. The reparameterisation indicated that if the profiles used were constructed to represent a broad range of realistic conditions while avoiding unrealistic conditions, the accuracy of this prediction could be improved.

In general terms, Chapter 2 provided strong justification for the construction of a dual-channel radiometer for measuring the brightness temperatures necessary for prediction of the required quantities.

10.2 DCR design and construction

The DCR was incrementally designed, constructed, calibrated and tested over a two and a half-year period between January 2000 and June 2002. Details are provided in Chapters 3, 4 and 5. The calibrations were not finalised until after the measurement program had begun in May 2002 – Appendix A describes adjustments that were necessary for re-calibration of the data from most measurement nights.

The convergence to the final instrument design is described in Chapter 3. The finished DCR incorporated a pyroelectric detector within a blackbody cavity. The cavity was windowed to the outside through an alternating pair of filters corresponding to the instrument's two measurement channels. A chopping wheel provided the required modulation of the incident radiation, alternating between 'open' (free view) and 'closed' (reflective surface) states at approximately 1.1 Hz.

An important part of the instrument design was the development of a definition of a 'measurement'. The relatively high-frequency chopping cycle yielded multiple samples of the detector's response, which could then be averaged to improve the signal-to-noise ratio of the final value. A significant amount of testing was performed in order to establish an optimum measurement sequence that yielded a sufficiently accurate measurement without taking too long. The final sequence took approximately 2 minutes and 10 seconds to complete, yielded a single brightness temperature measurement in each channel. The measurement sequence was controlled external to the instrument using a Campbell CR10X data logger. The development of the measurement sequence is described in Chapter 4.

An instrument mount was constructed so that the instrument could be rotated during field measurement. The mount allowed a high degree of rotational control. It was also controlled by the CR10X datalogger, allowing complex sequences of measurements to be pre-programmed.

The field-of-view of the instrument was determined empirically by an experiment to be approximately $\pm 18^\circ$, wider than was initially expected based on the cavity design but sufficiently narrow for directional measurements. A further experiment yielded the optimum chopping speed for the instrument, which was balanced between the measurement speed, the weaker signal yielded by faster chopping and the elimination of microphonic noise in the detector due to the chopping motor.

The DCR was calibrated using a purpose-built blackbody source, filled with water and oil for ambient and cold temperature calibrations respectively. Because the detector's response was dependent on both the internal instrument temperature and the target temperature, the calibration required a broad as possible range of each. The final calibration (a combination of ambient temperature and cold-room calibrations) covered a range of 10 to 30°C of the instrument's internal temperature and -18 to 28°C target temperature. The lower limit on the range of target temperatures proved insufficient for window-channel measurements of the clear night sky. The errors in the brightness temperature measurements were limited to 0.42 and 0.37°C in the active and window channels respectively. Further analysis of the residuals yielded no consistent dependencies of the residuals on any of the measurable calibration parameters. The laboratory testing of the DCR is described in detail in Chapter 5.

10.3 DCR measurement results and cooling analysis

The field-testing of the DCR used data from a measurement program described in detail in Chapter 6. Chapter 7 details additional data from each measurement night, sourced from additional instruments that were part of the field installation and from data provided upon request by the Bureau of Meteorology.

Chapter 8 describes the conversion of measured brightness temperatures into the various quantities listed in Table 10.1. In the case of the downwelling longwave irradiance L_d , a direct radiometric comparison was available through data from the Eppley pyrgeometer. The comparison initially yielded poor results, with RMS errors of 66.3 W/m² for predictions using equation (2.34) and 50.0 W/m² for predictions using equation (2.33).

The results were improved by rejecting the data from the 30th July (see Section 8.4) and further by reparameterisation of equation (2.34) based on new model profiles that included variable visibility. The original profiles used the MODTRAN model's default mid-latitude winter visibility of 23km (see Appendix C). Even further improvement was gained by adjusting the window-channel brightness temperatures for a suspected change in the calibration curve below the calibration range of -18°C. These changes together yielded improvements in the RMS errors: 26.4 W/m² for the values predicted by the revised form of equation (2.34) and 9.3 W/m² for those predicted by the revised form of equation (2.33).

The accuracy with which the MODTRAN model predicted the Eppley-measured downwelling irradiance and the accuracy with which the prediction equations calculated it using modeled brightness temperatures indicated that the use of the prediction equations with a more accurate instrument calibrated over a wider range would yield significantly more accurate results.

Section 8.8 describes the comparison between DCR-measured and MODTRAN-modeled brightness temperatures in the instrument's active channel. Window-channel measurements were used as the ground temperature in the modeled profiles, which yielded coupling between the measured and modeled values of the window-channel brightness temperature. The RMS error in the active-channel data was 1.14 °C. A simple linear correction was applied to the measured values to compensate for the consistent differences between the two, and the corrected values were used for further calculations.

Upwelling radiance divergence $divR_{\uparrow}$ was predicted by equation (2.28) from the original DCR-measured brightness temperatures in Section 8.9. The RMS error between the predicted and modeled values was 0.94 W/m²/steradian. Using equation (2.28) to calculate $divR_{\uparrow}$ from the modeled brightness temperatures yielded an RMS error of 0.08 W/m²/steradian. The linear correction of the DCR's active-channel brightness temperature reduced the RMS error between the predicted and modeled values of $divR_{\uparrow}$ from 0.94 to 0.64 W/m²/steradian. Comparison of predicted and modeled values of $divR_{\uparrow}$ at angles away from the vertical (see Section 8.10) yielded an RMS error of 0.59 W/m²/steradian.

Prediction of the upwelling irradiance divergence $divL_{\uparrow}$ was possible via equation (2.31), which uses $divR_{\uparrow}$ predicted by equation (2.28), and equation (2.32), which uses the brightness temperatures directly. Equation (2.31) failed to properly predict $divL_{\uparrow}$ from modeled brightness temperatures and was therefore excluded from consideration with the measured brightness temperatures. Equation (2.32) predicted $divL_{\uparrow}$ from modeled brightness temperatures with an RMS error of 0.32 W/m², justifying its use with the measured brightness temperature data. The values predicted from corrected brightness temperatures gave an RMS error of 2.69 W/m² when compared with directly modeled values (see Section 8.11).

The downwelling irradiance divergence $divL_{\downarrow}$ was calculated by necessity from a combination of Eppley-measured L_{\downarrow} and MODTRAN-derived relationships between $divL_{\downarrow}$ and L_{\downarrow} (see Section 8.12). However a revised form of equation (2.35) was shown to be able

to calculate $divL_{\downarrow}$ from modeled brightness temperatures with an RMS error (against directly modeled values) of 0.32 W/m^2 , compared with an RMS error of 2.48 W/m^2 when the original form of equation (2.35) was used.

The net longwave radiative divergence $divL^*$ was calculated by subtraction of $divL_{\downarrow}$ and $divL_{\uparrow}$. It was then converted to a radiative cooling rate and compared with observed cooling rates that were calculated as part of the field program (see Section 9.1). The following phenomena were observed:

1. Upwelling radiative divergence $divL_{\uparrow}$ dominates the downwelling and yields positive net radiative divergence in the early hours of the night (between sunset and midnight).
2. The net longwave radiative divergence decreases as the night progresses.
3. Radiative cooling dominates the total cooling under calm, stable, clear-sky conditions before midnight. It is significantly suppressed by downward turbulent heat flux under stronger wind conditions.
4. Radiative cooling can lead to saturation of the air layer nearest the ground, causing condensation and therefore warming via the release of latent heat. These warming events destabilise the layer and decrease the relative humidity, and can occur repeatedly if domination by radiative cooling is able to resume. Condensation events can occur without the onset of radiation fog or visible condensation.

10.4 Extensions and improvements

The highest-priority improvement to the project would be the improvement of the accuracy of the radiometer. While the prototype version of the DCR used here had brightness temperature accuracy of approximately 0.4°C in both channels, ideally this figure would be of the order of 0.1°C . Many of the virtual instrument equations are highly sensitive to the brightness temperatures and errors in the temperatures translate to large errors in the predicted quantities. In this study it was not possible to find conclusive reasons for the differences observed between modeled and predicted values because any systematic inconsistencies were most likely masked by the effects of errors in the brightness temperature measurements. A more accurate radiometer would allow these differences to be meaningfully attributed to the possible failure of the virtual instrument equations.

Possible improvements to the DCR could be made via the use of a more sensitive detector and through adjustments to the instrument cavity to ensure a more stable and more easily measured internal instrument temperature. The calibration could possibly be improved via the use of a reference radiometer to test the blackbody output and provide side-by-side verification of the instrument output. A regulated internal blackbody for in-situ calibration could address the issue of calibration drift.

Ideally, the DCR could also produce measurements much more quickly than the two-minute measurements of the prototype version. This would allow for faster scanning of the instrument to build maps of the brightness temperatures over the full sphere of measurement. Internal scanning through the use of a mirror could then provide measurements across a range of zenith angles without the need for physical rotation of the instrument, which could then be used to rotate it through multiple azimuth angles to provide a full spherical or hemispherical map.

Assuming the use of the prototype version of the DCR, improvements could be made by extending the calibrated range of the instrument. This would allow more definitive comparison between predicted and modeled or Eppley-measured downwelling irradiance and would remove one barrier to direct DCR-based measurement of the downwelling irradiance divergence, which was impossible in Section 8.12 due to this problem.

For the virtual instrument development, improvements could be made through advances in computing power since the beginning of the project as well as insight gained throughout the project. The models used in Section 8.12 required almost two weeks of computing time – these would have required several months of computing time if performed on the same PC that was used for the modelling in Chapter 2. An extension to the virtual instrument development would allow for a broader ensemble of more realistic model profiles of temperature and relative humidity and incorporating variable visibility, carbon dioxide and other atmospheric constituents.

It is conceivable that a more generic virtual instrument could be developed, one that is not specific to the selected spectral channels. If the atmospheric band activity could be characterised in a more general fashion, then adaptation of the equations to specific filters might be possible without the need for a full re-development of the equations. As mentioned in Chapter 2, it might also be possible to generate an algorithm that ‘finds’ optimum channels in the spectrum by analysing the full broadband spectra from the model results.

For the field program, the obvious extension would be the addition of radiometers to provide reference values of radiant flux and radiative divergence. While these are not intended to be a part of field programs in which the DCR would replace them, comparisons in the testing phase would have served to validate either the predicted or modeled values wherever the two do not agree.

Extensions could also be made through the use of the radiometer in less spatially homogeneous conditions such as a forest canopy or urban canyon. This would require the scanning capability mentioned above. It would also require the development of a model for the conversion of the measured radiance divergences into an overall radiative divergence for the measured volume.

In summary, despite the broad range of obvious improvements, this project has proved the feasibility of the application of dual-channel radiance measurements to prediction of multiple radiative quantities. The full process has been described, including development of the required theory for a virtual instrument, the design and construction of a prototype radiometer and extensive field-testing of the prototype.

Bibliography

- Andre, J.C. and L. Mahrt, The nocturnal surface inversion and influence of clear-air radiative cooling, *J. Atmos. Sci.*, **39**, 864-878, 1982.
- Arnfield, A.J., Evaluation of empirical expressions for the estimation of hourly and daily totals of atmospheric longwave emission under all sky conditions, *Quart. J. R. Met. Soc.*, **105**, 1041-1052, 1979.
- Arnfield, A.J., An approach to the estimation of the surface radiative properties and radiation budgets of cities, *Phys. Geog.*, **3**, 97-122, 1982.
- Bergot, T. and D. Guedalia, Numerical forecasting of radiation fog. Part I: numerical model and sensitivity tests, *Mon. Wea. Rev.*, **122**, 1218-1230, 1994.
- Berk, A, L.S. Bernstein and D.C. Robinson, MODTRAN: A moderate resolution model for LOWTRAN 7, Spectral Sciences Inc., Burlington, MA, Rep. GL-TR-89-0122, 1989.
- Berk, A., G.P. Anderson, P.K. Acharya, J.H. Chetwynd, L.S. Bernstein, E.P. Shettle, M.W. Matthew, and S.M. Adler-Golden MODTRAN 4 User's manual, 1999.
- Brooks, D.L., A tabular method for the computation of temperature change by infrared radiation in the free atmosphere, *J. Meteorol.*, **7**, 313-321, 1950.
- Brunt, D., Notes on radiation in the atmosphere 1, *Quart. J. R. Met. Soc.*, **58**, 389-420, 1932.
- Brutsaert, W., On a derivable formula for long-wave radiation from clear skies, *Water Resour. Res.*, **11**, 742-744, 1975.
- Burns, S.P., J. Sun, A.C. Delaney, S.P. Oncley and T.W. Horst, Radiative flux divergence measurements during CASES-99, *14th Symposium on boundary layers and turbulence*, Aspen CO, Amer. Met. Soc., 2000.
- Cerni, T.A. and T.R. Parish, A radiative model of the stable nocturnal boundary layer with application to the polar night, *J. Clim. Appl. Meteor.*, **23**, 1563-1572, 1984.

- Chehbouni, A., Y. Nouvellon, Y.H Kerr, M.S. Moran, C. Watts, L. Prevot, D.C. Goodrich, S. Rambal, Directional effect on radiative surface temperature measurements over a semiarid grassland site, *Rem. Sens. Env.*, **76**, 360-372, 2001.
- Choudhury, B.J., R.J. Reginato and S.B. Idso, An analysis of infrared temperature observations over wheat and calculation of latent heat flux, *Agric. For. Meteorol.*, **37**, 75-88, 1986.
- Clerbaux, N., S. Dewitte, L. Gonzalez, C. Bertrand, B. Nicula and A. Ipe, Outgoing longwave flux estimation: improvement of angular modelling using spectral information, *Remote Sens. Environ.*, **85**, 389-395, 2003.
- Coantic, M. and B. Seguin, On the interaction of turbulent and radiative transfers in the surface layer, *Bound. Layer. Met.*, **1**, 245-263, 1971.
- Coll, C. and V. Caselles, A split-window algorithm for land surface temperature from advanced very high resolution radiometer data: validation and algorithm comparison, *J. Geophys. Res.*, 16697-16713, 1997.
- Delage, Y., A numerical study of the nocturnal atmospheric boundary layer, *Quart. J. R. Met. Soc.*, **100**, 351-364, 1974.
- Elliott, W.P., The height variation of vertical heat flux near the ground, *Quart. J. R. Met. Soc.*, **385**, 260-265, 1964.
- Estournel, C. and D. Guedalia, Influence of geostrophic wind on atmospheric nocturnal cooling, *J. Atmos. Sci.*, **42**, 2695-2698, 1985.
- Fasullo, J. and D. Sun, Radiative sensitivity to water vapor under all-sky conditions, *J. Climate*, **14**, 2798-2807, 2001.
- Feigelson, E.M., B.A. Fomin, A. Gorchakova, E.V. Rozanov, Yu.M. Timofeyev, A.N. Trotsenko and M. Daniel Schwarzkopf, Calculation of longwave radiation fluxes in atmospheres, *J. Geophys. Res.*, **96**, 8985-9001, 1991.
- Funk, J.P., Measured radiative flux divergence near the ground at night, *Quart. J. R. Met. Soc.*, **86**, 382-392, 1960.

- Funk, J.P., A numerical method for the computation of the radiative flux divergence near the ground, *J. Meteorol.*, **18**, 388-392, 1961.
- Funk, J.P., Radiative flux divergence in radiation fog, *Quart. J. R. Met. Soc.*, **88**, 233-249, 1962.
- Gaevskaya, G.N., K.Y. Kondratyev and K.E. Yakushevskaya, Radiative heat flux divergence and heat regime in the lowest layer of the atmosphere, *Arch. Meteorol. Geophys. Biokl.*, **B12**, 95-107, 1963.
- Gardner, W.K., G.K. McDonald, S.E. Ellis, M. Platt and R.G. Flood, A review of factors affecting minimum temperature reached on clear, windless nights, *Aust. J. Agric. Res.*, **42**, 191-203, 1991.
- Garratt, J.R. and R.A. Brost, Radiative cooling effects within and above the nocturnal boundary layer, *J. Atmos. Sci.*, **38**, 2730-2746, 1981.
- Garratt, J.R., Clear-sky longwave irradiance at the earth's surface – evaluation of climate models, *J. Climate*, **14**, 1647-1670, 2001.
- Grisogono, B., A mathematical note on the slow diffusive character of the long-wave radiative transfer in the stable atmospheric nocturnal boundary layer, *Bound. Layer Met.*, **52**, 221-225, 1990.
- Grisogono, B. and R.E. Keislar, Radiative destabilization of the nocturnal stable atmospheric boundary layer over the desert, *Bound. Layer Met.*, **61**, 1-12, 1992.
- Heinze, M., Pyroelectric detectors – application notes, *Web document*, Available: http://infratec.de/sensorik/application_en.shtml, 1999.
- Hossain, A. and M.H.Rashid, Pyroelectric detectors and their applications, *IEEE Trans. Ind. Appl.*, **27**, 824-829, 1991.
- Iziomon, M.G., H. Mayer and A. Matzarakis, Downward atmospheric longwave irradiance under clear and cloudy skies: measurement and parameterisation, *J. Atmos. Solar-Terr. Phys.*, **65**, 1107-1116, 2003.

- Jimenez, J.I., L. Alados-Arboledas, Y. Castro-Diez and G. Ballester, On the estimation of long-wave radiation flux from clear skies, *Theor. Appl. Climatol.*, **38**, 37-42, 1987.
- Karlsson, I.M., Nocturnal air temperature variations between forest and open areas, *J. App. Met.*, **39**, 851-862, 2000.
- Kobayashi, T., M. Mori and K. Wakimizu, An observational study of a thermal belt on hillsides, *J. Met. Soc. Japan*, **72**, 387-399, 1994.
- Kobayashi, T. and T. Takamura, Upward long-wave radiation from a non-black urban canopy, *Bound. Layer Met.*, **69**, 201-213, 1994.
- Kondo, J., O. Kanechika and N. Yasuda, Heat and momentum transfers under strong stability in the atmospheric surface layer, *J. Atmos. Sci.*, **35**, 1012-1021, 1978.
- Kondratyev, K.Y., Radiation processes in the atmosphere, WMO No. 309, Geneva, pp. 139.
- Koracin, D., B. Grisogono and N. Subanovic, A model of radiative heat transfer effects in the atmospheric boundary layer, *Geofizika*, **6**, 75-87, 1989.
- Kyle, T.G., The energy budget in a valley nocturnal flow, *Tellus*, **39A**, 226-234, 1987.
- Lagouarde, J., H. Ballans, P. Moreau, D. Guyon and D. Coraboeuf, Experimental study of brightness surface temperature angular variations of maritime pine (*pinus pinaster*) stands, *Remote Sens. Environ.*, **72**, 17-34, 2000.
- Legrand, M., C. Pietras, G. Brogniez, M. Haeffelin, N.K. Abuhassan and M. Sicard, A high-accuracy multiwavelength radiometer for in situ measurements in the thermal infrared. Part I: characterisation of the instrument, *J. Atmos. Ocean. Tech.*, **17**, 1203-1214, 1999.
- Leuning, R. and K.W. Cremer, Leaf temperatures during radiation frost part I. Observations, *Agric. For. Meteorol.*, **42**, 121-133, 1988.
- Leuning, R., Leaf temperatures during radiation frost part II. A steady state theory, *Agric. For. Meteorol.*, **42**, 135-155, 1988.

- Lhomme, J., N. Katerji, A. Perrier and J. Bertolini, Radiative surface temperature and convective flux calculation over crop canopies, *Bound. Layer Met.*, **43**, 383-392, 1988.
- Liang, S., Narrowband to broadband conversions of land surface albedo I, algorithms, *Remote Sens. Environ.*, **76**, 213-238, 2000.
- Mahrt, L., J. Sun, W. Blumen, T. Delaney and S. Oncley, Nocturnal boundary-layer regimes, *Bound. Layer Met.*, **88**, 255-278, 1998.
- McAtee, B. K., A.J. Prata and M.J. Lynch, The angular behaviour of emitted thermal infrared radiation (8-12 μ m) at a semiarid site, *J. App. Met.*, **42**, 1060-, 2003.
- Michael, K.J. and M. Nunez, Derivation of ocean-atmosphere heat fluxes in a tropical environment using satellite and surface data, *Int. J. Climate*, **11**, 559-575, 1991.
- Nkemdirim, L.C., A comparison of radiative and actual nocturnal cooling rates over grass and snow, *J. App. Met.*, **17**, 1643-1646, 1978.
- Nunez, M. and T.R. Oke, Long-wave radiative flux divergence and nocturnal cooling of the urban atmosphere II: within an urban canyon, *Bound. Layer Met.*, **10**, 121-135, 1976.
- Nunez, M. and D. Sander, Protection from cold stress in a eucalyptus shelterwood, *J. Climatol.*, **2**, 141-146, 1982.
- Okamoto, M. and J.P. Funk, The divergence of eddy heat flux and the temperature fluctuations in stable conditions, *Geophys. Mag. (Japan Meteorol. Agency)*, **35**, 135-150, 1971.
- Oke, T.R., The energetic basis of the urban heat island, *Quart. J. R. Met. Soc.*, **108**, 1-24, 1982.
- Olyphant, G.A., Longwave radiation in mountainous areas and its influence on the energy balance of alpine snowfields, *Water Resour. Res.*, **22**, 62-66, 1986.

- Otterman, J., T.W. Brakke, M. Fuchs, V. Lakshmi and M. Cadeddu, Longwave emission from a plant/soil surface as a function of the view direction: dependence on the canopy architecture, *Int. J. Remote Sens.*, **20**, 2195-2201, 1999.
- Pascal, R.W. and S.A. Josey, Accurate radiometric measurement of the atmospheric longwave flux at the sea surface, *J. Atmos. Oceanic Tech.*, **17**, 1271-1283, 2000.
- Philipona, R., Sky-scanning radiometer for absolute measurements of atmospheric long-wave radiation, *Applied Optics*, **40**, 2376-2383, 2001.
- Platt, C.M.R. and A.J. Prata, Nocturnal effects in the retrieval of land surface temperatures from satellite measurements, *Remote Sens. Environ.*, **45**, 127-136, 1993.
- Prata, A.J. and I.J. Barton, A multichannel, multiangle method for the determination of infrared optical depth of semitransparent high cloud from an orbiting satellite. Part I: formulation and simulation, *J. App. Met.*, **32**, 1623-1637, 1993.
- Prata, A.J., A new long-wave formula for estimating downward clear-sky radiation at the surface, *Quart. J. R. Met. Soc.*, **122**, 1127-1151, 1996.
- Rider, N.E. and G.D. Robinson, A study of the transfer of heat and water vapour above a surface of short grass, *Quart. J. R. Met. Soc.*, **77**, 375-401, 1951.
- Robinson, G.D., Notes on the measurement and estimation of atmospheric radiation 2, *Quart. J. R. Met. Soc.*, **76**, 37-51, 1950.
- Saunders, I.R. and W.G. Bailey, Longwave radiation modeling in mountainous environments, *Phys. Geog.*, **18**, 37-52, 1997.
- Schadlich, S, F.M. Gottsche and F.-S. Olesen, Influence of land surface parameters and atmosphere on METEOSAT brightness temperatures and generation of land surface temperature maps by temporally and spatially interpolating atmospheric correction, *Remote Sens. Environ.*, **75**, 39-46, 2001.
- Soux, A., T.R. Oke, M. Nunez and M. Wilson, Measuring Longwave Radiative Flux Divergence in an Urban Canyon, *Eos Trans. AGU*, 84(46), Fall Meet. Suppl., Abstract U51C-06, 2003.

- Sun, J., S.P. Burns, A.C. Delaney, S.P. Oncley, T.W. Horst and D.H. Lenschow, Heat balance in nocturnal boundary layers, *J. App. Met.*, **42**, 1649-1666, 2003.
- Swinbank, W.C., Long-wave radiation from clear skies, *Quart. J. R. Met. Soc.*, **89**, 339-348, 1963.
- Tjemkes, S.A. and P.G. Duynkerke, The nocturnal boundary layer: model calculations compared with observations, *J. App. Met.*, **28**, 161-175, 1989.
- Tjemkes, S.A. and F.T.M. Nieuwstadt, A longwave radiation model for the nocturnal boundary layer, *J. Geophys. Res.*, **95**, 867-872, 1990,
- Unsworth, M.H. and J.L. Monteith, Long-wave radiation at the ground. I: Angular distribution of incoming radiation, *Quart. J. R. Met. Soc.*, **101**, 13-24, 1975.
- Wan, Z and J. Dozier, A generalized split-window algorithm for retrieving land-surface temperature from space, *IEEE Trans. Geosci. Remote Sensing*, **34**, 892-905, 1996.
- Wilson, M.P. and M. Nunez, Nocturnal clear-sky directional downwelling infrared temperature measurements in a forest canopy, *Proc. SPIE Vol. 4168*, 124-133, 2001.

Appendix A

Calibration reversal procedure

A.1 Introduction

The calibration reversal procedure was made necessary by two facts. One was the change in calibration equation when the cold calibration data was combined with the original warm calibration data (see Chapter 5). The second was an error in the data logger program, yielding incorrect values for the instrument signal output and internal temperatures.

The change to the calibration equation could easily be implemented in post-processing if the correct values of S_i , $T_{i,1}$ and $T_{i,2}$ could be obtained. These are the properly averaged values from which the original data logger program calculated the brightness temperature T_i in each channel. The new equation could simply be applied to the values of the instrument output to generate new values for T_i .

The logger program should have been programmed to output the averaged measured values of S_i , $T_{i,1}$ and $T_{i,2}$ along with the calculated brightness temperatures. However the logger program was incorrectly programmed to output the final sample of each quantity rather than the average of 145 samples that was used to calculate the brightness temperatures. This Appendix details the procedure that was used to regenerate the correct (averaged) instrument output data so that the new calibration equation could be applied.

A.2 Data logger program output

The output from the data logger program contained the following values for each channel:

$T_i(\overline{S_i}, \overline{T_{i,1}}, \overline{T_{i,2}})$, S_i , $T_{i,1}$ and $T_{i,2}$. The brightness temperatures were calculated using the averaged values as denoted by the over bars, while the average values were not output directly. The logger program calculated the brightness temperatures T_i using equation (5.3) with the coefficients listed in Table 5.2. The aim of the calibration reversal was to recalculate $\overline{S_i}$, $\overline{T_{i,1}}$ and $\overline{T_{i,2}}$ using only the values output by the program.

A.3 Internal instrument temperature extrapolation

The difference between the averaged internal instrument temperatures and the individual output sample is illustrated in Figure B.1. It is obvious from the figure that a gradient of any measurable strength in the instrument’s internal temperature will not be properly reflected by the output value.

The average instrument internal temperature was extrapolated from the available output values. This was achieved through the assumption that the gradient of instrument internal temperature was linear over each measurement interval. This was a reasonable assumption given the stable nature of the instrument’s internal temperature (see Chapters 3 and 5). The small changes that would be expected over a 5-minute interval would be well characterized by a linear approximation.

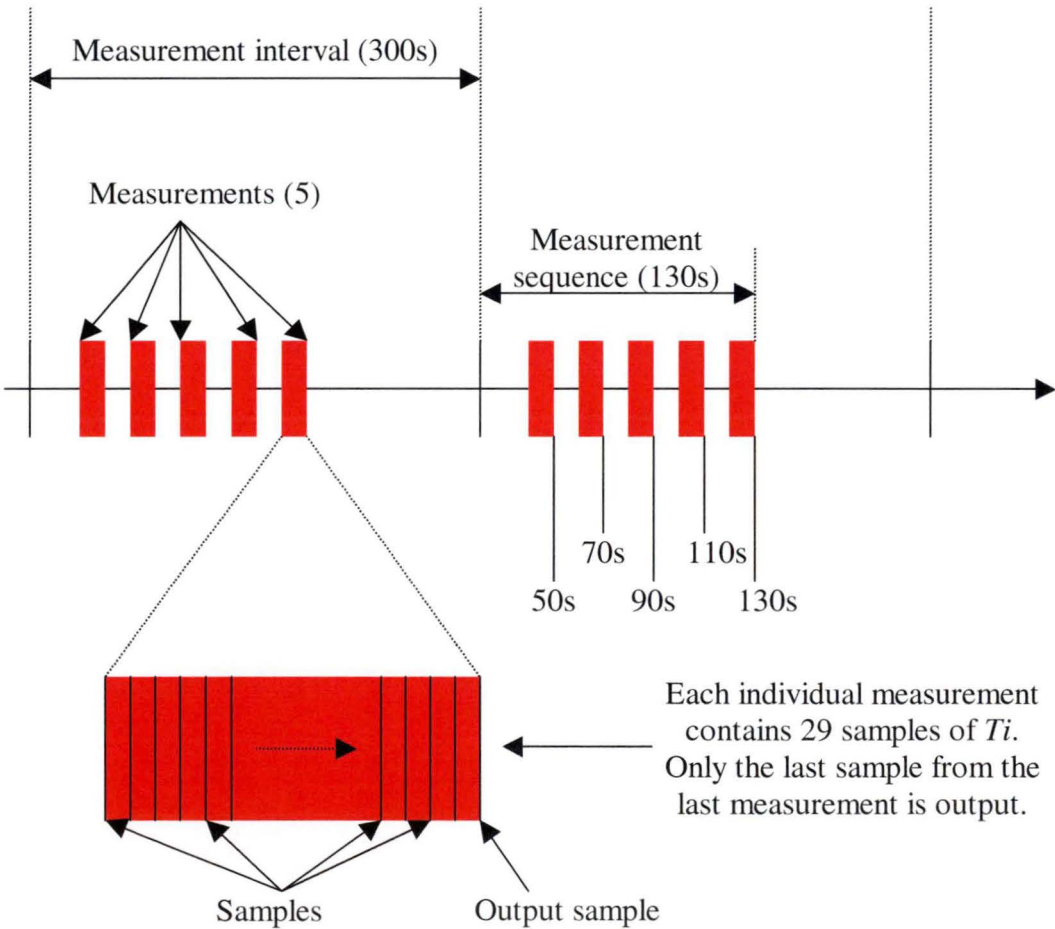


Figure A.1

The average temperature value for each measurement sequence was extrapolated from the gradient between one output sample and the next by the following equation:

$$\overline{Ti_{i,j}} = Ti_{i,j} - \frac{\sum_{k=1}^5 \Delta Ti_{i,j} \Delta t_k}{5}, \quad (\text{A.1})$$

where $\Delta Ti_{i,j}$ is the change in temperature from one sample output to the next, and Δt_k scales the gradient to the position of the measurement in the sequence. The values for Δt_k were calculated from each measurement's position in the sequence, scaled to the measurement interval. For the measurement times shown in Figure A.1 (50, 70, 90, 110, 130 seconds) the corresponding values of Δt_k were 0.27, 0.2, 0.13, 0.7, and 0.

With the values calculated by equation (A.1) approximating the original values of $\overline{Ti_{i,1}}$ and $\overline{Ti_{i,2}}$, the calibration equation could be restated in the following form:

$$c_{i,7} \overline{S_i} + c_{i,6} \sqrt{\overline{S_i}} + f_i = 0, \quad (\text{A.2})$$

with

$$f_i = -T_i + c_{i,1} + c_{i,5} \overline{Ti_{i,2}} + c_{i,4} \overline{Ti_{i,1}} + c_{i,3} \overline{Ti_{i,2}}^2 + c_{i,2} \overline{Ti_{i,1}}^2. \quad (\text{A.3})$$

Using the brightness temperature T_i that was calculated from the averaged instrument output values and the averaged instrument temperature values yielded by equation (A.1), the value of f_i was then calculated. Equation (A.2) was then solved as a quadratic in $\sqrt{\overline{S_i}}$, yielding the averaged value of $\overline{S_i}$.

The values of $\overline{Ti_{i,1}}$, $\overline{Ti_{i,2}}$ and $\overline{S_i}$ were tested by substituting them into the original calibration equation and calculating the difference between the resulting value for T_i and the value calculated by the data logger. If the averaged instrument output values calculated by the above method were correct then there should be no difference between the values for T_i . This test was performed for all recalibrated data and yielded a maximum difference of the order of 10^{-14} °C. This result validated the reversal of the calibration by the method described above.

Appendix B

‘Standard’ MODTRAN input data

B.1 Introduction

This Appendix describes a ‘standard’ MODTRAN input file, as used throughout the project. While many parameters such as the temperature and relative humidity profiles were varied to describe the model atmosphere at a given time, others were maintained throughout. Section B.2 contains an example input file and Section B.3 describes the contents of the file and the meaning of each parameter. Further information on the various parameters can be found in the MODTRAN users manual (Berk *et al* 1999).

B.2 Example MODTRAN input file

Below is the MODTRAN input file for 21:00 on the 10th of May. It includes a cloud layer as used in Section 8.13 to model liquid water droplets in the atmosphere at ground level. The following section examines each parameter in the file.

```
[Card 1]
t  7    3    1    1    0    0    3    3    3    3    1    1    1
0.00

[Card 1A]
t8   f2   355.0

[Card 2]
  1    0      0 3    1    0    0.000    0.00    000.0    0.00000
0.00000

[Card 2A]
-9.000 -9.000 -9.000 3   -9  0.000   -1.000  -1.000  86.70
0.000   0.000

[Card 2C]
86    0      0   Rural
```

[Card 2C1 (multiple)]
0.0000 1020.700 5.8000 86.7000 0 0
ABH3333333333 3

<Additional profile data>

40.0 3.33 -15.5 4.780E11 0 0
ABB3333333333 3

[Card 2E1 (multiple)]
0.00000 1.04000 0.00000 0.00000

0.01000 1.04000 0.00000 0.00000

0.01500 0.00000 0.00000 0.00000

[Card 3]
0.00001 0 180.0

[Card 4]
200 3333 2 2 rwmotranswla

[Card 5]
3

[Repeat Card 3]
0.001 0 180.0

<Additional height/angle combinations>

[Repeat Card 3]
0.050 0 180.0

[Card 5]
0

B.3 MODTRAN parameters

Card 1:

Parameter	Value	Description
MODTRN	t	Use MODTRAN band model
MODEL	7	Use a user-specified model atmosphere
ITYPE	3	Model a vertical or slant path to space or ground
IEMSCT	1	Execute program in spectral thermal radiance mode.
IMULT	1	Program executes with multiple scattering
M1	0	Use user-defined temperature data
M2	0	Use user-defined relative humidity data
M3	3	Use default mid-latitude winter profile for O ₃
M4	3	Use default mid-latitude winter profile for CH ₄
M5	3	Use default mid-latitude winter profile for N ₂ O
M6	3	Use default mid-latitude winter profile for CO
MDEF	1	Use default heavy species profiles (O ₂ , NO, SO ₂ , NO ₂ , NH ₃ , and HNO ₃)
IM	1	Use user-entered model profiles
NOPRNT	1	Minimise printing of radiance tables in tape 6
TPTEMP	<blank>	Use temperature of lowest layer for boundary temperature
SURREF	0.00	Surface albedo is zero (since brightness temperature incorporates emissivity)

Card 1A:

DIS	t	Use DISORT discrete ordinate multiple scattering algorithm
NSTR	8	Use 8 streams in the DISORT algorithm
LSUN	f	Use default 5cm ⁻¹ binned solar irradiance data
ISUN	2	Use 2 wavenumber FWHM triangular scanning function
CO2MX	355.0	Use CO ₂ mixing ratio of 355 ppmv
H2OSTR	<blank>	Use default vertical water vapour column
O3STR	<blank>	Use default vertical ozone column
LSUNFL	<blank>	Not applicable with LSUN set to 'f'
LBMNAM	<blank>	Use default 1cm ⁻¹ bin band model database
LFLTNM	<blank>	Not applicable since user-defined filter function not used
SOLCON	<blank>	TOA solar irradiance is irrelevant

Card 2:

APLUS	<blank>	Use default aerosol optical properties
IHAZE	1	Use rural extinction, default visibility 23.0 km
CNOVAM	<blank>	Do not use Navy Oceanic Vertical Aerosol Model
ISEASN	0	Determine season by value of MODEL
IVULCN	0	Use background stratospheric volcanic aerosol profile and extinction
ICSTL	3	Use default air mass character for NAM algorithm
ICLD	1	Cumulus cloud layer (set to 0 - no cloud – for all other models)
IVSA	1	Do not use the Army Vertical Structure algorithm for aerosols
VIS	0	Use default visibility set by IHAZE (the visibility was varied for the reparameterisation in Section 8.5 and for visibility tests in Section 8.13)
WSS	0.0	Wind speed irrelevant with this model
WHH	0.0	24-hour average wind speed irrelevant with this model
RAINRT	0.0	Rain rate is zero
GNDALT	0.0	Ground altitude relative to profile data is zero

Card 2A:

CTHIK	-9.0	Use default cloud vertical thickness (actual cloud thickness was set using card 2E1)
CALT	-9.0	Use default cloud altitude (actual cloud altitude was set using card 2E1)
CEXT	-9.0	Use default cloud liquid water droplet and ice particle vertical extinction
NCRALT	3	Use 3 user-defined cloud boundary layer altitudes in card 2E1
NCRSPC	-9	Use default spectral data for ICLD
CWAVLN	0.0	Use default cloud extinction reference wavelength
CCOLWD	-1.0	Do not scale cloud liquid water droplet vertical column density
CCOLIP	-1.0	Do not scale cloud ice particle vertical column density
CHUMID	86.7	Use the ground-level relative humidity (profile dependent) for the relative humidity at all layer boundaries with a positive cloud density
ASYMWD	0.0	Use default water droplet Henyey-Greenstein scattering phase function asymmetry factor at all wavelengths
ASYMIP	0.0	Use default ice particle Henyey-Greenstein scattering phase function asymmetry factor at all wavelengths

Card 2C:

ML	86	The user-defined atmospheric profile has 86 levels
IRD1	0	Do not use card 2C2
IRD2	0	Do not use card 2C3
HMODEL	Rural	Arbitrary name for the profile

Card 2C1 (executed 86 times, once for each profile level):

ZM	0.000	Altitude of layer boundary, zero for the first layer
P	1020.7	Pressure for the first layer
T	5.80	Temperature for the first layer
WMOL(1)	86.7	Relative humidity for the first layer
WMOL(2)	0	Use default CO ₂ for the first layer
WMOL(3)	0	Use default O ₃ for the first layer
JCHAR(1)	A	Pressure is in mb
JCHAR(2)	B	Temperature is in °C
JCHAR(3)	H	Relative humidity is in % (number density was used, with code H for levels at 25, 30 and 40 km)
JCHAR(X)	3	JCHAR was set to 3 (default for midlatitude winter) for X=4 to 14
JCHARX	3	Use default midlatitude winter parameter value for entire set of CFCs and other heavy molecules

Card 2E1 (3 repetitions for 3 cloud boundary layers specified by NCRA1T):

Note that card 2E1 was only used for the liquid water droplet tests in Section 8.13.

ZCLD(1,0)	0.00	Cloud base is at ground level
CLD(1,0)	1.04	Liquid water droplet density at 0 km level set to 1.04 g/m ³
CLDICE(1,0)	0.00	Ice particle density set to zero at 0 km level
RR(1,0)	0.00	Rain rate set to zero at 0 km level

Card 3:

H1	0.00001	Start of path or height of 'instrument' – 1cm was used to approximate ground level
H2	0.00	End of path (instrument was pointed at the ground)
ANGLE	180.00	Angle of path set to 180.00 (instrument pointed directly downwards)

Card 4:

V1	200	Initial frequency in wavenumber (cm^{-1})
V2	3333	Final frequency in wavenumber (cm^{-1})
DV	2	Frequency increment used for spectral outputs (cm^{-1})
FWHM	2	Slit function full width at half maximum (cm^{-1})
YFLAG	R	Radiances output to *.plt file
XFLAG	W	Output units for *.plt file set to wavenumbers
DLIMIT	modtrans	Text delimiter for output files
FLAGS(1:1)	W	Set units for input parameters V1, V2, DV and FWHM to wavenumbers
FLAGS(2:2)	1	Use triangular slit function
FLAGS(3:3)	A	FWHM is absolute
FLAGS(4:4)	<blank>	Degrade only total radiance and transmittance
FLAGS(5:5)	<blank>	Do not save non-degraded results
FLAGS(6:6)	<blank>	Do not use saved results
FLAGS(7:7)	<blank>	Do not write a spectral flux table

Card 5:

Two values were used for Card 5. A value of '3' repeated the model run using the same data with the exception of a new Card 3. This was used to produce output from a range of different modeled geometries (e.g 0 and 10m instrument position, upward looking and downward looking, 0, 15, 30, 45, 60 and 75° angle) in the same model run. A Card 5 value of '0' signaled the end of the run.

Appendix C

Analysis of the effects of errors in the measured temperatures on the quantities calculated by the predictive equations

This Appendix describes an analysis of the errors that would be introduced into the predictive equations by the presence of errors in the brightness temperatures measured by the DCR. For each equation, the process used to calculate the error was based on the data that was used to generate the equation. Where relevant, the temperatures that were used as inputs to the multiple regression fit were adjusted by the RMS error in their respective calibrations: 0.428°C for channel one and 0.390°C for channel two.

In every relevant case, the adjustments to the temperatures were made to yield the largest possible divergence in the input values. In cases where the inputs to the equation are derived from another equation and not directly from measured brightness temperatures, the error value calculated for the relevant equation was used to adjust the inputs.

The results of the predictive equation using adjusted input values were then compared to the results of the same equation using the original input values using root mean square error and mean bias error calculations. The results are presented in Table C.1 below. Results of the same calculations using temperature corrections of 0.1°C on each channel are shown in Table C.2 for comparison. The results in Table C.2 serve to illustrate the potential in accuracy that could be achieved using a more accurate instrument.

The derived errors are in some cases (particularly the upwelling irradiance divergence $divL_{\uparrow}$) alarmingly large but must be treated with some caution as their derivation was deliberately designed to reflect the extremes of the possible errors in the instrument's brightness temperature measurements. Their effects have also been magnified by the use of the RMS error in both cases and the deliberate adjustment of the values to yield the most divergent result. As would be expected, the calculations that involve the window-channel brightness temperature of the night sky yield much lower error values because the input temperatures are an order of magnitude larger in most cases.

In most cases the magnitude of the mean bias error is very closely (if not exactly) matched to the RMS error. This is to be expected due to the constant offsets that were applied in each case, which yielded a consistent bias across the predicted values.

Quantity	Units	Equation	Inputs	Adjustments to inputs	RMS Error	Mean bias error
$divR_{\uparrow}$	W/m ² /ster	2.28	$T_{\uparrow 1}, T_{\uparrow 2}$	$T_{\uparrow 1}-0.428,$ $T_{\uparrow 2}+0.390$	0.632	-0.629
$divL_{\uparrow}$	W/m ²	2.29	$divR_{\uparrow}(\theta)$	$divR_{\uparrow}(\theta) +$ 0.632	3.792	3.792
$divL_{\uparrow}$	W/m ²	2.31	$divR_{\uparrow}(0)$	$divR_{\uparrow}(0) +$ 0.632	2.14	2.05
$divL_{\uparrow}$	W/m ²	2.32	$T_{\uparrow 1}, T_{\uparrow 2}$	$T_{\uparrow 1}-0.428,$ $T_{\uparrow 2}+0.390$	2.59	-2.59
$R_{\downarrow B}$	W/m ² /ster	2.33	$T_{\downarrow 1}, T_{\downarrow 2}$	$T_{\downarrow 1}+0.428,$ $T_{\downarrow 2}-0.390$	0.0975	0.0975
L_{\downarrow}	W/m ²	2.34	$T_{\downarrow 1}, T_{\downarrow 2}$	$T_{\downarrow 1}+0.428,$ $T_{\downarrow 2}-0.390$	0.187	0.187
$divL_{\downarrow}$	W/m ²	2.35	$T_{\uparrow 1}, T_{\uparrow 2},$ $T_{\downarrow 1}, T_{\downarrow 2}$	$T_{\uparrow 1}-0.428,$ $T_{\uparrow 2}+0.390,$ $T_{\downarrow 1}+0.428,$ $T_{\downarrow 2}-0.390$	0.139	0.135

Table C.1: the results of the predictive equations developed in Chapter 2, using input values modified to represent the effects of the extremes of the instrument's inaccuracy.

The values in Table C.2, calculated using brightness temperature errors of 0.1°C in both channels, yield much lower errors as would be expected from a more accurate instrument. This emphasises the need for improved instrument design and performance as discussed in Chapters 5 and 10.

Quanityty	Units	Equation	Inputs	Adjustments to inputs	RMS Error	Mean bias error
$divR_{\uparrow}$	$W/m^2/ster$	2.28	$T_{\uparrow 1}, T_{\uparrow 2}$	$T_{\uparrow 1}-0.1,$ $T_{\uparrow 2}+0.1$	0.154	-0.154
$divL_{\uparrow}$	W/m^2	2.29	$divR_{\uparrow}(\theta)$	$divR_{\uparrow}(\theta) +$ 0.154	0.924	0.924
$divL_{\uparrow}$	W/m^2	2.31	$divR_{\uparrow}(0)$	$divR_{\uparrow}(0) +$ 0.154	0.567	0.560
$divL_{\uparrow}$	W/m^2	2.32	$T_{\uparrow 1}, T_{\uparrow 2}$	$T_{\uparrow 1}-0.1,$ $T_{\uparrow 2}+0.1$	0.633	-0.633
$R_{\downarrow B}$	$W/m^2/ster$	2.33	$T_{\downarrow 1}, T_{\downarrow 2}$	$T_{\downarrow 1}+0.1, T_{\downarrow 2}-$ 0.1	0.017	0.017
L_{\downarrow}	W/m^2	2.34	$T_{\downarrow 1}, T_{\downarrow 2}$	$T_{\downarrow 1}+0.1, T_{\downarrow 2}-$ 0.1	0.0724	0.0724
$divL_{\downarrow}$	W/m^2	2.35	$T_{\uparrow 1}, T_{\uparrow 2},$ $T_{\downarrow 1}, T_{\downarrow 2}$	$T_{\uparrow 1}-0.1,$ $T_{\uparrow 2}+0.1,$ $T_{\downarrow 1}+0.1, T_{\downarrow 2}-$ 0.1	0.0274	0.0257

Table C.2: the results of the predictive equations developed in Chapter 2, using input values modified to represent the increased accuracy that could be achieved through the use of a more accurate instrument with RMS calibration errors of 0.1°C on both channels.